COORDINATION CHEMISTRY INSPIRED BY NICKEL SUPEROXIDE DISMUTASE: UNDERSTANDING NICKEL AND SULFUR IN THE CONTEXT OF ANTI-OXIDANT DEFENSE

by

ERIC MICHAEL GALE

(Under the Direction of Todd Harrop)

ABSTRACT

Nickel superoxide dismutase (Ni-SOD) catalyzes the disproportionation of the cytotoxic superoxide radical ($O_2^{\bullet -}$) to O_2 and H_2O_2 via toggling between the Ni(II) and Ni(III) oxidation states. The Ni ion is found within a highly unusual coordination sphere. In the reduced (Ni(II)) resting state, the Ni coordination motif entails a primary amine from His1, an anionic carboxamido-N from Cys2 and two thiolato-S arising from Cys2 and Cys6 in a square-planar geometry. In the oxidized (Ni(III)) resting state, the geometry is square-pyramidal, with the imidazole-N from His1 occupying the apical position. In an effort to elucidate the molecular features imparting SOD activity to this unusual assembly, we have undertaken a synthetic modeling approach and prepared a library of targeted Ni-complexes accurately modeling aspects of the Ni-SOD active site. Employing synthetic protocols developed in our laboratory, we pursued a modular strategy allowing for modifications to specific ligand components while leaving other parameters unperturbed. Utilizing X-ray crystallography, spectroscopic analysis, electrochemical measurements and various reactivity studies, we probed the structural, electronic and reactivity effects imparted by fine tuning electronic contributions of singular components. Thus, we could effectively deduce the roles played by individual

molecular parameters. The results of the studies described in this dissertation provide experimental evidence supporting various hypotheses regarding mechanisms by which the coordinated cysteinates are protected from oxidative modifications under the harshly oxidizing conditions encountered during Ni-SOD catalytic turnover. In particular, we demonstrate that S-directed hydrogen-bonding is capable of providing kinetic protection against S-oxidation in the presence of reactive oxygen species. Our results also support a stabilizing role played by the His1 imidazole side chain for the highly unstable Ni(III) catalytic intermediate.

INDEX WORDS: Superoxide Dismutase, Metalloenzyme, Nickel, Sulfur

COORDINATION CHEMISTRY INSPIRED BY NICKEL SUPEROXIDE DISMUTASE: UNDERSTANDING NICKEL AND SULFUR IN THE CONTEXT OF ANTI-OXIDANT DEFENSE

by

ERIC MICHAEL GALE

B. A., Rutgers University, 2006

A Dissertation Submitted to the Graduate Faculty of The University of Georgia in Partial Fulfillment of the Requirements for the Degree

DOCTOR OF PHILOSOPHY

ATHENS, GEORGIA

2012

COORDINATION CHEMISTRY INSPIRED BY NICKEL SUPEROXIDE DISMUTASE: UNDERSTANDING NICKEL AND SULFUR IN THE CONTEXT OF ANTI-OXIDANT DEFENSE

by

ERIC MICHAEL GALE

Major Professor: Todd C. Harrop

Committee: Robert A. Scott

Michael K. Johnson

Electronic Version Approved:

Maureen Grasso
Dean of the Graduate School
The University of Georgia
May 2012

DEDICATION

For Veda Kumari and Turiya Devi LeVasseur, who breathe new life into all.

ACKNOWLEDGEMENTS

First and foremost, I would like to thank my mentor, Dr. Todd Harrop, for fostering an atmosphere for aspiring chemists to explore and thrive. Todd's passion for our research is contagious, and the precedence he has set has provided a template for myself and my colleagues to evolve into independent scientists. Our friendship will continue throughout my independent career and life.

In research, as in life, no man is an island. Success can rarely be attributed to individual virtue alone; much is dictated by the environment in which one finds himself situated. In this regard, I have been fortunate to not only benefit from wonderful mentorship but to share a laboratory with exceptional colleagues and dear friends. Brian Sanders, Vivian Ezeh, Dr. Ashis Patra, Melody Rhine, Phan Truong, Ellen Broering, Koustubh Dube and Wren Cheatum have shared in my successes and failures throughout the course of this dissertation and each has provided invaluable contributions. The good vibrations spill outside of the Harrop lab and down the hall to the Douberly and Salguero labs, also of youthful disposition and always willing to provide outside scientific perspective or a good laugh, depending on the situation. I am also indebted to spectacular collaborators: the efforts of Dr. Andy Simmonett and Beulah Narendrapurapu of the Schaefer Group and Dr. Darin Cowart of the Scott Group have been indispensable to expanding the scope of this dissertation.

I would also like to thank Dr. Michael Johnson and Dr. Robert Scott for their kind support throughout the course of this dissertation and beyond.

I must thank my parents and sisters for their support and the solid foundation they provide for me. I would also like to acknowledge the friends I have made during the course of my graduate career who have contributed to years I will never forget. Last, but certainly not least, I would like to thank my lovely girlfriend, Kristen Fries, for supporting me in all that I do.

TABLE OF CONTENTS

Page

CHAPTER 1

INTRODUCTION

1.1 Superoxide Overview

Superoxide ($O_2^{\bullet-}$) is a cytotoxic radical anion inevitably present in all aerobic life forms.[1-3] Elevated levels of this reactive oxygen species (ROS) have been associated with the onset of various disease states including cancer,[4-5] diabetes,[6] artherosclerosis,[7] neurological disorders such as Parkinson's[8] and Alzheimer's[9], as well as myocardial[10-12] and cerebral[13-14] ischemic-reperfusion injury.

$O_2^{\bullet-}$ is largely produced as an adventitious respiratory byproduct, representing incomplete reduction of O_2 to H_2O, the oxidative terminus of aerobic respiration.[1-3] It is predicted that up to 0.1% of oxygen consumed by bacterial cells results in the formation of superoxide, and studies utilizing *Escherichia coli* have pinpointed auto-oxidation of the respiratory enzymes formate reductase and NADH oxidase as the primary sources.[15-18] However, other species capable of oxygen reduction, such as reduced flavin cofactors, have also been implicated.[19-22] In eukaryotes, it is estimated that up to 4% of oxygen metabolism may result in superoxide,[18] and production is believed to largely arise from auto-oxidation of ubiquinol and NADH dehydrogenase, a redox cofactor and enzyme involved in mitochondrial electron transport, respectively.[23-25] $O_2^{\bullet-}$ production can also be induced in the immunoresponse. For

example, several phagocytes utilize NADPH oxidase to generate $O_2^{\bullet-}$ to aid in the destruction of pathogenic microbes.[26-27]

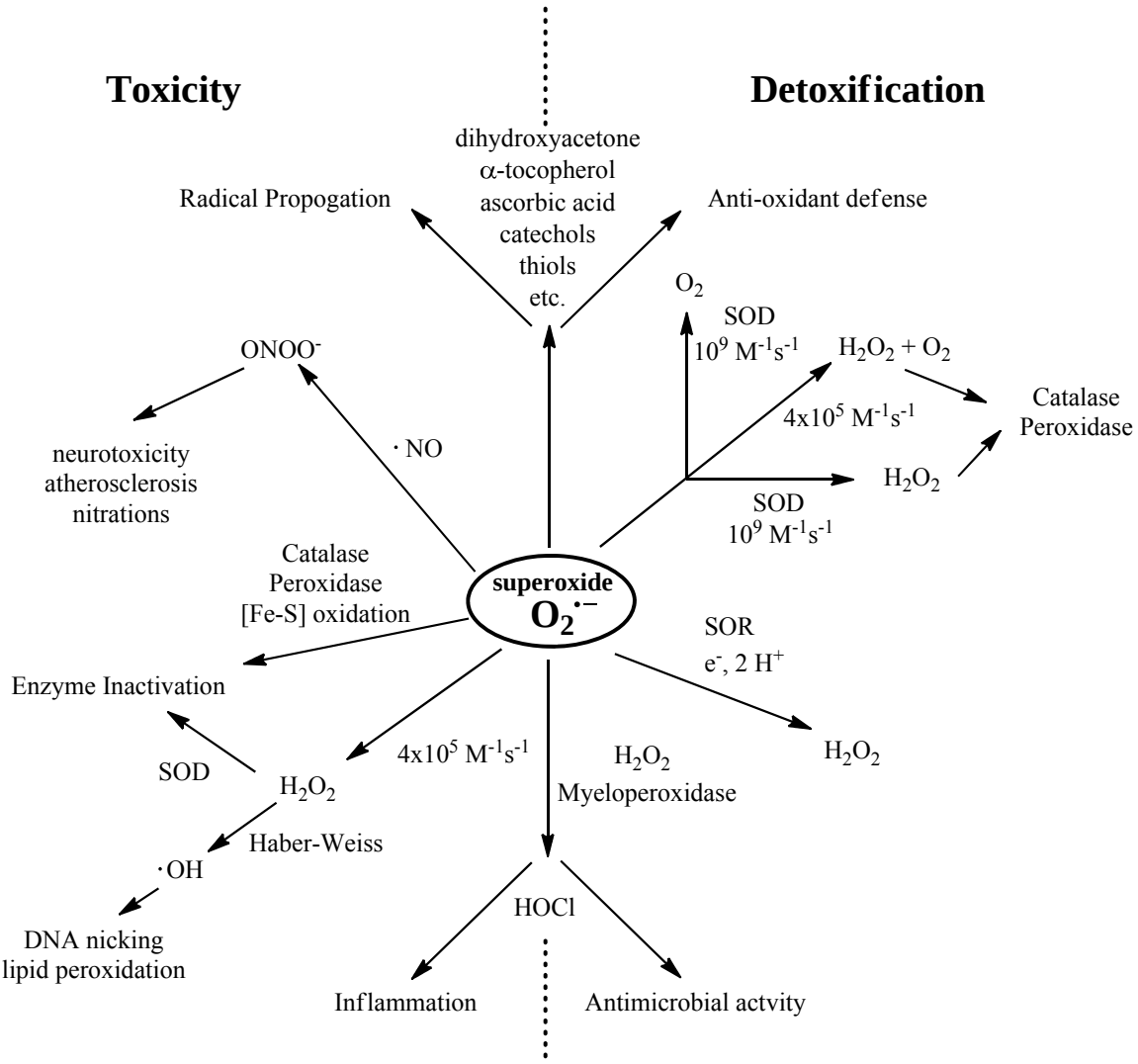

Figure 1. Schematic representation of some recognized roles of superoxide toxicity (left half) and methods of detoxification (right half) (Adapted from reference 1).

$O_2^{\bullet-}$ spontaneously disproportionates to hydrogen peroxide (H_2O_2) and O_2 at pH 7.4 at a rate of 4×10^{-5} $M^{-1}s^{-1}$, and much of the associated cytotoxicity can be attributed to stronger oxidants which descend from superoxide.[1] However, the disproportionation half-life of superoxide at normal intracellar concentrations (2×10^{-10} M) is 3.5 h, and the $O_2^{\bullet-}$ radical alone is capable of reacting with several specific intracellular entities in a deleterious fashion.[1] (See Figure 1)

Anti-oxidant enzymes such as catalase and glutathione peroxidase are inhibited by $O_2^{\bullet-}$,[28-29] and glutathione peroxidase activity is completely abolished via tandem treatment with $O_2^{\bullet-}$ followed by peroxides (the native enzymatic substrate).[29] Dehydratases such as 6-phosphoglucoate dehydratase,[30] aconitase[31-32] and fumarases A and B,[33] involved in glucose metabolism; and dihydroxyacid dehydratase,[34] involved in amino acid biosynthesis, represent another class of direct enzymatic targets of $O_2^{\bullet-}$. Dehydratase inactivation is generally believed to arise from $O_2^{\bullet-}$ oxidation of active site [Fe-S] clusters;[30-31] this is supported by the observation that the above listed enzymes can be reactivated by the addition of Fe(II) and an appropriate reductant.[30,35] Spectrophotometric monitoring of [Fe-S] clusters has proven useful in identifying sources of oxidative stress; the ratio of the active vs. inactive aconitase provides an accurate measure of intracellular $O_2^{\bullet-}$ concentration in live cells.[36] In fact, aconitase oxidation has also been implicated as a "circuit breaker" for aerobic metabolism, hindering the process by which further $O_2^{\bullet-}$ is formed.[31]

$O_2^{\bullet-}$ is also capable of interacting with several redox cofactors and metabolites including catechols,[37-38] α-tocopherol,[38-39] dihydroxyacetone,[40] thiols[41] and ascorbic acid.[38,42] Generally, these species serve as anti-oxidant defense systems,

but molecular interactions with $O_2^{\bullet-}$ can lead to propagation of further radical species capable of damaging cellular components.[43] Superoxide can also couple with endogenously produced nitric oxide (·NO) to form peroxynitrite ($ONOO^-$),[44] an extremely reactive species causing the oxidative nitrosylation of aromatic amino acids[45-47] and implicated in atherosclorис[48-49] and neurological damages.[50-53] Yet another mode of $O_2^{\bullet-}$ toxicity arises from its role as the reductant in the catalytic Haber-Weiss reaction, perpetuating a process by which H_2O_2 is converted to the severely toxic hydroxyl radical (·OH) by free Fe(II).[54-55]

The perhydroxyl radical (·OOH), the conjugate acid of $O_2^{\bullet-}$, has been associated with the oxidation of unsaturated fatty acids,[56] causing harm to cellular membranes, and oxidative lesions in DNA.[57] However, with a pK_a of 4.8,[1] perhydroxyl is a minor constituent, representing ~0.02% of the $O_2^{\bullet-}$ speciation under normal cellular conditions.[18]

1.2 Superoxide Dismutase

In order to manage $O_2^{\bullet-}$ concentrations and reduce the likelihood of the aforementioned hazards, aerobic organisms have ubiquitously developed an enzymatic defense system known as superoxide dismutase (SOD).[58-60] The SOD enzymes operate via alternate oxidation and reduction of $O_2^{\bullet-}$ to O_2 and H_2O_2, respectively (Scheme 1).[58-60] This disproportionation reaction operates near the diffusion control limit (10^9 M^{-1} s^{-1}).[1,60] All SODs utilize redox active metal cofactors to affect this reaction, carefully tuned by the coordination environment and overall protein architecture to operate at potentials within the window defined by the SOD

half reactions; -0.04 to 1.09 V vs Ag/AgCl (-0.16 to 0.89 V vs. NHE) at pH 7.0.[3,60] The three general isoforms of SOD can be classified according to the transition metal cofactor employed; Cu/Zn,[61] Mn[62] or Fe,[63-64] and the more recently discovered Ni containing SOD.[65-66]

$$\mathbf{M^{ox}} + O_2^{\bullet -} \longrightarrow \mathbf{M^{red}} + O_2 \qquad (1)$$

$$\mathbf{M^{red}} + O_2^{\bullet -} + 2\,H^+ \longrightarrow \mathbf{M^{ox}} + H_2O_2 \qquad (2)$$

Scheme 1. Chemistry of superoxide dismutase split into half reactions.

The Cu/Zn containing SOD is found in the cytoplasm of all eukaryotes and some bacterial organisms. It is known as SOD1 and SOD3 in humans, and mutations to this enzyme have been linked to amyotrophic lateral sclerosis (ALS, commonly known as Lou Gehrig's Disease).[67-69] Cu/Zn-SOD serves as the first entry into SOD biochemistry. This seminal discovery occurred in 1969, when McCord and Fridovich found that a Cu containing protein, originally coined hemocuprein,[70] inhibited the $O_2^{\bullet -}$ mediated reduction of cytochrome *c* by xanthine oxidase, representing the first realization of an SOD.[71-72]

Crystallographic characterization of Cu/Zn-SOD revealed a dimeric structure of identical Greek key eight-stranded *β*–barrel subunits connected via disulfide linkages, each containing one active site (Figure 2).[73-74] The active site resides at the outside of the *β*–barrel between two external loops,[73-74] at the terminus of a 3 Å × 5 Å substrate channel providing electrostatic guidance to the $O_2^{\bullet -}$ ion.[75]

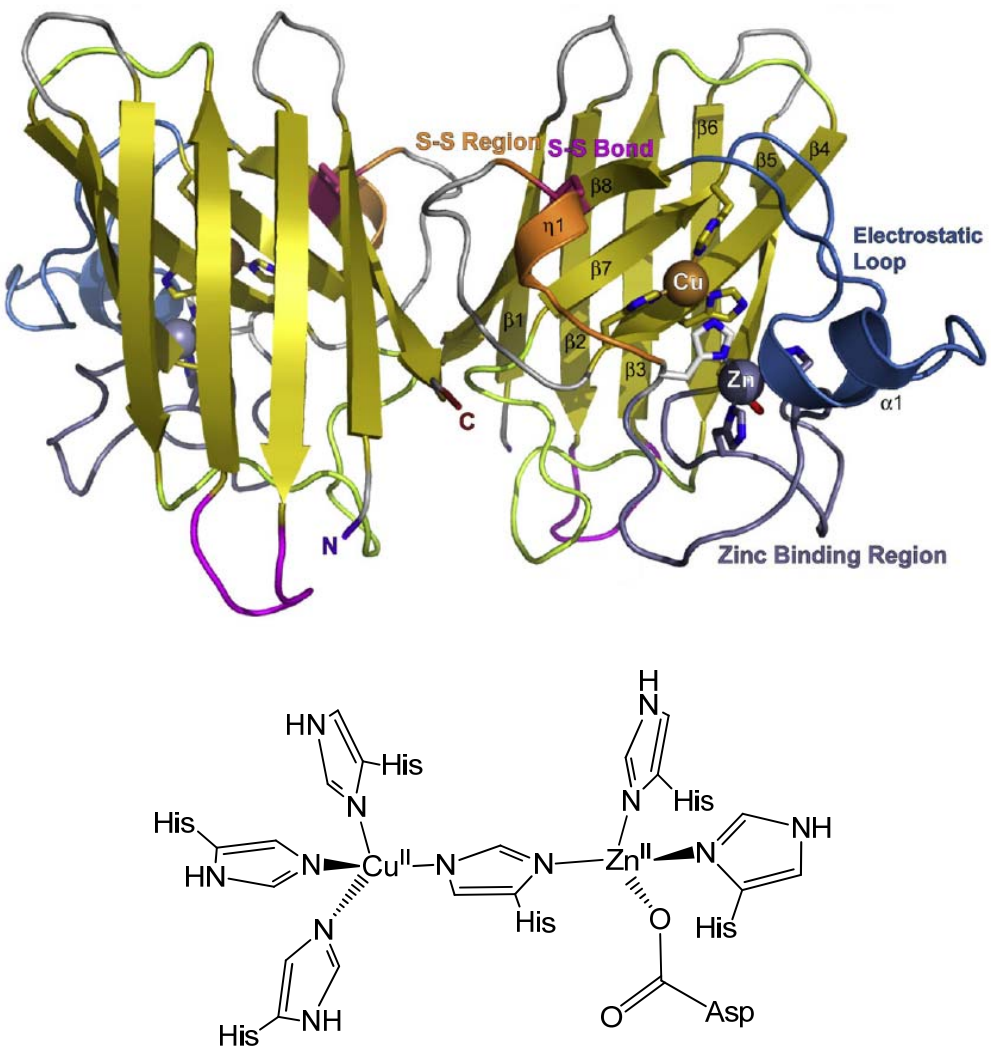

Figure 2. Crystal structure of Cu/Zn-SOD[60] from *Homo sapiens* (PDB code: 1SOS) (top) and depiction of the Cu/Zn active site in the catalytically active oxidized (Cu(II)) state (bottom).

In the oxidized (Cu(II)) resting, the active site Cu resides in a distorted square pyramidal environment and is bound by the imidazole side chains of four histidine residues, one of which is in the deprotonated form (Figure 2), as well as a coordinated H_2O.[61,74] This bound H_2O is not believed to be present during catalysis, leaving a vacant site at the Cu center for $O_2^{\bullet-}$ binding. The anionic imidazolate ligand is

bridged to the active site Zn(II) ion, found roughly 6 Å from the Cu center. Coordination of the Zn(II) ion is completed by two histidines and an aspartic acid.[61,74] It should be noted that the residue sequencing of Cu/Zn-SOD may vary depending on the organism from which it is isolated, but the ligands employed remain constant.[60,76] Upon reduction to Cu(I), the bridging histidine becomes protonated and dissociates from the Cu center.[76-77] It is believed that this bridging imidazolate, along with a protonated water/ arginine adduct, serve as a proton source during the reductive (with respect to $O_2^{\bullet-}$) half reaction.[61,76] This hypothesis is corroborated by the finding that the SOD activity is pH-independent over the range of pH 5.0–9.5,[78] indicative of a proton source buried within the active site, whereas the Zn-free congener displays pH-dependent activity.[61] It is also likely that the bridging interaction with the Zn ion serves to tune the pK_a of the imidazole functional group to a value capable of providing protons to the hydroperoxide anion (OOH^-).

The Mn- and Fe- containing SODs are structurally similar, share identical coordination spheres and operate via analogous mechanisms.[60] Mn-SOD is found in the mitochondria of eukaryotic cells,[62] where $O_2^{\bullet-}$ and ROS production is greatest.[18,79] In humans, mitochondrial Mn-SOD is often referred to as SOD2.[60] Both Mn and Fe forms can be found in the cytoplasm of bacterial organisms.[63] In fact, Mn- and Fe-SOD have been implicated in the protection of various facultative intracellular pathogens, enabling survival and replication within the macrophages deployed to destroy them.[80]

The monomeric subunits amongst the Mn- and Fe-SODs comprise two domains; an N-terminal helical hairpin domain consisting of two anti-parallel α-

helices, and a large C-terminal globular domain formed from three anti-parallel β-sheets and five α-helices.[62,81-83] The degree of multimerization varies depending on the organism in which the SOD is found, and is controlled by the helical N-terminal domain.[60,62] The majority of the bacterial structures are dimeric in nature,[60] and that from human SOD2 exists as a homotetramer (Figure 3).[62]

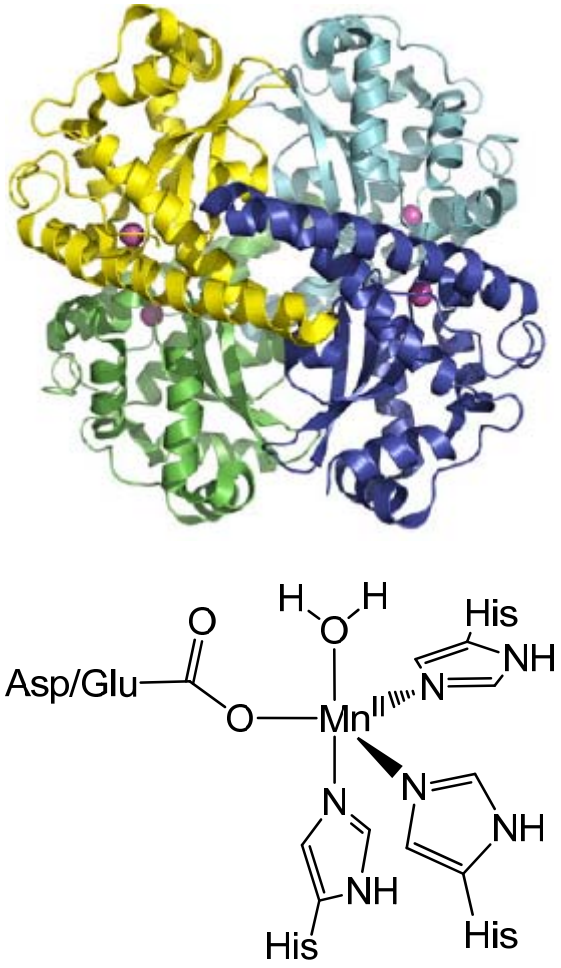

Figure 4. Cystal structure of Mn-SOD from *Homo sapiens*,[60] (PDB code: 1LUV) (top) and depiction of the Mn-SOD active site in the reduced (Mn(II)) state (bottom).

The active site of Mn- and Fe-SOD is located near the subunit interface[62,83] and consists of the metal ion in a trigonal bipyramidal coordination sphere, ligated

equatorially by two histidine imidazoles and a carboxylate from an aspartic acid or glutamic acid, and axially by a histidine imidazole and coordinated H_2O molecule (Figure 3).[63,84] Access to the active site is believed to be controlled by a "gatekeeper" tyrosine residue, which has been shown to aid in the rapid release of H_2O_2.[85-86] Mutations to this residue result in decreased catalytic rates and a build-up of product inhibited complex.

Inner vs. outer sphere electron transfer to and from the metal center remains a subject of study regarding the catalytic mechanism of Mn- and Fe-SOD. Crystal structures of azide (N_3^-) inhibited Mn- and Fe-SOD in the oxidized state (SOD_{ox}) reveal the N_3^- ligand coordinated to the metal center affording a distorted octahedron.[63] Spectroscopic and computational studies point towards an Mn-OOH complex for peroxide inhibited Mn-SOD,[87-88] lending credence to an inner sphere mechanism for the reductive half reaction. However, it has also been demonstrated that fluoride, an electrostatic mimic of $O_2^{\bullet-}$,[3] can inhibit the SOD activity by blocking the substrate channel in a non-coordinative fashion, somewhat obscuring the picture, and perhaps suggesting that the oxidative half reaction may occur via an outer sphere mechanism.[89]

The coordinated H_2O of Mn- and Fe-SOD is believed to play a role in proton transfer during catalysis, effectively storing a proton during $O_2^{\bullet-}$ oxidation and providing a proton during the reductive half reaction, resulting in an Mn- or Fe-OH adduct.[90] This H_2O is involved in an extensive hydrogen bonding network that extends to solvent exposed residues.[62] This arrangement likely serves to modulate the pK_a of the coordinated water molecule allowing proton transfer to a nascent

hydroperoxo species, and it is possible that protons may shuttle across this network to the active site.[60] Furthermore, slight mutations to residues involved in this hydrogen bonding system result in a marked decrease in catalytic activity.[91-92]

An interesting aspect of the Mn- and Fe- containing SODs is that despite the similarities in structure, homology and coordinating ligands, substitution of Fe for Mn (or *vice versa*) generally results in a catalytically inactive protein.[60,64] Substitution of Fe into Mn-SOD affords an indistinguishable chromophore to that observed in the native Fe-SOD, suggestive of identical active site geometric and electronic features.[93] Potentiometric titrations revealed that this inactivity can be ascribed to a redox mismatch with regards to $O_2^{\bullet-}$ dismutation imparted by metal substitution.[94] For example, substitution of Fe into Mn-SOD resulted in a redox potential of -0.240 V vs. NHE, a potential capable of reducing $O_2^{\bullet-}$, but incapable of performing the subsequent oxidation.[94] Analogously, substitution of Mn into Fe-SOD resulted in a complex with too great an oxidation potential to affect $O_2^{\bullet-}$ reduction.[94] Combined quantum mechanical/molecular mechanics calculations were also performed on a mutant featuring a glutamic acid in the place of a conserved secondary sphere glutamine in Fe substituted Mn-SOD.[93] The glutamine replaced is a participant in the above described hydrogen-bonding network extending from the metal bound H_2O to the surface of the protein. The calculations revealed that this change in hydrogen bonding residues resulted in pK_a modulation of the bound H_2O, and ultimately an increase in the potential of the proton-coupled redox event.[93,95] Upon close inspection of the protein tertiary structure, it is evident that subtle differences exist between the Mn and Fe congeners in the hydrogen-bonding networks leading to the active site,

and the results of this study highlight the drastic role secondary sphere residues can play in redox tuning of the catalytic metal center.[93,95]

The Ni-containing SOD represents the most recent entry to the SOD family. Ni-SOD is unique from the other SOD enzymes in terms of protein fold and active site, utilizing unusual N-donors such as an N-terminal amine and anionic carboxamido-N, along with cysteine thiolates, as ligands. Ni-SOD highlights an unusual role for both Ni and S in catalysis, neither of which are typically employed in enzymatic ROS control. Studies regarding unusual assembly and catalytic mechanism of Ni-SOD provide the main focus of the research described in this thesis.

1.3 Nickel-Containing Enzymes

Before beginning discussion on Ni-SOD, some background information on Ni-containing enzymes is required. To date, there are several enzymes which display Ni-dependent catalysis.[96-98] Urease,[99-101] NiFe-hydrogenase,[102-104] carbon monoxide dehydrogenase/acetyl coenzyme A synthase (CODH/ACS)[105-106] and methyl coenzyme M (CoM) reductase[107] represent the more well studied systems. However, an increasing number of metalloenzymes that display activity when nickel is introduced as a cofactor are appearing in the literature. These enzymes are involved in a diverse array of biological roles including glyoxal detoxification,[108-109] biosynthesis of methionine[110-113] and phosphoglycerolipids,[114] flavin metabolism[115] and the hydrolysis of urea-formaldyhede biopolymers.[98] The discussion below, however, will be limited to NiFe hydrogenase, CODH/ACS and methyl-CoM reductase, as these

enzymes utilize Ni as a redox cofactor, and provide discussion most relevant to the Ni-SOD catalytic mechanism.

NiFe-hydrogenase catalyzes the reversible oxidation of hydrogen gas (H_2) to protons (H^+),[102-104] performing a function that plays a pivotal role in the metabolism of several anaerobic microorganisms.[116] Most frequently, NiFe-hydrogenase is utilized in the uptake of H_2 in order to provide electrons for the reductive metabolism of O_2,[117] N_2,[117] SO_4^{2-},[118] or CO_2,[119] or to provide a H^+ gradient across cellular membranes.[98] However, under the proper conditions hydrogenase activity in the reductive direction can also be achieved, although this activity is generally the domain of the FeFe-hydrogenase enzyme.[120]

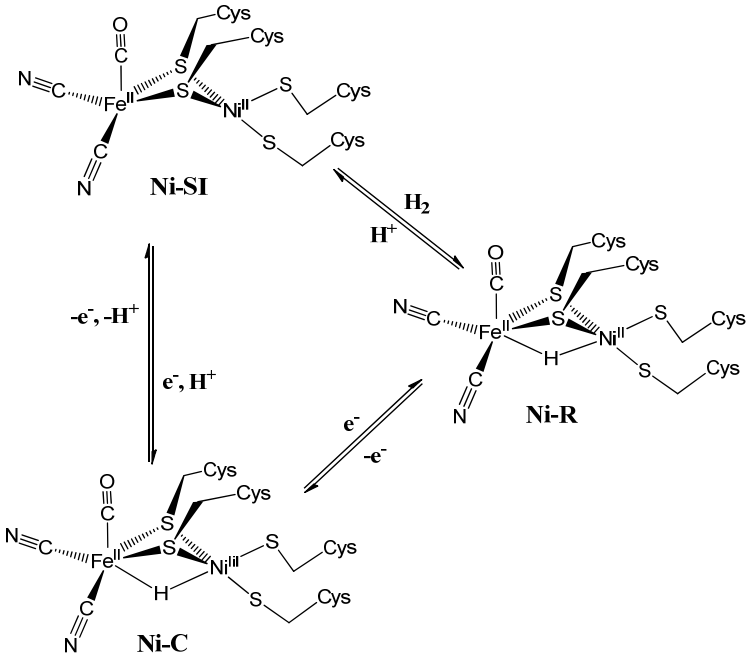

Figure 4. Proposed mechanism for reversible H_2 oxidation at the active site.

NiFe-hydrogenase is a heterodimeric protein with the dinuclear active site residing deep within the large subunit (Figure 4). The Ni ion is coordinated by four

cysteine residues, arising from two separate Cys-X-X-Cys motifs, in a distorted tetrahedral environment.[102-103] Two of the bound cysteinates are bridged to the neighboring low spin Fe(II) center, further coordinated by two cyanides (CN^-) and a carbon monoxide (CO),[121] completing a square pyramidal ligand arrangement (Figure 4).[102-103]

The mechanism of NiFe-hydrogenase has been much debated, and the precise mechanistic details remain unresolved to date.[97,122] The mechanistic picture at present is largely dictated by structural and spectroscopic analysis of the enzyme observed in several active[123-125] and inactive[126-127] states. Of the multiple species characterized, only three are considered relevant to the catalytic cycle; the state termed Ni-C features an oxidation state best described as Ni(III)Fe(II) with a hydride bridging the dinuclear active site, that termed Ni-R can be described as Ni(II)Fe(II) with a bridging hydride, and a state assigned as Ni(II)Fe(II) without a bridging hydride is coined Ni-SI (Figure 4).[125,128]

Access of H_2 to the NiFe-hydrogenase active site is provided by a hydrophobic tunnel extending several nanometers from the protein surface.[129-130] Once H_2 oxidation has taken place, the resultant electrons harvested are transported along a dyad of iron-sulfur clusters to a docked cytochrome.[131-132] The resultant H^+ ions are shuttled from the active site via an extensive network of hydrogen-bonding residues[133-134] which is believed to include active site cysteinates.[135-137]

H_2 represents a clean form of energy and the hydrogenase enzymes have been intensely studied as a potential means of clean and cheap H_2 production.[120,138] Along with fundamental studies regarding the structural biology and mechanism of the

hydrogenases, current efforts involve the study of enzyme immobilization on electrodes[139-141] or coupling to light harvesting systems[142] in efforts to achieve H_2 production via an electrochemical bias or photodriven processes, respectively. Although the FeFe-hydrogenase tends to be associated with H_2 production, the NiFe-hydrogenase system seems the most promising for practical application, as inhibition by O_2 is reversible whereas inhibition to the FeFe congener is irreparable.[140] It has recently been demonstrated that NiFe-hydrogenase enzymes containing a selenocysteine residue in place of an active site cysteine can catalyze H_2 production in the presence of oxygen.[143] In a related study, it has also been shown that mutation of valine and leucine residues in the hydrophobic substrate channel to methionine affords an air stable NiFe-hydrogenase.[144] The precise mechanistic explanations regarding how these subtle modifications impart O_2 tolerance remain unresolved at present. Studies regarding NiFe-hydrogenase will likely intensify as further promising developments unfurl and the environmental and economic problems associated with fossil fuels become increasingly pressing.

CODH/ACS is a bifunctional enzymatic system which catalyzes the reversible reduction of CO_2 to CO followed by the incorporation of CO into acetyl coenzyme A (CoA-SAc).[105-106,145] This process is an integral part of the Wood-Ljungdahl pathway by which autotrophic organisms fix cellular carbon.[105]

Crystallographic characterization of the CODH portion reveals a homodimeric assembly with one active site per subunit (Figure 5).[146] The CODH active site (termed the C-cluster) is buried 18 Å from the protein surface near the subunit interface. The C-cluster consists of an asymmetric assembly of composition [Ni-4Fe-4S-OH]; this

cluster is bound to the protein via five cysteine residues (one per metal center), and a histidine residue (Figure 6).[146] The Ni center resides in a distorted tetrahedral environment and is bound by two bridging sulfides (S^{2-}) and a bridging OH^- in addition to the aforementioned cysteinate. [147]

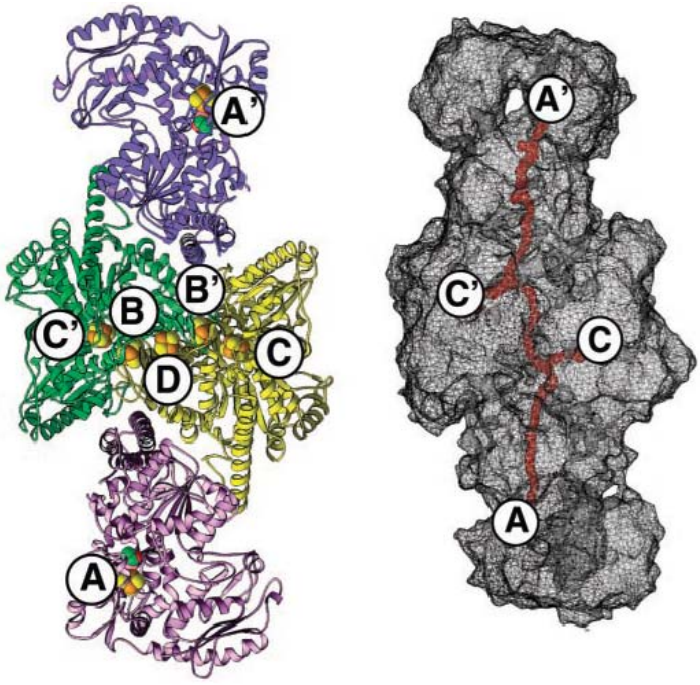

Figure 5. Left: Crystal structure of the bifunctional CODH/ ACS system from *Moorella thermoacetica*[148] depicting the CODH subunits (green and yellow) and those of ACS (blue and violet). Right: Depiction of the hydrophobic gas tunnel connecting the CODH and ACS active sites. Clusters labeled A and C refer to the active sites of ACS and CODH, respectively. Those labeled B and D are [4Fe-4S] clusters involved in electron transport.

Further crystallographic study of CO_2 bound CODH provided revealing details with regards to the enzymatic mechanism (Figure 6).[147] A likely mechanism

based on the structurally characterized intermediates involves two electron reduction of the C-cluster. The reduced active site was postulated to possess a formally Ni(0) center, but recent QM/MM investigations suggest that this process may be H^+ coupled, resulting in a Ni(II)-hydride.[149] CO_2 is then introduced along with H^+, displacing the OH^- ligand with a bridging CO_2, stabilized by a hydrogen-bond to a protonated second sphere histidine.[147] The final step involves reduction to CO with simultaneous H^+ release and restoration of the bridging OH^- ligand.[147,149]

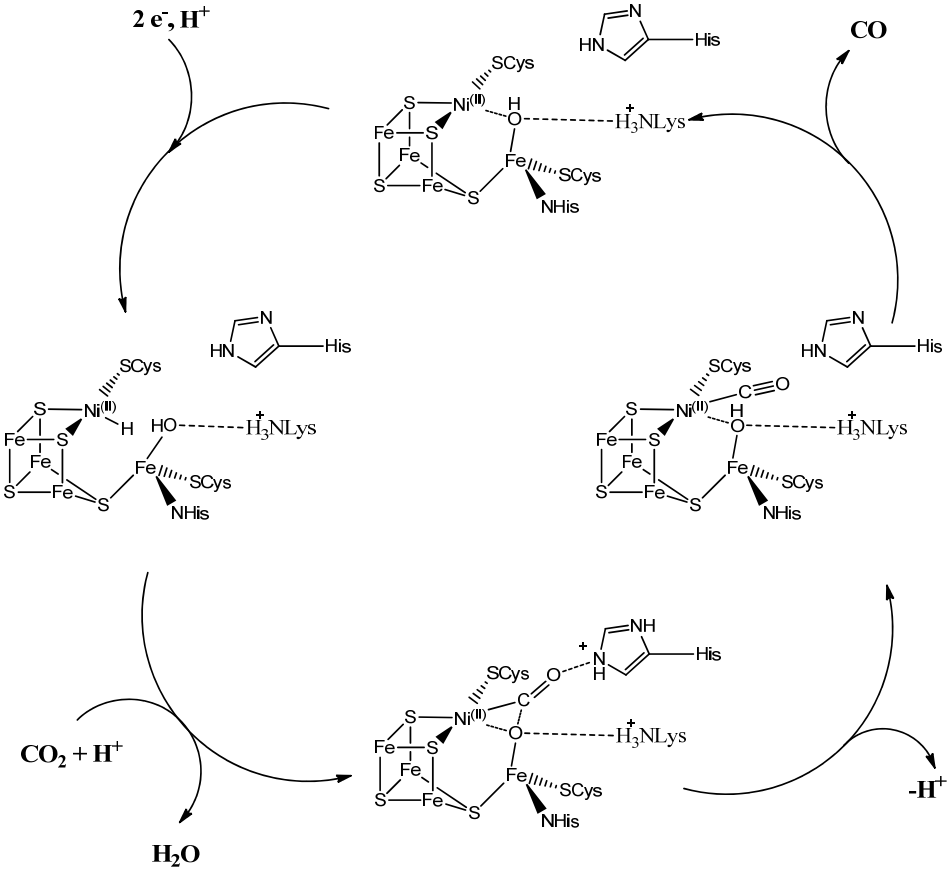

Figure 6. Proposed mechanism for the reversible reduction of CO_2 to CO at the C-cluster of CODH/ ACS (reaction depicted in the reductive direction).

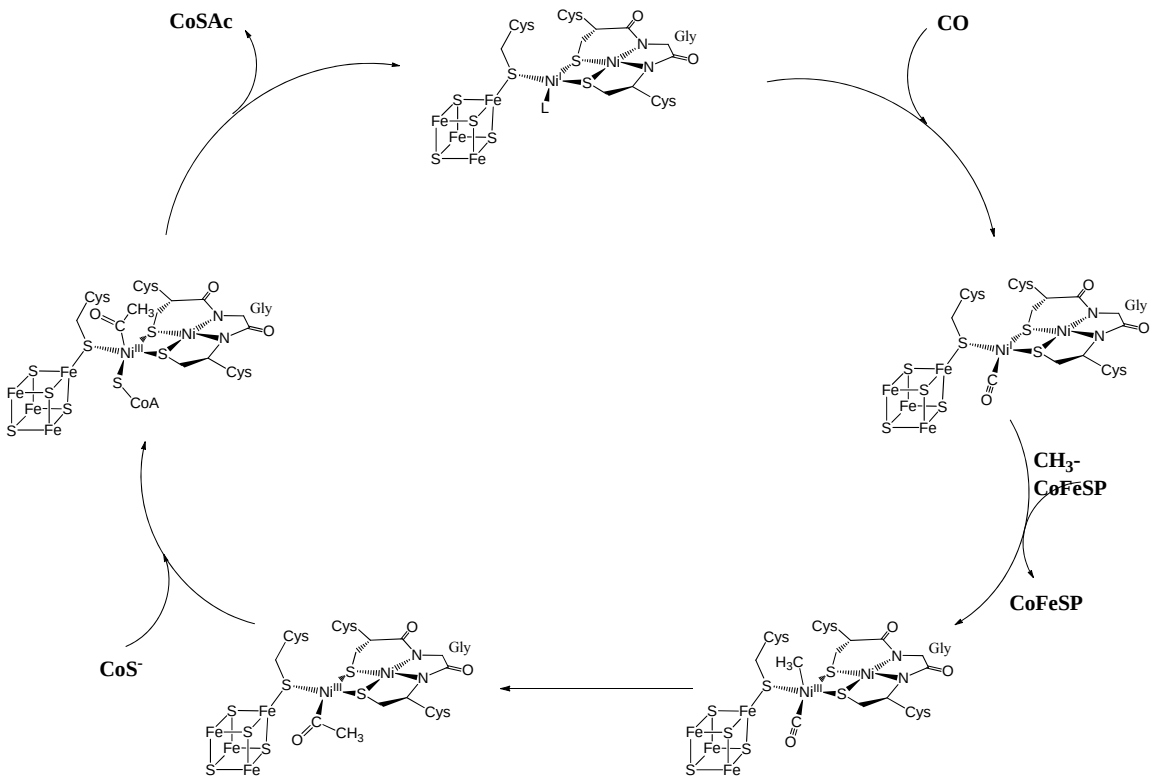

Figure 7. Proposed mechanistic scheme for incorporation of CO into Co-SAc at the A cluster of ACS (The undefined ligand L, see top center, is found in the resting state and likely absent during catalytic turnover).

Two ACS subunits flank the homodimeric CODH protein in a symmetrical fashion (Figure 5).[148,150] The ACS active site is termed the A-cluster, and is comprised of a dinuclear Ni assembly appended to a [4Fe-4S] cluster via a bridging cysteine. One Ni of the dinuclear assembly (termed the distal Ni, named for its position relative to the [4Fe-4S] cluster) is ligatated in a square planar bis-cysteinate/bis-carboxamide N_2S_2 environment by a Cys-Gly-Cys motif. The second Ni, termed proximal, is tetra-coordinate and bridged to the cysteinates of the Cys-Gly-Cys unit, the cysteinate appended to the adjacent [Fe-S] cluster and one labile

ligand of unkown composition (Figure 7, top center).[148,150] The true identity of the ion proximal to the [Fe-S] cluster was highly contested in the early structural literature, and proteins with both Cu[148] and Zn[151] in its place have been characterized. However, studies involving the removal and reconstitution of this metal cofactor have firmly established that ACS activity is contingent upon Ni occupancy.[152-153] The A-cluster is connected to the CODH C-cluster through a hydrophobic tunnel which serves as a conduit for CO between the active sites (Figure 5).[154] In fact, crystallographic studies of CODH/ACS treated with Xe gas reveal high occupancy of Xe atoms, a van der Waals mimic of CO, throughout the hydrophobic passageway.[151,155]

The precise mechanistic details of acetyl formation and incorporation into acetyl coenzyme A remain unresolved to date.[97] The process likely occurs via binding of CO to the proximal Ni in the Ni(I) oxidation state.[156-157] A methyl group is then provided by a methylated cobalt corrinoid iron-sulfur protein (CoFeSP) resulting in a transient methylated-Ni(III) species.[158-159] Methyl group migration results in an acetyl bound Ni(III) species. The final step of the catalytic cycle involves binding of the thiol of coenzyme A (CoA-SH) followed by reductive elimination affording CoA-SAc and regenerating the Ni(I) species (Figure 7).[160]

Methyl-CoM reductase, the enzyme responsible for methane (CH_4) production in methanogenic archaea, catalyzes the oxidation of coenzyme M (CoM-SMe, 2-(methylthio)ethanesulfonate) and coenzyme B (CoB-SH, 7-thioheptanoyl-threoninephosphate) (Figure 8) to the corresponding heterodisulfide with concurrent generation of CH_4. [161] The enzyme crystallizes as a hexameric protein assembly which can be viewed as a dimer of hetero-trimers.[107] The two methyl-CoM active

sites consist of a non-covalently bound Ni-corrinoid cofactor, coenzyme F430 (Figure 8). The two F430 cofactors are found deeply burrowed within the protein, at the end of a 30 Å substrate channel which serves to accommodate the reaction substrates.[107]

The active form of methyl-CoM reductase is a square pyramidal Ni(I) species, with the corrinoid of coenzyme F430 comprising the equatorial plane and the carbonyl oxygen of a glutamine residue near the C-terminus of the enzyme occupying the axial postion (Figure 8, coenzyme F430).[162] Nucleophilic attack of the Ni(I) species on the methyl group of CoM-SMe results in a methylated Ni(III) intermediate (Figure 9).[163] Decay of this intermediate is rapid and undetectable by spectroscopic methods and this assignment has been highly contested as formation of a Ni(II)-methyl radical species appears equally likely.[164] However, recent studies utilizing 6-thiohexanoyl-threoninephosphate in place of CoB-SH resulted in a decrease of enzyme kinetics by three orders of magnitude and allowed for characterization of this Ni(III) species by EPR.[165] Shortly thereafter, this intermediate was crystallographically characterized following treatment of the reduced enzyme with methyl iodide.[166] Following formation of the Ni(III)-methyl intermediate, this transient species is reduced to the Ni(II) form via the resultant CoM-SH.[167] Deprotonation of the CoM-SH^+ ion by the reactive organometallic methyl species then results in the formation of CH_4 and CoMS-thiyl radical.[165] Finally, a radical cascade reaction results in re-reduction to the active Ni(I) species by CoB-S-, and formation of the heterodisulfide product.[165,167] The precise mechanistic details remain unknown for this final step (Figure 9).

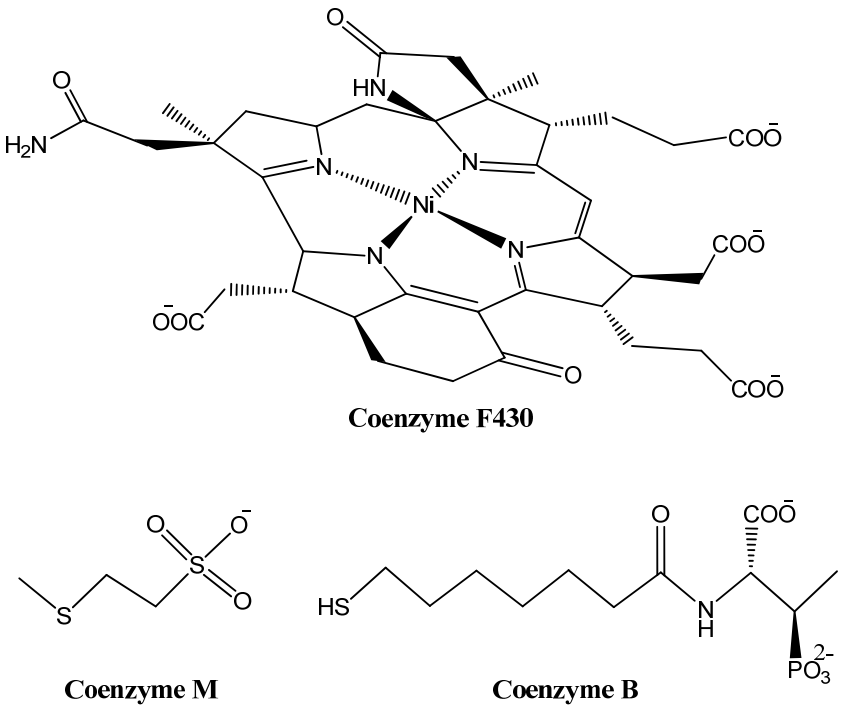

Figure 8. Chemical structures of coenzyme F430, coenzyme M and coenzyme B.

These three fascinating enzymes share the common theme of redox active Ni in the presence of thiolate ligands. Much of what has been learned from the Ni-thiolate chemistry of these enzymes pertains to arguments rationalizing the unusual chemistry of Ni-SOD. In turn, lessons learned regarding the active site assembly and mechanistic details of Ni-SOD can be applied to the rich chemistry of the above discussed enzymes, involved in a diverse array of catalytic processes of geochemical, environmental and economic significance.

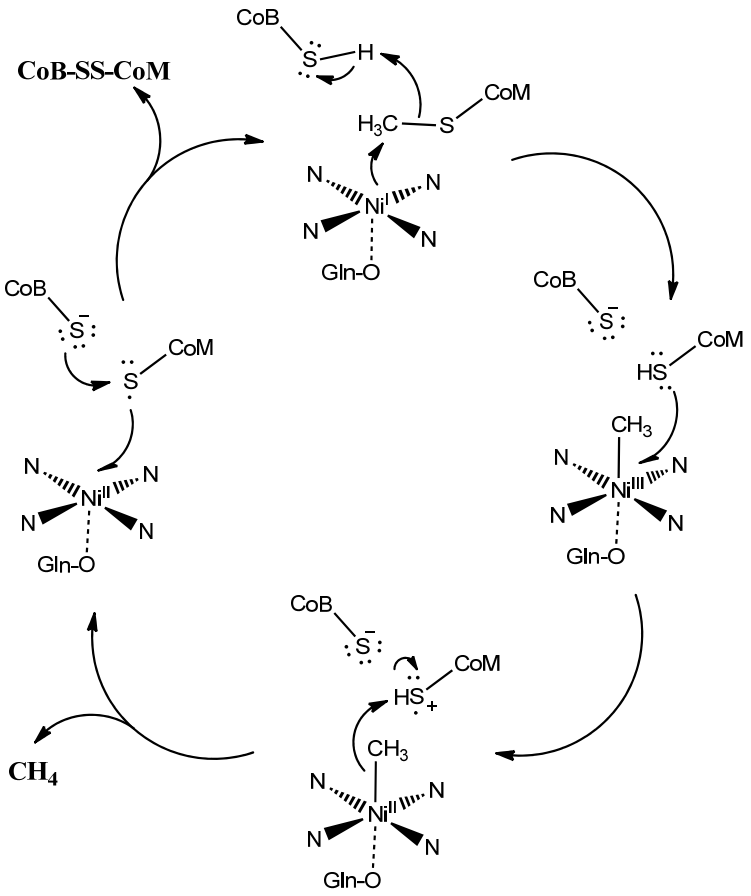

Figure 9. Postulated mechanism for methanogenesis via methyl-CoM reductase.

1.4 Nickel Superoxide Dismutase Overview

Ni-SOD shares little in common with the SOD enzymes described above and appears to have arisen via an independent evolutionary pathway.[168] The seminal discovery of Ni-SOD was the result of a hunt for an SOD as a possible H_2O_2 source in *Streptomyce,*[65-66] a search initiated upon the identification of catalase-peroxidase in this actinobacterial species.[169] Subsequent data mining has revealed the presence of Ni-SOD homologues in cyanobacteria, proteobacteria, intracellular pathogens such as chlamydiae and even green algae eukarya.[170-171] Several of these organisms tend to be found in soil and marine environments rich in Ni. In fact, a gene sequence believed to

be a transcriptional/ translational regulatory element controlling Ni- vs Fe-SOD production has been identified in *Streptomyces*, suggesting that certain organisms can tailor ROS control to their local ecology.[171] Ni-SOD is encoded by the gene sodN, which transcribes for an additional 14 amino acids at the N-terminus that are not found in the mature protein. Linked to sodN is an endopeptidase gene,[171] which is believed to remove this 14 residue leader sequence simultaneously with Ni uptake, affording active Ni-SOD.[172]

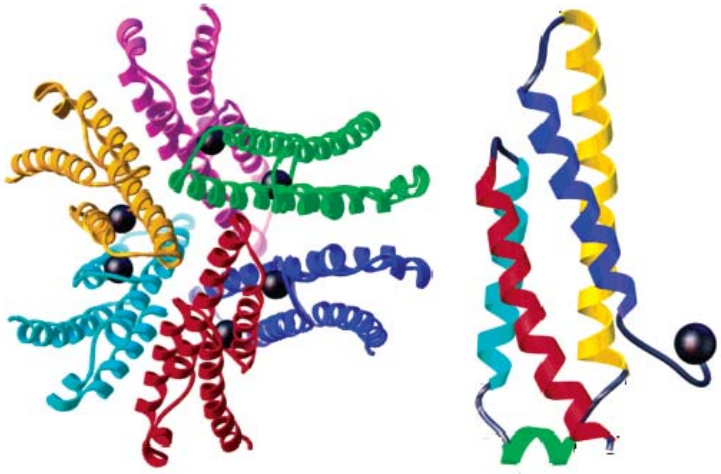

Figure 10. Crystal structure of Ni-SOD from *Streptomyces coelicolor*[173] (PDB code: 1T6U) (left) and one subunit displaying the Ni center at the N-terminus (right).

Ni-SOD crystallizes as a spherical homo-hexameric array of four-helix bundles, each containing one active site at the N-terminus (Figure 10).[173-174] The active sites are spaced considerably apart with no less than 23 Å between neighbors, and together may be considered as the vertices of an octahedron within the solvent filled interior cavity of the spherical assembly. The Ni ion is located within a "Ni-hook motif" consisting of residues one through nine (His-Cys-Asp-Leu-Pro-Cys-Gly-

Val-Tyr). This peptide chain is disordered in the apo protein but wrapped neatly around the Ni in the mature protein. Interestingly, the peptide bond of Pro5 must lock in the more energetic cis conformation in order to accommodate Ni binding by this nine residue motif.[173-174] Furthermore, apo Ni-SOD exists in monomeric form, and Ni-binding is believed to trigger assembly of the hexameric construct.[175]

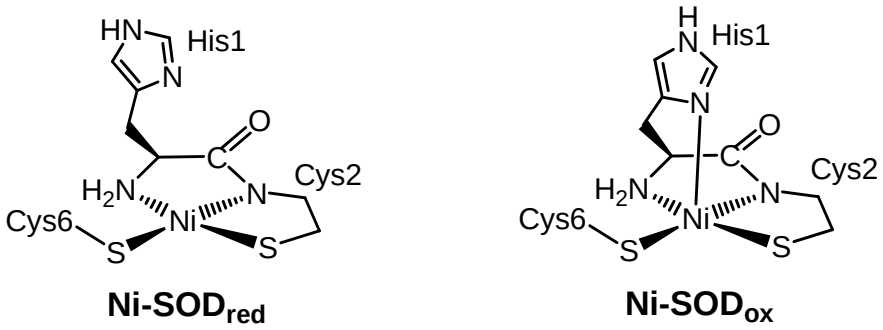

Figure 11. Ni-SOD active site in the reduced (left) and oxidized (right) resting states.

Initial characterization of the active site by extended X-ray absorption fine structure (EXAFS) spectroscopy indicated a dinuclear Ni center bridged by cysteine thiolates.[176] However, crystallographic studies of Ni-SOD from two separate organisms revealed the active site to be monomeric and of an unusual disposition.[173-174] In the reduced Ni(II) state, the metal is bound by the N-terminal amine of His1, the anionic carboxamido-N of Cys2, and the cysteine thiolates of Cys2 and Cys6 to complete an N_2S_2 square planar geometry. In the oxidized Ni(III) state, the coordination geometry is square pyramidal with the imidazole-N of His1 occupying the apical position (Figure 11, see Table 1 for bond distances).[173-174]

Table 1. Comparison of Ni–N/S bond distances (Å) reported for Ni-SOD from two crystallographic studies. Due to redox heterogeneity (equal amount of Ni(II) and Ni(III) centers) in the crystallographic samples, Ni-S and Ni-N bond lengths could not be reported precisely for Ni-SOD_{red} and Ni-SOD_{ox}, with the exception of the Ni-N(His1) bond from *S. coelicolor*.

	S. coelicolor[173]	*S. seoulensis*[174]
Ni(II)-N(His1)	1.87	2.11
Ni(III)-N(His1)	2.02	2.11
Ni-N(Cys2)	1.91	1.93
Ni(III)-N(His1-axial)	2.35	2.63
Ni-S(Cys2)	2.16	2.24
Ni-S(Cys6)	2.19	2.26

An equal amount of reduced (Ni-SOD_{red}) and oxidized (Ni-SOD_{ox}) active sites occupy the as-isolated enzyme.[66,173-174] Unlike the other SODs, the sequencing of the ligating residues remains invariant amongst identified homologues.[171] The Ni-SOD active site is distinct from any other metalloenzyme. Metal-carboxamido-N complexes are rare in biological systems, with the A-cluster of CODH/ACS,[148] the oxidized P cluster of nitrogenase[177] and nitrile hydratase[178-180] providing notable exceptions. Furthermore, the N-terminal amine ligand is unprecedented in any presently known metalloenzyme system. The presence of two cysteine thiolates is also quite intriguing. Although the thiolate ligands appear requisite for modulating the Ni(II)/Ni(III) redox couple to physiologically relevant potentials,[176,181] cysteine residues are rarely found in enzymes participating in ROS detoxification due to the deleterious effects of O_2 and ROS on sulfur containing species.[182-183] Each Ni-bound

residue is considered crucial to enzymatic activity. For example, mutation of His1 results in a decrease of enzyme kinetics by at least two orders of magnitude.[174-175] Mutation of either cysteine to a serine residue results in formation of an octahedral Ni(II) center without cysteine ligation that display no catalytic activity.[184-185]

Whether or not electrostatic guidance of substrate to the catalytic center occurs remains a matter of debate. The crystal structure of Ni-SOD reveals the presence of three conserved lysine residues which form a positively charged triangle at an opening on the protein surface 15 Å above the active site.[173] However, unlike Cu/Zn- and the Mn- and Fe-containing SODs, the catalytic rate constant of the Ni enzyme demonstrates little dependence on solvent ionic strength, suggesting that electrostatic steering may not be crucial to catalytic activity.[176] A secondary sphere tyrosine (Tyr9) residue is located 5.5 Å above the vacant Ni coordination site and mutations to this residue afford an enzyme which displays saturation kinetics indicative of inhibition by product buildup.[168] This is redolent of that observed upon mutation of a tyrosine residue near the active site of Mn-SOD, and the Tyr9 of Ni-SOD may also be considered a "gatekeeper" residue, assisting in the release of product from the enzyme active site.[85] Mutations at Asp3 result in weakened inter-subunit interactions via disruption of an extensive hydrogen bonding network between monomers as well as a re-positioning of Tyr9 1 Å closer to the Ni center, and while this mutation causes no observable change to the Ni-coordination environment or redox potential, enzymatic activity is completely abolished. In fact, treatment with H_2O_2 results in the formation of a tyrosyl radical species and indicates

that the catalytic properties of Ni-SOD are highly sensitive to subtle effects of secondary sphere residues and that Tyr9 plays a crucial role in reactivity tuning.[168]

In Ni-SOD_{red}, the square-planar Ni ion is of a diamagnetic d^8 configuration. The absorption spectra of Ni-SOD_{red} displays ligand field transitions at 458 nm (480 M^{-1} cm^{-1}) and 555 nm (150 M^{-1} cm^{-1}) consistent with spectrally characterized square planar Ni(II)N_2S_2 complexes featuring thiolate donors.[186] In fact, these transitions arise in between values obtained for NiN_2S_2 complexes of bis-amine[187-190] and bis-amide[181,191] N-donors. A more intense transition is observed at 342 nm (880 M^{-1} cm^{-1}),[186] although the origin of this transition has not been addressed in the spectroscopic literature. The absorption spectrum of Ni-SOD_{ox} provides more intense transitions and dominates the spectral features of the as-isolated enzyme.[186] There are few spectrally characterized Ni(III) complexes in mixed N/S coordination environments available for comparison.[191-192] However, the strongly absorbing nature of these bands is suggestive of charge-transfer character,[193] likely arising from S→Ni(III) transitions.[186]

Ni-SOD_{ox} gives rise to a rhombic EPR spectrum consistent with low spin, S = ½ Ni(III) in a tetragonal coordination environment (Figure 12).[194] The spectrum is comprised of g_x and g_y at 2.30 and 2.22, respectively, and a g_z at 2.01 featuring ^{14}N hyperfine splitting (A_{zz} = 69.7 MHz).[66,173,176] This hyperfine has been attributed to interaction of the axial imidazole side chain with the unpaired electron in the d_z^2 orbital based on prior Ni(III)-peptides[195] and synthetic complexes[181,191,196] of tetragonal symmetry, as well as computational evaluation.[186,197] However, this ^{14}N hyperfine pattern is retained upon mutation of His1 to glutamine, suggestive that this

feature may arise from another interaction, or there may be a redefinition of the *x*, *y*, *z* axes upon imidazole ligation.[175]

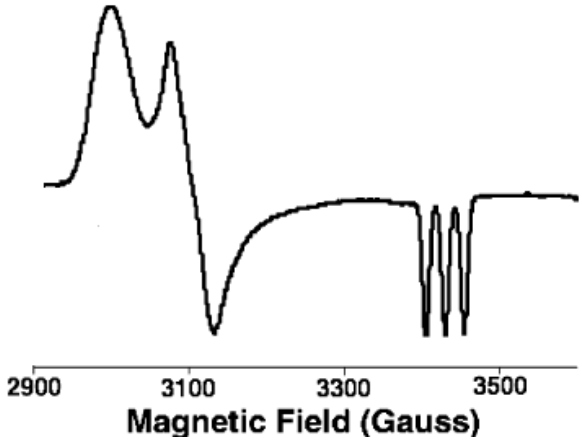

Figure 12. X-band EPR spectrum of Ni-SOD_{ox} (0.72 Ni(III)/Ni center) taken in pH 7.4 phosphate buffer at 77 K.[66,173,176]

The resonance Raman spectrum of as-isolated Ni-SOD aquired upon 413 nm irradiation at 0°C reveals the presence of vibrational features at 349, 365 and 391 cm^{-1}.[186] The lower energy stretches are believed to arise from Ni(III)-S stretching, and the calculated force constants of 1.79 and 1.68 mdyn $Å^{-1}$ for Ni(III)-S(Cys2) and Ni(III)-S(Cys6), respectively, suggest that the Ni-SOD_{ox} possesses some of the strongest and most covalent metal-thiolate bonds of any metalloenzyme system.[197]

Density functional theory (DFT) analysis of geometry optimized, truncated models of Ni-SOD_{red} provided bond lengths similar to those observed in the crystallographic studies (Table 2).[186] Frontier molecular orbital analysis revealed the highest occupied molecular orbitals (HOMOs) to be largely localized on the Ni and S atoms with the HOMO comprised of 25 % Ni and 68 % S character, and the nearly isoelectronic HOMO-1 comprised of 37 % Ni and 44 % S. The wavefunctions are of

π-antibonding character between the Ni d_{xz} and d_{yz} orbitals and the S lone pairs, providing a bonding scheme previously demonstrated to be strongly destabilizing at both the Ni and S positions (Figure 13).[183]

Table 2. Comparison of Ni–N/S bond distances (Å) reported for Ni-SOD from *S. coelicolor* and from DFT generated models.

	S. coelicolor[173]	Ni-SOD_{red}[186]	Ni-SOD_{ox}[186]
Ni(II)-N(His1)	1.87	1.99	
Ni(III)-N(His1)	2.02		2.02
Ni-N(Cys2)	1.91	1.89	1.91
Ni-N(His1-axial)	2.35		2.16
Ni-S(Cys2)	2.16	2.18	2.17
Ni-S(Cys6)	2.19	2.22	2.25

Geometry optimized models of Ni-SOD_{ox} replicate the crystallographically determined bond lengths of the equatorial ligands fairly well but greatly underestimate the axial Ni-N bond (Table 2).[186] In an effort to overcome this discrepancy, residues (Glu17 and Arg47) capable of hydrogen-bonding with the imidazole N-H and constrained to account for their natural positioning in the protein were introduced. This added interaction effected a lengthening of the Ni-N bond by 0.1 Å, still much shorter than the experimentally determined value. MO analysis of truncated Ni-SOD_{ox} reveals a major re-shuffling of the bonding scheme upon binding of the His1 imidazole side chain. The SOMO is 77 % Ni based and resides in the d_z^2

orbital with a bonding vector that does not engage in S-antibonding interactions. Furthermore, the SOMO of Ni-SOD$_{ox}$ displays only a 7 % S orbital composition (Figure 13).[186]

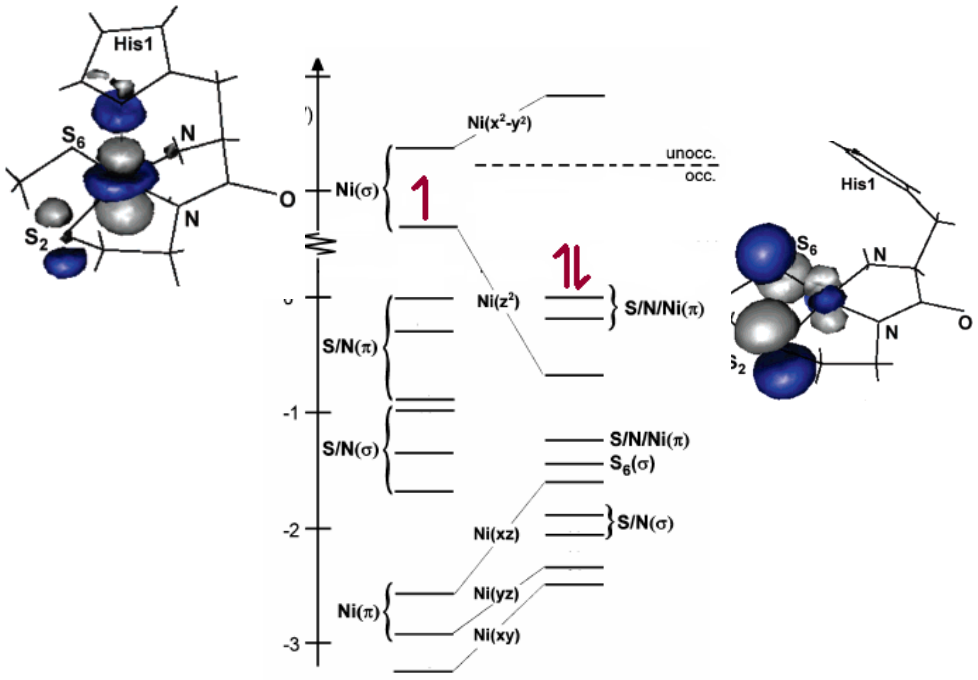

Figure 13. DFT generated MO plots and HOMO composition of Ni-SOD$_{ox}$ (left) and Ni-SOD$_{red}$ (right) on truncated active site models.[186]

1.5 Unresolved Chemistry Relevant to the Catalytic Activity of Nickel Superoxide Dismutase

Structural, spectroscopic, mutagenic and theoretical studies have been useful in elucidating aspects of the unique active site assembly, electronic properties and reactivity of Ni-SOD. However, much remains to be understood regarding the chemistry at play in Ni-SOD. In particular, outstanding questions remain regarding the precise role played by the imidazole side chain of His1, protection of the

cysteinate ligands from oxidative modifications during catalytic turnover, the mechanism by which protons are delivered during the reduction half reaction and whether substrate dismutation occurs via an inner vs. outer sphere mechanism.

As described above, mutations to His1 result in a drastic decrease, if not complete abolishment, in catalytic activity.[174-175] The specific reasons for this loss of efficacy remain speculative. One possibility is that the imidazole side chain serves to tune the redox potential to the midpoint requisite for superoxide oxidation and reduction.[186] The redox potential measured for Ni-SOD has been measured at 0.29 V vs. NHE via redox titrations.[168] Binding of the axial N-donor is expected to raise the reduction potential of Ni-SOD_{ox} by ~0.20 V and it is expected that the redox potential would shift from the calculated midpoint.[186] Despite this, the redox potential should remain well within the window requisite for SOD behavior. To date, no protein studies have been performed regarding the redox potentials of His1 mutants.

Because the rate of SOD catalysis occurs on a timescale faster than nuclear motions, crystallographically characterized Ni-SOD_{red} can likely be viewed as a resting state, and it is likely that the active site remains five coordinate during catalysis. Using DFT calculations on truncated models, the inner sphere re-organizational energy between Ni-SOD_{red} and Ni-SOD_{ox} was calculated and found to be 34.8 kcal/mol.[198] When the imidazole ligand was constrained to interact with Ni-SOD_{red}, affording a square pyramidal Ni(II) species, the inner sphere re-organizational energy was calculated at 15.9 kcal/mol, a value similar to that obtained for the blue copper site of azurin.[199-200] The calculated value between Ni-SOD_{red} and Ni-SOD_{ox} with the imidazole unbound afforded a similar result. It should be noted

that these calculated values do not account for interactions with solvent, secondary sphere interactions or substrate.[198] The possibility that the axial N-donor may serve to exert a labilizing trans effect on bound substrate can not be excluded.

Binding of the axial N-donor also may serve to protect the coordinated cysteinates from oxidative modifications by almost completely removing S-contributions from the SOMO of Ni-SOD_{ox}, as described above (Figure 13).[186] However, no studies regarding the fate of the cysteine residues have been performed on His1 mutants. Hydrogen-bonding to the coordinated cysteinates has also been implicated in a protective role against S-oxidation via lowering the energy of S(p) lone pairs, effectively decreasing destabilizing Ni-S anti-bonding contributions to the HOMO.[183,201]

At first glance, it appears likely that the His1 imidazole is the ligand responsible for delivery of H^+ during the reductive half reaction, with hydrogen-bonding interactions involving backbone residues serving to modulate the pK_a as the Zn(II) ion does to the bridging imidazole ligand in Cu/Zn SOD. However, in light of results suggesting a five coordinate species throughout catalytic turnover,[198] and the fact that the imidazole is located at a face opposite to the vacant site available for substrate,[173-174] new sources must be sought. Intriguingly, S K-edge X-ray absorption (XAS) studies on H_2O_2 reduced Ni-SOD reveal ionization potentials more akin to Ni bound thioethers (and by analogy, thiols) than thiolates, suggestive that the coordinated cysteinates may in fact be protonated.[202] Furthermore, DFT analysis modeling protonation at either cysteine in geometry optimized truncated models of Ni-SOD_{red} reveal no significant structural changes.[186] Rather, the Ni-S bond length

decreases by 0.03 Å as Ni-S antibonding is alleviated,[186] and it is proposed that bound cysteine may play a role analogous to that outlined above for coordinated water in the Mn- and Fe- containing SODs.[90,203-204] It should be noted that a similar role for coordinated cysteine residues has been described in removal of protons from the NiFe-hydrogenase active site.[135-137]

Evidence supporting both inner vs. outer sphere disproportionation of superoxide has been presented, and the topic remains an open discussion. The enzyme is inhibited by N_3^- treatment.[176] However, treatment of Ni-SOD_{ox} with ^{15}N-labeled N_3^- results in a nearly identical EPR spectrum as that treated with natural abundance ^{14}N-N_3^- (Figure 12) (no changes to ^{14}N hyperfine splittings) and it appears that N_3^- inhibition arises from structural perturbations rather than Ni binding.[173] Crystallographic studies of the Tyr9 mutants revealed the presence of a chloride anion 3.5 Å from the Ni center, pointing towards a likely anion binding pocket above the active site.[168] However, treatment with cyanide resulted in Ni sequestration and is demonstrative that the Ni center can be accessed by diatomic anions.[173]

The above discussion highlights several unresolved speculations regarding Ni-SOD. In terms of experimental approaches, structural and spectroscopic techniques have proven critical to an understanding of Ni-SOD in resting conditions.[168,173-174,186] However, the vast majority of insights regarding the more dynamic aspects of the catalytic mechanism have been provided by theoretical approaches alone.[186,198,203-204] It is clear that the study of Ni-SOD could benefit from the study of carefully constructed small molecule biomimetics. Cleverly designed and properly applied, systems allowing for facile manipulation of coordinating functionalities allow for

analysis of electronic fine tuning on structural, electronic and reactivity properties relevant to enzyme catalysis.

1.6 Models of Nickel Superoxide Dismutase

Three general approaches have been utilized in the preparation of Ni-SOD biomimetics: (1) chelation of Ni using short polypeptide chains of similar or identical homology to the "Ni-hook motif;" (2) the preparation of small molecule Ni complexes employing ligands approximating aspects of the Ni-SOD coordination environment; and (3) the preparation of Ni complexes housed within ligand frameworks accurately modeling the spatial and electronic features of the Ni coordinating ligands of SOD.

1.7 Models of Nickel Superoxide Dismutase Utilizing Short Polypeptides

To date, utilization of short polypeptides has been the most successful approach towards modeling Ni-SOD. A peptide maquette comprised of the first 12 amino acids of the Ni-SOD N-terminus has been shown to coordinate Ni(II) in a ~1:1 ratio at pH 7.2.[205] The Ni K-edge XAS obtained for the species formed upon metallation displays a $1s \rightarrow 4p_z$ pre-edge transition at 8337.4(2) eV as well as a $1s \rightarrow 3d$ transition, consistent with Ni(II) in a square planar environment.[104,206] The EXAFS region is best fit with two Ni-N scatterers at 1.93(2) Å and two Ni-S scatterers at 2.18(2) Å, consistent with N_2S_2 ligation.[205] Characterization of this Ni-peptide maquette by UV-vis reveals two weak ligand field transitions at 458 nm (510 M^{-1} cm^{-}

) and 552 nm (240 M^{-1} cm^{-1}), as well as a higher energy feature at 337 nm (1,060 M^{-1} cm^{-1}), all consistent with the UV-vis spectrum of Ni-SOD_{red}.[205]

Utilizing protein thin-film voltammetry methods, a redox potential of 0.70 V vs. Ag/AgCl was determined for the metallated peptide species.[205] Despite the reversibility of this electrochemical event, the Ni(III)-peptide was found to be unstable and could not be observed by spectroscopic techniques.[205]

Utilizing the NBT/formazan spectrophotometric assay, which affords a deep blue formazan species upon $O_2^{\bullet-}$ reduction of the colorless tetrazolium salt (NBT),[207] it was determined that the Ni-peptide maquette served as a functional SOD.[205] It was observed that 10 μM of the metallated peptide species could protect against quantitative formazan production (33 μM NBT) in the presence of 16,500 equiv. of $O_2^{\bullet-}$ at pH 7.2. In the absence of this Ni-SOD mimetic, this conversion could be achieved by $\leq$ 1,400 equiv. $O_2^{\bullet-}$. This SOD activity could not be sustained for prolonged periods of time, as both O_2 and H_2O_2 were found to lead to the degradation of the metallo-peptide.[205]

Abridging the polypeptide maquette to the first seven residues found at the N-terminus of Ni-SOD afforded a species which displayed similar catalytic behavior, and a series of septa-peptide biomimetics were prepared with variations at the position previously occupied by His1.[198] Along with the septa-peptide true to the Ni-hook motif, variants containing aspartic acid (Asp1) or alanine (Ala1) at the N-terminus were employed in order to probe the effects imparted on the spectroscopic, electrochemical and catalytic properties of the metallo-peptide species.[198]

Substitution of the N-terminal residue minimally effected the structural and electronic properties of the Ni(II)-peptide species. All were found to possess square planar NiN_2S_2 coordination by EXAFS, and the UV-vis spectra provide similar features across the series.[198] As described for the twelve residue congener, the Ni(III)-peptide species are unstable. However, immediate freezing of the His1 containing septa-peptide upon addition of substoichiometric $O_2^{\bullet-}$ resulted in the trapping of a Ni(III) species similar to that observed for Ni-SOD_{ox} which could be detected by EPR.[198]

The redox potentials of the His1, Asp1 and Ala1 metallopeptides were measured at 0.52, 0.48, and 0.62 V vs. Ag/AgCl at pH 7.4, respectively. The oxidation and reduction events of the His1 and Asp1 variants display separations of 0.24 V and 0.26 V, respectively. Interestingly, the Ala1 variant which possesses no available side chain for Ni coordination, displays a peak to peak separation of only 0.11 V, suggestive that no major structural rearrangement occurs between redox events.[198]

Upon observation of the electrochemical behavior in solution, the metallopeptides were immobized via a *N*,*N*'-dimethyldidodecylammonium bromide surfactant bilayer in order to allow for fast scanning techniques un-obscured by diffusion from the electrode.[198] Scanning at rates from 0.01 V/s to 50 V/s only resulted in a slight increase in the separation between the oxidative and reductive events of the Ala1 metallopeptide (Figure 14). Plotting the scan rate (logarithmically) vs. peak to peak separation affords a well behaved "trumpet plot" indicative of reversible redox behavior with minimal structural rearrangement (Figure 14).[208]

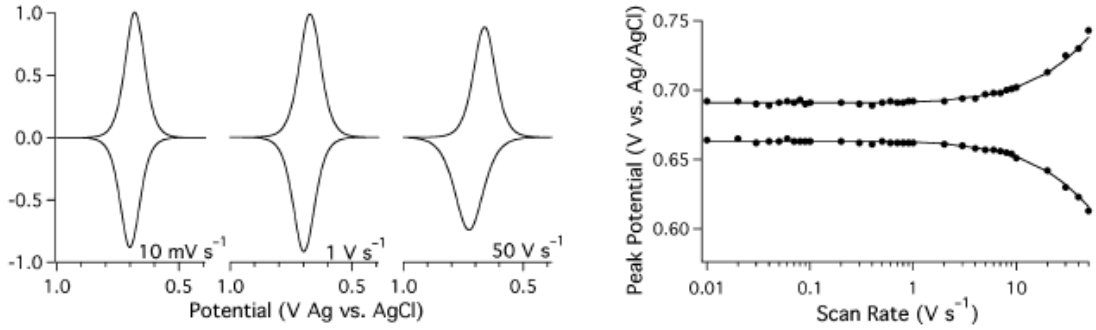

Figure 14. Left: Cyclic voltammograms of septa-peptide Ni-SOD mimic with alanine substituted for His1 obtained at varying scan rates. Right: Plot of scan rate (logarithmic) vs. separation between oxidative and reductive events.[198]

Performing the same experiment on the His1 variant provided a more complex scenario (Figure 15). When initiating scans from the oxidative direction at slow scan velocities (0.01 V/s), the redox event is reversible and displays a rather large peak to peak separation between events, as in the solution studies described above. At slightly faster scan velocities such as 1 V/s, the re-oxidation peak is no longer observed. However, at very fast scan rates such as 10 V/s and above, the re-oxidation wave returns albeit with a greatly decreased peak to peak separation from that observed at slow rates (Figure 15). Plotting peak to peak separation as a function of scan rate as described above reveals ideal "trumpet plot" behavior only for the fast scan regime.[198] This dependence of redox character on scan rate can be attributed to a "gating process" antecedent to re-oxidation of the metallopeptide species. Thus, the large peak to peak separation at slow scan rates can be attributed to a substantial structural reorganization between the correlated redox events. The decrease in this gap at fast scan rates can be attributed to a scenario where redox occurs with minimal structural

realignment. The disappearance of the return event at intermediate scan rates may be attributed to the presence of both four and five coordinate Ni(II) species at the electrode surface, and the re-oxidation wave could be expected to be broad and ill-defined, if observed at all (Figure 16).[198] In sum, the information obtained from this metallo-peptide modeling approach suggests a catalytic scenario for Ni-SOD where the active species is five-coordinate throughout, consistent with the computational evaluation of electron transfer discussed above.[198]

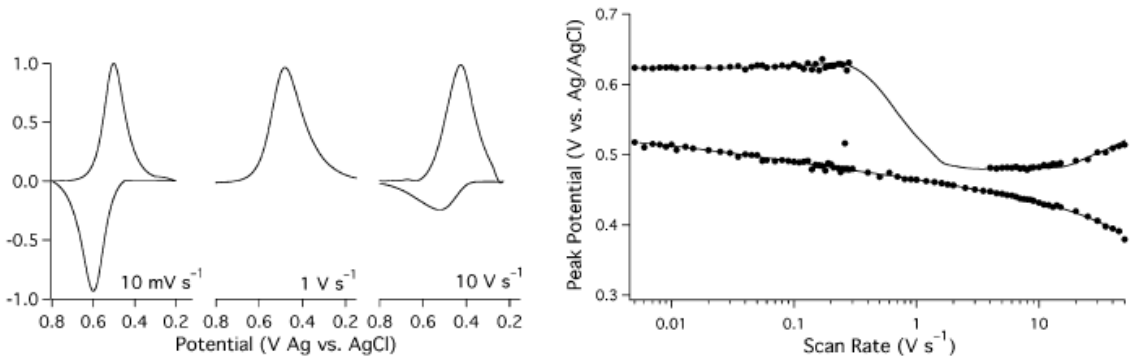

Figure 16. Left: Cyclic voltammograms of septa-peptide Ni-SOD mimic obtained at varying scan rates. Right: Plot of scan rate (logarithmic) vs. separation between oxidative and reductive events.[198]

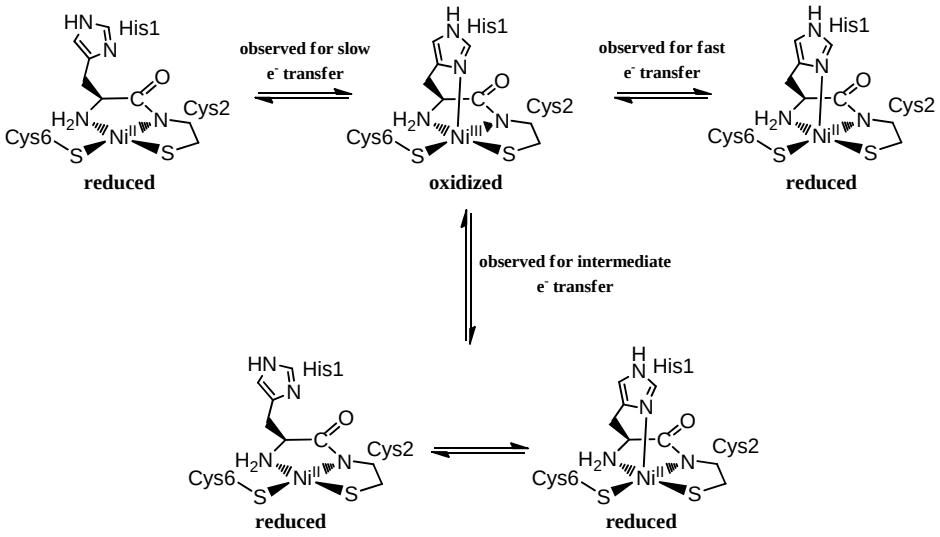

Figure 17. Structural rearrangements of metallopeptide Ni-SOD mimic observed for slow, fast and intermediate electron transfer scenarios (adopted from ref. 198).

In a related study, twelve residue maquettes featuring the ε-nitrogen of the His1 imidazole side chain with methyl, dinitrophenyl and tosyl substituents, as well as the unmodified His residue were studied.[209] As expected, the nature of the imidazole substituent had little effect on the structural and electronic properties of the Ni(II)-peptide species as evidenced by EXAFS and UV-vis spectroscopy, respectively. Also predictably, the redox potentials shifted to more positive values as the nature of the N-substituent becomes more electron withdrawing.[209] It was observed that the N-methyl substituted maquette was thermally stable in the Ni(III) state at pH 7.4 and could be reduced and re-oxidized through several cycles with no observable damage to the metallopeptide. However, isolation of this species remained elusive.[209]

The square pyramidal structure of the oxidized methyl substituted species was confirmed by XAS.[209] The Ni absorption edge is shifted by 2.8(6) eV higher in

energy, consistent with the Ni(III) oxidation state, and the formally symmetry forbidden 1s→3d transition intensifies as an inversion center is absent in the square pyramidal species. The EXAFS region is best fit to three Ni-N scatterers at 1.89 Å and two Ni-S scatterers at 2.19 Å, nearly identical to that obtained for Ni-SOD_{ox}.[176]

The Ni(III) state of the metallopeptide species could be trapped cryogenically for each of the N-substituted peptides.[209] The EPR spectra acquired at 77 K in pH 7.4 buffer were similar to that of Ni-SOD_{ox} for all species. Interestingly, the coupling constant of the ^{14}N hyperfine observed within the g_z tensor (see Figure 12) decreased as the N-substituent became more electron withdrawing, with that of the N-dinitrophenyl and N-tosyl substituted maquettes, 65 and 67 MHz, respectively, best reproducing the coupling constant of that found in Ni-SOD_{ox}. DFT generated MO plots and EPR simulations reveal that the g_z vector orients along the N_{amine}-Ni-S_{Cys2} bond for the N-dinitrophenyl and N-tosyl substituted metallopeptides, and along the Ni-$N_{imidazole}$ bond for the most electron donating imidazole and N-methyl imidazole His side chains.[209]

The resonance Raman spectra obtained by 405 nm excitation at 77 K in pH 7.4 buffer reveal a blue shift in the Ni(III)-S stretching frequencies as the N-substituents become more electron withdrawing.[209] This gradual shift to higher energy is consistent with stronger Ni(III)-S bonding, and stretching frequencies obtained for the N-dinitrophenyl (338 and 349 cm^{-1}) and N-tosyl (343 and 352 cm^{-1}) substituted maquettes match most closely with those obtained from Ni-SOD_{ox}.[209] Along with providing more accurate spectroscopic mimics of Ni-SOD_{ox}, the N-

dinitrophenyl and N-tosyl substituted peptide effect more efficient SOD catalysis by two orders of magnitude, as measured by stop-flow kinetic analysis.[209]

In light of the fact that the metallopeptides featuring electron withdrawing groups at the imidazole ε-nitrogen of His1 afford closer spectral mimics and more efficient SOD catalysts, this electronic modulation can be viewed as an approximation of the Ni(III)-$N_{imidazole}$ bond elongation observed in Ni-SOD_{ox}.[209] The molecular orbital depiction described above for the N-dinitrophenyl and N-tosyl substituted maquettes is of particular note with regards to earlier electronic depictions of Ni-SOD_{ox}.[186] In fact, this new depiction may explain the retainment of the g_z hyperfine observed in mutants of Ni-SOD_{ox} where His1 has been replaced by a glycine.[176] Considering the underestimation of the Ni(III)-$N_{imidazole}$ bond length in the truncated models used for DFT analysis,[186] and the experimental accord between Ni-SOD_{ox} and the metallopeptides featuring electron withdrawing substituents,[209] new considerations must be accounted for in our electronic description of Ni-SOD_{ox}. It must also be noted, however, that there is great disagreement between the DFT-generated MO depictions provided by truncated models of Ni-SOD_{ox} and those provided to rationalize the trends of the N-substituted metallopeptides. In contrast to the largely Ni-based MOs generated by the truncated models with regards to Ni-SOD_{ox},[186] those determined for the N-substituted maquettes suggest no more than 7 % Ni contribution to the SOMO.[209] The metallopeptide research described above has served to experimentally validate many hypotheses regarding the behavior of the axial N-donor of Ni-SOD, as well as the effects of electronic modulations.[198,209] However, the accompanying computational analysis provides new and somewhat

contrary data points with regards to earlier electronic depictions of Ni-SOD_{ox}, obscuring our theoretical understanding.[186,209]

Nona- and tri-peptide models have also been utilized as Ni-chelators modeling the "Ni-hook" motif.[210-213] Treatment of Ni(II)-nona-peptide models with CN^- result in CN^- bound Ni species, supported by solution state IR spectroscopy and by both solid- and solution-state ^{13}C and ^{15}N NMR spectroscopies utilizing selectively ^{13}C and ^{15}N labeled CN^-. It was found that only one equivalent of CN^- would bind per Ni(II) present, as evidenced by UV-vis, IR and NMR titration studies. This study serves to show that species similar to Ni-SOD_{red} are capable of accommodating a single anionic ligand.[211] However, CN^- can be viewed as an indiscriminately strong field ligand with an exceedingly high affinity for all transition metal ions, and one must be careful in extrapolating analogies of CN^- binding to the behavior of anions such as $O_2^{\bullet-}$. Furthermore, structural considerations of the cyanide bound Ni(II) species were not addressed in this study.[211]

The tri-peptide containing models of Ni-SOD do not employ the first three peptides found at the N-terminus of Ni-SOD. Rather, a NH_2-Asn-Cys-Cys-COOH motif is employed.[212] This metallopeptide model displays a reversible redox event within the window requisite for SOD catalysis and serves to protect NBT reduction from $O_2^{\bullet-}$ generated by xanthine oxidase, although this species afforded less protection than the above described twelve residue maquettes.[212] This species thus far serves as the most minimal Ni-containing peptide capable of conferring SOD activity.

One feature to note regarding the tripeptide models is that a chiral inversion at Asn1 and Cys3 occurred over the course of hours at pH 7.4.[213] This inversion was

first detected via the observation of time dependent changes to the CD spectrum. Aging in buffered D_2O affords the incorporation of two D atoms, as evidenced by mass spectral analysis. The position of the chiral inversion was identified via the independent metallation of all possible stereoisomeric peptide permutations. DFT analysis confirmed that the new metallopeptide featuring Asn1 and Cys3 in the *D*-configuration were more stable than the corresponding *L*-configured diastereomer. The resultant chirally inverted species displayed SOD activity comparable to the all *L*-configured species.[213] This result may best be rationalized as proof of concept that square planar $Ni(II)N_2S_2$ coordination is thermodynamically favored, and the surrounding polypeptide environment may assume new configurations in order to accommodate this coordination motif; as is observed in the cis-locked configuration of Pro5 of Ni-SOD.[173-174]

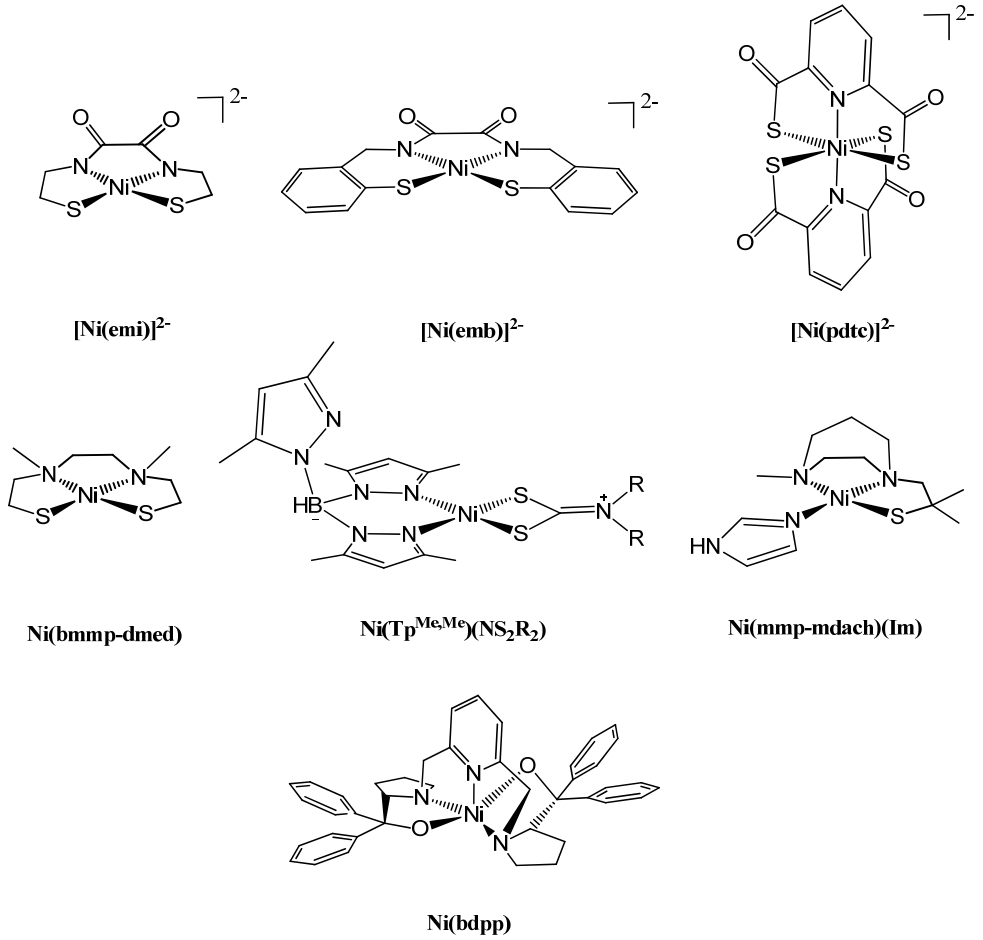

Figure 17. Ni(II) complexes approximating aspects of the Ni-SOD active site.

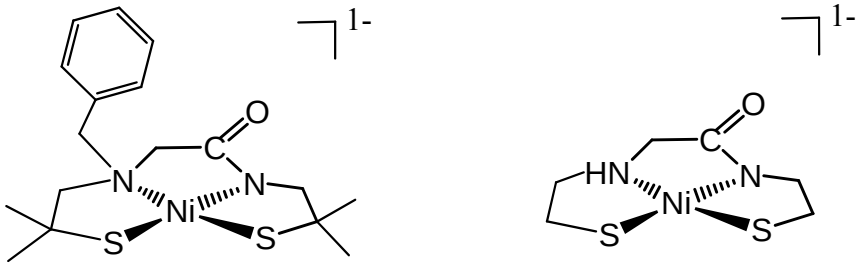

Figure 18. Ni(II) complexes accurately modeling Ni-SOD_{red}.

1.8 Low Molecular Weight Models Approximating Aspects of the Nickel Superoxide Dismutase Active Site

Several small molecules featuring Ni(II) in N- and S-rich environments have been reported as model complexes approximating certain aspects of the Ni-SOD primary coordination sphere (Figure 17).[197,214-219] Of these models, none can stabilize the Ni(III) oxidation state with the exception of those housed in a bis-amide/bis-thiolate N_2S_2 and bis-pyridyl/tetra-thioacetate N_4S_2 environments (Figure 17, top row),[197] although the reported redox potentials (-465 to -80 mV vs. Ag/AgCl) lie beyond the negative limits necessary for SOD catalysis. None of the N and S containing models are shown to be capable of significant SOD activity. When treated with 100 equiv. of superoxide, Ni(mmp-mdach)(Im) (Figure 17, center row, right) can scavenge 40% at pH 7.4 by the NBT/formazan assay. However, the mode of action has not been explored in any detail. Recently, a Ni complex housed in a square pyramidal N_3O_2 environment comprised of three neutral N-donors and two alkoxide O-donors Ni(bdpp) (Figure 17, bottom) has been shown to affect $O_2^{\bullet-}$ dismutation.[220] While this small molecule certainly qualifies as a functional SOD, it holds little in common with the enzymatic species, and few lessons can be applied to the naturally occurring system.

Table 3. Comparison of Ni–N/S bond distances (Å) of Ni-SOD_{red} with those approximating the corresponding bond in Ni(II) complexes modeling Ni-SOD.

	S. coelicolor[173]	*S. seoulensis*[1] 74	$[Ni(N_2S_2)]^-$ 221	[Ni(BEAAM)] -222
Ni-N(His1)	1.87	2.11	1.937(3)	1.989(7)
Ni-N(Cys2)	1.91	1.93	1.862(2)	1.858(6)
Ni-S(Cys2)	2.16	2.24	2.1671(8)	2.137(2)
Ni-S(Cys6)	2.19	2.26	2.1711(7)	2.177(2)

1.9 Low Molecular Weight Complexes Accurately Modeling the Nickel Superoxide Dismutase Active Site

Prior to the research to be discussed in this dissertation, two small molecule NiN_2S_2 complexes ($[Ni(BEAAM)]^-$ (Figure 18, left) and $Ni(N_2S_2)]^-$ (Figure 18, right)) have been prepared which accurately model the mixed amine-amide/bis-thiolate ligation of Ni-SOD_{red}.[221-222] Both models have been structurally characterized and provide Ni-N and Ni-S bond lengths comparable to the anologous values observed for Ni-SOD_{red} (Table 1, Table 3). The oxidation potentials of $[Ni(BEAAM)]^-$ (in MeCN) and $[Ni(N_2S_2)]^-$ (in DMF) are 0.07 V and -0.06 V vs Ag/AgCl, respectively, intermediate between similar Ni(II)N_2S_2 complexes of bis-amine and bis-amide ligation (see Figure 17). However, neither model can be isolated in the Ni(III) oxidation state; nor is either model capable of affecting SOD catalysis.[221-222] S K-edge and Ni L-Edge XAS in conjunction with DFT analysis of $[Ni(BEAAM)]^-$ in relation to bis-amine ligated Ni(bmmp-dmed) and bis-amide ligated $[Ni(emi)]^{2-}$ (Figure 17 center-left and top-left, respectively) was also performed.[223] The results of this study suggest that $[Ni(BEAAM)]^-$ possesses the

strongest and most covalent Ni-S bonding of the series. This study also suggests that the mixed amine/amide coordination serves to destabilize Ni(II) relative to S vs. Ni(II)(bmmp-dmed) while maintaining a redox potential within the window necessary for $O_2^{\bullet -}$ dismutation.[223]

1.10 Goals of the Present Research

The overall goal of this research is to elucidate the fundamental coordination chemistry at play in Ni-SOD utilizing a synthetic modeling approach. In particular, this project is aimed towards the design, preparation and utilization of judiciously constructed complexes which replicate the structural, spatial and electronic disposition of the Ni-SOD active site. In particular, heavy emphasis is placed on the design of models allowing for facile modifications of particular aspects of the coordination motif while leaving other facets unchanged. This approach allows for a systematic study of the effects of modulations of individual components. Our strategy begins with the study of simplistic models modeling the primary coordination sphere; then moves out to model aspects brought about by secondary sphere effects, protein architecture and beyond.

Specific questions this research aims to answer regard the mechanism by which the cysteinate ligands are protected from oxidative modifications, the precise role played by the His1 imidazole side chain with regards to Ni(III) stabilization and an enhanced understanding of factors controlling Ni-based redox activity in a highly covalent Ni-S assembly. Specific challenges this research ultimately aims to meet include the stabilization of Ni(III) and the achievement of SOD catalysis utilizing

complexes accurately replicating the Ni-SOD active site. Meeting these challenges will reflect a full mastery of the interplay between ligands, metal, substrate and products with regards to Ni-SOD. Once mastered, this chemistry can be applied in the context of therapeutics against oxidative stress or towards optimization of Ni-S containing catalysts such as hydrogenase or CODH, systems which provide prescient catalytic processes of environmental and societal import.

1.11 References

(1) Auchére, F.; Rusnak, F. *J. Biol. Inorg. Chem.* **2002**, *7*, 664.

(2) Valentine, J. S.; Wertz, D. L.; Lyons, T. J.; Liou, L.-L.; Goto, J. J.; Gralla, E. B. *Curr. Opin. Chem. Biol.* **1998**, *2*, 253.

(3) Sawyer, D. T.; Valentine, J. S. *Acc. Chem. Res.* **1981**, *14*, 393.

(4) Ishikawa, K.; Takenaga, K.; Akimoto, M.; Koshikawa, N.; Yamaguchi, A.; Imanishi, H.; Nakada, K.; Honma, Y.; Hayashi, J.-I. *Science* **2008**, *320*, 661.

(5) Kumar, B.; Koul, S.; Khandrika, L.; Meacham, R. B.; Koul, H. K. *Cancer Res.* **2008**, *68*, 1777.

(6) Maritim, A. C.; Sanders, R. A.; Watkins, J. B., III *J. Biochem. Mol. Toxicol.* **2003**, *17*, 24.

(7) Steinberg, D. *J. Biol. Chem.* **1997**, *272*, 20963.

(8) Kocatürk, P. A.; Akbostanci, M. C.; Tan, F.; Kavas, G. O. *Pathophysiology* **2000**, *7*, 63.

(9) De Leo, M. E.; Borrello, S.; Passantino, M.; Palazzotti, B.; Mordente, A.; Daniele, A.; Filippini, V.; Galeotti, T.; Masullo, C. *Neurosci. Lett.* **1998**, *250*, 173.

(10) McCord, J. M. *Adv. Free Rad. Biol. Med.* **1986**, *2*, 325.

(11) McCord, J. M. *Free Rad. Biol. Med.* **1988**, *4*, 9.

(12) Fortunato, G.; Pastinese, A.; Intrieri, M.; Lofrano, M. M.; Gaeta, G.; Censi, M. B.; Boccalatte, A.; Salvatore, F.; Sacchetti, L. *Clin. Biochem.* **1997**, *30*, 569.

(13) Chan, P. H.; Yang, G. Y.; Chen, S. F.; Carlson, E.; Epstein, C. J. *Ann. Neurol.* **1991**, *29*, 482.

(14) Yang, G. Y.; Chan, P. H.; Chen, J.; Carlson, E.; Chen, S. F.; Epstein, P.; Kamii, H. *Stroke* **1994**, *25*, 165.

(15) Messner, K. R.; Imlay, J. A. *J. Biol. Chem.* **2002**, *277*, 42563.

(16) Messner, K. R.; Imlay, J. A. *J. Biol. Chem.* **1999**, *274*, 10119.

(17) Imlay, J. A. *J. Biol. Chem.* **1995**, *270*, 19767.

(18) Imlay, J. A.; Fridovich, I. *J. Biol. Chem.* **1991**, *266*, 6957.

(19) Eberlein, G.; Bruice, T. C. *J. Am. Chem. Soc.* **1982**, *104*, 1449.

(20) Massey, V. *J. Biol. Chem.* **1994**, *269*, 22459.

(21) Pennati, A.; Gadda, G. *Biochemistry* **2011**, *50*, 1.

(22) Daithankar, V. N.; Wang, W.; Trujillo, J. R.; Thorpe, C. *Biochemistry* **2012**, *52*, ASAP.

(23) Cadenas, E.; Boveris, A.; Ragan, C. I.; Stoppani, A. O. M. *Arch. Biochem. Biophys.* **1977**, *180*, 248.

(24) Boveris, A.; Cadenas, E.; Stoppani, A. O. M. *Biochem. J.* **1976**, *156*, 435.

(25) Samoilova, R. I.; Crofts, A. R.; Dikanov, S. A. *J. Phys. Chem. A* **2011**, *115*, 11589.

(26) Miller, R. A.; Britigan, B. E. *Clin. Microbiol. Rev.* **1997**, *10*, 1.

(27) Harth, G.; Horwitz, M. A. *J. Biol. Chem.* **1999**, *274*, 4281.

(28) Kono, Y.; Fridovich, I. *J. Biol. Chem.* **1982**, *257*, 5751.

(29) Blum, J.; Fridovich, I. *Arch. Biochem. Biophys.* **1985**, *240*, 500.

(30) Gardner, P. R.; Fridovich, I. *J. Biol. Chem.* **1991**, *266*, 1478.

(31) Gardner, P. R.; Fridovich, I. *J. Biol. Chem.* **1991**, *266*, 19328.

(32) Gardner, P. R.; Fridovich, I. *Arch. Biochem. Biophys.* **1993**, *301*, 98.

(33) Liochev, S. I.; Fridovich, I. *Arch. Biochem. Biophys.* **1993**, *301*, 379.

(34) Flint, D. H.; Smykrandall, E.; Tuminello, J. F.; Draczynskalusiak, B.; Brown, O. R. *J. Biol. Chem.* **1993**, *268*, 25547.

(35) Myers, J. W. *J. Biol. Chem.* **1961**, *236*, 1414.

(36) Gardner, P. R.; Fridovich, I. *J. Biol.Chem.* **1992**, *267*, 8757.

(37) Sawyer, D. T.; Gibian, M. J.; Morrison, M. M.; Seo, E. T. *J. Am. Chem. Soc.* **1978**, *100*, 627.

(38) Nanni, E. J.; Stallings, M. D.; Sawyer, D. T. *J. Am. Chem. Soc.* **1980**, *102*, 4481.

(39) Grisar, J. M.; Marciniak, G.; Bolkenius, F. N.; Vernemismer, J.; Wagner, E. R. *J. Med. Chem.* **1995**, *38*, 2880.

(40) Mashino, T.; Fridovich, I. *Arch. Biochem. Biophys.* **1987**, *254*, 547.

(41) Cardey, B.; Foley, S.; Enescu, M. *J. Phys. Chem. A* **2007**, *111*, 13046.

(42) Frimer, A. A.; Gilinskysharon, P. *J. Org. Chem.* **1995**, *60*, 2796.

(43) Fridovich, I. *Ann. Rev. Pharmacol. Toxicol.* **1983**, *23*, 239.

(44) Koppenol, W. H.; Moreno, J. J.; Pryor, W. A.; Ischiropoulos, H.; Beckman, J. S. *Chem. Res. Toxicol.* **1992**, *5*, 834.

(45) Reiter, C. D.; Teng, R. J.; Beckman, J. S. *J. Biol. Chem.* **2000**, *275*, 32460.

(46) Roberts, B. R.; Beckman, J. S. *Free Rad. Biol. Med.* **2003**, *35*, S109.

(47) Daiber, A.; Bachschmid, M.; Beckman, J. S.; Munzel, T.; Ullrich, V. *Biochem. Biophys. Res. Commun.* **2004**, *317*, 873.

(48) Beckman, J. S. *Arch. Biochem. Biophys.* **2009**, *484*, 114.

(49) Crow, J. P.; Sampson, J. B.; Zhuang, Y. X.; Thompson, J. A.; Beckman, J. S. *J. Neurochem.* **1997**, *69*, 1936.

(50) Estevez, A. G.; Spear, N.; Manuel, S. M.; Barbeito, L.; Radi, R.; Beckman, J. S. *Nitric Oxide in Brain Development, Plasticity and Disease* **1998**, *118*, 269.

(51) Ye, Y. Z.; Quijano, C.; Robinson, K. M.; Ricart, K. C.; Strayer, A. L.; Sahawneh, M. A.; Shacka, J. J.; Kirk, M.; Barnes, S.; Accavitti-Loper, M. A.; Radi, R.; Beckman, J. S.; Estevez, A. G. *J. Biol. Chem.* **2007**, *282*, 6324.

(52) Li, X. H.; De Sarno, P.; Song, L.; Beckman, J. S.; Jope, R. S. *Biochem. J.* **1998**, *331*, 599.

(53) Spear, N.; Estevez, A. G.; Barbeito, L.; Beckman, J. S.; Johnson, G. V. W. *J. Neurochem.* **1997**, *69*, 53.

(54) Rush, J. D.; Bielski, B. H. J. *J. Phys. Chem.* **1985**, *89*, 5062.

(55) Weinstein, J.; Bielski, B. H. J. *J. Am. Chem. Soc.* **1979**, *101*, 58.

(56) Bielski, B. H. J.; Arudi, R. L.; Sutherland, M. W. *J. Biol. Chem.* **1983**, *258*, 4759.

(57) Dix, T. A.; Hess, K. M.; Medina, M. A.; Sullivan, R. W.; Tilly, S. L.; Webb, T. L. L. *Biochemistry* **1996**, *35*, 4578.

(58) Fridovich, I. *J. Biol. Chem.* **1997**, *272*, 18515.

(59) Miller, A.-F. *Curr. Opin. Chem. Biol.* **2004**, *8*, 162.

(60) Perry, J. J. P.; Shin, D. S.; Getzoff, E. D.; Tainer, J. A. *Biochim. Biophys. Acta* **2010**, *1804*, 245.

(61) Tainer, J. A.; Getzoff, E. D.; Richardson, J. S.; Richardson, D. C. *Nature* **1983**, *306*, 284.

(62) Borgstahl, G. E. O.; Parge, H. E.; Hickey, M. J.; Beyer, W. F.; Hallewell, R. A.; Tainer, J. A. *Cell* **1992**, *71*, 107.

(63) Tierney, D. L.; Fee, J. A.; Ludwig, M. L.; Penner-Hahn, J. E. *Biochemistry* **1995**, *34*, 1661.

(64) Miller, A.-F. *Acc. Chem. Res.* **2008**, *41*, 501.

(65) Youn, H.-D.; Youn, H.; Lee, J.-W.; Yim, Y.-I.; Lee, J. K.; Hah, Y. C.; Kang, S.-O. *Arch. Biochem. Biophys.* **1996**, *334*, 341.

(66) Youn, H.-D.; Kim, E.-J.; Roe, J.-H.; Hah, Y. C.; Kang, S.-O. *Biochem. J.* **1996**, *318*, 889.

(67) Rosen, D. R.; Siddique, T.; Patterson, D.; Figlewicz, D. A.; Sapp, P.; Hentati, A.; Donaldson, D.; Goto, J.; Oregan, J. P.; Deng, H. X.; Rahmani, Z.; Krizus, A.; McKennayasek, D.; Cayabyab, A.; Gaston, S. M.; Berger, R.; Tanzi, R. E.; Halperin, J. J.; Herzfeldt, B.; Vandenbergh, R.; Hung, W. Y.; Bird, T.; Deng, G.; Mulder, D. W.; Smyth, C.; Laing, N. G.; Soriano, E.; Pericakvance, M. A.; Haines, J.; Rouleau, G. A.; Gusella, J. S.; Horvitz, H. R.; Brown, R. H. *Nature* **1993**, *362*, 59.

(68) DiDonato, M.; Craig, L.; Huff, M. E.; Thayer, M. M.; Cardoso, R. M. F.; Kassmann, C. J.; Lo, T. P.; Bruns, C. K.; Powers, E. T.; Kelly, J. W.; Getzoff, E. D.; Tainer, J. A. *J. Mol. Biol.* **2003**, *334*, 175.

(69) Andersen, P. M. *Curr. Neurol. Neurosci. Rep.* **2006**, *6*, 37.

(70) Mann, T.; Keilin, D. *Proc. Roy. Soc. Ser. B-Biol. Sci.* **1938**, *126*, 303.

(71) McCord, J. M.; Fridovich .I *J. Biol. Chem.* **1968**, *243*, 5753.

(72) McCord, J. M.; Fridovich .I *J. Biol. Chem.* **1969**, *244*, 6049.

(73) Thomas, K. A.; Rubin, B. H.; Bier, C. J.; Richardson, J. S.; Richardson, D. C. *J. Biol. Chem.* **1974**, *249*, 5677.

(74) Richardson, J. S.; Thomas, K. A.; Rubin, B. H.; Richardson, D. C. *Proc. Natl. Acad. Sci. U.S.A.* **1975**, *72*, 1349.

(75) Getzoff, E. D.; Tainer, J. A.; Weiner, P. K.; Kollman, P. A.; Richardson, J. S.; Richardson, D. C. *Nature* **1983**, *306*, 287.

(76) Shin, D. S.; DiDonato, M.; Barondeau, D. P.; Hura, G. L.; Hitomi, C.; Berglund, J. A.; Getzoff, E. D.; Cary, S. C.; Tainer, J. A. *J. Mol. Biol.* **2009**, *385*, 1534.

(77) Rotilio, G.; Calabres.L; Mondovi, B.; Blumberg, W. E. *J. Biol. Chem.* **1974**, *249*, 3157.

(78) Klug, D.; Rabani, J.; Fridovich, I. *J. Biol. Chem.* **1972**, *247*, 4839.

(79) Chance, B.; Sies, H.; Boveris, A. *Physiol. Rev.* **1979**, *59*, 527.

(80) Lynch, M.; Kuramitsu, H. *Microbes Infect.* **2000**, *2*, 1245.

(81) Parker, M. W.; Blake, C. C. F. *J. Mol. Biol.* **1988**, *199*, 649.

(82) Stallings, W. C.; Metzger, A. L.; Pattridge, K. A.; Fee, J. A.; Ludwig, M. L. *Free Rad. Res. Commun.* **1991**, *12-3*, 259.

(83) Stoddard, B. L.; Howell, P. L.; Ringe, D.; Petsko, G. A. *Biochemistry* **1990**, *29*, 8885.

(84) Han, W.-G.; Lovell, T.; Noodleman, L. *Inorg. Chem.* **2002**, *41*, 205.

(85) Guan, Y.; Hickey, M. J.; Borgstahl, G. E. O.; Hallewell, R. A.; Lepock, J. R.; O'Connor, D.; Hsieh, Y. S.; Nick, H. S.; Silverman, D. N.; Tainer, J. A. *Biochemistry* **1998**, *37*, 4722.

(86) Perry, J. J. P.; Hearn, A. S.; Cabelli, D. E.; Nick, H. S.; Tainer, J. A.; Silverman, D. N. *Biochemistry* **2009**, *48*, 3417.

(87) Bull, C.; Niederhoffer, E. C.; Yoshida, T.; Fee, J. A. *J. Am. Chem. Soc.* **1991**, *113*, 4069.

(88) Jackson, T. A.; Karapetian, A.; Miller, A.-F.; Brunold, T. C. *Biochemistry* **2005**, *44*, 1504.

(89) Miller, A. F.; Sorkin, D. L.; Padmakumar, K. *Biochemistry* **2005**, *44*, 5969.

(90) Bull, C.; Fee, J. A. *J. Am. Chem. Soc.* **1985**, *107*, 3295.

(91) Hearn, A. S.; Fan, L.; Lepock, J. R.; Luba, J. P.; Greenleaf, W. B.; Cabelli, D. E.; Tainer, J. A.; Nick, H. S.; Silverman, D. N. *J. Biol. Chem.* **2004**, *279*, 5861.

(92) Greenleaf, W. B.; Jefferson, J.; Perry, P.; Hearn, A. S.; Cabelli, D. E.; Lepock, J. R.; Stroupe, M. E.; Tainer, J. A.; Nick, H. S.; Silverman, D. N. *Biochemistry* **2004**, *43*, 7038.

(93) Grove, L. E.; Xie, J.; Yikilmaz, E.; Karapetyan, A.; Miller, A.-F.; Brunold, T. C. *Inorg. Chem.* **2008**, *47*, 3993.

(94) Vance, C. K.; Miller, A.-F. *J. Am. Chem. Soc.* **1998**, *120*, 461.

(95) Grove, L. E.; Xie, J.; Yikilmaz, E.; Miller, A.-F.; Brunold, T. C. *Inorg. Chem.* **2008**, *47*, 3978.

(96) Li, Y.; Zamble, D. B. *Chem. Rev.* **2009**, *109*, 4617.

(97) Harrop, T. C.; Mascharak, P. K. In *Concepts and Models in Bioinorganic Chemistry*; Kraatz, H.-B., Metzler-Nolte, N., Eds.; Wiley-VCH: Weinheim, 2006, p 309.

(98) Mulrooney, S. B.; Hausinger, R. P. *FEMS Microbiol. Rev.* **2003**, *27*, 239.

(99) Mobley, H. L. T.; Hausinger, R. P. *Microbiol. Rev.* **1989**, *53*, 85.

(100) Karplus, P. A.; Pearson, M. A.; Hausinger, R. P. *Acc. Chem. Res.* **1997**, *30*, 330.

(101) Ciurli, S.; Benini, S.; Rypniewski, W. R.; Wilson, K. S.; Miletti, S.; Mangani, S. *Coord. Chem. Rev.* **1999**, *192*, 331.

(102) Volbeda, A.; Charon, M. H.; Piras, C.; Hatchikian, E. C.; Frey, M.; Fontecillacamps, J. C. *Nature* **1995**, *373*, 580.

(103) Volbeda, A.; Garcin, E.; Piras, C.; deLacey, A. L.; Fernandez, V. M.; Hatchikian, E. C.; Frey, M.; Fontecilla-Camps, J. C. *J. Am. Chem. Soc.* **1996**, *118*, 12989.

(104) Gu, Z.; Dong, J.; Allan, C. B.; Choudhury, S. B.; Franco, R.; Moura, J. J. G.; Moura, I.; LeGall, J.; Przybyla, A. E.; Roseboom, W.; Albracht, S. P. J.; Axley, M. J.; Scott, R. A.; Maroney, M. J. *J. Am. Chem. Soc.* **1996**, *118*, 11155.

(105) Ragsdale, S. W.; Kumar, M. *Chem. Rev.* **1996**, *96*, 2515.

(106) Lindahl, P. A. *Biochemistry* **2002**, *41*, 2097.

(107) Ermler, U.; Grabarse, W.; Shima, S.; Goubeaud, M.; Thauer, R. K. *Science* **1997**, *278*, 1457.

(108) Davidson, G.; Clugston, S. L.; Honek, J. F.; Maroney, M. J. *Inorg. Chem.* **2000**, *39*, 2962.

(109) He, M. M.; Clugston, S. L.; Honek, J. F.; Matthews, B. W. *Biochemistry* **2000**, *39*, 8719.

(110) Dai, Y.; Wensink, P. C.; Abeles, R. H. *J. Biol. Chem.* **1999**, *274*, 1193.

(111) Pochapsky, T. C.; Pochapsky, S. S.; Ju, T. T.; Mo, H. P.; Al-Mjeni, F.; Maroney, M. J. *Nat. Struct. Biol.* **2002**, *9*, 966.

(112) Al-Mjeni, F.; Ju, T.; Pochapsky, T. C.; Maroney, M. J. *Biochemistry* **2002**, *41*, 6761.

(113) Chai, S. C.; Ju, T. T.; Dang, M.; Goldsmith, R. B.; Maroney, M. J.; Pochapsky, T. C. *Biochemistry* **2008**, *47*, 2428.

(114) Guldan, H.; Sterner, R.; Babinger, P. *Biochemistry* **2008**, *47*, 7376.

(115) Merkens, H.; Kappl, R.; Jakob, R. P.; Schmid, F. X.; Fetzner, S. *Biochemistry* **2008**, *47*, 12185.

(116) Hausinger, R. P. *Microbiol. Rev.* **1987**, *51*, 22.

(117) Adams, M. W. W.; Mortenson, L. E.; Chen, J.-S. *Biochim. Biophys. Acta* **1981**, *594*, 105.

(118) Odom, J. M.; Peck, H. D., Jr. *Annu. Rev. Microbiol.* **1984**, *38*, 551.

(119) Daniels, L.; Sparling, R.; Sprott, G. D. *Biochim. Biophys. Acta* **1984**, *768*, 113.

(120) Frey, M. *ChemBioChem* **2002**, *3*, 153.

(121) Fichtner, C.; Laurich, C.; Bothe, E.; Lubitz, W. *Biochemistry* **2006**, *45*, 9706.

(122) Lill, S. O. N.; Siegbahn, P. E. M. *Biochemistry* **2009**, *48*, 1056.

(123) Flores, M.; Agrawal, A. G.; van Gastel, M.; Gartner, W.; Lubitz, W. *J. Am. Chem. Soc.* **2008**, *130*, 2402.

(124) Pandelia, M. E.; Infossi, P.; Giudici-Orticoni, M. T.; Lubitz, W. *Biochemistry* **2010**, *49*, 8873.

(125) Ogata, H.; Lubitz, W.; Higuchi, Y. *Dalton Trans.* **2009**, 7577.

(126) Volbeda, A.; Martin, L.; Cavazza, C.; Matho, M.; Faber, B. W.; Roseboom, W.; Albracht, S. P. J.; Garcin, E.; Rousset, M.; Fontecilla-Camps, J. C. *J. Biol. Inorg. Chem.* **2005**, *10*, 239.

(127) Ogata, H.; Hirota, S.; Nakahara, A.; Komori, H.; Shibata, N.; Kato, T.; Kano, K.; Higuchi, Y. *Structure* **2005**, *13*, 1635.

(128) Barton, B. E.; Whaley, C. M.; Rauchfuss, T. B.; Gray, D. L. *J. Am. Chem. Soc.* **2009**, *131*, 6942.

(129) Montet, Y.; Amara, P.; Volbeda, A.; Vernede, X.; Hatchikian, E. C.; Field, M. J.; Frey, M.; Fontecilla-Camps, J. C. *Nat. Struct. Biol.* **1997**, *4*, 523.

(130) Wang, P.-h.; Best, R. B.; Blumberger, J. *J. Am. Chem. Soc.* **2011**, *133*, 3548.

(131) Rousset, M.; Montet, Y.; Guigliarelli, B.; Forget, N.; Asso, M.; Bertrand, P.; Fontecilla-Camps, J. C.; Hatchikian, E. C. *Proc. Natl. Acad. Sci. U.S.A.* **1998**, *95*, 11625.

(132) Morris, R. H. In *Concepts and Models in Bioinorganic Chemistry*; Kraatz, H.-B., Metzler-Nolte, N., Eds.; Wiley-VCH: Weinheim, 2006, p 331

(133) Teixeira, V. H.; Soares, C. M.; Baptista, A. M. *Proteins: Stuct. Funct. Bioinf.* **2008**, *70*, 1010.

(134) Galvan, I. F.; Volbeda, A.; Fontecilla-Camps, J. C.; Field, M. J. *Proteins: Stuct. Funct. Bioinf.* **2008**, *73*, 195.

(135) Pavlov, M.; Siegbahn, P. E. M.; Blomberg, M. R. A.; Crabtree, R. H. *J. Am. Chem. Soc.* **1998**, *120*, 548.

(136) Niu, S. Q.; Thomson, L. M.; Hall, M. B. *J. Am. Chem. Soc.* **1999**, *121*, 4000.

(137) Amara, P.; Volbeda, A.; Fontecilla-Camps, J. C.; Field, M. J. *J. Am. Chem. Soc.* **1999**, *121*, 4468.

(138) Lubitz, W.; Tumas, W. *Chem. Rev.* **2007**, *107*, 3900.

(139) Sezer, M.; Frielingsdorf, S.; Millo, D.; Heidary, N.; Utesch, T.; Mroginski, M. A.; Friedrich, B.; Hildebrandt, P.; Zebger, I.; Weidinger, I. M. *J. Phys. Chem. B.* **2011**, *115*, 10368.

(140) McIntosh, C. L.; Germer, F.; Schulz, R.; Appel, J.; Jones, A. K. *J. Am. Chem. Soc.* **2011**, *133*, 11308.

(141) Gutierrez-Sanchez, C.; Olea, D.; Marques, M.; Fernandez, V. M.; Pereira, I. A. C.; Velez, M.; De Lacey, A. L. *Langmuir* **2011**, *27*, 6449.

(142) Lubner, C. E.; Knorzer, P.; Silva, P. J. N.; Vincent, K. A.; Happe, T.; Bryant, D. A.; Golbeck, J. H. *Biochemistry* **2010**, *49*, 10264.

(143) Parkin, A.; Goldet, G.; Cavazza, C.; Fontecilla-Camps, J. C.; Armstrong, F. A. *J. Am. Chem. Soc.* **2008**, *130*, 13410.

(144) Dementin, S.; Leroux, F.; Cournac, L.; de Lacey, A. L.; Volbeda, A.; Leger, C.; Burlat, B.; Martinez, N.; Champ, S.; Martin, L.; Sanganas, O.; Haumann, M.; Fernandez, V. M.; Guigliarelli, B.; Fontecilla-Camps, J. C.; Rousset, M. *J. Am. Chem. Soc.* **2009**, *131*, 10156.

(145) Ferry, J. G. *Annu. Rev. Microbiol.* **1995**, *49*, 305.

(146) Dobbek, H.; Svetlitchnyi, V.; Gremer, L.; Huber, R.; Meyer, O. *Science* **2001**, *293*, 1281.

(147) Jeoung, J.-H.; Dobbek, H. *Science* **2007**, *318*, 1461.

(148) Doukov, T. I.; Iverson, T. M.; Seravalli, J.; Ragsdale, S. W.; Drennan, C. L. *Science* **2002**, *298*, 567.

(149) Amara, P.; Mouesca, J. M.; Volbeda, A.; Fontecilla-Camps, J. C. *Inorg. Chem.* **2011**, *50*, 1868.

(150) Drennan, C. L.; Doukov, T. I.; Ragsdale, S. W. *J. Biol. Inorg. Chem.* **2004**, *9*, 511.

(151) Darnault, C.; Volbeda, A.; Kim, E. J.; Legrand, P.; Vernede, X.; Lindahl, P. A.; Fontecilla-Camps, J. C. *Nat. Struct. Biol.* **2003**, *10*, 271.

(152) Bramlett, M. R.; Tan, X. S.; Lindahl, P. A. *J. Am. Chem. Soc.* **2003**, *125*, 9316.

(153) Seravalli, J.; Xiao, Y. M.; Gu, W. W.; Cramer, S. P.; Antholine, W. E.; Krymov, V.; Gerfen, G. J.; Ragsdale, S. W. *Biochemistry* **2004**, *43*, 3944.

(154) Maynard, E. L.; Lindahl, P. A. *J. Am. Chem. Soc.* **1999**, *121*, 9221.

(155) Doukov, T. I.; Blasiak, L. C.; Seravalli, J.; Ragsdale, S. W.; Drennan, C. L. *Biochemistry* **2008**, *47*, 3474.

(156) George, S. J.; Seravalli, J.; Ragsdale, S. W. *J. Am. Chem. Soc.* **2005**, *127*, 13500.

(157) Harrop, T. C.; Olmstead, M. M.; Mascharak, P. K. *Inorg. Chem.* **2006**, *45*, 3424.

(158) Lu, W. P.; Harder, S. R.; Ragsdale, S. W. *J. Biol. Chem.* **1990**, *265*, 3124.

(159) Barondeau, D. P.; Lindahl, P. A. *J. Am. Chem. Soc.* **1997**, *119*, 3959.

(160) Seravalli, J.; Ragsdale, S. W. *J. Biol. Chem.* **2008**, *283*, 8384.

(161) Ellefson, W. L.; Wolfe, R. S. *J. Biol. Chem.* **1981**, *256*, 4259.

(162) Tang, Q.; Carrington, P. E.; Horng, Y. C.; Maroney, M. J.; Ragsdale, S. W.; Bocian, D. F. *J. Am. Chem. Soc.* **2002**, *124*, 13242.

(163) Sarangi, R.; Dey, M.; Ragsdale, S. W. *Biochemistry* **2009**, *48*, 3146.

(164) Li, X. H.; Telser, J.; Kunz, R. C.; Hoffman, B. M.; Gerfen, G.; Ragsdale, S. W. *Biochemistry* **2010**, *49*, 6866.

(165) Dey, M.; Li, X. H.; Kunz, R. C.; Ragsdale, S. W. *Biochemistry* **2010**, *49*, 10902.

(166) Cedervall, P. E.; Dey, M.; Li, X. H.; Sarangi, R.; Hedman, B.; Ragsdale, S. W.; Wilmot, C. M. *J. Am. Chem. Soc.* **2011**, *133*, 5626.

(167) Piskorski, R.; Jaun, B. *J. Am. Chem. Soc.* **2003**, *125*, 13120.

(168) Herbst, R. W.; Guce, A.; Bryngelson, P. A.; Higgins, K. A.; Ryan, K. C.; Cabelli, D. E.; Garman, S. C.; Maroney, M. J. *Biochemistry* **2009**, *48*, 3354.

(169) Youn, H.-D.; Yim, Y.-I.; Kim, K.; Hah, Y. C.; Kang, S.-O. *J. Biol. Chem.* **1995**, *270*, 13740.

(170) Palenik, B.; Brahamsha, B.; Larimer, F. W.; Land, M.; Hauser, L.; Chain, P.; Lamerdin, J.; Regala, W.; Allen, E. E.; McCarren, J.; Paulsen, I.; Dufresne, A.; Partensky, F.; Webb, E. A.; Waterbury, J. *Nature* **2003**, *424*, 1037.

(171) Schmidt, A.; Gube, M.; Kothe, E. *J. Basic Microbiol.* **2009**, *49*, 109.

(172) Kim, E.-J.; Chung, H.-J.; Suh, B. S.; Hah, Y. C.; Roe, J.-H. *Mol. Microbiol.* **1998**, *27*, 187.

(173) Barondeau, D. P.; Kassmann, C. J.; Bruns, C. K.; Tainer, J. A.; Getzoff, E. D. *Biochemistry* **2004**, *43*, 8038.

(174) Wuerges, J.; Lee, J.-W.; Yim, Y.-I.; Yim, H.-S.; Kang, S.-O.; Carugo, K. D. *Proc. Natl. Acad. Sci. U.S.A.* **2004**, *101*, 8569.

(175) Bryngelson, P. A.; Arobo, S. E.; Pinkham, J. L.; Cabelli, D. E.; Maroney, M. J. *J. Am. Chem. Soc.* **2004**, *126*, 460.

(176) Choudhury, S. B.; Lee, J. W.; Davidson, G.; Yim, Y. I.; Bose, K.; Sharma, M. L.; Kang, S. O.; Cabelli, D. E.; Maroney, M. J. *Biochemistry* **1999**, *38*, 3744.

(177) Peters, J. W.; Stowell, M. H. B.; Soltis, S. M.; Finnegan, M. G.; Johnson, M. K.; Rees, D. C. *Biochemistry* **1997**, *36*, 1181.

(178) Huang, W. J.; Jia, J.; Cummings, J.; Nelson, M.; Schneider, G.; Lindqvist, Y. *Structure* **1997**, *5*, 691.

(179) Miyanaga, A.; Fushinobu, S.; Ito, K.; Wakagi, T. *Biochem. Biophys. Res. Commun.* **2001**, *288*, 1169.

(180) Arakawa, T.; Kawano, Y.; Kataoka, S.; Katayama, Y.; Kamiya, N.; Yohda, M.; Odaka, M. *J. Mol. Biol.* **2007**, *366*, 1497.

(181) Krüger, H.-J.; Peng, G.; Holm, R. H. *Inorg. Chem.* **1991**, *30*, 734.

(182) Jenney, F. E.; Verhagen, M.; Cui, X. Y.; Adams, M. W. W. *Science* **1999**, *286*, 306.

(183) Grapperhaus, C. A.; Darensbourg, M. Y. *Acc. Chem. Res.* **1998**, *31*, 451.

(184) Ryan, K. C.; Johnson, O. E.; Cabelli, D. E.; Brunold, T. C.; Maroney, M. J. *J. Biol. Inorg. Chem.* **2010**, *15*, 795.

(185) Johnson, O. E.; Ryan, K. C.; Maroney, M. J.; Brunold, T. C. *J. Biol. Inorg. Chem.* **2010**, *15*, 777.

(186) Fiedler, A. T.; Bryngelson, P. A.; Maroney, M. J.; Brunold, T. C. *J. Am. Chem. Soc.* **2005**, *127*, 5449.

(187) Colpas, G. J.; Kumar, M.; Day, R. O.; Maroney, M. J. *Inorg. Chem.* **1990**, *29*, 4779.

(188) Mills, D. K.; Reibenspies, J. H.; Darensbourg, M. Y. *Inorg. Chem.* **1990**, *29*, 4364.

(189) Maroney, M. J.; Choudhury, S. B.; Bryngelson, P. A.; Mirza, S. A.; Sherrod, M. J. *Inorg. Chem.* **1996**, *35*, 1073.

(190) Smee, J. J.; Miller, M. L.; Grapperhaus, C. A.; Reibenspies, J. H.; Darensbourg, M. Y. *Inorg. Chem.* **2001**, *40*, 3601.

(191) Hanss, J.; Krüger, H.-J. *Angew. Chem., Int. Ed.* **1998**, *37*, 360.

(192) Gennari, M.; Orio, M.; Pécaut, J.; Neese, F.; Collomb, M.-N.; Duboc, C. *Inorg. Chem.* **2010**, *49*, 6399.

(193) Gewirth, A. A.; Solomon, E. I. *J. Am. Chem. Soc.* **1988**, *110*, 3811.

(194) Lappin, A. G.; Murray, C. K.; Margerum, D. W. *Inorg. Chem.* **1978**, *17*, 1630.

(195) Sugiura, Y.; Mino, Y. *Inorg. Chem.* **1979**, *18*, 1336.

(196) Krüger, H.-J.; Holm, R. H. *Inorg. Chem.* **1987**, *26*, 3645.

(197) Fiedler, A. T.; Brunold, T. C. *Inorg. Chem.* **2007**, *46*, 8511.

(198) Neupane, K. P.; Gearty, K.; Francis, A.; Shearer, J. *J. Am. Chem. Soc.* **2007**, *129*, 14605.

(199) DiBilio, A. J.; Hill, M. G.; Bonander, N.; Karlsson, B. G.; Villahermosa, R. M.; Malmstrom, B. G.; Winkler, J. R.; Gray, H. B. *J. Am. Chem. Soc.* **1997**, *119*, 9921.

(200) Davidson, V. L. *Acc. Chem. Res.* **2000**, *33*, 87.

(201) Mullins, C. S.; Grapperhaus, C. A.; Kozlowski, P. M. *J. Biol. Inorg. Chem.* **2006**, *11*, 617.

(202) Szilagyi, R. K.; Bryngelson, P. A.; Maroney, M. J.; Hedman, B.; Hodgson, K. O.; Solomon, E. I. *J. Am. Chem. Soc.* **2004**, *126*, 3018.

(203) Prabhakar, R.; Morokuma, K.; Musaev, D. G. *J. Comput. Chem.* **2006**, *27*, 1438.

(204) Pelmenschikov, V.; Siegbahn, P. E. M. *J. Am. Chem. Soc.* **2006**, *128*, 7466.

(205) Shearer, J.; Long, L. M. *Inorg. Chem.* **2006**, *45*, 2358.

(206) Colpas, G. J.; Maroney, M. J.; Bagyinka, C.; Kumar, M.; Willis, W. S.; Suib, S. L.; Baidya, N.; Mascharak, P. K. *Inorganic Chemistry* **1991**, *30*, 920.

(207) Tabbì, G.; Driessen, W. L.; Reedijk, J.; Bonomo, R. P.; Veldman, N.; Spek, A. L. *Inorg. Chem.* **1997**, *36*, 1168.

(208) Vincent, K. A.; Armstrong, F. A. *Inorg. Chem.* **2005**, *44*, 798.

(209) Shearer, J.; Neupane, K. P.; Callan, P. E. *Inorg. Chem.* **2009**, *48*, 10560.

(210) Schmidt, M.; Zahn, S.; Carella, M.; Ohlenschläger, O.; Görlach, M.; Kothe, E.; Weston, J. *ChemBioChem* **2008**, *9*, 2135.

(211) Tietze, D.; Breitzke, H.; Imhof, D.; Kothe, E.; Weston, J.; Buntkowsky, G. *Chem. - Eur. J.* **2009**, *15*, 517.

(212) Krause, M. E.; Glass, A. M.; Jackson, T. A.; Laurence, J. S. *Inorg. Chem.* **2010**, *49*, 362.

(213) Krause, M. E.; Glass, A. M.; Jackson, T. A.; Laurence, J. S. *Inorganic Chemistry* **2011**, *50*, 2479.

(214) Ma, H.; Chattopadhyay, S.; Petersen, J. L.; Jensen, M. P. *Inorg. Chem.* **2008**, *47*, 7966.

(215) Ma, H.; Wang, G.; Yee, G. T.; Petersen, J. L.; Jensen, M. P. *Inorg. Chim. Acta* **2009**, *362*, 4563.

(216) Mullins, C. S.; Grapperhaus, C. A.; Frye, B. C.; Wood, L. H.; Hay, A. J.; Buchanan, R. M.; Mashuta, M. S. *Inorg. Chem.* **2009**, *48*, 9974.

(217) Herdt, D. R.; Grapperhaus, C. A. *Dalton Trans.* **2011**, *41*, 364.

(218) Jenkins, R. M.; Singleton, M. L.; Almaraz, E.; Reibenspies, J. H.; Darensbourg, M. Y. *Inorg. Chem.* **2009**, *48*, 7280.

(219) Jenkins, R. M.; Singleton, M. L.; Leamer, L. A.; Reibenspies, J. H.; Darensbourg, M. Y. *Inorg. Chem.* **2010**, *49*, 5503.

(220) Lee, W.-Z.; Chiang, C.-W.; Lin, T.-H.; Kuo, T.-S. *Dalton Trans.* **2012**, *18*, 50.

(221) Mathrubootham, V.; Thomas, J.; Staples, R.; McCraken, J.; Shearer, J.; Hegg, E. L. *Inorg. Chem.* **2010**, *49*, 5393.

(222) Shearer, J.; Zhao, N. *Inorg. Chem.* **2006**, *45*, 9637.

(223) Shearer, J.; Dehestani, A.; Abanda, F. *Inorg. Chem.* **2008**, *47*, 2649.

CHAPTER 2

COMPLEXES MODELING Ni-SOD$_{RED}$ FEATURING ELECTRONICALLY VARIANT THIOLATE LIGANDS: PROBING THE EFFECTS OF THIOLATE MODIFICATIONS ON STRUCTURE, PROPERTIES AND REACTIVITY[1,2]

[1] Gale, E. M., Patra, A. K., Harrop, T. C. *Inorg, Chem*. **2009**, *48*, 5620. Reprinted here with permission of publisher.
[2] Gale, E. M.. Narendrapurapu, B. S., Simmonett, A. C. Schaefer, H. F., III, Harrop, T. C. *Inorg. Chem*. **2010**, *49*, 7080. Reprinted here with permission of publisher.

2.1 Abstract

We have utilized the tri-dentate N_2S-chelate *N*-(2-mercaptoethyl)picolinamide ($nmpH_2$, where Hs represents dissociable protons) in order to model the contributions provided by the His1Cys2 chelate to Ni-SOD_{red}. A mono-dentate thiolate ligand was employed to model Cys6. This exogenously added RS^- ligand could be readily manipulated through a variety of synthetic protocols. We exploited this synthetic versatility to prepare a small library of Ni-SOD_{red} models featuring variant RS^-, some with appended secondary sphere peptides capable of engaging in NH•••S hydrogen-bonding. This strategy enabled us to probe the effects imparted on the structural, electronic and reactivity properties imparted by electronic modulation at the component modeling Cys6. X-ray structural analysis, spectroscopic characterization, cyclic voltammetry measurements and reactivity studies with O_2 and various reactive oxygen species served to elucidate the role played by hydrogen-bonding in tuning the physical and reactivity properties of NiN_2S_2 complexes of similar disposition to Ni-SOD_{red}. In conjuction with theoretical analysis, we have determined that S-directed hydrogen-bonding is capable of stabilizing S-based atomic orbitals relative to those arising from Ni. This occurs through alleviation of a strongly anti-bonding Ni(π)-S(π) interaction in the highest occupied molecular orbital, effectively promoting Ni vs. S based reactivity.

2.2 Introduction

The unprecedented ligand framework and unique reactivity of the Ni-SOD active site provide a source of inspiration for the synthetic inorganic chemist. As discussed in Chapter 1, it is clear that every component of the primary coordination sphere as well as contributions from the secondary sphere and beyond serve to carefully tune the Ni ion towards optimal catalytic activity. We have set out to design accurate mimics of the Ni-SOD active site using a modular approach by which ligand contributions of a representative Ni-complex can be readily tuned and substituted, leaving other contributions unchanged. This approach allows us to hone our focus on the contributions of one particular aspect of the active site assembly.

The research discussed in this chapter represents our initial foray into modeling the Ni-SOD active site. The models presented below enabled our focus to turn specifically towards contributions modeling the Ni-S(Cys6) bond. Observing trends in structural, electronic and reactivity properties brought about by subtle perturbations to this bond has afforded unique insight into the electronic role played by Cys6. The incorporation of secondary sphere residues capable of intramolecular hydrogen-bonding has provided experimental evidence in support of the hypothesis that directed hydrogen-bonding to coordinated cysteinates serves to aid in the avoidance of S-oxidation and promotion of Ni-based redox activity during SOD catalysis.[1-2]

2.3 Ligand Design and Preparation of Complexes of Formula $[Ni(nmp)(SR)]^-$

There were several design criteria we set out to meet in our initial models of Ni-SOD. First, we desired ligands accurately modeling the spatial and electronic disposition of the primary coordination sphere of Ni-SOD. Secondly, we wanted to model in a component which could be easily modified at no cost to the remainder of the complex, allowing us to pursue this chemistry from the modular approach outlined above. Also, complexes amenable to structural characterization and existing as singular, identifiable species in the solution state are highly desirable in that such models allow for rigorous study by conclusive characterization techniques and provide an un-obscured scenario by which trends across a series can be rationalized.

Consideration of the aforementioned criteria culminated in the tri-dentate chelate *N*-(2-mercaptoethyl)picolinamide ($nmpH_2$, where H represents dissociable protons) as the ligand of choice (Figure 1). This ligand features a pyridyl-N approximating the terminal N-amine of His1 and a carboxamido-N and thiolato-S modeling the chelation arising from Cys2.[3-4] The ligand could be easily prepared in four steps (Scheme 1). S-trityl protection of cysteamine occurred in 78% yield. Next, reaction of S-trityl-cysteamine with picolinoyl chloride (prepared by treatment of picolinic acid with refluxing $SOCl_2$) afforded the S-protected pre-ligand in 87% yield. Deprotection in TFA afforded $nmpH_2$ as a tan oil in 73% yield.

Deprotonation of $nmpH_2$ with two mol-equiv. NaH followed by addition of $[Ni(H_2O)_6](ClO_4)_2$ in DMF affords $Ni_2(nmp)_2$ (**1**) (Scheme 2), a dimeric metallo-synthon with built-in contributions modeling those of His1 and Cys2 to Ni-SOD_{red} at each individual Ni center, in 96% yield. Complex **1** is isolated as an orange solid that

is insoluble in all solvents and inherently stable due to a square-planar d^8 configuration. Despite the robust nature and unfavorable solubility properties, we presumed that **1** would serve as a viable precursor to complexes of formula $[Ni(nmp)(SR)]^-$ modeling Ni-SOD_{red}. Indeed, addition of two mol-equivs. of the K^+ salts of 4-chlorobenzenethiolate (KSC_6H_4-*p*-Cl) or ^{t}butyl thiolate (KS^tBu) followed by cation exchange with Et_4NCl resulted in $(Et_4N)[Ni(nmp)(SC_6H_4$-*p*-Cl)] (**2**) and $(Et_4N)[Ni(nmp)(S^tBu)]$ (**3**), respectively, in ~70% yield (Scheme 2). Similar $Ni_2(\mu$-$SR)_2$ bridge splitting procedures using thiocarboxylate and imidazole ligands were simultaneously reported by Holm[5] and Darensbourg[6], respectively.

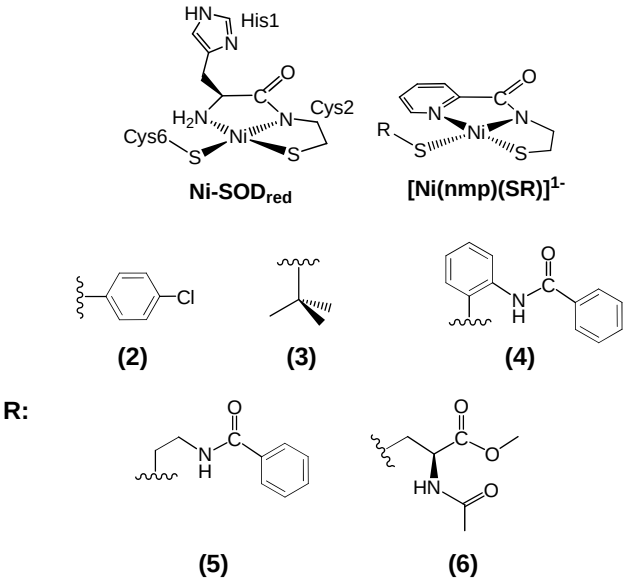

Figure 1. (Top): Active site of Ni-SOD_{red} (left) and Ni-SOD model system described in this chapter, $[Ni(nmp)(SR)]^-$ (right). (Bottom): R groups used in this study (RSH = HSC_6H_4-*p*-Cl (**2**), HS^tBu (**3**), *o*-benzoylaminobenzene thiol (**4**), *N*-(2-mercaptoethyl)benzyamide (**5**) and *N*-acetyl-L-cysteine methyl ester (**6**)).

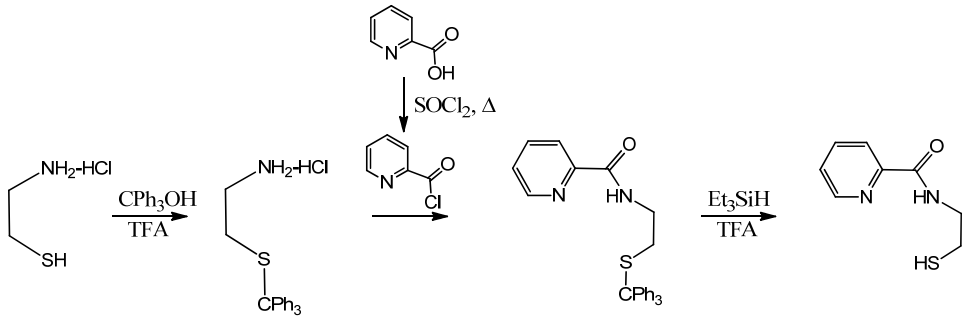

Scheme 1. Synthesis of *N*-(2-mercaptoethyl)picolinamide ($nmpH_2$).

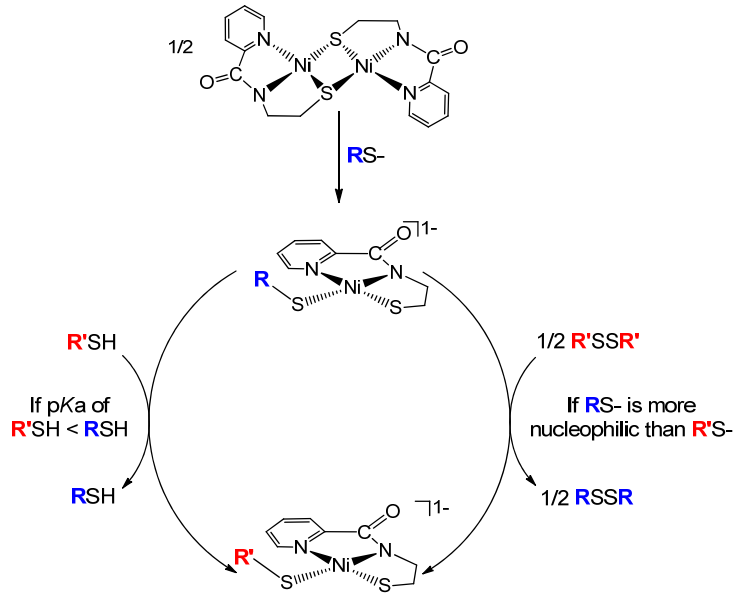

Scheme 2. Synthetic protocols by which complexes of general formula $[Ni(nmp)(SR)]^-$ were obtained.

The RS^- ligand could be readily interchanged by two additional synthetic protocols; namely, via redox driven disulfide/coordinated thiolate and/or pK_a driven thiol/coordinated thiolate exchange procedures (Scheme 2). Specifically, (Et_4N)[Ni(nmp)(S-*o*-babt)] (**4**) (HS-*o*-babt = *o*-benzoylaminobenzenthiolate) could be prepared by addition of 0.5 mol-equivs. *o*-babt disulfide to **3**. Also, (Et_4N)[Ni(nmp)(S-meb)] (**5**) (HS-meb = *N*-(2-mercaptoethyl)benzamide) and K[Ni(nmp)(S-NAc)] (**6**) (HS-NAc = *N*-acetyl-L-cysteine methyl ester) could be

prepared by addition of one mol-equiv. of the corresponding RSH to **3** (**6** prepared from **3** as the K^+ salt). Along with versatility, these additional protocols also afford a way around pitfalls potentially encountered during the S,S'-bridge splitting method when using more complex S-containing ligands, such as inherently reactive thiol groups (*o*-carboxamidothiophenols can spontaneously undergo intramolecular condensation to benzothiazoles).[7] Thus, our vision of a versatile model amenable to modular tuning was realized in the series represented by complexes **2**-**6**. The exchangeable nature of the monodentate thiolate ligand allowed for focused study of the component modeling the Ni-S(Cys6) bond of Ni-SOD_{red} while leaving those modeling His1 and Cys2 undisturbed. In particular, our focus was directed towards the effects imparted by intramolecular hydrogen-bonding interactions with this bond.

2.4 Structure and Properties

Complexes **2**-**5** have been structurally characterized by single crystal X-ray diffraction allowing for insights into solid-state manifestations of subtle modulations to the Cys6 model component (Figures 2-5 for complexes **2**-**5**, respectively; see Table 1 for selected bond distances and angles). A slightly distorted square-planar configuration about Ni(II) is retained for all complexes, and the structural parameters of the Ni(nmp) synthon remain relatively invariant throughout the series. The Ni-$N_{carboxamide}$ bond (avg: 1.871 Å ± 0.0095) and Ni-$N_{pyridine}$ bond (avg: 1.950 Å ± 0.0088) distances reflect the electronic asymmetry between the two N-donors, consistent with the strongly σ-donating character of the anionic N-carboxamide donor. Similar Ni(II)N_2S_2 complexes featuring mixed amide/amine,[8-9] bis-

carboxamide[10-11] and bis-amine[12-13] N-donors report analogous distances to the Ni-$N_{carboxamide}$ and Ni-$N_{pyridine}$ bonds reported in **2-5**. The Ni-S bond distances arising from the nmp^{2-} ligand (Ni-S_{nmp}, avg: 2.155 Å ± 0.0060) also compare well to those reported from analogous square-planar Ni(II) complexes featuring thiolato-S donors.[8-13] The $N_{carboxamide}$-Ni-$N_{pyridine}$ and $N_{carboxamide}$-Ni-S_{nmp} bond angles (avg: 83.16° ± 0.62 and 87.85° ± 0.39) arising from the two five-member chelate rings afforded by the nmp^{2-} ligand are slightly acute and also change little throughout the series. The metric parameters arising from the Ni(nmp) synthon match well with those observed for the Ni-(His1Cys2) unit of Ni-SOD_{red} (see Table 1).[3-4]

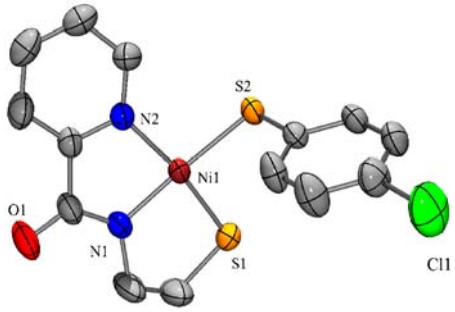

Figure 2. ORTEP diagram of the anion of (Et_4N)[Ni(nmp)(SC_6H_4-*p*-Cl)] (**2**) showing 50% thermal ellipsoids for all non-hydrogen atoms.

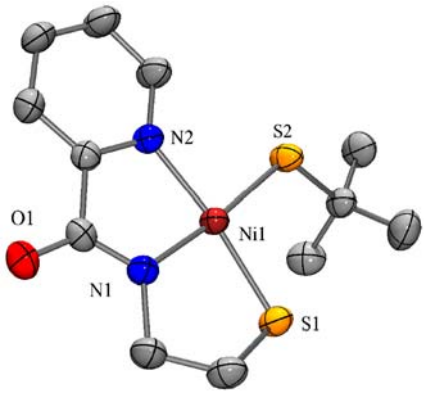

Figure 3. ORTEP diagram of the anion of (Et_4N)[Ni(nmp)(S^{t}Bu)] (**3**) showing 50% thermal ellipsoids for all non-hydrogen atoms.

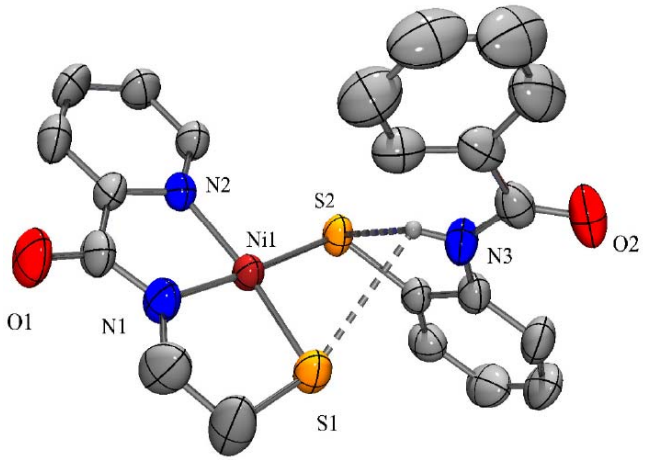

Figure 4. ORTEP diagram of the anion of (Et_4N)[Ni(nmp)(S-*o*-babt)] (**4**) showing 50% thermal ellipsoids for all non-hydrogen atoms. Hydrogen atoms omitted for clarity with the exception of that attached to N3 to exemplify the presence of intramolecular hydrogen-bonding.

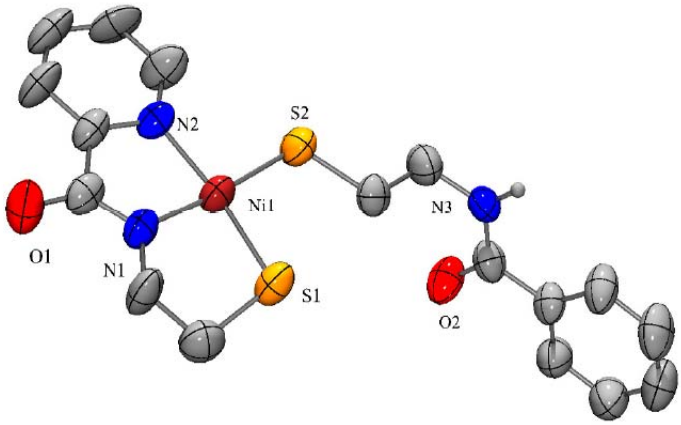

Figure 5. ORTEP diagram of the anion of (Et_4N)[Ni(nmp)(S-*o*-babt)] (**5**) showing 50% thermal ellipsoids for all non-hydrogen atoms. Hydrogen atoms omitted for clarity with the exception of that attached to N3.

Table 1. Selected Bond Distances [Å] and Bond Angles [deg] for (Et_4N)[Ni(nmp)(SC_6H_4-*p*-Cl)] (**2**), (Et_4N)[Ni(nmp)(S^{t}Bu)] (**3**), (Et_4N)[Ni(nmp)(S-*o*-babt)] (**4**), (Et_4N)[Ni(nmp)(S-meb)] (**5**) and Ni-SOD_{red}[3] (in Ni-SOD_{red}: N(1), N(2), S(1) and S(2) correspond to the terminal amine of His1, the amide of Cys2, the thiolate of Cys2 and the thiolate of Cys6, respectively; PDB code 1T6U).

	2	**3**	**4**	**5**	**Ni-SOD_{red}[3]**
Ni(1)-N(1)	1.8638(14)	1.882(2)	1.877(3)	1.863(7)	1.91(3)
Ni(1)-N(2)	1.9470(14)	1.9635(19)	1.947(3)	1.944(7)	1.87(6)
Ni(1)-S(1)	2.1492(5)	2.1629(7)	2.1518(12)	2.156(3)	2.19(2)
Ni(1)-S(2)	2.2139(4)	2.1938(7)	2.1939(14)	2.172(3)	2.16(2)
N(1)-Ni(1)-N(2)	83.25(6)	82.30(8)	83.77(13)	83.3(3)	83.6(1.6)
N(1)-Ni(1)-S(1)	88.31(5)	87.41(6)	87.67(10)	88.0(2)	88.2(7)
N(1)-Ni(1)-S(2)	176.73(5)	174.21(6)	175.92(10)	175.3(2)	
N(2)-Ni(1)-S(1)	170.64(4)	169.41(6)	171.43(9)	171.3(3)	
N(2)-Ni(1)-S(2)	98.18(4)	92.07(6)	92.16(10)	92.3(3)	93.3(1.3)
S(1)-Ni(1)-S(2)	90.45(2)	98.14(3)	96.40(5)	96.42(11)	95.0(6)
Ni(1)-S(1)-C(1)	99.07(8)	98.42(9)	99.22(16)	98.3(3)	
Ni(1)-S(2)-C(9)	103.32(6)	119.54(8)	115.21(12)	112.2(3)	

Despite the general invariance in metric parameters amongst the Ni(nmp) synthon, the Ni-$N_{carboxamide}$ bond length is somewhat sensitive to the trans effect of the exogenously added thiolate. Comparing complexes featuring aromatic and aliphatic mono-dentate S-thiolates separately, it is evident that Ni-$N_{carboxamide}$ bond lengths of **4**

and **5**, containing less strongly donating thiolate ligands are slightly contracted relative to those of **2** and **3**, respectively (Table 1).

The variance amongst the Ni-S bond arising from the exogenously added thiolate ligands (denoted as Ni-S_{exo}, avg: 2.193 Å ± 0.0171) is slightly more significant, with the Ni-S_{exo} bond of **2** measuring 0.042 Å longer than that of **3** (Table 1). The Ni-S_{exo} bond length appears to contract as the strength of the S-donor is diminished; the Ni-S_{exo} bonds of **4** and **5** are ~0.02 Å shorter than those observed for **2** and **3**, respectively. The Ni-S_{exo} bond lengths of **2-5** also compare favorably to the Ni-S(Cys6) bond of Ni-SOD.[3-4] The $N_{pyridine}$-Ni-S_{exo} (avg: 93.68° ± 3.003) and S_{nmp}-Ni-S_{exo} (avg: 95.41 ± 3.369) bond angles also display more noticeable changes across the series (Table 1). This may be attributable to an increase in relative degrees of freedom of S_{exo} when compared against donors arising form the Ni(nmp) synthon.

The crystal structure of **4** reveals intramolecular hydrogen-bonding interactions between the coordinated thiolate ligands and the secondary sphere carboxamide NH functional group. This hydrogen-bonding interaction appears to be bifurcated between both thiolate ligands, with N•••S_{exo} and N•••S_{nmp} distances of 2.954 Å and 3.308 Å, respectively; less than the sum of the van der Waal's radii of N and S (3.55 Å).[14-15] The corresponding NH•••S_{exo} and NH•••S_{nmp} distances can be modeled at 2.524 Å and 2.855 Å, respectively. Similar hydrogen-bonding interactions have been implicated in the Ni-SOD active site between Cys6 and the peptide NH functionalities of Gly7 and Val8, with N•••S distances of 3.45 Å and 3.35 Å, respectively.[3] Analogous Ni-SR[16] and Zn-SR[17-18] complexes, as well as Fe-S clusters[19] with similarly positioned carboxamide-NH groups also afford analogous

N•••S distances. No such NH•••S interaction is observed in the solid-state structure of **5**, and the carboxamide-NH appears to be directed to the carbonyl O-atom of a neighboring unit.

The Ni-S_{exo} contraction of **4** relative to that observed for **2** may be rationalized in terms of the observed NH•••S interaction. Modifications such as methylation or oxygenation to thiolates in square-planar Ni(II) complexes has been known to result in Ni-S bond contraction.[20] This is attributed to the alleviation of antibonding interactions between Ni($d_{xz/yz}$) orbitals with the lone pair residing on the S-thiolate (oft referred to as Ni(dπ)-S(pπ) repulsion).[20-22] In fact, a recent DFT study on truncated models of Ni-SOD_{red} suggests a similar 0.02 Å contraction upon protonation at Cys6.[22] Rationalization of the contraction of the Ni-S_{exo} bond of **5** is not as obvious. This contraction likely arises from electronic differences between **3** and **5**, with the S(pπ) orbitals of the S-meb$^-$ ligand slightly retracted when compared to those of S^{t}Bu$^-$.

Complexes **2-6** are soluble in polar aprotic solvents such as MeCN and DMF and, with the exception of **6**, are partially soluble in non-polar solvents such as CH_2Cl_2 and THF. Complexes **2-5** display poor aqueous solubility whereas **6** is highly soluble; however, all of the species are unstable in protic solvents, and eventually revert back to dimeric **1** and the RSH form of S_{exo} upon dissolution.

The ^{1}H NMR spectra of **2-6** in both donor (CD_3CN, d_6-DMSO, d_6-acetone) and non-donor ($CDCl_3$, d_8-THF) solvents is consistent with the diamagnetic behavior displayed by square-planar d^8 coordination complexes. Hydrogen-bonding interactions are present in solution for **4**, **5** and **6** as evidenced by the large downfield

shift of δ_{NH} in the coordinated S_{exo}^- vs. that of free HS_{exo} (Figure 6, Table 2). For example, δ_{NH} of S-*o*-babt disulfide, HS-meb and HS-NAc are found at 8.95 ppm in $CDCl_3$, 6.74 ppm in $CDCl_3$ and 7.43 ppm in d_6-acetone, respectively. The corresponding δ_{NH} of **4**, **5** in **6** in the same solvents are shifted ~1.5 ppm downfield and found at 10.57 ppm, 8.52 ppm and 8.73 ppm, respectively. This downfield shift is due to an increasingly deshielded environment arising from a weakened interaction of the NH proton with the electronegative carboxamido-N.

The FTIR spectra of **2-6** support the anionic and metal coordinated nature of the carboxamido-N ligand, as the ν_{CO} band has shifted from 1658 cm^{-1} in $nmpH_2$ to 1574-1623 cm^{-1} for **2-6**. The red-shift in the solid state (KBr pellet) ν_{NH} stretches of **4** and **6** (3271 and 3264 cm^{-1}, respectively) vs. those corresponding to S-*o*-babt disulfide or HS-NAc (3374 and 3307 cm^{-1}, respectively) supports the participation of the carboxamide-NH in hydrogen-bonding (Table 2). Similar red-shifts in ν_{NH} have been observed in prior characterized *o*-benzamide containing thiols upon coordination in anionic form to Fe-S clusters[19] or Pt(II) complexes.[15] Interestingly, the ν_{NH} remains invariant between **5** and HS-meb, and in conjunction with the above discussed crystal structure, suggests that **5** is devoid of NH•••S interactions in the solid state.

Similar to the ^1H NMR data, the solution IR measurements support hydrogen-bonding interactions for **4**, **5** and **6** (Figure 6, Table 2). The ν_{NH} stretches of S-*o*-babt disulfide in CH_2Cl_2, HS-meb in CH_2Cl_2, and HS-NAc in MeCN are found at 3379 cm^{-1}, 3452 cm^{-1} and 3371 cm^{-1}, respectively. This ν_{NH} stretch in the corresponding solvents is red-shifted to ~3274 cm^{-1}, 3261 cm^{-1}, and 3235 cm^{-1} for **4**, **5** and **6**, respectively (avg: -144 cm^{-1}). Participation of the carboxamide-NH in hydrogen-

bonding is also reflected in a slight red-shift of the carboxamide ν_{CO} in solution (Table 2). However, this effect is much more subtle, affording shifts of 12-18 cm^{-1}.

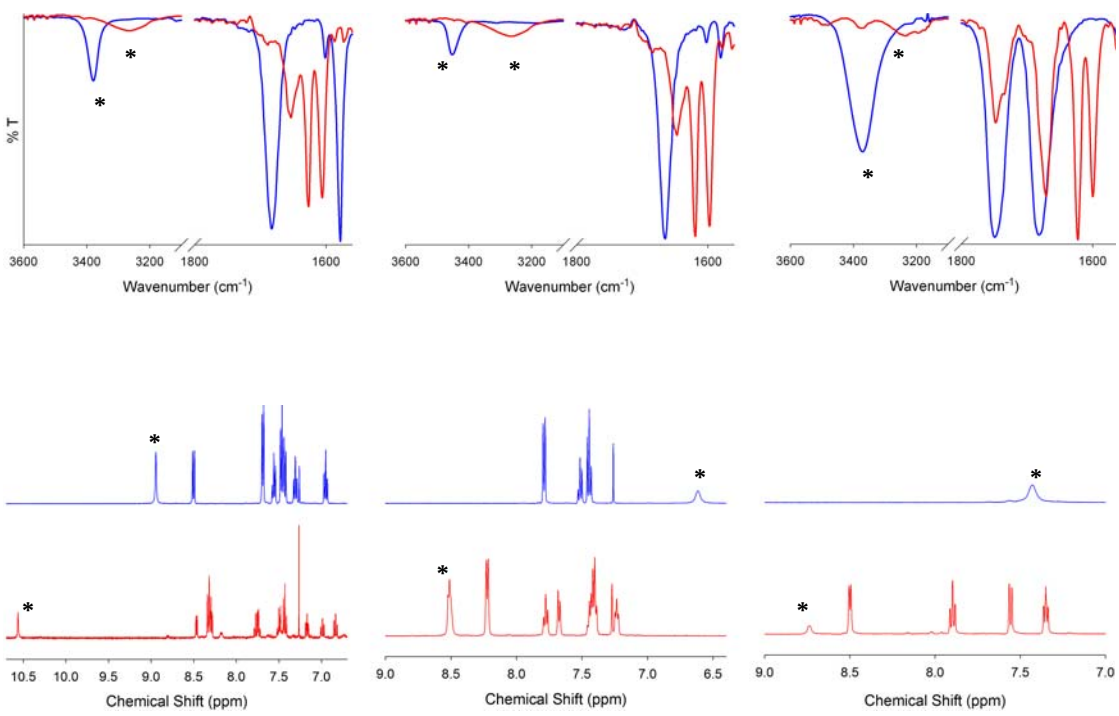

Figure 6. Comparison of shifts in the ν_{NH} and δ_{NH} (denoted by *) of the disulfide or thiol forms of S_{exo} ligands (blue) and upon complexation to the Ni(nmp) unit (red) by solution FTIR (top) and ^{1}H NMR (bottom). Left: **4** and disulfide of S-*o*-babt (IR in CH_2Cl_2, ^{1}H NMR in $CDCl_3$). Center: **5** and HS-meb (IR in CH_2Cl_2, ^{1}H NMR in $CDCl_3$). Right: **6** and HS-NAc (IR in MeCN, ^{1}H NMR in CD_3CN).

Table 2. Changes in the ^{1}H NMR chemical shift (ppm) of δ_{NH} and IR stretching frequencies (cm^{-1}) of ν_{CO} and ν_{NH} of the carboxamide group of S_{exo} ligands upon binding to the Ni(nmp) metallosynthon ([a]$CDCl_3$, [b]CH_2Cl_2 , [c]CD_3CN, [d]MeCN recorded at 298 K).

	***o*-babt-S_2**	**4**	**HS-meb**	**5**	**HS-NAc**	**6**
δ_{NH}	8.95[a]	10.57[a]	6.74[a]	8.52[a]	7.43[c]	8.73[c]
$\Delta\delta_{NH}$		1.63		1.78		1.30
$\nu_{NH\ (liquid)}$	3379[b]	3274[b]	3452[b]	3261[b]	3371[d]	3235[d]
$\Delta\nu_{NH\ (liquid)}$		-105		-191		-136
$\nu_{CO\ (liquid)}$	1682[b]	1670[b]	1665[b]	1647[b]	1682[d]	1671[d]
$\Delta\nu_{CO\ (liquid)}$		-12		-18		-11
$\nu_{NH\ (KBr)}$	3374, 3326	3271	3299	3298	3307	3264
$\Delta\nu_{NH\ (KBr)}$		-103, -55		-1		-43
$\nu_{CO\ (KBr)}$	1680	1652	1634	1643	1644	1662
$\Delta\nu_{CO\ (KBr)}$		-28		9		18

Complexes **2-6** afford richly colored red-orange solutions. The strong visible absorption bands are believed to be charge-transfer in nature and arise from the S-ligands (Figure 7), as has been observed in prior square-planar Ni(II)N_2S_2 complexes.[8-9,11-12,23-24] The λ_{max} values in MeCN appear to be somewhat sensitive to the nature of the S_{exo} donor, with transitions moving towards lower energy with increasing S_{exo} donor strength (Table 3). For example, the λ_{max} of **6** occurs at 442 nm whereas that of **3** is found at 464 nm.

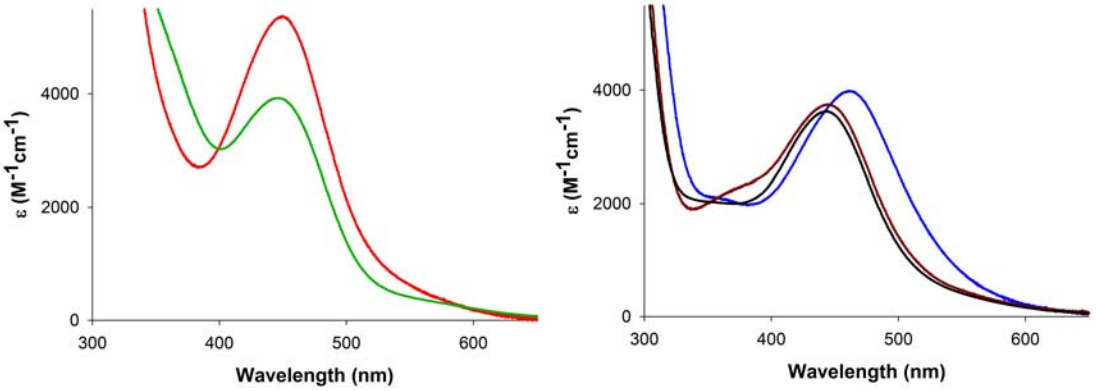

Figure 7. UV-vis spectra of **2** (red), **3** (blue), **4** (green), **5** (maroon) and **6** (black) in MeCN at 298 K. Spectral data of complexes featuring aromatic- (**2** and **4**; left) and aliphatic- (**3**, **5** and **6**; right) RS^- ligands are separated for comparative purposes.

Table 3. Electronic absorption spectral properties and oxidation potentials of complexes **2-6** reported in MeCN at 298 K. Potentials reported vs. Ag/AgCl.

	2	**3**	**4**	**5**	**6**
λ_{max} (nm)	450	464	450	449	442
ε (M^{-1} cm^{-1})	5,450	4,540	3,500	3,900	3,710
E^{ox} (mV)	236	75	276	214	286

Cyclic voltammetry revealed irreversible oxidation potentials (vs. Ag/AgCl) in MeCN for **2-6** (Figure 8). The irreversible nature of the oxidation event is likely due to either ligand-based oxidation or a highly unstable Ni(III) species. The Ni(III) state in thiolate-bound complexes is notoriously unstable due to spontaneous autoredox affording Ni(II) and disulfide. In fact, bulk oxidation studies on **2-6** using ferrocenium hexafluorophosphate as a stoichiometric, one-electron oxidant

quantitatively afford 0.5 mol-equivs. of **1** and the corresponding disulfide of S_{exo}. To our knowledge, only two Ni(III) complexes featuring thiolate ligands have been isolated, and both have employed multi-dentate and sterically robust ligand frames.[25-26]

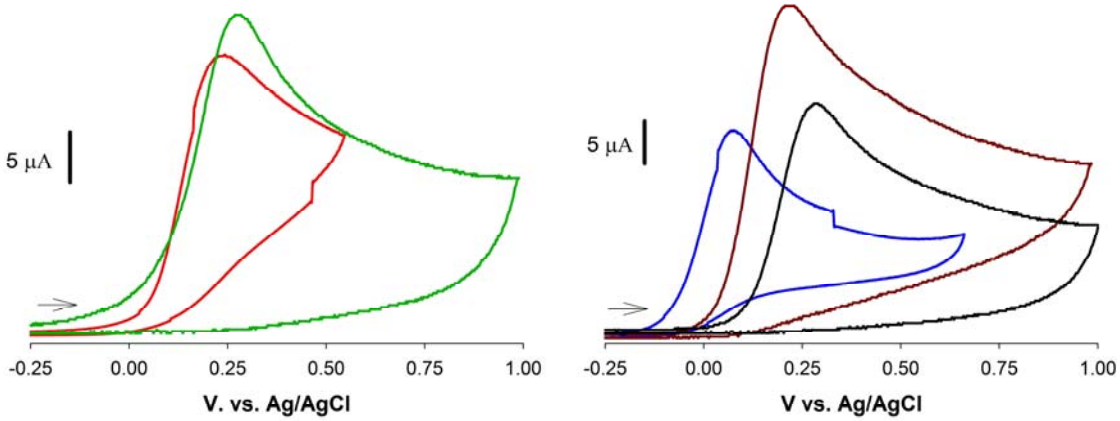

Figure 8. Cyclic voltammograms of 5 mM solutions of **2** (red), **3** (blue), **4** (green), **5** (maroon) and **6** (black) (vs. Ag/AgCl in MeCN, 0.1M $^{n}Bu_4NPF_6$ supporting electrolyte, glassy carbon working electrode, scan rate: 100 mV/s, RT). CV data of complexes featuring aromatic- (**2** and **4**; left) and aliphatic- (**3**, **5** and **6**; right) RS^- ligands are separated for comparative purposes (arrow indicates the direction of the scan).

The oxidation potentials of **2**-**6** all fall within the window defined by the two SOD half reactions (Table 3), and it appears as if these complexes are electrochemically poised towards SOD chemistry, but lack the requisite Ni(III) stabilization to be catalytically competent.[27-28] Separately analyzing complexes with aryl- and alkyl-S_{exo}, the oxidation potentials appear to reflect the donor strength of the ligand. For example, aryl-S_{exo} containing complex **4**, featuring an intramolecular

NH•••S bond oxidizes at 276 mV, 40 mV greater than that observed for **2** (236 mV). A similar cathodic shift of 140 mV has been observed in $[Fe_2S_2(SR)_4]^{2-}$ clusters upon switching RS^- to *o*-acetylaminobenzenethiolate from benzene thiolate, which corresponds to a roughly 35 mV shift per H-bond. However, it should be noted that Hammett constants indicate the chloro substituent is far more electron withdrawing (σ_p = 0.227) than the benzamide functional group (σ_p = 0.078),[29] and this difference in electron withdrawing capability may somewhat de-emphasize the effect imparted on the oxidation potentials upon introduction of NH•••S bonding in our models. Examination of the Hammett constants also indicates that the observed shift in oxidation potentials is indeed due to secondary sphere interactions and not strictly contingent upon resonance/inductive effects, in which case we would expect the trend to be reversed.

The dependence of oxidation potentials on S_{exo} is more noticeable for **3**, **5** and **6**, as the redox potentials occur at 75 mV, 214 mV and 286 mV, respectively. Thus, it appears that the hydrogen-bond induced dipole is of greater magnitude in the systems featuring alkyl-S (more cysteine like) donors. It is likely that the directed hydrogen-bonding interactions to Cys6 in Ni-SOD serve a similar role in tuning the redox potential towards the midpoint of the SOD half reactions.

2.5 Reactivity with O_2 and Reactive Oxygen Species

Studies regarding how modifications at the component modeling Cys6 manifest in the reactivity of **2-6** with $O_2^{\bullet-}$, O_2 and H_2O_2 were performed. These experiments were undertaken in order to glean insights into how oxidative modifications at the active site cysteinates are avoided under the harshly oxidizing conditions to which Ni-SOD is exposed. The propensity of Ni(II)-bound thiolates to form disulfides and/or S-oxygenates in the presence of O_2 or reactive oxygen species (ROS) is well documented,[20,30-34] and as described above, directed hydrogen-bonding interactions to the coordinated cysteinates of Ni-SOD has been proposed as a mode of S-protection.[21] These studies were performed in MeCN because of the common solubility and well behaved nature of **2-6** in this solvent.

Complexes **2-6** treated with 12 mol-equivs. KO_2 (solubilized in THF with 18-crown-6) displayed only negligible changes as monitored by UV-vis spectroscopy. Although the oxidation potentials of **2-6** are poised within the window requisite for $O_2^{\bullet-}$ reduction, the fact that no such redox reaction was observed is not surprising as $O_2^{\bullet-}$ reduction is a proton-coupled event.[27-28] The series **2-6** were also treated with 12 mol-equivs. of N_3^- (as the $^nBu_4N^+$ salt), an oft used $O_2^{\bullet-}$ surrogate.[35-37] This treatment also imparted no changes to the UV-vis spectrum (with the exception of **4**), consistent with the generally inert behavior of square-planar d^8 complexes with respect to ligand binding. Treatment of **4** with N_3^- yielded yellow colored solutions with a markedly different UV-vis profile. ESI-MS analysis revealed the formation of $[Ni(nmp)(N_3)]^-$; 45 mol-equivs. KO_2 were required to affect similar changes. This somewhat divergent behavior of **4** is likely attributed to a weakening of the Ni-S_{exo} bond

through charge neutralization effects imparted via the NH•••S interaction. Experiments were also performed in the presence of 10 mol-equivs. imidazole to test whether an exogenously added N-donor could support an inner sphere Ni(III)-peroxo adduct, as Ni(III) stabilization has been postulated for the imidazole side chain of His1.[22,38-39] However, this addition also failed to promote any reactivity with $O_2^{\bullet-}$.

O_2(g) was purged through 0.13 mM solutions of **2-6** for 1 min (affording O_2 saturated, pseudo-first order conditions) and the UV-vis spectra monitored every 15 min for 4 h. The intense ~450 nm charge-transfer band was monitored as an indicator of complex consumption/S-modification. Disappearance of this band occurred rather slowly and was accompanied by the concurrent appearance of a new optical transition in the 370-400 nm range (Figure 9 depicts **3** as a representative example). These changes to the absorption profiles of **2-6** were isosbestic for ~2 h before all transitions began to increase in intensity, consistent with degradation of the newly formed species. The rate at which the ~450 nm charge-transfer band disappeared remained relatively invariant for **3-6**, transpiring at a rate of ~ 2×10^{-4} s^{-1} (Table 4). Inexplicably, the rate of disappearance of **2** occurred more slowly by a full order of magnitude.

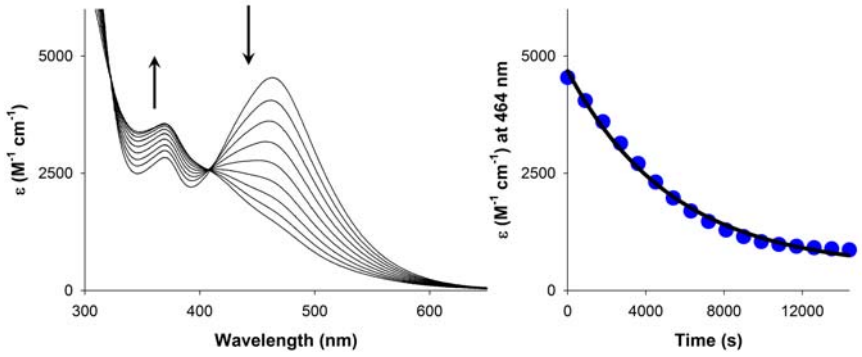

Figure 9. (Left): Dissappearance of λ_{max} = 464 nm of **3** in MeCN (0.13 mM) with concurrent rise and appearance of peak at 370 nm after 2 h exposure to O_2(g) at 298

K. (Right): Change in absorbance at 464 nm vs. time (s); blue dots and black line respresent experimental data points and the exponential best fit, respectively.

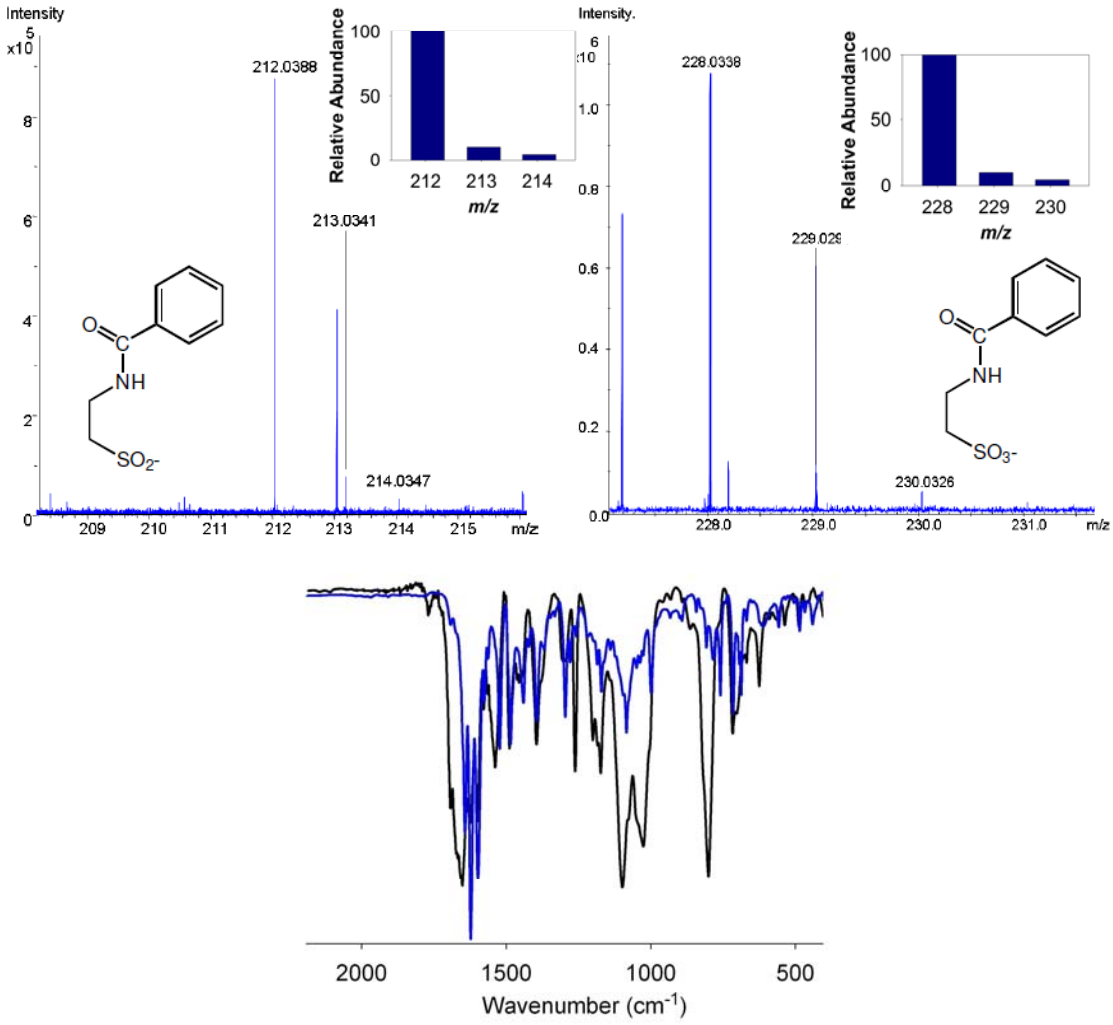

Figure 10. (Top): High-resolution ESI-MS (negative mode) of the MeCN reaction mixture of **5** and O_2(g) after 4 h exposure displaying peaks consistent with oxygenation of S_{exo} to the corresponding sulfinato (*m/z* = 212; left) and sulfonato (*m/z* = 228; right) species (Insets depict the theoretical isotopic distribution pattern in dark blue). (Bottom): FTIR spectral overlay of **5** prepared before (blue) and after (black) 4 h exposure to O_2(g) at 298 K (KBr matrix).

Table 4. Pseudo-first order kinetic rate constants of complexes **2-6** upon exposure to excess O_2(g) (~60 mol-equiv) over 4 h and H_2O_2 (20 mol-equiv) over 5 min in MeCN at 298 K.

Complex	**O_2** (k_{obs} in s^{-1})	**H_2O_2** (k_{obs} in s^{-1})
2	$4.22 \pm 0.69 \times 10^{-5}$	$1.27 \pm 0.07 \times 10^{-2}$
3	$2.61 \pm 0.65 \times 10^{-4}$	$5.77 \pm 0.66 \times 10^{-2}$
4	$1.63 \pm 0.03 \times 10^{-4}$	$1.32 \pm 0.39 \times 10^{-2}$
5	$2.13 \pm 0.04 \times 10^{-4}$	$1.04 \pm 0.04 \times 10^{-2}$
6	$1.77 \pm 0.09 \times 10^{-4}$	$1.59 \pm 0.09 \times 10^{-2}$

FTIR analysis of the products formed upon O_2 treatment of **3**, **5** and **6** revealed the presence of strong ν_{SO} stretches at ~1100 cm^{-1} and ~1000 cm^{-1}, consistent with the formation of S-oxygenates (Figure 10). Furthermore, analysis by ESI-MS revealed the presence of RSO_2^- and RSO_3^- species corresponding to oxygenation of S_{exo} (Figure 10). Fully intact **3**, **5** and **6** were also found in varying degrees of oxygenation (**M**$^-$ + *n*O, *n* = 1-4). Interestingly, 2 h subsequent to O_2(g) treatment of **5**, a significant degree of precipitate began to form. Isolation of these solids and characterization by FTIR revealed the formation of pure **1**, indicative of selective oxygenation at the S_{exo} position. The S,S'-bridged nature of **1** would be expected to preclude any further S-modification. The formation of S-oxygenates was less prominent for **2** and **4**; this suggests that disulfide formation may be the prevalent form of oxidative modification by O_2 in the models features aromatic S_{exo} ligands.

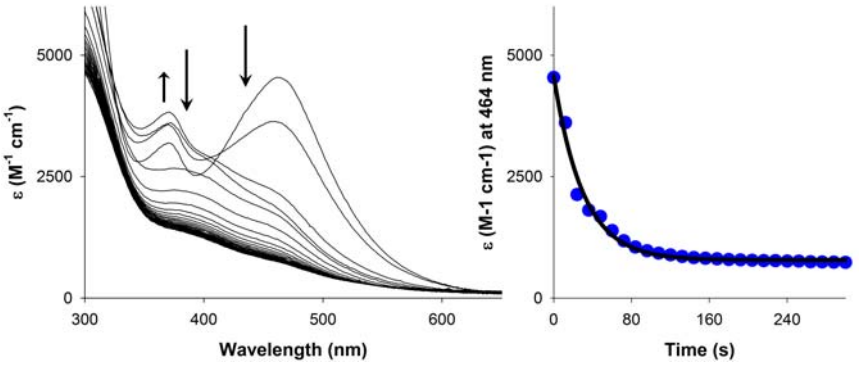

Figure 11. (Left): Disappearance of λ_{max} = 464 nm of (Et_4N)[Ni(nmp)(S^{t}Bu)] (**3**) (0.13 mM) in MeCN after addition of 20 mol-equiv of H_2O_2•urea at 298 K (arrows depict the change in intensity with time; peak at 370 nm increases initially over the first 45 s (small arrow) and decreases during the remaining time (large arrow)). Each spectrum was obtained at 15 s intervals for a total time of 5 min. (Right): Change in absorption at 464 nm versus time (s); blue dots and black line represent experimental data points and the exponential best-fit, respectively.

Treatment of **2**-**6** with 20 mol-equivs. of H_2O_2 (pseudo-first order conditions) resulted in a more rapid and indiscriminate reactivity profile (Figure 11), as monitored by UV-vis. FTIR and ESI-MS analysis revealed evidence of S-oxygenation for **2**-**6** upon H_2O_2 treatment The rapid bleaching of the ~450 nm charge transfer band occurred on the order of $\sim 1\times10^{-2}$ s^{-1} for **2** and **4**-**6**, and at a rate of 5.77×10^{-2} s^{-1} for **3** (Table 4). It appears that the introduction of NH•••S bonding does not appear to provide any kinetic protection against S-modification for models possessing aromatic S_{exo}, but provides almost six-fold protection in the case of those containing aliphatic S_{exo} ligands. Similar kinetic protection has been observed upon

the introduction of NH•••S interactions to Zn(II) bound thiolates with respect to methylation under similar conditions.[18,40]

Drawing conclusions from the kinetics of S-oxygenation provides a more complicated scenario than that with regards to methylation, and a detailed mechanistic depiction cannot be extrapolated from the present study. However, it does appear that the introduction of hydrogen-bonding in models containing aliphatic, cysteine like thiolate ligands is capable of affording substantial kinetic protection against oxidative modifications by H_2O_2, even under forcing conditions.

2.6 Electronic Structure Calculations

DFT computations were performed on **2-6** in an effort to obtain a theoretical rationale regarding the experimentally observed spectroscopic, electrochemical and reactivity trends. Prior theoretical examinations of Ni-SOD_{red} models have focused on the unique nitrogenous disposition of the active site and have concluded that the mixed amide/amine motif observed affords an optimal combination of N-donors for promoting Ni- vs. S-based redox while maintaining potentials in the SOD realm.[22,41] A study modeling a peptide NH adjacent to DFT-generated NiN_2S_2 complexes relevant to Ni-SOD_{red} suggested that hydrogen-bonding interactions are capable of reducing the electron density at S relative to Ni.[21] However, a separate study regarding the hydrogen-bonding interactions between coordinated thiolates of square-planar NiN_2S_2 complexes and solvating water molecules concluded that hydrogen-bonding with Ni(II)-bound thiolate ligands was "passive" with regards to electronic structure contributions.[42] Employing

DFT calculations on **2-6** afforded a unique opportunity to theoretically validate observations regarding the effects of NH•••S bonding grounded in experimental rigor.

The input coordinates for **2-5** were obtained from the crystallographic data whereas those for **6** were from an estimate built from the coordinates of **2**. The geometries were optimized utilizing the pure exchange OLYP functional (def2-TZVPP basis set) and compare well with the experimentally obtained metric parameters (Figure 12 shows the DFT-optimized structures of **3** and **5** as representative examples; see Table 5 for relevant DFT derived metric parameters, NBO (natural bond orbital) atomic charges and electrostatic potentials). The Ni-S bond lengths are overestimated by ~0.05 Å, but remain well within the accuracy of the OLYP functional. The DFT-generated models accurately reproduce the electronic asymmetry of the N-donors, as the anionic Ni-$N_{carboxamide}$ bond is contracted relative to the Ni-$N_{pyridine}$ bond. Similarly, the Ni-S_{exo} bond is elongated relative to that of Ni-S_{nmp} in a manner reflective of that observed in the crystal structures. One significant difference between the DFT-generated structure and that observed crystallographically is observed for **5**, as the DFT model shows the carboxamide-NH involved in a directed hydrogen-bonding interaction with S_{exo}. This is not surprising, considering that intramolecular hydrogen-bonding in **5** is observed via spectroscopic measurements in solution. In fact, NH•••S bonding directed at S_{exo} was observed for **4-6**.

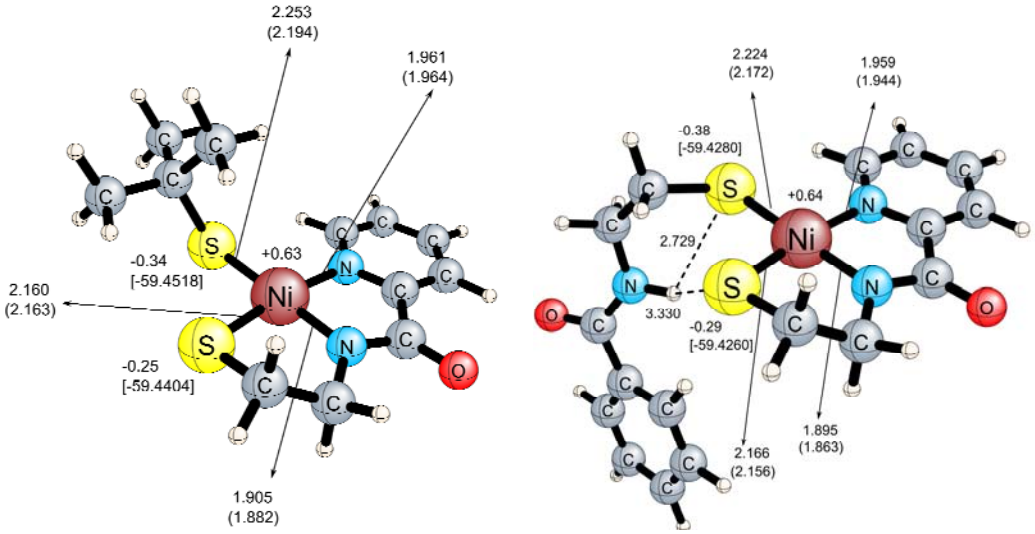

Figure 12. Geometry optimized structures of complexes **3** (left) and **5** (right) featuring relevant bond distances (crystallographically determined distances shown in parentheses), NBO atomic charges and electrostatic potentials at the Ni and S nuclei [in a.u. shown in brackets].

Table 5. Relevant bond lengths (Å), bond angles (deg), atomic charges and electrostatic potentials (ESPs) (a.u.) of DFT geometry optimized structures of complexes **2**-**6**.

	2	**3**	**4**	**5**	**6**
Ni-N_{am}	1.891	1.905	1.891	1.895	1.897
Ni-N_{py}	1.955	1.961	1.955	1.959	1.960
Ni-S_{nmp}	2.156	2.160	2.156	2.166	2.167
Ni-S_{exo}	2.239	2.253	2.253	2.224	2.228
N_{pep}•••S_{exo}			2.935	3.209	3.106
N_{pep}-H			1.022	1.012	1.018
N-H_{pep}•••S_{exo}			2.271	2.729	2.533
N_{am}-Ni-N_{py}	82.7	82.3	82.8	82.7	82.6
N_{am}-Ni-S_{nmp}	88.7	88.4	88.5	87.9	87.7
N_{am}-Ni-S_{exo}	173.9	178.3	175.2	175.2	176.4
N_{py}-Ni-S_{nmp}	170.7	170.6	171.2	170.3	170.2
N_{py}-Ni-S_{exo}	98.6	97.0	97.9	93.5	94.3
S_{nmp}-Ni-S_{exo}	90.3	92.3	90.9	96.1	95.4
Ni-S_{nmp}-Cα	98.1	97.8	98.0	98.2	97.8
Ni-S_{exo}-Cα	111.9	113.5	112.1	117.4	113.1
N-H_{pep}•••S_{exo}			121.3	109.4	115.2
Atomic Charge N_{am}	-0.56	-0.57	-0.56	-0.56	-0.56
Atomic Charge N_{py}	-0.43	-0.43	-0.43	-0.42	-0.42
Atomic Charge S_{nmp}	-0.23	-0.25	-0.24	-0.29	-0.28
Atomic Charge S_{exo}	-0.18	-0.34	-0.26	-0.38	-0.35
Atomic Charge Ni	0.62	0.63	0.63	0.64	0.64
ESP S_{nmp} (a.u.)	-59.4286	-59.4404	-59.4237	-59.4260	-59.4277
ESP S_{exo} (a.u.)	-59.4201	-59.4518	-59.4114	-59.4280	-59.4245

The influence of NH•••S hydrogen-bonding on the electronic and structural parameters of DFT generated **2-6** can be most clearly understood if the complexes with aromatic- and aliphatic-S_{exo} ligands are separately examined. The Ni-S_{exo} bond length of **4** is 0.014 Å elongated relative to that of **2**, while the Ni-ligand bond lengths arising from the Ni(nmp) synthon were identical between the two models. Furthermore, the bond angles comprising the square-planar coordination unit varied by no more than 0.5° throughout the Ni(nmp) unit. Even the Ni-S_{exo}-C_{α} bond angle, which arises from an unconstrained monodentate ligand, varied only by 0.2°; and it appears that hydrogen-bonding to a coordinated, aromatic-S affords minimal discrepancies in the structural properties of models relevant to Ni-SOD_{red}.

Comparison of the DFT structures of **5** and **6** against that of **3** revealed that the effects imparted by NH•••S hydrogen-bonding are more notable for the aliphatic-S donor ligands. For example, the Ni-S_{exo} bonds of **5** and **6** are contracted 0.03 Å relative to that of **3**. The Ni-$N_{carboxamide}$ bonds of the models with intramolecular NH•••S interactions are also contracted ~0.10 Å relative to **3**, presumably due to a hydrogen-bonding induced weakening of the trans effect of S_{exo}. A Ni-S contraction of a similar magnitude is observed upon Cys6 protonation in DFT-generated truncated models of Ni-SOD, and this contraction has been attributed to alleviation of the antibonding interaction between the filled Ni($d_{xz/yz}$) orbital and lone pair residing on the Cys6-S.[22]

The highest occupied molecular orbitals (HOMO) of **2-6** are largely comprised of Ni and S contributions and are highly antibonding in nature. The S contributions to the HOMO of **2** and **4** are largely due to S_{nmp} whereas S_{exo} is a

relatively minor contributor to the three filled orbitals of highest energy, contributing less than 1% to the HOMO of either. However, S_{exo} is a large contributor to the HOMO of **3**, **5** and **6**; and the presence of S_{exo}-directed hydrogen-bonding is demonstrated in the composition of Ni vs. S in the theoretically generated MOs (Figure 13). Within this series the contributions of S_{exo} (and total S) of **3**, **5** and **6** decrease from 29.2% (39.0 % total S), 21.0 % (and 26.3% total S) and 17.9% (22% total S), respectively (see Tables 6, 7 and 8 for frontier orbital compositions of **3**, **5** and **6**, respectively; Figure 13 for isosurface plots of frontier orbitals). This decrease in S-based contributions is accompanied by an increase in contributions arising from Ni-based orbitals; the Ni contributions of **3**, **5** and **6** increase to 48.6%, 58.4% and 61.2%, respectively. It should be noted that the relative HOMO energies of **3**, **5** and **6** correspond to -0.34 eV, -0.52 eV and -0.57 eV, respectively. Consistent with Koopman's theorem, the relative energies trend well with the observed oxidation potentials.[43] Thus, it appears that S-directed hydrogen-bonding is capable of significantly stabilizing Ni(II)-bound alkyl thiolate ligands relative to other atomic orbitals within complexes **5** and **6**, effectively promoting Ni-based redox

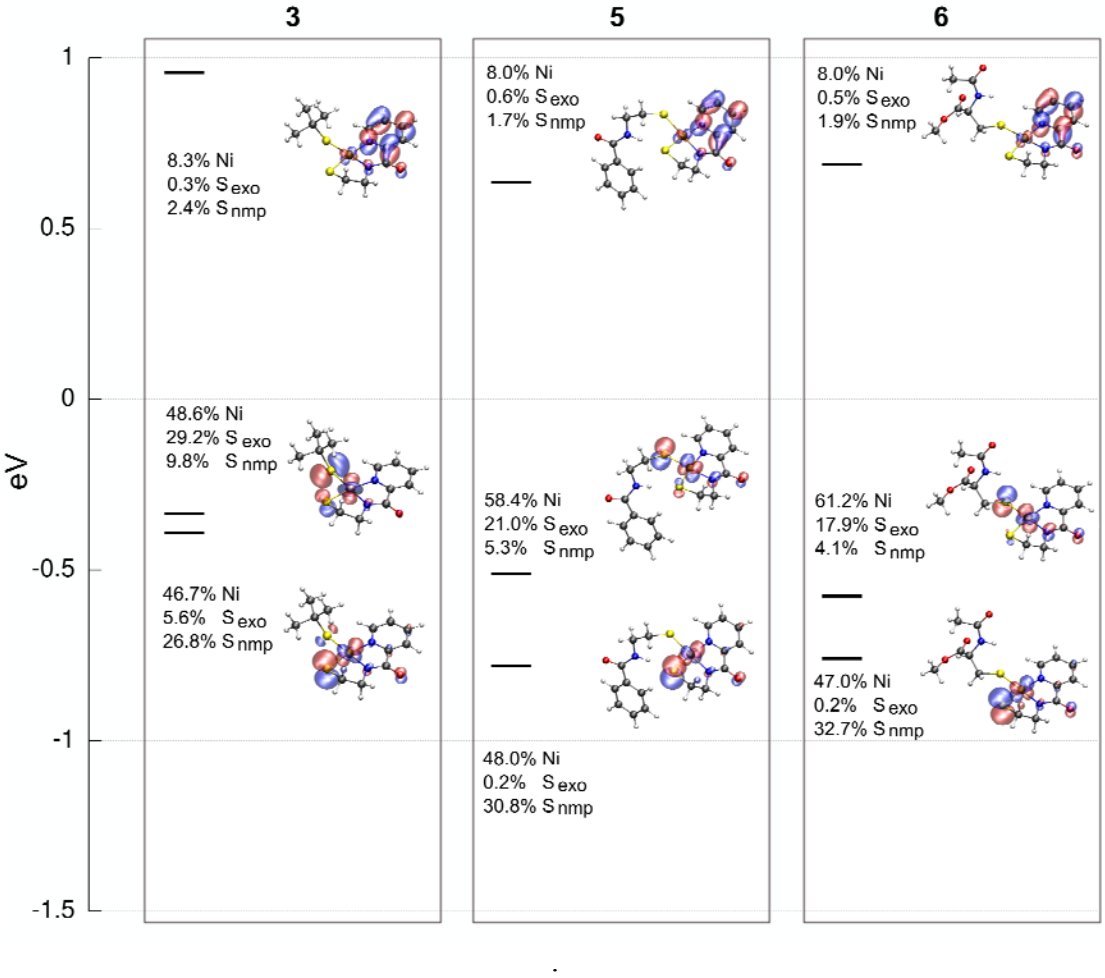

Figure 13. DFT-generated isosurface plots of the frontier molecular orbitals of the geometry optimized structures of the alkyl S_{exo} complexes **3, 5,** and **6**. In each column, the orbitals descend in the order LUMO, HOMO, and HOMO-1.

Table 6. Löwdin orbital compositions derived from the DFT calculations for selected molecular orbitals of complex **3**. ([a]MO contribution from the Ni AOs. [b]MO contribution from the N AOs of $N_{pyridine}$ and the coordinated $N_{carboxamide}$. [c]MO contribution from the S AOs. The composition is given in order of AO contribution to the MO. [d]The major contributions to the LUMO involves C(pπ) AOs from the pyridine ring of nmp (56.2%). Bonding interactions are represented with a + and antibonding interactions are denoted with a –. The coordinate system used for figuring out the type of AO on Ni, N and S are as follows: z-axis is normal to the square-planar ligand field; x-axis is parallel to S_{nmp}–Ni–$N_{pyridine}$; y-axis is parallel to S_{exo}–Ni–$N_{carboxamide}$).

MO label	MO	E (eV)	%Ni[a]	%N[b]	%S[c]	Orbital Composition
LUMO[d]	86	0.95	8.3	18.8	2.7	$Ni(d_{xz}) - N_{py}(p_z)$, $N_{am}(p_z)$
HOMO	85	-0.34	48.6	1.9	39.0	$Ni(d_{yz})/Ni(d_{xz}) - S_{exo}(p_x)$, $S_{nmp}(p_z)$
HOMO-1	84	-0.40	46.7	2.7	32.4	$Ni(d_{xz})/Ni(d_{yz}) - S_{nmp}(p_z)$
HOMO-2	83	-0.59	88.7	2.7	3.6	$Ni(d_{z2})$
HOMO-3	82	-0.68	54.0	5.4	26.7	$Ni(d_{yz})/Ni(d_{xy}) - N_{am}(p_z)$, $S_{exo}(p_x)$
HOMO-4	81	-1.58	32.8	4.9	38.2	$Ni(d_{xz})$, $N_{am}(p_y)/N_{am}(p_z)$, $S_{nmp}(p_z)/S_{nmp}(p_y)$, $S_{exo}(p_y)/S_{exo}(p_z)/S_{exo}(p_x)$
HOMO-5	80	-1.73	32.7	3.7	30.6	$Ni(d_{xy}) + N_{am}(p_y)/N_{am}(p_x)$, $S_{exo}(p_x)/S_{exo}(p_z)$
HOMO-6	79	-1.90	30.4	9.2	13.9	$Ni(d_{xy})/Ni(d_{yz}) + N_{am}(p_z)/N_{am}(p_x)$, $S_{nmp}(p_z)/S_{nmp}(p_y)$

Table 7. Löwdin orbital compositions derived from the DFT calculations for selected molecular orbitals of complex **5**. ([a]MO contribution from the Ni AOs. [b]MO contribution from the N AOs of $N_{pyridine}$ and the coordinated $N_{carboxamide}$. [c]MO contribution from the S AOs. The composition is given in order of AO contribution to the MO. [d]The major contributions to the LUMO involves C(pπ) AOs from the pyridine ring of nmp (56.9%). Bonding interactions are represented with a + and antibonding interactions are denoted with a –. The coordinate system used for figuring out the type of AO on Ni, N and S are as follows: z-axis is normal to the square-planar ligand field; x-axis is parallel to S_{nmp}–Ni–$N_{pyridine}$; y-axis is parallel to S_{exo}–Ni–$Nc_{arboxamide}$).

MO label	**MO**	**E (eV)**	**%Ni[a]**	**%N[b]**	**%S[c]**	**Orbital Composition**
LUMO[d]	109	0.64	8.0	19.4	2.3	$Ni(d_{xz}) - N_{py}(p_z)$, $N_{am}(p_z)$
HOMO	108	-0.51	58.4	3.4	26.3	$Ni(d_{yz}) - N_{am}(p_z) - S_{exo}(p_z)$
HOMO-1	107	-0.78	48.0	2.6	31.0	$Ni(d_{xz}) - S_{nmp}(p_z)$
HOMO-2	106	-0.93	93.5	1.7	3.1	$Ni(d_{z2})$
HOMO-3	105	-1.66	48.8	6.5	25.3	$Ni(d_{xy})/Ni(d_{xz})$, $N_{am}(p_z)$, $S_{exo}(p_z)/S_{exo}(p_x)$
HOMO-4	104	-1.85	29.9	8.4	35.8	$Ni(d_{xy})/Ni(d_{xz})$, $N_{am}(p_z)/N_{am}(p_y)$, $S_{exo}(p_z)$
HOMO-5	103	-2.10	20.4	5.4	19.5	$Ni(d_{xy})/Ni(d_{xz})$, $N_{am}(p_x)/N_{am}(p_y)/N_{am}(p_z)$, $S_{nmp}(p_z)/S_{nmp}(p_y)$
HOMO-6	102	-2.30	34.3	1.1	42.4	$Ni(d_{xz})/Ni(d_{yz})/Ni(d_{x2-y2})$ + $S_{nmp}(p_z)$, $S_{exo}(p_z)$

Table 8. Löwdin orbital compositions derived from the DFT calculations for selected molecular orbitals of complex **6**. ([a]MO contribution from the Ni AOs. [b]MO contribution from the N AOs of $N_{pyridine}$ and the coordinated $N_{carboxamide}$. [c]MO contribution from the S AOs. The composition is given in order of AO contribution to the MO. [d]The major contributions to the LUMO involves C(pπ) AOs from the pyridine ring of nmp (56.7%). Bonding interactions are represented with a + and antibonding interactions are denoted with a –. The coordinate system used for figuring out the type of AO on Ni, N and S are as follows: z-axis is normal to the square-planar ligand field; x-axis is parallel to S_{nmp}–Ni–$N_{pyridine}$; y-axis is parallel to S_{exo}–Ni–$N_{carboxamide}$).

MO label	MO	E (eV)	%Ni[a]	%N[b]	%S[c]	Orbital Composition
LUMO[d]	108	0.69	8.0	19.6	2.4	$Ni(d_{xz}) - N_{py}(p_z)$, $N_{am}(p_z)$
HOMO	107	-0.57	61.2	4.0	2.0	$Ni(d_{yz}) - N_{am}(p_z) - S_{exo}(p_z)$
HOMO-1	106	-0.75	47.0	2.5	32.9	$Ni(d_{xz})$, $N_{am}(p_z)$, $S_{nmp}(p_z)$
HOMO-2	105	-0.91	93.2	1.6	3.5	$Ni(d_{z2})$
HOMO-3	104	-1.62	50.3	6.1	25.1	$Ni(d_{xy})$, $N_{am}(p_z)$, $S_{exo}(p_z)/S_{exo}(p_x)$
HOMO-4	103	-1.93	23.1	8.6	31.1	$Ni(d_{xy})/Ni(d_{xz})$, $N_{am}(p_z)/N_{am}(p_y)$, $S_{exo}(p_z)/S_{exo}(p_y)$
HOMO-5	102	-2.09	24.7	5.6	33.5	$Ni(d_{xy})/Ni(d_{xz})$, $N_{am}(p_z)/N_{am}(p_x)$, $S_{nmp}(p_z)/S_{nmp}(p_y)$, $S_{exo}(p_z)$
HOMO-6	101	-2.22	34.3	2.6	29.4	$Ni(d_{xz})/Ni(d_{xy})/Ni(_{yz})$, $N_{am}(p_z)/N_{am}(py)/N_{am}(p_x)$, $S_{nmp}(p_z)$

We aimed to utilize NBO atomic charges as another index by which to rationalize the effects imparted by hydrogen-bonding on trends observed across the series **2**-**6**. Past studies have shown the overall charge of metal thiolate complexes to correlate well with trends in O_2 reactivity.[44-45] The atomic charges at S_{exo} for **2** and **4** were -0.18 and -0.26, respectively, and appear to reflect the electron withdrawing nature of the benzenethiolate substituents rather than the expected charge neutralization imparted by hydrogen-bonding. Similarly, no clear trend emerges from the S_{exo} of **3**, **5** and **6**, which possess atomic charges of -0.36, -0.39 and -0.37, respectively. The inconclusiveness of this analysis is not surprising in hindsight. Regardless of distribution, charge will be assigned to the closest nuclei. Therefore, polarization of electron density is not accurately reflected in atomic charge in the model systems at hand.

Electrostatic potential, however, can provide a more accurate view of charge distribution, although this method can be computationally quite expensive. A simpler yet quantitative approach involves computing the electrostatic potentials analytically at the point of the nuclei, and this has been benchmarked as an accurate index of reactivity.[46-47] Indeed, the electrostatic potentials (in a.u.) calculated at S_{exo} of **2** and **4** are -59.4201 a.u. and -59.4114 a.u., respectively. This stabilization of -0.0087 a.u. at S_{exo} of **4** is now reflective of that experimentally observed and attributed to S-directed hydrogen-bonding. Similarly, the calculated electrostatic potentials at S_{exo} of **3**, **5** and **6** are -59.4518 a.u., -59.4280 a.u. and -59.4245 a.u., respectively. This corresponds to ~0.03 a.u. (~0.65 eV or 15 kcal/mol) stabilization induced by NH•••S bonding.

Conversely, it could be said that addition of an O atom to S_{exo} will be 15 kcal/mol more stabilizing for **3** than for **5** and **6**.

The above discussed trends in the physical characterization of **2-6** can be discussed in terms of this theoretical analysis. For example, the trends in oxidation potentials are reflective of the relative energies of the HOMOs; also, the relative energies of the charge-transfer transitions observed by UV-vis mirror the hydrogen-bonding induced stabilization at S_{exo} vs. the rest of the Ni(nmp) synthon. The reactivity kinetics with H_2O_2 can also be viewed through the lens of these electronic structure calculations. The rather negligible contributions to the HOMO and two next highest energy orbitals of S_{exo} from **2** and **4** did not allow for hydrogen-bonding induced kinetic protection against H_2O_2 oxidation of the thiolate ligands, and the rates of complex consumption did not vary. However, for **5** and **6**, where intramolecular NH•••S bonding reduced S-based contributions to the MO scheme, roughly six-fold kinetic protection against excess H_2O_2 was afforded relative to that observed for **3**. Clearly, hydrogen-bonding induced stabilization of S-based atomic orbitals, coupled with the concurrent decrease in electrostatic potentials, is capable of litigating the effects of S-based reactivity with potent O-atom transfer agents such as H_2O_2.

2.7 Conclusions and Relevance to Cysteinate Protection in Ni-SOD

Complexes **2-6** could be prepared from a common synthon via three distinct synthetic procedures: S,S'-bridge splitting of **1**. Then, from the bridge-split products; a redox driven disulfide/coordinated-thiolate exchange and a pK_a driven thiol/

coordinated-thiolate exchange. Thus, a synthetic system enabling the focused study of the component modeling Ni-Cys6 bonding through a modular approach has been achieved. Specifically, we chose to study the effects on the structural, electronic and reactivity properties imparted by the introduction of S-directed hydrogen-bonding interactions.

Complexes **2-5** conformed as good structural models of Ni-SOD_{red} via crystallographic characterization. Intramoleuclar NH•••S bonding in **4**, **5** and **6** was confirmed from the large red-shift in ν_{NH} by solution-state IR and the downfield ^1H NMR shift of the carboxamide-NH of S_{exo} upon metallation. The NH•••S bonding is manifest in the oxidation potentials of this series, affecting cathodic shifts of 40 mV for **4** relative to **2**, and of 150-200 mV in the same direction for **5** and **6** relative to **3**. It appears very likely that the S-directed hydrogen-bonding interactions found at the Ni-SOD active site serve to tune the enzymatic redox potential in a similar manner towards the midpoint of the window defined by the SOD half reactions.

The reactivity of **2-6** with excess $O_2^{\bullet-}$, O_2 and H_2O_2 was probed in MeCN, due to insolubility and/or instability in protic media. Not surprisingly, **2-6** did not participate in redox chemistry with $O_2^{\bullet-}$ in this aprotic media, even in the presence of an exogenously added N-donor approximating the His1 imidazole side chain. The reaction kinetics were sluggish ($\sim 10^{-4}$ s^{-1}) and relatively invariant with respect to oxidation by O_2, indicating sufficient kinetic stability to protect against O_2 encountered during Ni-SOD activity. The reaction also appeared clean and controlled as evidenced by the isosbestic nature of the UV-vis profile during the course of the reaction. In fact, product analysis of **5** indicated selective reactivity at the S_{exo}

position and reflects the electronic asymmetry of the equatorial N-donors in our Ni-SOD models, highlighting the fact that thiolate (and by analogy) cysteinate reactivity can be commandingly controlled via seemingly subtle and remote chemical features. The introduction of NH•••S hydrogen-bonding afforded nearly six-fold kinetic protection against S-oxidation of **5** and **6** relative to that observed for **3**.

DFT models were generated and were in good agreement with the crystallographically obtained metric data. Computationally produced **4**, **5** and **6** displayed NH•••S interactions directed at S_{exo}, and the electronic changes relative to **2** and **3** brought about by this feature served to rationalize many of the aforementioned experimental observations. The effects of NH•••S bonding were prevalent in the MO compositions of **3**, **5** and **6**. This interaction served to reduce the contributions of S_{exo} to the largely Ni-S_{exo} antibonding HOMO, stabilizing the S-based atomic orbitals relative to Ni. Hydrogen-bonding also provided a 0.03 a.u (15 kcal/mol) stabilization of the electrostatic potentials at S_{exo} of **5** and **6** relative to that of **3**.

Together, these stabilizing electronic modifications brought about by one S-directed hydrogen-bond appear to dictate the reactivity trends of **3**, **5** and **6** with H_2O_2. It is likely that similar interactions, identified in Ni-SOD and seemingly enforced by the protein tertiary structure serve to provide kinetic protection of the coordinated cysteinates of Ni-SOD during the harshly oxidizing conditions to which this enzyme is exposed. This effect would be particularly important in the Ni-SOD_{red} state, where strongly antibonding Ni-S interactions destabilize the cysteinates greatly.

Hydrogen-bonding to the cysteinate ligands is likely not the only molecular factor reducing the probability of S-based reactivity in Ni-SOD. The His1 imidazole

side chain has been implicated in reshuffling the molecular orbital distribution to a largely Ni(d_z^2) scenario upon binding to Ni(III),[22] and this additional N-donor most likely remains bound to Ni(II) during the catalytic cycle as SOD catalysis occurs on a time scale faster than nuclear motion.[38] However, no studies have yet been performed addressing the electronic disposition of Ni-SOD_{red} in a five-coordinate state. Regardless, through a joint experimental and theoretical examination of carefully designed models accurately modeling Ni-SOD_{red}, we have been able to provide profound evidence in support of S-directed hydrogen-bonding as a molecular feature serving to protect the Ni-SOD active site from oxidative modifications during catalysis.

2.8 Experimental Section

General Information. All reagents were purchased from commercial suppliers and used as received unless otherwise noted. Acetonitrile (MeCN), methylene chloride (CH_2Cl_2), tetrahydrofuran (THF), diethyl ether (Et_2O) and pentane were purified by passage through activated alumina columns using an MBraun MB-SPS solvent purification system and stored under a dinitrogen (N_2) atmosphere before use. *N,N*-dimethylformamide (DMF) was purified with a VAC Solvent Purifier containing 4 Å molecular sieves and stored under similar conditions. Triethylamine (TEA) was purified by static drying over Na_2SO_3. All reactions were performed under an inert atmosphere of N_2 using standard Schlenk line techniques or in an MBraun Unilab glovebox under an atmosphere of purified N_2. The molecule, *o*-benzoylaminobenzene thiolate disulfide (disulfide of S-*o*-babt) was synthesized

according to a published procedure.[48] The purity was confirmed by comparison with previously reported spectral data.

Physical Methods. FTIR spectra were collected on a ThermoNicolet 6700 spectrophotometer running the OMNIC software. Solid-state samples were prepared as pressed KBr pellets and solution samples were prepared in an airtight Graseby-Specac solution cell with CaF_2 windows and 0.1 mm spacers. Electronic absorption spectra were run at 298 K using a Cary-50 spectrophotometer containing a Quantum Northwest TC 125 temperature control unit. The UV-vis samples were prepared in gas-tight Teflon-lined screw cap quartz cells equipped with a rubber septum and an optical pathlength of 1 cm. Cyclic voltammetry measurements were performed with a PAR Model 273A potentiostat using a Ag/AgCl reference electrode, Pt counter electrode and a Glassy Carbon millielectrode (2 mm diameter) working electrode. Measurements were performed at ambient temperature using 5.0 mM analyte in the appropriate solvent under Ar containing 0.1 M $^{n}Bu_4NPF_6$ as the supporting electrolyte. The "Maximize Stability" mode was utilized in the PAR PowerCV software utilizing a low-pass 5.3 Hz filter. To ensure accuracy in the measured CVs, these experiments were performed in triplicate while polishing the working electrode between each run and report an average E_{ox}. Additionally, potentials were checked and corrected by recording the CV of a ferrocene standard under the same experimental conditions as the complexes before each run. NMR spectra were recorded in the listed deuterated solvent on a 400 MHz Bruker BZH 400/52 NMR Spectrometer or 500 MHz Varian Unity INOVA NMR spectrometer at ambient temperature with chemical shifts referenced to TMS or residual protio signal of the

deuterated solvent.[49] Low resolution ESI-MS data were collected using a Perkin Elmer Sciex API I Plus quadrupole mass spectrometer and high resolution ESI-MS data were collected using a Bruker Daltonics 9.4 T APEX Qh FT-ICR-MS. Elemental analysis for C, H, and N was performed at QTI-Intertek in Whitehouse, NJ.

Synthesis of Compounds. *N*-(2-mercaptoethyl)picolinamide ($nmpH_2$): The synthesis of the ligand comprises the following steps:

Step 1. 2-(tritylthio)ethanamine (S-Trityl-cysteamine). This compound was synthesized according to a modified literature procedure.[50] A batch of 10.710 g (41.12 mmol) of triphenylmethanol was dissolved in 50 mL of TFA to form a clear orange solution. To this solution was added 4.682 g (41.21 mmol) of cysteamine hydrochloride resulting in a dark red homogeneous solution. After stirring for 90 min at room temperature (RT), the reaction mixture was concentrated to a dark red residue which was partitioned between 300 mL of CH_2Cl_2 and 300 mL of H_2O. To this mixture was added K_2CO_3 until fizzing ceased and the aqueous layer remained basic. The organic layer was subsequently separated, washed with satd. $NaHCO_3$, brine, dried over $MgSO_4$, filtered and the solution evaporated to afford 10.20 g (31.92 mmol, 78%) of product as a white solid. mp: 85 ^oC (dec). ^1H NMR (400 MHz, $CDCl_3$, δ from TMS): 7.43-7.41 (m, 6H), 7.29-7.18 (m, 9H), 2.57 (t, 2H, H_2N-CH_2CH_2-S), 2.31 (t, 2H, H_2N-CH_2CH_2-S), 1.22 (br s, 2H, NH_2). ^{13}C NMR (75.4 MHz, $CDCl_3$, δ from TMS): 145.17, 129.84, 128.14, 126.88, 66.80 (CPh_3), 41.32 (H_2N-CH_2CH_2-S), 36.55 (H_2N-CH_2CH_2-S). FTIR (ATR-diamond, powder) ν_{max} (cm^{-1}): 3364 (br, w, NH), 3056 (w), 3014 (w), 2915 (w), 1591 (w), 1484 (m), 1439

(m), 1179 (w), 1153 (w), 1076 (w), 1030 (w), 999 (w), 924 (w), 840 (w), 764 (m), 741 (s), 697 (s), 674 (s) 624 (m).

Step 2. *N*-(2-(tritylthio)ethyl)picolinamide (S-Trityl-nmp). A batch of 500 mg (4.06 mmol) of picolinic acid was refluxed in 5 mL of $SOCl_2$ for 1 h and cooled to RT. The resulting purple solution was concentrated to a lavender residue, which was triturated three times with 5 mL portions of dry CH_2Cl_2. The lavender residue was then re-dissolved in 5 mL of CH_2Cl_2 and to it was added dropwise a 15 mL CH_2Cl_2 solution containing 1.24 g (3.87 mmol) of S-trityl-cysteamine and 3.260 g (32.22 mmol) of TEA at 0 °C. A blue-green solution resulted which turned brown upon overnight stirring at RT. This solution was then washed with saturated $NaHCO_3$, brine, dried over $MgSO_4$ and the solvent evaporated to afford 1.43 g (3.38 mmol, 87%) of product as a tan colored foam. mp: 41 ^oC (dec). ^1H NMR (400 MHz, $CDCl_3$, δ from TMS): 8.55 (d, 1H), 8.15 (m, 2H, Py*H* and N*H*), 7.82 (t, 1H), 7.44-7.41 (m, 8H), 7.27-7.17 (m, 8H) 3.32 (t, 2H, OC-HN-CH_2CH$_2$-S), 2.51 (t, 2H, OC-HN-CH$_2$CH_2-S). ^{13}C NMR (75.4 MHz, $CDCl_3$, δ from TMS): 164.36 (*C*=O), 150.03, 148.33, 144.93, 137.52, 129.83, 128.18, 126.99, 126.38, 122.43, 67.07 (*C*Ph$_3$), 38.40 (OC-NH-*C*H$_2$CH$_2$-S), 32.39 (OC-NH-CH$_2$*C*H$_2$-S). FTIR (ATR-diamond, powder) ν_{max} (cm^{-1}): 3368 (br, w, NH), 3053 (w, CH), 1667 (vs, C=O), 1590 (m), 1568 (w), 1514 (s), 1463 (m), 1432 (m), 1281 (w), 1241 (w), 1082 (w), 1031 (w), 997 (w), 817 (w), 740 (vs), 696 (s), 615 (w).

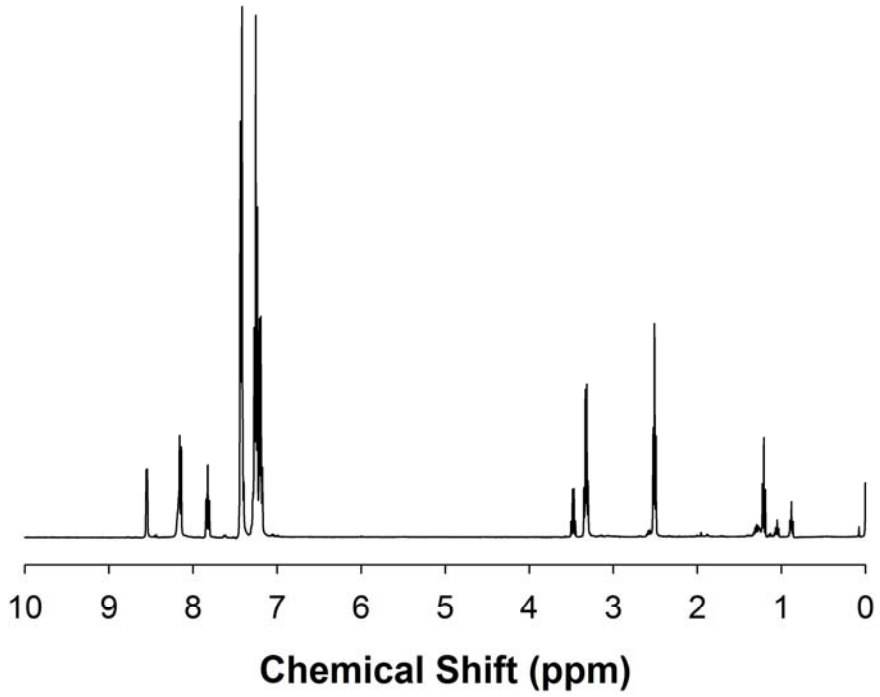

Figure 13. ^{1}H NMR of S-Trityl-nmp in $CDCl_3$ (peaks at 3.48 and 1.21 ppm are from Et_2O in the sample).

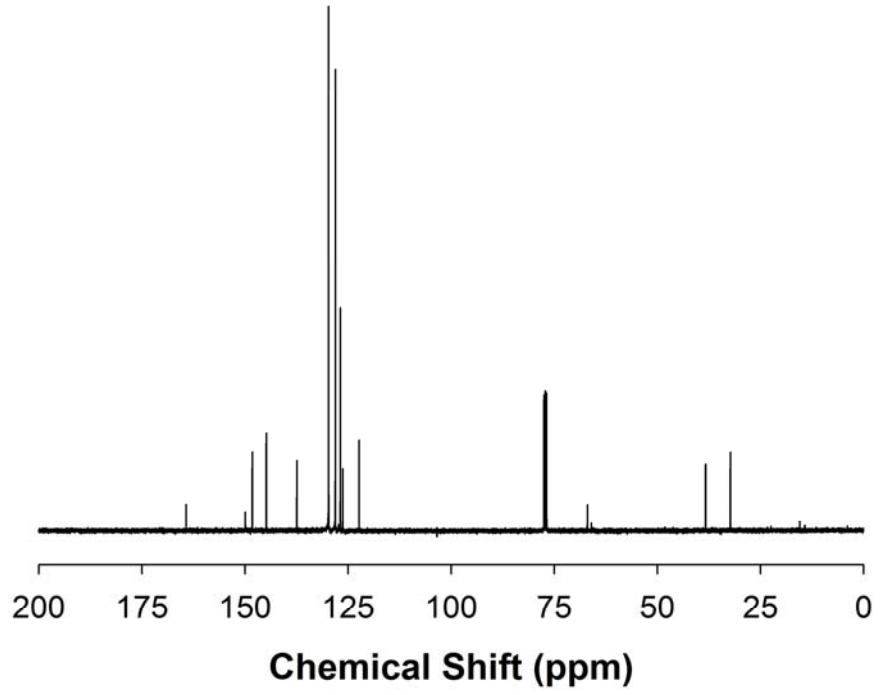

Figure 14. ^{13}C NMR of S-Trityl-nmp in $CDCl_3$ (peak at 77.16 ppm is from solvent, 65.91 and 15.20 ppm are from Et_2O in the sample).

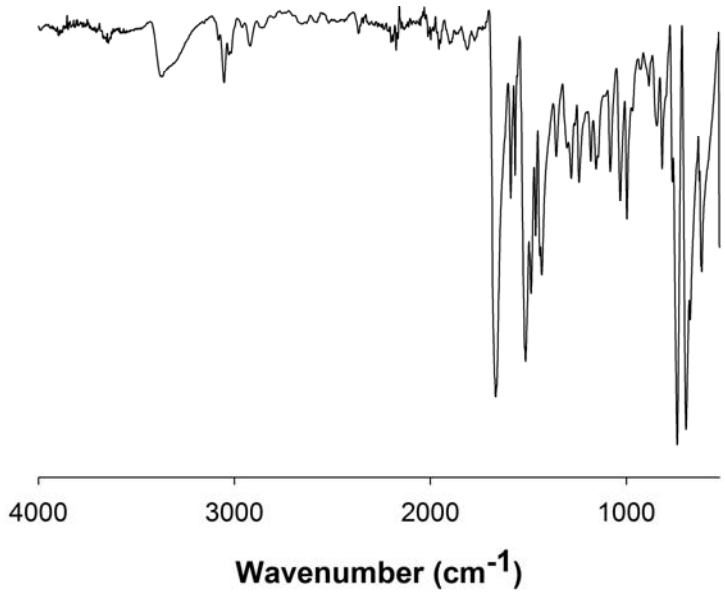

Figure 15. FTIR (ATR-diamond) of S-trityl-nmp.

Step 3. *N*-(2-mercaptoethyl)picolinamide (nmpH$_2$). S-Trityl-nmp (1.43 g, 3.38 mmol) was dissolved in 16 mL of a 1:1 TFA:CH_2Cl_2 mixture to form a clear bright red solution. To this solution was added 472 mg (4.06 mmol) of Et_3SiH dropwise and the solution turned tan in color. After stirring for 90 min at RT, the solution was concentrated to ~ 50% original volume and the resulting insoluble triphenylmethane byproduct ($HCPh_3$) was filtered off. The solution was then concentrated to afford a brown-colored oil, which was taken up in CH_2Cl_2, washed with satd. $NaHCO_3$, brine, dried over $MgSO_4$ and the solution evaporated to afford 448 mg (2.46 mmol, 73%) of product as a brown oil. ^{1}H NMR (400 MHz, $CDCl_3$, δ from TMS): 8.57 (d, 1H), 8.42 (br s, 1H, N*H*), 8.20 (d, 1H), 7.86 (t, 1H), 7.45 (t, 1H), 3.68 (t, 2H, OC-HN-C*H*$_2$CH$_2$-S), 2.80 (t, 2H, OC-HN-CH$_2$C*H*$_2$-S), 1.47 (t, 1H, S*H*). ^{13}C NMR (75.4 MHz, $CDCl_3$, δ from TMS): 164.67 (*C*=O), 148.39, 137.62, 126.52,

122.50, 103.53, 42.68 (OC-NH-*C*$H_2$$CH_2$-S), 24.89 (OC-NH-$CH_2$*C*$H_2$-S). FTIR (ATR-diamond, oil) ν_{max} (cm^{-1}): 3338 (br, w, NH), 3054 (w, CH), 2930 (w, CH), 2540 (br, w, SH), 1658 (vs, C=O), 1589 (m), 1568 (m), 1514 (vs), 1463 (s), 1432 (s), 1359 (m), 1283 (m), 1240 (m), 1194 (m), 1160 (m), 1087 (m), 1041 (w), 996 (m), 955 (w), 896 (w), 819 (w), 746 (m), 689 (w), 619 (w) . LRMS-ESI (*m/z*): $[M + H]^+$ calcd for $C_8H_{11}N_2OS$, 183.2; found, 183.0.

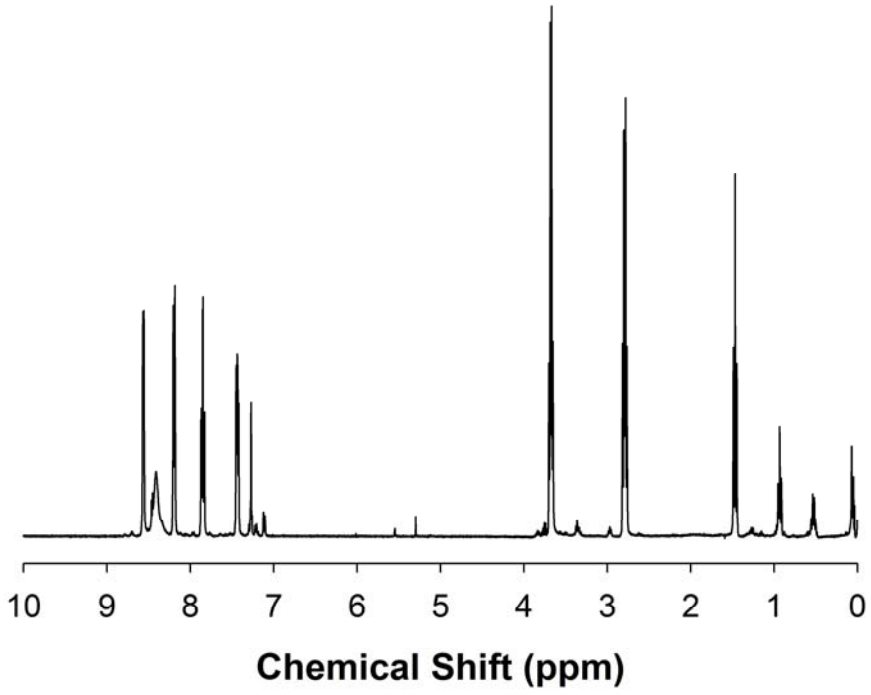

Figure 16. ^1H NMR of $nmpH_2$ in $CDCl_3$.

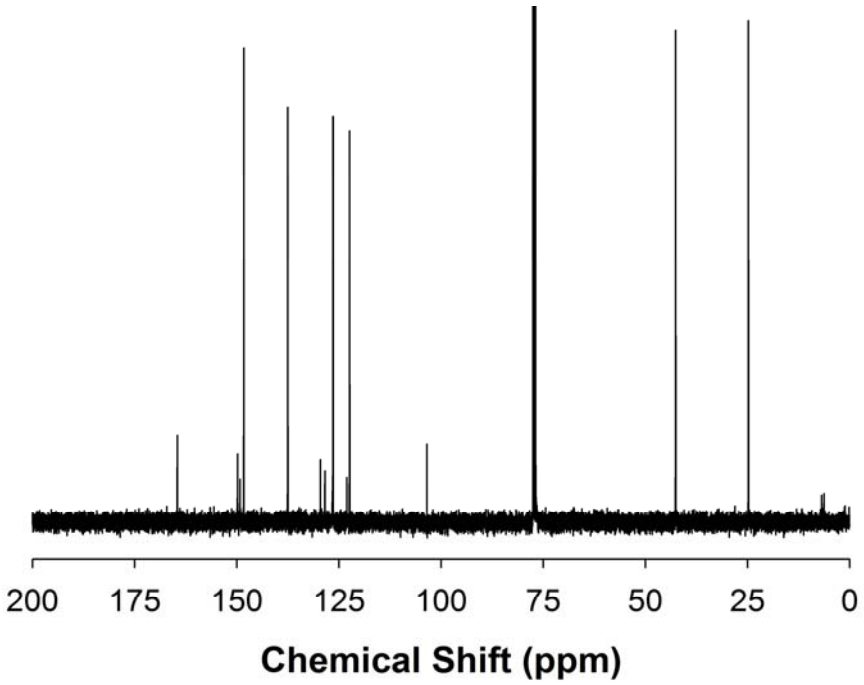

Figure 17. ^{13}C NMR of $nmpH_2$ in $CDCl_3$ (peak at 77.16 ppm is from solvent).

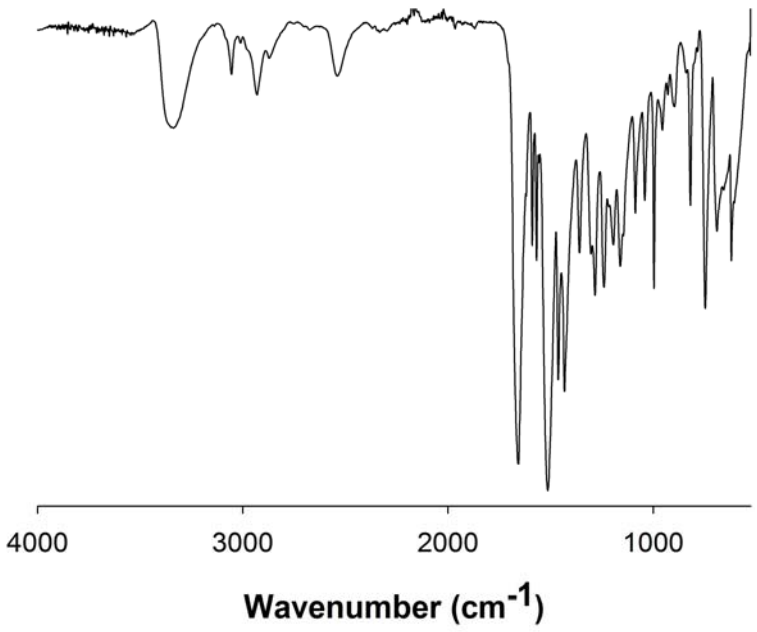

Figure 18. FTIR (ATR-diamond) of $nmpH_2$.

$[Ni_2(nmp)_2]$ (1): To 448 mg (2.46 mmol) of $nmpH_2$ dissolved in 2 mL of DMF was added a slurry of 121 mg (5.04 mmol) of NaH in 4 mL of DMF. Immediate effervescence was observed and the solution was allowed to stir for 20 min before 900 mg (2.46 mmol) of $[Ni(H_2O)_6](ClO_4)_2$ in 8 mL of DMF (stirred overnight over 3 Å molecular sieves to dry) was added to the tan colored solution. After addition, a scarlet-red heterogeneous solution formed immediately which was subsequently heated at 45 ºC for 2 h before being concentrated to a scarlet-red residue. This residue was then stirred in 50 mL of MeCN (to remove $NaClO_4$) overnight at RT forming a red suspension from which 567 mg (1.19 mmol, 96%) of **1** as a red solid was isolated by vacuum filtration. FTIR (ATR-diamond, powder) ν_{max} (cm^{-1}): 1623 (vs, C=O), 1594 (vs, C=O), 1563 (m), 1389 (w), 767 (m), 683 (m), 677 (w), 671 (w). Anal. Calcd for $C_{16}H_{16}N_4Ni_2O_2S_2 \bullet 0.5H_2O$: C, 39.47; H, 3.52; N, 11.51. Found: C, 39.61; H, 3.69; N, 10.42.

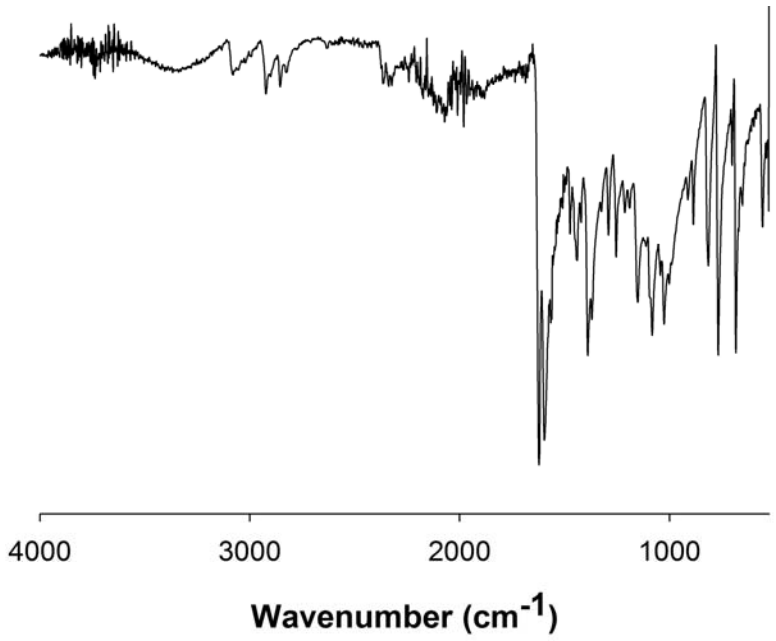

Figure 19. FTIR (ATR-diamond) of **1**.

$(Et_4N)[Ni(nmp)(SC_6H_4$-*p*-Cl)] (2). To 171 mg (1.18 mmol) of 4-chlorobenzenethiol in 2 mL DMF was added a slurry of 48 mg (1.2 mmol) of KH in 3 mL of DMF at RT. Immediate effervescence was observed and the resulting solution became clear and homogeneous after 20 min. To this solution was added 310 mg (0.66 mmol) of **1** as a slurry in 5 mL of DMF at RT and a homogeneous dark red-orange solution formed within minutes. After heating overnight at 45 ºC the solution was concentrated to a dark-red residue and taken up in 5 mL of cold MeCN and left in the freezer for 1 h. The 25 mg of unreacted **1** was filtered off and the mother liquor was concentrated to 1 mL and saturated with 20 mL of Et_2O to precipitate out $K[Ni(nmp)(SC_6H_4$ –*p*-Cl)] as an orange solid (450 mg, 1.07 mmol, 91%) after vacuum filtration. For cation exchange, 39 mg (0.24 mmol) of Et_4NCl and 95 mg (0.23 mmol) of $K[Ni(nmp)(SC_6H_4$-*p*-Cl)] were stirred in 9 mL MeCN at RT for 3 h. A white precipitate formed immediately (presumably KCl) and the solution was left to stir for 3 h after which the KCl was filtered off and the mother liquor was concentrated to a red residue. The residue was taken up in 8 mL of THF and left to stir overnight at RT. The following morning the solution was filtered through celite to remove any remaining Et_4NCl and concentrated to a red residue. Stirring this oily residue in Et_2O overnight resulted in a red-orange solid that was collected via vacuum filtration (83 mg, 0.16 mmol, 70% from K^+ salt). Dark red blocks suitable for X-ray diffraction were obtained via slow diffusion of Et_2O into a saturated anaerobic THF solution of **2**. ^1H NMR (400 MHz, $(CD_3)_2CO$, δ): 8.65 (d, 1H), 7.96 (d, 2H), 7.86 (t, 1H), 7.54 (d, 1H), 7.26 (t, 1H), 6.84 (d, 2H), 3.50 (q, 8H, $(CH_3C\mathit{H}_2)_4N$), 3.27

(t, 2H, OC-HN-CH_2CH$_2$-S), 2.14 (t, 2H, OC-HN-CH$_2$CH_2-S), 1.38 (t, 12H, (CH_3CH$_2$)$_4$N). FTIR (ATR-diamond, powder) ν_{max} (cm^{-1}): 2981 (w), 2921 (w), 2837 (w), 1614 (vs, C=O), 1588 (vs, C=O), 1478 (m), 1463 (m), 1390 (m), 1286 (w), 1257 (m), 1186 (w), 1086 (s, CCl), 999 (m), 889 (w), 804 (m), 785 (w), 771 (s), 688 (m), 669 (m), 557 (w), 538 (m). LRMS-ESI (*m/z*): [M–Et$_4$N]$^-$ calcd for $C_{14}H_{12}ClN_2NiOS_2$, 380.9; found, 381.0. UV-vis (MeCN) λ_{max}, nm (ε): 299 (20,860), 450 (5,450). UV-vis (THF) λ_{max}, nm (ε): 303 (16,680), 464 (4,390). E_{ox} (MeCN): 236 mV. E_{ox} (THF): 351 mV. Anal. Calcd for $C_{22}H_{32}ClN_3NiOS_2$: C, 51.53; H, 6.29; N, 8.19. Found: C, 51.68; H, 6.12; N, 9.03.

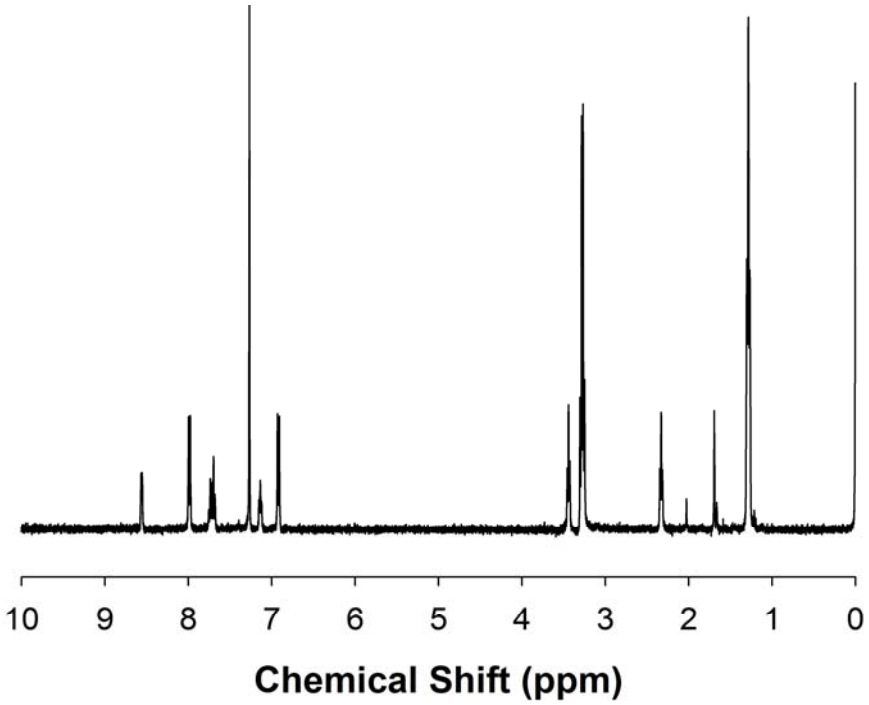

Figure 20. ^{1}H NMR of **2** in $CDCl_3$ (peak at 7.27 ppm is from protio solvent, 1.60 ppm is from HOD present in sample and 0.00 from TMS).

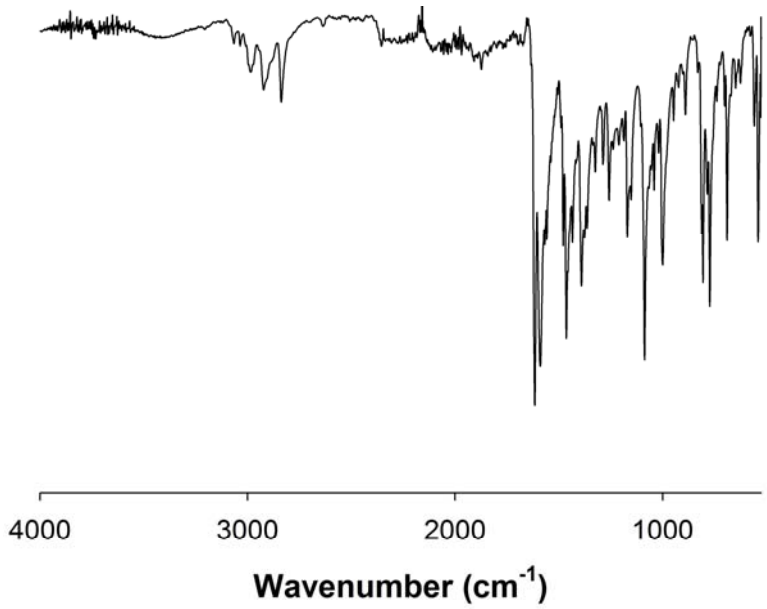

Figure 21. FTIR (ATR-diamond) of **2**.

(Et_4N)[Ni(nmp)(S^tBu)] (3): To 70 μL (0.62 mmol) of 2-methyl-2-propanethiol in 2 mL of DMF was added 25 mg of KH (0.62 mmol). Immediate effervescence was observed and the solution was allowed to stir for 20 min at RT. To the clear yellow solution was added 184 mg (0.385 mmol) of **1** as a red slurry in 5 mL of DMF to form a dark red solution. After overnight stirring at RT, the solution was concentrated to a dark red residue which was taken up in 5 mL of MeCN and placed in a -20 ^oC freezer. After 3 h, the resulting insolubles were filtered off and the mother liquor was concentrated to 1 mL and saturated with 20 mL of Et_2O to precipitate out 198 mg (0.539 mmol, 87%) of K[Ni(nmp)(S^tBu)] as a red-orange solid after vacuum filtration. For cation exchange, 39 mg (0.24 mmol) of Et_4NCl and 86 mg (0.23 mmol) of K[Ni(nmp)(S^tBu)] were stirred in 6 mL of MeCN. A white precipitate (presumably KCl) formed immediately and the solution was left to stir for 3 h at RT after which the KCl was filtered off and the mother liquor was concentrated to afford a red

residue. This residue was taken up in 8 mL of THF and stirred overnight. The solution was then filtered through celite to remove any remaining Et_4NCl and concentrated to a red residue. Overnight standing in Et_2O afforded a red-brown solid (72 mg, 0.16 mmol, 70% K^+ salt) after vacuum filtration. Dark red blades suitable for X-ray diffraction were obtained via slow diffusion of Et_2O into a saturated anaerobic THF solution of **3**. ^1H NMR (400 MHz, $(CD_3)_2CO$, δ): 9.35 (d, 1H), 7.83 (t, 1H), 7.48 (d, 1H), 7.31 (t, 1H), 3.53 (q, 8H, $(CH_3CH_2)_4N$), 3.18 (t, 2H, OC-HN-CH_2CH_2-S), 2.15 (t, 2H, OC-HN-CH_2CH_2-S), 1.47 (s, 9H, ^{t}Bu*H*), 1.40 (t, 12H, $(CH_3CH_2)_4N$). FTIR (ATR-diamond, powder) ν_{max} (cm^{-1}): 2906 (w), 2841 (w), 1613 (s, C=O), 1588 (vs, C=O), 1560 (m), 1449 (w), 1392 (m), 1287 (w), 1258 (w), 1171 (w), 1154 (w), 1092 (m), 1001 (w), 799 (w), 771 (w), 687 (w), 669 (w). UV-vis (MeCN) λ_{max}, nm (ε): 298 (8,770), 464 (4,540). UV-vis (THF), λ_{max}, nm (ε): 298 (7,120), 370 (1,880), 473 (3,570). E_{ox} (MeCN): 75 mV. E_{ox} (THF): 226 mV. Elemental analysis was unable to be successfully performed due to slow decomposition of the compound.

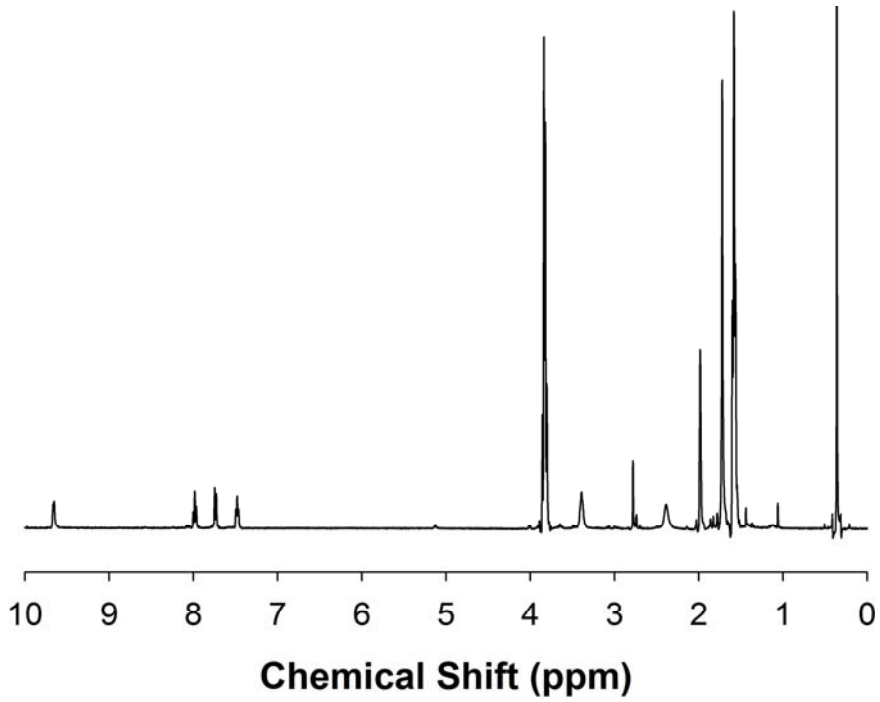

Figure 22. ^{1}H NMR of **3** in d_8-THF (peaks at 3.58 (coincidental with complex) and 1.72 are from protio solvent, 2.50 ppm is from HOD present in the sample and 0.36 ppm is from TMS).

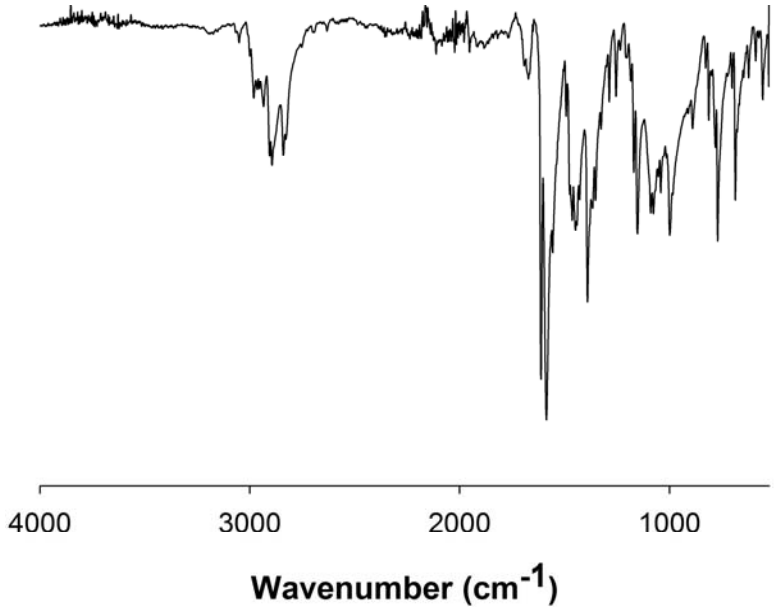

Figure 23. FTIR (KBr matrix) of **3**.

(Et_4N)[Ni(nmp)(S-*o*-babt)] (4). A batch of 81.0 mg (0.177 mmol) of **3** and 44.7 mg (0.0975 mmol) of the disulfide of S-*o*-babt were combined in 10 mL of a 1:1 MeCN/THF mixture at room temperature (RT) to form a red-orange solution. After 16 h of stirring, the reaction mixture was filtered through a 0.2 μm nylon filter and the mother liquor was concentrated to a red-orange residue. The residue was stirred for 4 h in a mixture of 1:1 THF/Et_2O after which 71.1 mg (0.119 mmol, 67%) of product was isolated as hard red chunks. Dark red blades suitable for X-ray structural analysis were grown by slow diffusion of pentane into a THF solution of **4** at RT. ^{1}H NMR (400 MHz, $CDCl_3$, δ from TMS): 10.57 (s, 1H, NH), 8.47 (d, 1H), 8.32 (m, 4H), 7.76 (m, 2H), 7.48 (m, 4H), 7.19 (t, 1H), 6.99 (t, 1H), 6.84 (t, 1H), 3.45 (t, 2H, OC-NH-C*H*$_2$-CH_2-S), 3.11 (q, 8H, (CH_3C*H*$_2$)$_4$N), 2.26 (t, 2H, OC-NH-CH_2-C*H*$_2$-S), 1.18 (t, 12H, (C*H*$_3CH_2$)$_4$N). FTIR (KBr pellet) ν_{max} (cm^{-1}): 3271 (w, NH), 3054 (w), 2979 (w), 2921 (w), 2844 (w), 1652 (s, C=O), 1620 (s, C=O), 1590 (s, C=O), 1574 (s, C=O), 1562 (m), 1525 (m), 1491 (m), 1448 (w), 1428 (m), 1388 (m), 1364 (w), 1331 (w), 1321 (w), 1294 (w), 1254 (w), 1221 (w), 1186 (w), 1171 (w), 1153 (w), 1083 (br, m), 1059 (w), 1031 (w), 997 (m), 942 (w), 896 (w), 813 (w), 786 (w), 768 (m), 761 (s), 715 (w), 686 (w), 669 (w), 623 (w), 587 (w), 557 (w), 542 (w), 484 (w), 463 (w), 449 (w), 432 (w). FTIR (CH_2Cl_2, CaF_2 windows) ν_{max} (cm^{-1}): 3274 (br, w, NH), 3040 (w), 2952 (m), 1670 (m), 1623 (s, C=O), 1600 (s, C=O), 1572 (m), 1521 (s), 1491 (m), 1457 (w), 1429 (m), 1393 (m), 1367 (w). LRMS-ESI (*m/z*): $[M–Et_4N]^-$ calcd for $C_{21}H_{18}N_3NiO_2S_2$, 466.0; found, 466.0. UV-vis (MeCN) λ_{max}, nm (ε): 450 (3,500). Anal. Calcd for $C_{29}H_{38}N_4NiO_2S_2$•0.5THF•0.5H_2O: C, 57.95; H, 6.75; N, 8.72. Found: C, 57.63; H, 6.81; N, 8.70.

Synthesis of HS-meb. The synthesis of the ligand comprised the following steps:

Step 1. *N*-(2-(tritylthio)ethyl)benzamide (S-trityl-meb). A batch of 0.975 g (3.05 mmol) of S-trityl-cysteamine and 1.039 g (10.27 mmol) of TEA was dissolved in 10 mL of CH_2Cl_2 and added dropwise over the course of 10 min to a solution of 0.640 g (4.55 mmol) of benzoyl chloride stirring in 2 mL of CH_2Cl_2 at 0 °C. The resulting heterogeneous yellow solution was slowly warmed to RT and stirred for another 48 h before being diluted to homogeneity with CH_2Cl_2 and washed with $NaHCO_3$(aq) and brine. The organic layer was dried over $MgSO_4$, filtered and concentrated to a yellow oil, which was stirred overnight in a 1:4 mixture of Et_2O/pentane to afford 0.722 g (1.70 mmol, 56%) of product as a fluffy white solid. mp: 125-126 °C. ^{1}H NMR (400 MHz, $CDCl_3$, δ from TMS): 7.71 (m, 2H), 7.51 (m, 2H), 7.43 (m, 8H), 7.26 (t, 6H), 7.21 (t, 3H), 6.25 (br s, 1H, NH), 3.31 (q, 2H, OC-NH-C*H*$_2$-CH$_2$-S), 2.54 (t, 2H, OC-NH-CH$_2$-C*H*$_2$-S). ^{13}C NMR (100.6 MHz, $CDCl_3$, δ from TMS): 167.36 (*C*=O), 144.74, 134.58, 131.60, 129.65, 128.66, 128.13, 127.05, 126.97, 67.03 (*C*Ph$_3$), 45.91 (OC-NH-*C*H$_2$-CH$_2$-S), 32.35 (OC-NH-CH$_2$-*C*H$_2$-S). FTIR (KBr pellet) ν_{max} (cm^{-1}): 3392 (br, m, NH), 3053 (w), 3029 (w), 2930 (w), 1633 (s, C=O), 1601 (w), 1577 (m), 1538 (s), 1488 (m), 1445 (m), 1430 (w), 1361 (w), 1324 (w), 1302 (m), 1235 (w), 1186 (w), 1156 (w), 1077 (w), 1002 (w), 970 (w), 848 (w), 803 (w), 768 (m), 752 (m), 743 (w), 703 (s), 630 (w), 615 (m), 507(w), 474 (w).

Step 2. *N*-(2-mercaptoethyl)benzamide (HS-meb). A batch of 0.533 g (1.26 mmol) of S-trityl-meb was stirred in 10 mL of a 1:1 CH_2Cl_2/TFA solution resulting

in a bright yellow solution. After 1 h, 218 mg (1.88 mmol) of Et_3SiH was added dropwise to the solution causing bleaching of the bright yellow solution to a clear and pale yellow color. After 3 h of stirring, the solution was concentrated to ~50% of its original volume and the resulting insoluble triphenylmethane ($HCPh_3$) byproduct was filtered off and washed with TFA. The solution was then concentrated to a light yellow residue and taken up in 20 mL of CH_2Cl_2 and washed with $NaHCO_3$(aq) and brine. The organic layer was dried over $MgSO_4$, filtered and concentrated to dryness. The resulting residue was stirred in pentane for 1 h after which 0.218 g (1.20 mmol, 95%) of a white solid product was isolated. mp: 65-66 °C. ^{1}H NMR (400 MHz, $CDCl_3$, δ from TMS): 7.79 (d, 2H), 7.52 (t, 1H), 7.43 (t, 2H), 6.74 (br s, 1H, NH), 3.64 (q, 2H, OC-NH-C*H*$_2$-CH$_2$-S), 2.78 (q, 2H, OC-NH-CH$_2$-C*H*$_2$-S), 1.41 (t, 0.6H, SH, integrates for slightly less due to exchangeable nature of SH). ^{13}C NMR (100.6 MHz, $CDCl_3$, δ from TMS): 167.66 (*C*=O), 134.46, 131.72, 128.79, 127.07, 42.87 (OC-NH-*C*H$_2$-CH$_2$-S), 24.93 (OC-NH-CH$_2$-*C*H$_2$-S). FTIR (KBr pellet) ν_{max} (cm^{-1}): 3299 (br, m, NH), 3065 (w), 2939 (w), 2840 (w), 2574 (w, SH), 1634 (vs, C=O), 1602 (w), 1579 (m), 1542 (vs), 1491 (m), 1438 (w), 1361 (w), 1310 (s), 1240 (w), 1187 (w), 1155 (w), 1076 (w), 1001 (w), 890 (w), 835 (w), 804 (w), 691 (s), 644 (br, w), 616 (w), 508 (w). FTIR (CH_2Cl_2, CaF_2 windows) ν_{max} (cm^{-1}): 3452 (w, NH), 2977 (w), 2931 (w), 2871 (w), 1665 (s, C=O), 1602 (w), 1581 (w), 1519 (s), 1486 (m), 1414 (w), 1365 (w). LRMS-ESI (*m/z*): $[M–H]^-$ calcd for $C_9H_{10}NOS$, 180.1; Found, 180.0.

(Et_4N)[Ni(nmp)(S-meb)] (5). A batch of 68.3 mg (0.149 mmol) of **3** and 32.0 mg (0.177 mmol) of HS-meb were combined in 5 mL of MeCN to afford a red-

orange solution. After 16 h of stirring, the reaction mixture was filtered through a 0.2 μm nylon filter and the mother liquor was concentrated to a red-orange residue. The resulting residue was stirred for 2 h after which 68.4 mg (0.124 mmol, 83%) of red-orange solids were isolated via vacuum filtration. Dark red blades suitable for X-ray crystallography were grown by slow diffusion of Et_2O into a 5:1 THF/DMF solution of **5** at -20 °C. ^{1}H NMR (500 MHz, $CDCl_3$, δ from TMS): 8.51 (br m, 2H, NH and aromatic CH), 8.21 (d, 2H), 7.78 (t, 1H), 7.67 (d, 1H), 7.44 – 7.39 (m, 3H), 7.23 (t, 1H), 3.58 (br, m, 2H), 3.47 (br, t, 2H), 3.40 (q, 8H, $(CH_3C\mathit{H}_2)_4N$), 2.40 (br, s, 2H), 2.31 (br, t, 2H), 1.29 (t, 12H, $(C\mathit{H}_3CH_2)_4N$). FTIR (KBr pellet) ν_{max} (cm^{-1}): 3298 (br, w, NH), 2991 (w), 2932 (w), 2917 (w), 2842 (w), 1643 (s, C=O), 1623 (s, C=O), 1598 (s, C=O), 1575 (w), 1563 (w), 1522 (m), 1485 (m), 1441 (m), 1395 (m), 1296 (m), 1279 (w), 1259 (w), 1185 (w), 1171 (w), 1140 (w), 1084 (m), 1049 (w), 999 (w), 808 (w), 784 (w), 759 (w), 715 (m), 694 (w), 687 (w), 557 (w), 485 (w). FTIR (CH_2Cl_2, CaF_2 windows) ν_{max} (cm^{-1}): 3261 (br, w, NH), 3041 (w), 2962 (w), 2843 (w), 1647 (m, C=O), 1619 (s, C=O), 1598 (s, C=O), 1578 (w), 1563 (w), 1533 (w), 1484 (m), 1458 (w), 1393 (m). LRMS-ESI (*m/z*): $[M–Et_4N]^–$ calcd for $C_{17}H_{18}N_3NiO_2S_2$, 418.0; Found, 418.0. UV-vis (MeCN) λ_{max}, nm (ε): 449 (3900). Anal. Calcd for $C_{25}H_{38}N_4NiO_2S_2•1.25H_2O$: C, 52.50; H, 7.14; N, 9.80. Found: C, 52.51; H, 7.02; N, 9.82.

K[Ni(nmp)(S-NAc)] (6). To a batch of 159.9 mg (0.4355 mmol) of the K^+ salt of **3** in 10 mL of MeCN was added 82.3 mg (0.464 mmol) of N-acetyl-L-cysteine methyl ester in 3 mL of MeCN at RT. Upon addition, the reaction mixture rapidly changed from red-orange to a brown-tinged orange solution. After 16 h of stirring, the

reaction mixture was filtered through a 0.2 μm nylon filter and the mother liquor was concentrated to a red-orange residue. Stirring the residue in 1:1 THF/Et_2O afforded free flowing red-brown solids of which 163.0 mg (0.3588 mmol, 82%) were isolated via vacuum filtration. ^{1}H NMR (500 MHz, d_6-acetone, δ from protio solvent): 8.73 (s, 0.3 H, NH, integrates for slightly less due to exchangeable nature of NH), 8.50 (d, 1H), 7.89 (t, 1H), 7.55 (d, 1H), 7.35 (t, 1H), 4.18 (t, 1H, S_{cys}-CH_2-C*H*-), 3.59 (s, 3H, C*H*$_3$-O-CO), 3.36 (m, 1H, S_{nmp}-CH_2-C*(H)(H)*-N-CO), 3.32 (m, 1H, S_{nmp}-CH_2-C*(H)(H)*-N-CO), 2.29 (m, 3H, S_{cys}-C*H*$_2$-CH- and S_{nmp}-C*(H)(H)*-CH_2-N-CO), 2.17 (m, 1H, S_{nmp}-C*(H)(H)*-CH_2-N-CO), 2.02 (s, 3H, C*H*$_3$-NH-CO). FTIR (KBr pellet) ν_{max} (cm^{-1}): 3246 (br, w, NH), 2916 (w), 2841 (w), 1735 (m, C=O ester), 1662 (s, C=O), 1620 (s, C=O carboxamide), 1595 (s, C=O), 1562 (m), 1533 (br, m), 1435 (w), 1398 (m), 1373 (m), 1292 (w), 1261 (w), 1214 (w), 1129 (m), 1078 (m), 1005 (w), 761 (w), 687 (w), 633 (w), 625 (w), 560 (w), 487 (w). FTIR (MeCN, CaF_2 windows) ν_{max} (cm^{-1}): 3481 (br, w, NH), 3372 (br, w, NH), 3235 (br, w, NH), 2987 (m), 2937 (m), 2845 (w), 1747 (m, C=O ester), 1671 (s, C=O), 1623 (s, C=O carboxamide), 1600 (s, C=O), 1539 (w). LRMS-ESI (*m/z*): $[M-K]^-$ calcd for $C_{14}H_{18}N_3NiO_4S_2$, 414.0; Found, 414.0. HRMS-ESI (*m/z*): $[M-K]^-$ calcd for $C_{14}H_{18}N_3NiO_4S_2$ (relative abundance), 414.0092 (100.0), 415.0113 (18.2), 416.0046 (49.9), 417.0067 (10.5), 418.0021 (10.5); Found, 414.0099 (100.0), 415.0137 (14.1), 416.0052 (47.1), 417.0084 (7.0), 418.0022 (8.0). UV-vis (MeCN) λ_{max}, nm (ε): 442 (3,710). Anal. Calcd for $C_{14}H_{18}KN_3NiO_4S_2 \cdot 3H_2O$: C, 33.08; H, 4.76; N, 8.27. Found: C, 33.54; H, 4.13; N, 7.83.

Oxidation of 2. A batch of 23 mg (0.045 mmol) of **2** was combined with 14.8 mg (0.045 mmol) of ferrocenium hexafluorophosphate in 5 mL of MeCN at RT. A red precipitate was observed within seconds and the reaction was left to stir. After 2 h, 10.6 g (0.022 mmol, 98% yield) of **1** was isolated via vacuum filtration. The pale yellow mother liquor was concentrated to dryness and taken up in 10 mL of Et_2O from which 11.0 mg (0.040 mmol, 89% yield) Et_4NPF_6 were isolated via vacuum filtration. The Et_2O portion was concentrated to 14 mg of a yellow and white residue from which both the disulfide or 4-chlorobenzenethiol and ferrocene were detected by ^{1}H NMR.

Reactivity Studies with O_2 and ROS. All measurements were carried out in gas-tight Teflon-lined screw cap quartz UV-vis cells of 1 cm pathlength equipped with a rubber septum. All samples were prepared under an anaerobic atmosphere in a glovebox prior to addition of oxidants. The kinetic data were obtained by monitoring the decay of λ_{max} for each Ni complex with respect to time at 298 K. The average rate constants (k_{obs}) along with their standard deviations were calculated from triplicate runs under identical experimental conditions. An absorbance versus time plot was generated in the Cary 50 Scanning Kinetics program and the data was fit according to the equation $y = (A_0 - A_\infty)e^{-kt} + A_\infty$ where y is the absorbance at λ_{max}, A_0 is the absorbance at time = 0, A_∞ is the absorbance when the oxidation reaction is over, t is time (s), and k (or k_{obs}) is the observed pseudo first-order rate constant.

O_2 reactions: After the initial spectrum of a 0.13 mM MeCN solution (3.00 mL total volume) of each Ni complex (**2-6**) was recorded, dry O_2 gas (via passage through a Drierite column) was bubbled through the septum and into the solution

through a long stainless steel syringe needle for 60 s. Assuming saturation, this would afford ~ 60 mol-equiv O_2 with respect to complex (O_2 solubility in MeCN at 298 K: 8.1 ± 0.6 mM).[51] The UV-vis spectra were then recorded every 15 min for a total time of 4 h under an atmosphere of O_2. FTIR data were obtained via evaporation of reaction solvent to dryness (after 4 h for **3**, **5** and **6**; 18 h for **4** and **6**), addition of KBr and fresh MeCN and re-evaporation; suitable pellets were pressed from the dried mixture of products and KBr.

H_2O_2 reactions: After the initial spectrum of a 0.13 mM MeCN solution (3.00 mL total volume) of each Ni complex (**2-6**) was recorded, addition of a 0.100 mL aliquot of an MeCN solution of H_2O_2•urea (81.0 mM, 20 mol-equiv) was added through the septum via syringe needle. The solution was mixed immediately and the resulting UV-vis spectra were recorded every 12 s for 5 min. An identical procedure was performed employing 50% by wt. H_2O_2(aq) and an analogous decay profile was observed with comparable kinetics. No significant changes in the UV-vis spectrum were observed after adding 20 mol-equiv urea to an MeCN solution of the Ni complexes (**2-6**). FTIR data were recorded in a similar fashion to the O_2(g) experiments (H_2O_2(aq) was used since urea would swamp out the FTIR signals from the complex – as a result degradation of the complex due to the presence of H_2O occurs and results in an intense ν_{CO} peak in the carbonyl region due to protonated nmpH_2 ligand).

KO_2 reactions: After the initial spectrum of a 0.13 mM MeCN solution (3.00 mL total volume) of each Ni complex (**2-6**) was recorded, addition of a 0.020 mL aliquot of a THF solution (solubilized with 18-crown-6) of KO_2 (29.7 mM, 12 mol-

equiv) was added and the UV-vis spectrum monitored. The same procedure was utilized in the presence of excess imidazole (10 mol-equiv) added to the solution for complexes **4** and **5**.

X-ray Data Collection and Structure Solution Refinement. Suitable crystals were mounted and sealed inside a glass capillary. All geometric and intensity data were measured at 293 K on a Bruker SMART APEX II CCD X-ray diffractometer system equipped with graphite-monochromatic Mo Kα radiation (λ = 0.71073 Å) with increasing ω (width 0.5° per frame) at a scan speed of 10 s/frame or 15 s/frame controlled by the SMART software package.[52] The intensity data were corrected for Lorentz-polarization effects and for absorption[53] and integrated with the SAINT software. Empirical absorption corrections were applied to structures using the SADABS program.[54] The structures were solved by direct methods with refinement by full-matrix least-squares based on F^2 using the SHELXTL-97 software[55] incorporated in the SHELXTL 6.1 software package.[56] The hydrogen atoms were fixed in their calculated positions and refined using a riding model. All non-hydrogen atoms were refined anisotropically. Perspective views of the complexes were obtained using ORTEP.[57] Crystallographic properties are reported in Table 9.

Table 9. Summary of Crystal Data and Intensity Collection and Structure Refinement Parameters for **2**, **3**, **4** and **5.**

[a] $R_1 = \Sigma| \, |F_o| - |F_c| \, | / \Sigma |F_o|$; [b] $wR_2 = \{\Sigma[w(F_o^2 - F_c^2)^2] / \Sigma[w(F_o^2)^2]\}^{1/2}$.

Parameters	**2**	**3**	**4**	**5**
Formula	$C_{22}H_{32}ClN_3NiOS_2$	$C_{20}H_{37}N_3NiOS_2$	$C_{29}H_{38}N_4NiO_2S_2$	$C_{25}H_{38}N_4NiO_2S_2$
Formula weight	512.79	458.36	597.46	549.42
Crystal system	Triclinic	Monoclinic	Orthorhombic	Orthorhombic
Space group	*P*-1	$P2_1/c$	$P2_12_12_1$	$P2_12_12_1$
Crystal color, habit	red rectangle	red plate	red plate	Red plate
a, Å	9.4268(5)	16.0011(18)	8.4750(5)	11.087(5)
b, Å	9.4493(5)	10.2682(12)	13.1020(5)	13.944(5)
c, Å	15.4461(8)	15.3266(17)	27.3430(5)	17.948(5)
α, deg	89.6870(10)	90.00	90.00	90.00
β, deg	83.5130(10)	110.734(2)	90.00	90.00
γ, deg	66.3710(10)	90.00	90.00	90.00
V, Å^3	1251.26(11)	2355.1(5)	3036(2)	2774.7(18)
Z	2	4	4	4
ρ_{calcd}, g/cm^3	1.361	1.293	1.307	1.315
T, K	293(2)	293(2)	293(2)	293(2)
abs coeff, μ (Mo Kα), mm^{-1}	1.067	1.015	0.808	0.878
θ limits, deg	2.35-30.51	2.41-28.39	2.2-28.3	2.2-27.9
total no. of data	19789	31319	42216	27766
no. of unique data	7601	5893	7540	6625
no. of parameters	271	244	343	307
GOF on F^2	1.037	1.067	1.003	0.940
R_1,[a] %	3.69	3.68	4.60	6.80
wR_2,[b] %	10.18	7.76	9.42	13.78

max, min peaks, e/ Å^3	0.619, -0.697	0.502, -0.355	0.413, -0.268	0.504, -0.718

Electronic Structure Calculations. Supporting theoretical studies were performed by optimizing the geometries of **2-6** using density functional theory (DFT). The OPTX pure exchange functional of Handy and Cohen[58] was used in conjunction with the Lee-Yang-Parr correlation functional;[59] this method is commonly denoted as OLYP. To correctly describe the more diffuse regions of the charge density within each molecule, where the negative charge resides, the large def2-TZVPP basis set[60] was used. In addition to geometry optimizations, the atomic charges and the contributions from each atom to the highest occupied molecular orbital (HOMO) were computed. The geometry optimizations were performed using the QChem3.2[61] package, which also provided atomic charges via its implementation of the natural bond orbital theory software NBO 5.0.[62] The ORCA[63] program was used to obtain orbital compositions within the Löwdin and Mulliken population analysis (MPA) definitions, which yielded essentially identical compositions; for this reason only the Löwdin compositions are reported. Electrostatic potentials were also computed with the ORCA package.

2.9 References

(1) Gale, E. M.; Patra, A. K.; Harrop, T. C. *Inorg. Chem.* **2009**, *48*, 5620.

(2) Gale, E. M.; Narendrapurapu, B. S.; Simmonett, A. C.; Schaefer, H. F., III; Harrop, T. C. *Inorg. Chem.* **2010**, *49*, 7080.

(3) Barondeau, D. P.; Kassmann, C. J.; Bruns, C. K.; Tainer, J. A.; Getzoff, E. D. *Biochemistry* **2004**, *43*, 8038.

(4) Wuerges, J.; Lee, J.-W.; Yim, Y.-I.; Yim, H.-S.; Kang, S.-O.; Carugo, K. D. *Proc. Natl. Acad. Sci. U.S.A.* **2004**, *101*, 8569.

(5) Huang, D.; Deng, L.; Sun, J.; Holm, R. H. *Inorg. Chem.* **2009**, *48*, 6159.

(6) Jenkins, R. M.; Singleton, M. L.; Almaraz, E.; Reibenspies, J. H.; Darensbourg, M. Y. *Inorg. Chem.* **2009**, *48*, 7280.

(7) Harrop, T. C.; Rodriguez, K.; Mascharak, P. K. *Synth. Commun.* **2003**, *33*, 1943.

(8) Shearer, J.; Zhao, N. *Inorg. Chem.* **2006**, *45*, 9637.

(9) Mathrubootham, V.; Thomas, J.; Staples, R.; McCraken, J.; Shearer, J.; Hegg, E. L. *Inorg. Chem.* **2010**, *49*, 5393.

(10) Krüger, H.-J.; Holm, R. H. *Inorg. Chem.* **1987**, *26*, 3645.

(11) Krüger, H.-J.; Peng, G.; Holm, R. H. *Inorg. Chem.* **1991**, *30*, 734.

(12) Mills, D. K.; Reibenspies, J. H.; Darensbourg, M. Y. *Inorg. Chem.* **1990**, *29*, 4364.

(13) Grapperhaus, C. A.; Mullins, C. S.; Kozlowski, P. M.; Mashuta, M. S. *Inorg. Chem.* **2004**, *43*, 2859.

(14) Adman, E.; Watenpaugh, K. D.; Jensen, L. H. *Proc. Natl. Acad. Sci. U.S.A.* **1975**, *72*, 4854.

(15) Kato, M.; Okamura, T.; Yamamoto, H.; Ueyama, N. *Inorg. Chem.* **2005**, *44*, 1966.

(16) Ariyananda, P. W. G.; Kieber-Emmons, M. T.; Yap, G. P. A.; Riordan, C. G. *Dalton Trans.* **2009**, 4359.

(17) Chiou, S.-J.; Riordan, C. G.; Rheingold, A. L. *Proc. Natl. Acad. Sci. U.S.A.* **2003**, *100*, 3695.

(18) Morlok, M. M.; Janak, K. E.; Zhu, G.; Quarless, D. A.; Parkin, G. *J. Am. Chem. Soc.* **2005**, *127*, 14039.

(19) Ueyama, N.; Yamada, Y.; Okamura, T.; Kimura, S.; Nakamura, A. *Inorg. Chem.* **1996**, *35*, 6473.

(20) Grapperhaus, C. A.; Darensbourg, M. Y. *Acc. Chem. Res.* **1998**, *31*, 451.

(21) Mullins, C. S.; Grapperhaus, C. A.; Kozlowski, P. M. *J. Biol. Inorg. Chem.* **2006**, *11*, 617.

(22) Fiedler, A. T.; Bryngelson, P. A.; Maroney, M. J.; Brunold, T. C. *J. Am. Chem. Soc.* **2005**, *127*, 5449.

(23) Harrop, T. C.; Mascharak, P. K. *Coord. Chem. Rev.* **2005**, *249*, 3007.

(24) Colpas, G. J.; Kumar, M.; Day, R. O.; Maroney, M. J. *Inorg. Chem.* **1990**, *29*, 4779.

(25) Fox, S.; Wang, Y.; Silver, A.; Millar, M. *J. Am. Chem. Soc.* **1990**, *112*, 3218.

(26) Hanss, J.; Krüger, H.-J. *Angew. Chem., Int. Ed.* **1998**, *37*, 360.

(27) Sawyer, D. T.; Valentine, J. S. *Acc. Chem. Res.* **1981**, *14*, 393.

(28) Perry, J. J. P.; Shin, D. S.; Getzoff, E. D.; Tainer, J. A. *Biochim. Biophys. Acta* **2010**, *1804*, 245.

(29) Jaffé, H. H. *Chem. Rev.* **1953**, *53*, 191.

(30) Farmer, P. J.; Solouki, T.; Mills, D. K.; Soma, T.; Russell, D. H.; Reibenspies, J. H.; Darensbourg, M. Y. *J. Am. Chem. Soc.* **1992**, *114*, 4601.

(31) Font, I.; Buonomo, R.; Reibenspies, J. H.; Darensbourg, M. Y. *Inorg. Chem.* **1993**, *32*, 5897.

(32) Farmer, P. J.; Solouki, T.; Soma, T.; Russell, D. H.; Darensbourg, M. Y. *Inorg. Chem.* **1993**, *32*, 4171.

(33) Tuntulani, T.; Musie, G.; Reibenspies, J. H.; Darensbourg, M. Y. *Inorg. Chem.* **1995**, *34*, 6279.

(34) Buonomo, R. M.; Font, I.; Maguire, M. J.; Reibenspies, J. H.; Tuntulani, T.; Darensbourg, M. Y. *J. Am. Chem. Soc.* **1995**, *117*, 963.

(35) Jackson, T. A.; Karapetian, A.; Miller, A.-F.; Brunold, T. C. *J. Am. Chem. Soc.* **2004**, *126*, 12477.

(36) Grove, L. E.; Xie, J.; Yikilmaz, E.; Miller, A.-F.; Brunold, T. C. *Inorg. Chem.* **2008**, *47*, 3978.

(37) Grove, L. E.; Xie, J.; Yikilmaz, E.; Karapetyan, A.; Miller, A.-F.; Brunold, T. C. *Inorg. Chem.* **2008**, *47*, 3993.

(38) Neupane, K. P.; Gearty, K.; Francis, A.; Shearer, J. *J. Am. Chem. Soc.* **2007**, *129*, 14605.

(39) Shearer, J.; Neupane, K. P.; Callan, P. E. *Inorg. Chem.* **2009**, *48*, 10560.

(40) Smith, J. N.; Shirin, Z.; Carrano, C. J. *J. Am. Chem. Soc.* **2003**, *125*, 868.

(41) Shearer, J.; Dehestani, A.; Abanda, F. *Inorg. Chem.* **2008**, *47*, 2649.

(42) Dey, A.; Green, K. N.; Jenkins, R. M.; Jeffrey, S. P.; Darensbourg, M. Y.; Hodgson, K. O.; Hedman, B.; Solomon, E. I. *Inorg. Chem.* **2007**, *46*, 9655.

(43) Perdew, J. P.; Levy, M. *Phys. Rev. B* **1997**, *56*, 16021.

(44) Mirza, S. A.; Pressler, M. A.; Kumar, M.; Day, R. O.; Maroney, M. J. *Inorg. Chem.* **1993**, *32*, 977.

(45) Mirza, S. A.; Day, R. O.; Maroney, M. J. *Inorg. Chem.* **1996**, *35*, 1992.

(46) Bobadova-Parvanova, P.; Galabov, B. *J. Phys. Chem. A* **1998**, *102*, 1815.

(47) Galabov, B.; Bobadova-Parvanova, P. *J. Phys. Chem. A* **1999**, *103*, 6793.

(48) Harrop, T. C.; Olmstead, M. M.; Mascharak, P. K. *Chem. Commun.* **2003**, 410.

(49) Fulmer, G. R.; Miller, A. J. M.; Sherden, N. H.; Gottlieb, H. E.; Nudelman, A.; Stoltz, B. M.; Bercaw, J. E.; Goldberg, K. I. *Organometallics* **2010**, *29*, 2176.

(50) Rao, P. V.; Bhaduri, S.; Jiang, J.; Holm, R. H. *Inorg. Chem.* **2004**, *43*, 5833.

(51) Achord, J. M.; Hussey, C. L. *Anal. Chem.* **1980**, *52*, 601.

(52) *SMART: Software for the CCD Detector System, v5.626*; Bruker AXS: Madison, WI, 2000.

(53) Walker, N.; Stuart, D. *Acta Crystallogr.* **1983**, *A39*, 158.

(54) Sheldrick, G. M. *SADABS: Area Detector Absorption Correction*; University of Göttingen: Göttingen, Germany, 2001.

(55) Sheldrick, G. M. *Program for Refinement of Crystal Structures*; University of Göttingen: Göttingen, Germany, 1997.

(56) Sheldrick, G. M. *SHELXTL 6.1, Crystallographic Computing System*; Siemans Analytical X-Ray Instruments: Madison, WI, 2000.

(57) Johnson, C. K. *ORTEP-III, Report ORNL - 5138*; Oak Ridge National Laboratory: Oak Ridge, TN, 1976.

(58) Cohen, A. J.; Handy, N. C. *Mol. Phys.* **2001**, *99*, 607.

(59) Lee, C.; Yang, W.; Parr, R. G. *Phys. Rev. B* **1988**, *37*, 785.

(60) Weigend, F.; Ahlrichs, R. *Phys. Chem. Chem. Phys.* **2005**, *7*, 3297.

(61) Shao, Y.; Molnar, L. F.; Jung, Y., et al. *Phys. Chem. Chem. Phys.* **2006**, *8*, 3172.

(62) Glendening, E. D.; Badenhoop, J. K.; Reed, A. E.; Carpenter, J. E.; Bohmann, J. A.; Morales, C. M.; Weinhold, F. *NBO 5.0.*; Theoretical Chemistry Institue, University of Wisconsin: Madison, WI, 2001.

(63) Neese, F. *ORCA - an ab initio, Density Functional and Semiempirical Program Package, version 2.7*; University of Bonn: Bonn, Germany, 2009.

CHAPTER 3

WATER SOLUBLE MODELS OF Ni-SOD_{RED}: SOLVENT EFFECTS ON THE COORDINATION CHEMISTRY OF DIPEPTIDE MODELS[1]

[1] Gale, E. M., Cowart, D. M., Scott, R. A., Harrop, T. C. *Inorg. Chem*. **2011**, *50*, 10460. Reprinted here with permission of publisher.

3.1 Abstract

We have utilized the tri-dentate N_2S-chelate NH_2-Gly-L-Cys-OMe (GC-OMeH_2, where Hs represents dissociable protons) in order to provide an electronically accurate mimic of the His1Cys2 chelate of Ni-SOD$_{red}$. The model complexes employing this ligand were also water soluble/stable and allowed for examination of the properties of Ni-complexes analogous to the Ni-SOD$_{red}$ active site under pseudo-physiologically relevant conditions when stripped of macromolecular surroundings. A mono-dentate thiolate ligand was employed to model Cys6. This exogenously added RS^- ligand could be readily manipulated through the various synthetic protocols introduced in Chapter 2. The physical properties of these model complexes were probed by ^{1}H NMR, UV-vis and cyclic voltammetry measurements and revealed differing behavior between polar aprotic solvent vs. pH 7.5 buffer. While our model complexes remained as monomeric [Ni(GC-OMe)(SR)]$^-$ species in polar aprotic solvent, the mono-dentate thiolate ligand became labile upon dissolution in water and oligomeric species, presumably connected through S,S'-bridging interactions, became the predominant form of speciation. Interestingly, the monomeric species could be reformed under aqueous conditions by titrating in a small excess of exogenous RS^-. The degree of thiolate lability at pH 7.5 can be loosely correlated to the basicity of the RS^- ligand. These results highlight a stabilizing role of the Ni-SOD$_{red}$ protein architecture. Furthermore, our observations are discussed in terms of d^8 (S = 0) ligand exchange mechanisms and suggest that binding of additional ligands to Ni-SOD$_{red}$ can be triggered by subtle perturbations to the coordinated cysteinates.

3.2 Introduction

The models studied in Chapter 2 served to shed insights pertaining to the structural, electronic and reactivity properties imparted via electronic modulations of the ligand modeling Cys6.[1-2] The results provided compelling evidence in support of a hypothesis implicating S-directed hydrogen-bonding as a mechanism of preventing S-based redox of Ni-SOD_{red}. Study of the systems, however, was limited to aprotic organic solvents, as these complexes were generally insoluble and unstable in water.

Presented in this chapter is a modified, peptide-based system similar in many ways to that discussed in Chapter 2 but of a water soluble and stable nature, allowing for study under more physiologically relevant conditions. The modular approach to the ligand components modeling Cys6 can still be applied to this new model system. The study discussed below was conceived as a unique opportunity to study well defined, isolable models utilizing definitive small molecule characterization techniques under aqueous conditions which have been otherwise utilized only for the Ni-polypeptide systems discussed in Chapter 1. In depth study of the behavior of this new library in both polar aprotic and aqueous media provided insights into the dynamic nature of electronically accurate models of Ni-SOD_{red} when stripped of the protein surroundings.[3]

3.3 Ligand Design and Preparation of Complexes of Formula [Ni(GC-OMe)(SR)]$^-$

The tridentate chelate employed in this study was the dipeptide-based ligand NH_2-Gly-Cys-OMe (abbreviated GC-$OMeH_2$, where H represents dissociable

protons) (Figure 1). This ligand identically reproduces the coordinative contributions afforded by His1 and Cys2 to Ni-SOD_{red}.[4-5] The ligand could be obtained in three steps by established peptide coupling techniques (Scheme 1). First, S-protection of L-cysteine methyl ester using the trityl group was achieved in 81% yield. Next, addition of BOC-Gly-OSu (BOC = ^{t}butoxycarbonyl) to this protected L-cysteine derivative afforded the pre-ligand BOC-Gly-Cys-(S-trityl)-OMe in 85% yield. Finally, removal of the N-BOC and S-trityl protecting groups with TFA afforded GC-$OMeH_2$•TFA as a white solid in 74% yield.

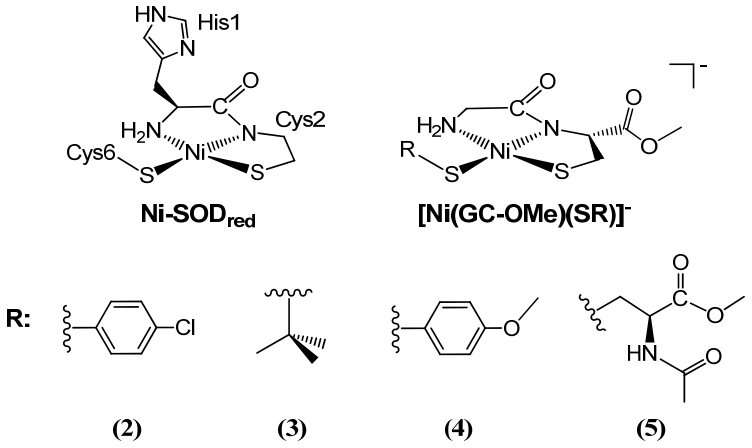

Figure 1. (Top): Active site of Ni-SOD_{red} (left) and analogue system presented in this chapter (right). (Bottom): R groups used in this study (RSH = 4-chlorobenzenethiol (**2**), HS^{t}Bu (**3**), 4-methoxybenzenethiol (**4**) and *N*-acetyl-L-cysteine methyl ester (**5**)).

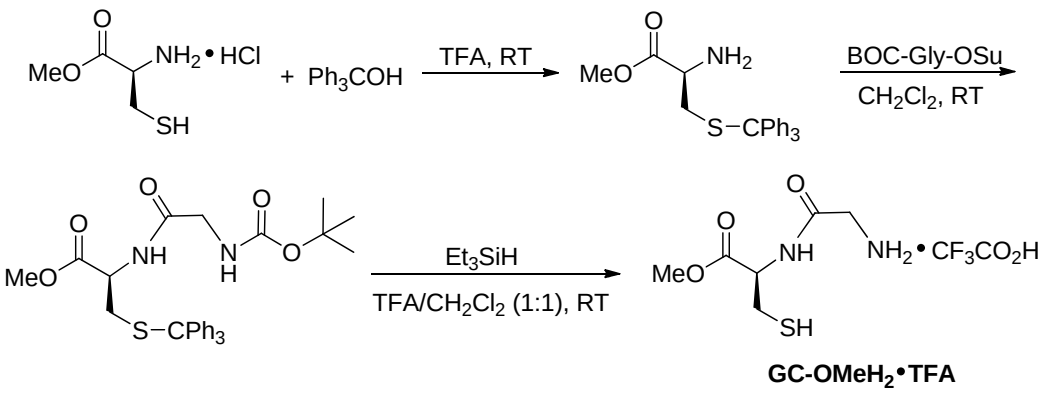

Scheme 1. Synthesis of GC-OMeH$_2$•TFA.

Addition of one mol-equiv. each Ni(OAc)$_2$•4H$_2$O and NaOAc to GC-OMeH$_2$•TFA in MeOH at RT afforded orange colored solutions from which peach solids were isolated. The solids were formulated as [Ni$_2$(GC-OMe)$_2$]•TFA•2H$_2$O (**1**•TFA•2H$_2$O) by elemental microanalysis. Heating **1**•TFA•2H$_2$O at 50 °C in MeOH for 16 h precipitated product formulated as [Ni$_2$(GC-OMe)$_2$] (**1**) as analytically pure pink solids. Complex **1** is relatively insoluble in both polar aprotic and polar solvents, consistent with the S,S'-bridging nature and similar to that observed for the dimeric synthon [Ni$_2$(nmp)$_2$] (see Chapter 2). Prolonged stirring of **1** in water eventually resulted in orange solutions, which afforded identical UV-vis (pH 7.5 buffer) and ^{1}H NMR (D$_2$O) spectral profiles similar to that observed for **1**•TFA•2H$_2$O. It appears that despite the differences in composition of the species isolated, those formulated as **1** and the corresponding aquated, TFA adduct are of a similar disposition in solution, with TFA likely dissociating from **1**•TFA•2H$_2$O in water. ESI-MS analysis of **1** revealed various species corresponding to [Ni$_n$(GC-OMe)$_n$ + H]$^+$ (n = 2-4), suggesting that various permutations of 1:1 Ni/GC-OMe stoichiometry are present upon

dissolution. Despite this, the ^{1}H NMR data revealed a chemical equivalency amongst any species present, as only one signal per GC-OMe^{2-} proton is observed (Figure 2).

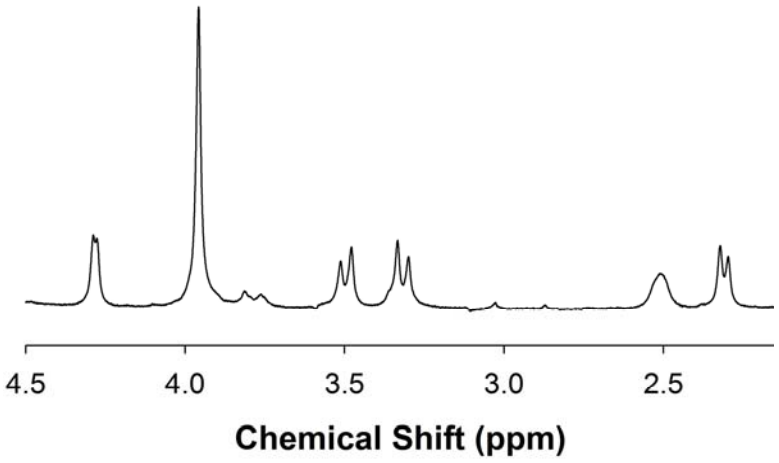

Figure 2. ^{1}H NMR of **1** in D_2O.

Complex **1** can also be obtained via spontaneous metalation with Ni(II) salts in buffer at pH 7.5. However, deprotonation of GC-OMeH_2•TFA with a strong base such as NaH in MeCN led only to formation of intractable brown solids upon metalation. The precise composition of this species was not determined, but FTIR analysis revealed loss of the methyl ester functional group. It appears that incorporation of Ni(II) into the GC-OMe ligand frame is facile and need not be assisted by strong base. This is analogous to the metalation observed at the Ni-hook motif of Ni-SOD, which occurs spontaneously under neutral conditions despite the highly basic nature of the Cys2 carboxamido-N ligand.[6-8]

Addition of two mol-equiv. of the K^+ salts of 4-chlorobenzenethiolate (KSC_6H_4-*p*-Cl), ^{t}butyl thiolate ($KS^{t}Bu$) and 4-methoxybenzenethiolate (KSC_6H_4-*p*-OMe) to **1** in DMF afforded K[Ni(GC-OMe)(SC_6H_4-*p*-Cl)] (**2**), K[Ni(GC-OMe)($S^{t}Bu$)] (**3**) and K[Ni(GC-OMe)(SC_6H_4-*p*-OMe) (**4**), respectively, in 87-90%

yields (Scheme 2). The pK_a driven thiol/coordinated thiolate and redox driven disulfide/coordinated thiolate exchange procedures outlined in Chapter 2.2 could analogously be applied to the current models at hand. In fact, K[Ni(GC-OMe)(S-NAc)] (HS-NAc = *N*-acetyl-L-cysteine methyl ester) (**5**) was obtained in 90% yield via the addition of one mol-equiv. HS-NAc to **3** in DMF. Complex **2** could also be obtained in high yield via the addition of 0.5 mol-equivs. of the disulfide of 4-chlorobenzenethiol to **3**.

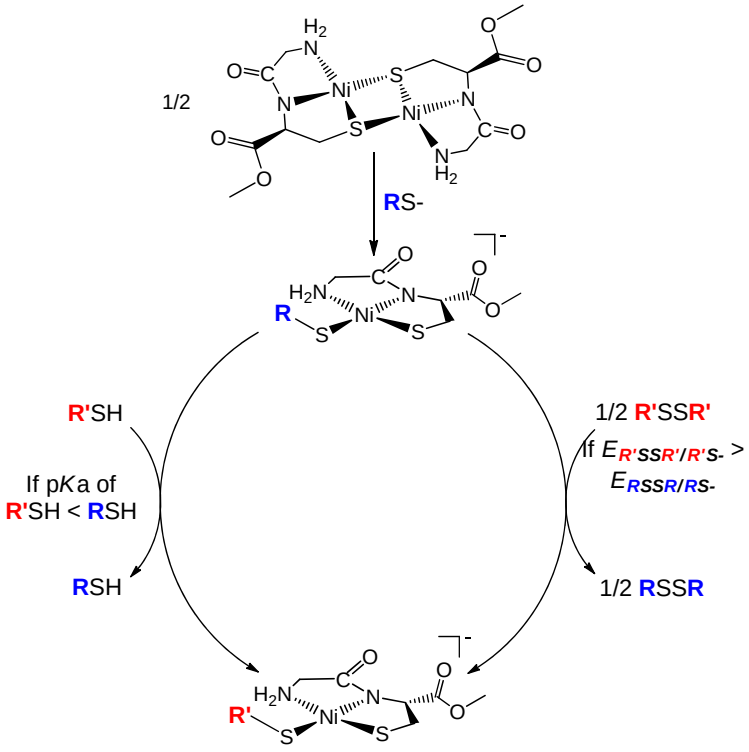

Scheme 2. Synthetic protocols by which complexes of formula [Ni(GC-OMe)(SR)]$^-$ were obtained.

3.4 Structure and Properties

Peptide deprotonation/metallation of the GC-OMe ligand is evidenced in **1**-**5** by a large red-shift in the peptide ν_{CO}. This signature feature is found at 1677 cm^{-1}

(KBr pellet) in GC-OMe•TFA and between 1578 cm^{-1} and 1589 cm^{-1} for **1**-**5**. The ν_{CO} stretch remained relatively constant across the series, and no trends could be correlated to the donor strength of the trans thiolate ligands. Naturally, no peptide-NH stretching frequencies were observed, consistent with this assignment. Ligation of the primary amine functional group could also be observed by the abnormally low energy of the amine ν_{NH} stretches. These features were found between 3042 cm^{-1} and 3108 cm^{-1} for **1**-**5**, whereas the ν_{NH} stretches of unligated primary amines are generally found at values of 3250 cm^{-1} and above.[9]

Attempts at obtaining **1**-**5** as single crystals were unsuccessful. Despite this, we were able to utilize Ni K-edge X-ray absorption spectroscopy (XAS) as a means of acquiring valuable structural information. Complexes **2** and **5** were chosen for characterization as representative examples and compared against [Ni(nmp)(SC_6H_4-*p*-Cl)]$^-$, [Ni(nmp)(S^{t}Bu)]$^-$ and [Ni(nmp)(S-*o*-babt)]$^-$, for which we have both crystallographic (See Chapter 2 for X-ray parameters) and XAS data (Figure 3 for relevant XAS data for **2** and **5**; see Table 1 for tabulation of relevant XAS parameters). As observed for complexes from the [Ni(nmp)(SR)]$^-$ series, the XAS spectra were consistent with Ni(II) systems of approximately square-planar coordination geometry. This assignment was further confirmed by analysis of the XANES region of the spectra, as **2** and **5** display intense pre-edge features corresponding to a 1s→4p_z transition at ~8336 eV, also characteristic of Ni(II) in pseudo-D_{4h} symmetry. Also consistent with the [Ni(nmp)(SR)]$^-$ series, the EXAFS region of **2** and **5** are best fit with two non-equivalent Ni-N scatterers. The non-equivalent Ni-N bond lengths of **2** and **5** are measured at 1.83(3) Å and 1.96(3) Å;

assigned as the Ni-$N_{peptide}$ and Ni-N_{amine} bonds, respectively. Two Ni-S scatterers averaging 2.16 Å are present as well, and complete the NiN_2S_2 coordination environment. The Ni-N and Ni-S bond distances measured compare well with those determined for the $[Ni(nmp)(SR)]^-$ series, as well as those observed in Ni-SOD_{red} by both EXAFS[7] and X-ray crystallography.[4-5]

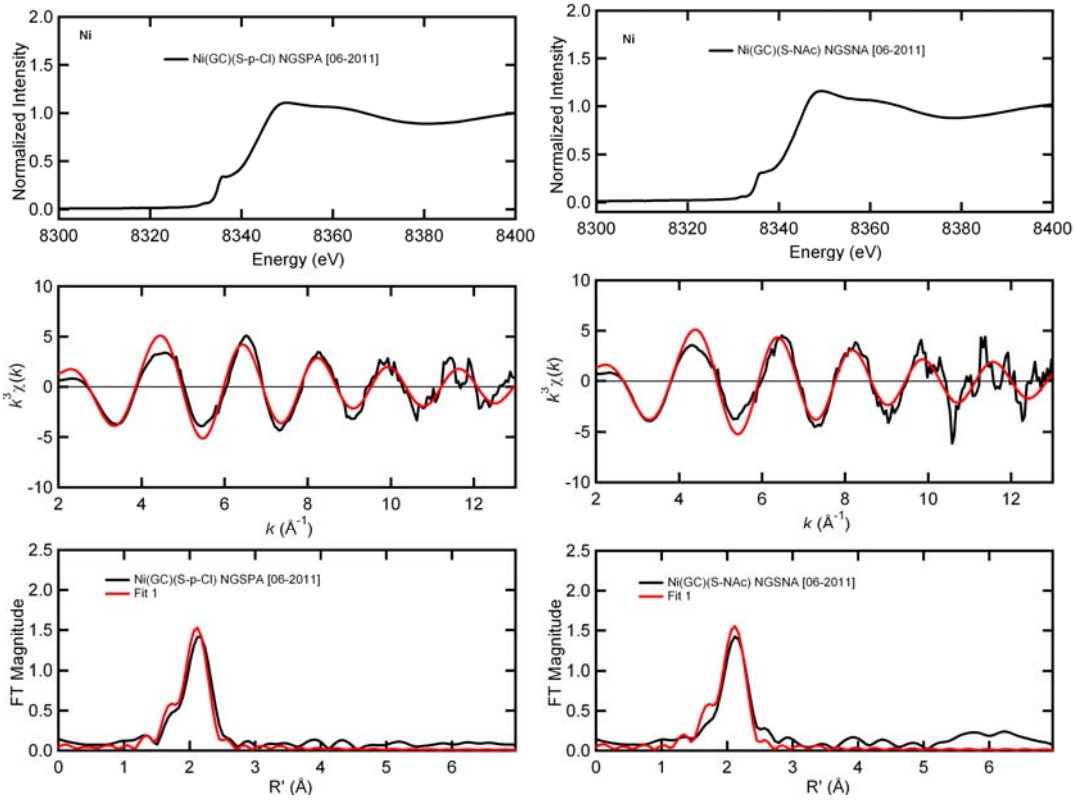

Figure 3. Ni K-edge X-ray absorption data for K[Ni(GC-OMe)(S-*p*-C_6H_4Cl)] (**2**) (left) and K[Ni(GC-OMe)(S-NAc)] (**5**) (right). (*Top*): Edge spectra displaying Ni (1s → $4p_z$) transition consistent with square-planar Ni(II). (*Middle*): EXAFS data. (*Bottom*): FT k^3 EXAFS data. Experimental data are in black with simulations in red.

Table 1. Ni-K-Edge X-ray absorption parameters for complexes **2** and **5** and $[Ni(nmp)(SR)]^-$ complexes (see Chapter 2). Shell is the chemical unit defined for the multiple scattering calculation. R_{as} is the metal-scatterer distance. σ_{as}^2 is a mean square deviation in R_{as}. f' is a normalized error (chi-squared):

$$f' = \frac{\left\{ \sum_i \left[k^3 \left(\chi_i^{obs} - \chi_i^{calc} \right) \right]^2 / N \right\}^{1/2}}{\left[\left(k^3 \chi^{obs} \right)_{max} - \left(k^3 \chi^{obs} \right)_{min} \right]}$$

Complex	*n*	shell	R_{as} (Å)	σ_{as}^2 (Å^2)	*f'*	E_o (eV)	pre-edge peak (eV)	intensity
K[Ni(GC-OMe)(SC_6H_4-*p*-Cl)] (**2**)	1	Ni-N	1.83	0.0024	0.088	8340	8335.8	0.31
	1	Ni-N	1.99	0.0024				
	2	Ni-S	2.16	0.0059				
K[Ni(GC-OMe)(S-NAc)] (**5**)	1	Ni-N	1.83	0.0024	0.100	8340	8335.7	0.34
	1	Ni-N	1.99	0.0024				
	2	Ni-S	2.17	0.0052				
K[Ni(nmp)(SC_6H_4-*p*-Cl)]	1	Ni-N	1.85	0.0024	0.075	8340	8337.6	0.42
	1	Ni-N	1.97	0.0024				
	2	Ni-S	2.16	0.0045				
(Et_4N)[Ni(nmp)(S-*o*-babt)]	1	Ni-N	1.86	0.0024	0.061	8340	8336.5	0.42
	1	Ni-N	1.96	0.0024				
	2	Ni-S	2.17	0.0028				
K[Ni(nmp)(S^{t}Bu)]	1	Ni-N	1.85	0.0024	0.076	8340	8336.4	0.35
	1	Ni-N	1.97	0.0024				
	2	Ni-S	2.16	0.0051				

Complex **1** is indefinitely air stable in aqueous solution as evidenced by ^{1}H NMR and UV-vis (pH 7.5) (see below for further discussion), consistent with the formulated S,S'-bridging nature. Aqueous solutions of **2**, **4** and **5** become cloudy over

prolonged periods (> 6 h) of atmospheric O_2 exposure but remain stable for up to 16 h under anaerobic conditions. No evidence for ligand protonation or ester hydrolysis is observed, in contrast to prior reported small molecule Ni(II)N_2S_2 complexes.[10] However, during re-crystallization attempts under various conditions (different solvent, cation), solutions of **2** (when balanced by Et_4N^+ cation) would deposit single crystals with unit cell parameters matching that of $(Et_4N)_2[Ni(SC_6H_4\text{-}p\text{-}Cl)_4]$ (Figure 4) as large blocks (the structure shown was solved from the re-crystallization byproduct of earlier studies employing a similarly disposed mimic of Ni-SOD_{red}; see appendix B). However, formation of this complex does not appear to be a significant contributor to the overall speciation, as no spectral evidence[11-12] of this species is observed over similar time periods. Thus, complexes **2-5** serve as suitably stable models of Ni-SOD_{red} amenable to facile characterization by standard small molecule techniques.

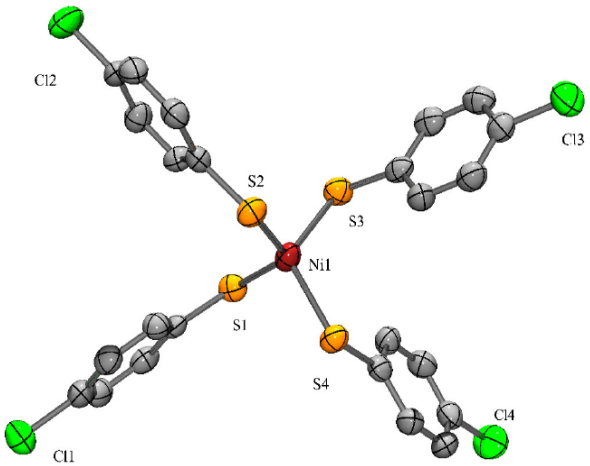

Figure 4. ORTEP diagram of the anion of $(Et_4N)_2[Ni(SC_6H_4\text{-}p\text{-}Cl)_4]$, a minor byproduct formed during various attempts at re-cyrstallization of (Et_4N)[Ni(GC-OMe)$(SC_6H_4\text{-}p\text{-}Cl)$] (**$(Et_4N)_2$•2**), showing 50% thermal ellipsoids for all non-hydrogen atoms.

The d^8 square-planar ($S = 0$) nature of **1-5** in solution is evidenced by the ^1H NMR spectra acquired. Analysis of the spectra corresponding to **2-5** in polar aprotic solvents such as CD_3CN and polar protic solvents like D_2O reveal divergent behaviors between the two media. The ^1H NMR spectra of **2-5** in CD_3CN at 298 K afforded neat, well resolved peaks consistent with the presence of one defined species, as observed for the $[Ni(nmp)(SR)]^-$ series. Contrary to the well defined spectra observed in CD_3CN, the D_2O spectra of as-isolated **2-5** provided broad, ill-resolved signals. Interestingly, titration of one mol-equiv. of the corresponding monodentate thiolate to solutions of **2-5** imparted well resolved spectra analogous to that observed in CD_3CN (see Figure 5 for a representative example).

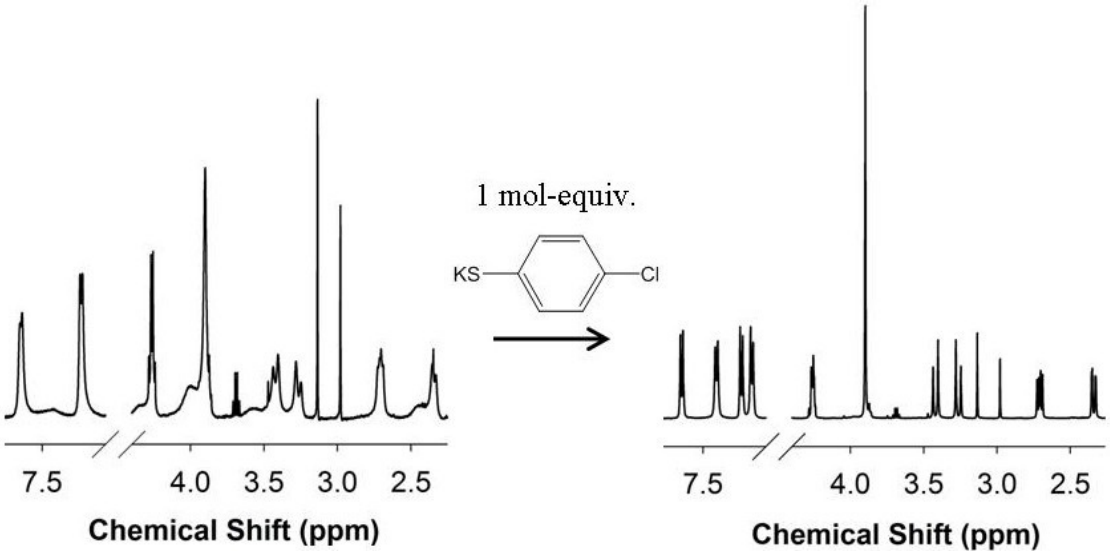

Figure 5. ^1H NMR spectrum of **2** recorded in D_2O under different conditions at 298 K. (Left): As-isolated **2** (signals at 3.01 and 2.85 ppm correspond to associated DMF from the reaction solvent). (Right): Complex **2** after the addition of one mol-equiv of KSC_6H_4-*p*-Cl (doublets at 7.41 and 7.19 correspond to non-coordinated KSC_6H_4-*p*-Cl).

The poorly resolved spectra observed upon dissolution of as-isolated **2-5** in D_2O is likely due to formation of an equilibrium mixture of Ni(II) species; most probably due to dissociation of the monodentate thiolate ligand and formation of $[Ni(GC\text{-}OMe)(OH_2)_x]$, or oligomeric species such as $[Ni_x(GC\text{-}OMe)_x]$ or $[Ni_x(GC\text{-}OMe)_x(SR)_y]$. Indeed, ESI-$MS^-$ analysis of **2** and **4** dissolved in protic solvent (MeOH) revealed ions corresponding to $[Ni_n(GC\text{-}OMe)_n(SR)]^-$ and $[Ni_n(GC\text{-}OMe)_n - H]^-$ (n = 2-4) along with the parent ion. Similarly, a species consistent with $[Ni_2(GC\text{-}OMe)_2(S\text{-}NAc)]^-$ and $[Ni_n(GC\text{-}OMe)_n - H]^-$ were found along with the parent anion of **5**. Interestingly, neither the parent ion of **3** or any derivative species containing ^{t}BuS$^-$ are observed via ESI-MS^- (the same is true for $[Ni(nmp)(S^tBu)]^-$; despite the fact that all other $[Ni(nmp)(SR)]^-$ species are observed).

The multinuclear speciation observed upon dissolution in protic solvent is indicative of dynamic behavior involving dissociation of the monodentate thiolate ligand, possible S,S'-bridging interactions and/or aquation of the Ni complexes. Similarly, models involving Ni(II)-polypeptide maquettes have been shown to exist as an equilibrium mixture of 1:1 Ni/peptide and 2:1 Ni/peptide by UV-vis titrations, while ESI-MS revealed species of 1:2 Ni/peptide composition.[13] It appears that 1:1 mixutres of Ni/L species (L = N/S-containing ligand of denticity ≤ 3) are likely to form multiple species under protic conditions.

The UV-vis spectra of **2-5** in DMF at 298 K (**1** is insoluble) are characterized by two broad features in the visible region arising at ~470 nm and ~550 nm, consistent with the red to violet color of these complexes (Figure 6 (left), Table 2). The ~470 nm band is the most intense visible feature and ranges from 463 nm (ε =

350 M^{-1} cm^{-1}) for **5** to 484 nm (ε = 440 M^{-1} cm^{-1}) for **3**. The lower energy feature is a bit less intense in nature and is found between 543 nm (ε = 160 M^{-1} cm^{-1}) for **5** and 570 nm (ε = 230 M^{-1} cm^{-1}) for **3**. Similar transitions have been observed in prior characterized Ni(II)N_2S_2 complexes[14-22] and mirror those observed in Ni-SOD_{red}.[23] The absorption bands are believed to be ligand-field in nature with some minor charge-transfer contribution.[23] Furthermore, complexes **3** and **5** possess a high energy shoulder at 358 nm (ε = 1,400 M^{-1} cm^{-1} for **3**; 1,200 M^{-1} cm^{-1} for **5**) that reflects a similar feature observed in the reduced enzyme at 361 nm (ε = 880 M^{-1} cm^{-1}). Whether or not such a feature exists in **2** and **4** cannot be discerned due to the presence of an overwhelmingly large UV band, presumably π-π* in nature. Taken together, comparison of the electron absorption transitions observed for **2-5** with those of Ni-SOD_{red} highlight the electronically similar dispositions between our models and the reduced enzyme active site.

The UV-vis spectra of **1-5** at pH 7.5 (PIPES buffer) at 298 K (Figure 6 (right), Table 2) are largely similar to that observed in DMF, indicative that the various species which may be present under these conditions are of similar electronic disposition to those observed in DMF. It must be noted, however, that identical UV-vis profiles are observed for **1** and **3**, presumably due to full dissociation of $^{t}BuS^{-}$ from **3**/reformation of **1**. The more prominent visible feature ranges from 458 nm (ε = 285 M^{-1} cm^{-1}/Ni) for **1** to 471 nm (ε = 430 M^{-1} cm^{-1}) for **2**. The lower energy feature is found between 545 nm (ε = 140 M^{-1} cm^{-1}) for **5** and 560 nm (ε = 240 M^{-1} cm^{-1}) for **2**, although this band is less defined than what is observed in DMF. A high energy

feature is observed at 338 nm for **1** and **3** (ε = 2, 240 M^{-1} cm^{-1}/Ni) and **5** (ε = 1,200 M^{-1} cm^{-1}) (Figure 7).

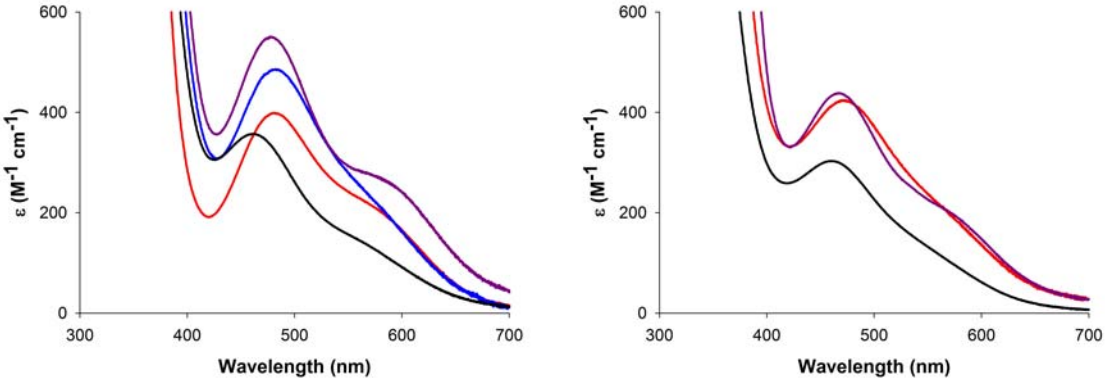

Figure 6. Ligand-field transitions arising from **2** (red), **3** (blue), **4** (purple) and **5** (black) in DMF (left) and from **2**, **4** and **5** (same color scheme) in pH 7.5 PIPES buffer (right) recorded at 298 K.

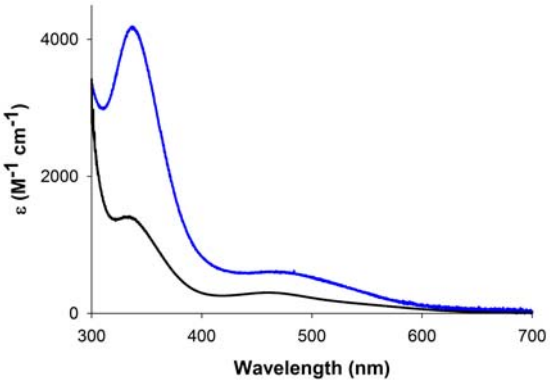

Figure 7. UV-vis spectra of **1** (**3** affords an identical spectrum, blue) and **5** (black) in pH 7.5 PIPES buffer recorded at 298 K.

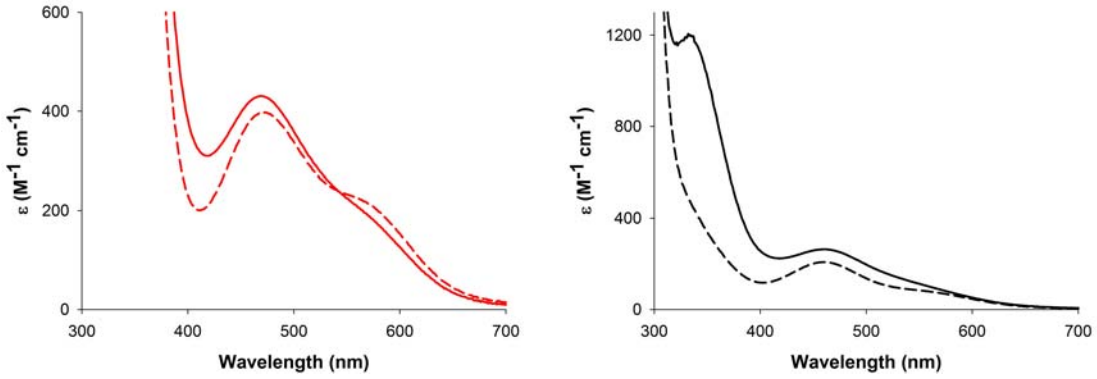

Figure 8. UV-vis spectra showing **2** (left, red) and **5** (right, black) before (solid line) and after addition of one mol-equiv. of the corresponding monodentate KSR ligand (dashed lines) in pH 7.5 PIPES buffer at 298 K.

As discussed above, the RS^- ligands of **2-5** are labile under aqueous conditions. Taking note of the aforementioned ^1H NMR experiments, one mol-equiv of the appropriate KSR were titrated into the UV-vis samples of **2-5**. In the case of **2** and **4**, only subtle changes were observed. Specifically, the broad lower energy visible feature took up a more defined nature and the two visible features became more distinguishable (Figure 8 (left) shows **2** as a representative example). Addition of one mol-equiv. KS-NAc (or HS-NAc) to **5** resulted in a similar re-definition of the visible portion of the absorption spectra (Figure 8, right). More noticeably, however, the ~338 nm feature disappeared from the spectra of **5**, and the resultant profile looked akin to that observed in DMF. It is likely that this high energy feature was due to partial formation **1** or some similar oligomeric species. No such results were observed upon titration of KS^{t}Bu into **3**. In fact, addition of up to five mol-equiv. of

KS^{t}Bu afforded no change to the UV-vis profile suggesting that ^{t}BuS$^-$ is highly labile at pH 7.5.

The UV-vis spectra of **5** recorded at pH 9.3 (CHES buffer), appeared more like that observed in DMF or in the addition of one mol-equiv NAc-S$^-$ in pH 7.5 buffer. This pH dependency on Ni-complex speciation supports proton-assisted dissociation of RS$^-$. The fact that the pH 9.3 spectra of **3** is still identical to that observed for **1** suggests that the degree by which this process occurs may be contingent upon the relative basicity of the exogenously added thiolate ligand.

It is also worth noting that the visible bands of **2** and **4** at pH 7.5 are blue-shifted ~10 nm relative to that observed in DMF. Interestingly, the λ_{max} of **5** does not shift at all. An attractive explanation is that intramolecular interactions between the peptide NH and thiolato-S are present in DMF and approximate the hydrogen-bonding interactions between the thiolates and aqueous solvent. In fact, the presence of intramolecular NH•••S bonding is supported by the large downfield shift of the peptide-NH of HS-NAc upon Ni-coordination observed in the ^{1}H NMR spectrum (7.43 ppm to 8.62 ppm) recorded in CD_3CN (see Chapter 2, Table 2).

Table 2. Spectroscopic (UV-vis) and electrochemical (CV) properties of **2-5** in the listed solvents in comparison to Ni-peptide maquettes and Ni-SOD_{red}. [a]UV-vis and CV (E_{ox} reported) recorded at 298 K; spectra recorded in pH 7.5 PIPES buffer, CV recorded in pH 7.4 phosphate buffer. [b]M1 = H_2N-HCDLPCGVYDPA-CO_2H;[28] UV-vis and CV recorded at RT in pH 7.2 phosphate buffer (quasi-reversible $E_{1/2}$ reported on a sample immobilized as a thin-film; 0.1 M NaCl electrolyte). [c]M2 = H_2N-HCDLPCG-CO_2H;[24] UV-vis and CV recorded at RT in pH 7.4 NEM buffer (quasi-reversible $E_{1/2}$ reported on a sample immobilized as a thin-film; 0.1 M $NaClO_4$ electrolyte).[24] [d]Redox titration recorded on Ni-SOD from *S. coelicolor* at RT in pH 7.5 phosphate buffer ($E_{1/2}$ originally referenced versus NHE = 0.290 V).[25] [e]Complex **3** reverts to dimer **1** in aqueous solutions (see the main text).

Complex	**λ_{max}, nm (ε, M^{-1} cm^{-1}) in DMF**	**λ_{max}, nm (ε, M^{-1} cm^{-1}) at pH 7.5**	***E* (mV vs. Ag/AgCl) in DMF**	***E* (mV vs. Ag/AgCl) at pH 7.4**
2[a]	481 (390) 560 (230)	471 (430) 560 (240)	220	285
3[a]	484 (440) 570 (230)	N/A[e]	80	N/A[e]
4[a]	480 (500) 565 (200)	467 (400) 550 (230)	170	315
5[a]	463 (350) 545 (160)	464 (300) 545 (140)	310	550
$[Ni(SOD^{M1})]$[b]	N/A	458 (510) 552 (240)	N/A	700
$[Ni(SOD^{M2})]$[c]	N/A	457 (350) 548 (130)	N/A	520
$Ni\text{-}SOD_{red}$[d]	N/A	450 (480) 543 (150)	N/A	487

Cyclic voltammetry (CV) measurement of **2-5** in DMF (Figure 9, left) revealed irreversible oxidation events consistent with either instability of the Ni(III) state or S-based redox, and subsequent structural changes upon oxidation. Independent measurement of the KSR corresponding to **2-5** revealed distinct

oxidation potentials, indicative that the redox observed arises from the highly covalent Ni(II)N_2S_2 complexes. Indeed, bulk oxidation studies by stoichiometric treatment with a one-electron oxidant such as ferrocenium hexafluorophosphate resulted in quantitative formation of 0.5 mol-equiv. each of **1** and the disulfide of the corresponding monodentate thiolate ligand. The oxidation potentials (vs. Ag/AgCl) in DMF across the series register at 220 mV for **2**, 80 mV for **3**, 170 mV for **4**, and 310 mV for **5** (Table 2). As observed across the $[Ni(nmp)(SR)]^-$ series, the oxidation potentials reflect the donor strength of the exogenously added thiolate ligand when comparing alkyl- and aromatic-S donors separately.

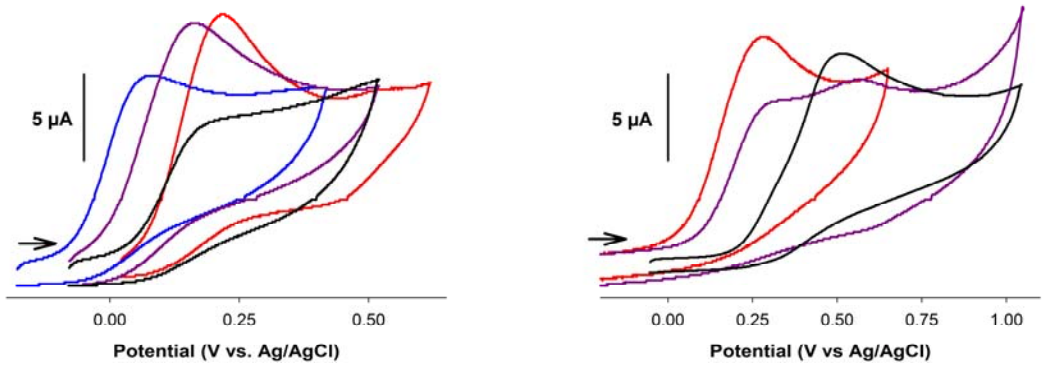

Figure 9. (Left): Cyclic voltammograms (CVs) of 5 mM solutions of **2** (red), **3** (blue), **4** (purple) and **5** (black) (vs. Ag/Ag^+ in DMF, 0.1 M $^n Bu_4NPF_6$ supporting electrolyte, glassy carbon working electrode, scan rate: 100 mV/s, RT). (Right): CVs of 5 mM solutions of **2**, **4** and **5** (vs. Ag/AgCl in pH 7.4 phosphate buffer, 0.5 M KNO_3 supporting electrolyte, glassy carbon working electrode, scan rate: 100 mV/s, RT). The CV of **5** in buffer was scaled down (33%). Arrow indicates direction of scan.

The oxidation potentials of **2**, **4** and **5** at pH 7.4 (phosphate buffer) are also irreversible and measure at 285 mV, 315 mV and 550 mV, respectively (Figure 9 (right), Table 2). These potentials fall near the midpoint of the electrochemical window defined by the SOD half reactions (-0.04 – 1.09 V),[26-27] but clearly these complexes lack the requisite stabilization to serve as effective SOD catalysts. Accordingly, no protection against $O_2^{\bullet-}$ affected NBT reduction to formazan (see Chapter 1) is afforded by **2**-**5** at pH 7.5. Interestingly, it appears that amongst **2** and **4**, the complex possessing the more weakly donating RS^- ligand is more difficult to oxidize under these conditions. Due to full dissociation of ^{t}BuS$^-$ under these conditions, no comparison between **3** and **5** is available (complex **1** shows no redox event between 0 and 1 V). It should be noted that the CV measurements of **4** revealed the presence of a second oxidation event at 500 mV (Figure 8, left) which corresponds to that observed upon independent oxidation of KSC_6H_4-*p*-OMe, providing support for thiolate dissociation in model complexes featuring aromatic-S donors. Analyzing the differences in oxidation potentials of these models in DMF and pH 7.4 buffer reflect cathodic shifts of 65 mV, 145 mV and 220 mV for **2**, **4** and **5**, respectively. This trend seems to correlate to relative RS^- basicity.

The above electrochemical observations suggest that hydrogen-bonding interactions between coordinated thiolates and solvent protons likely serve to stabilize the model complexes in a manner similar to that outlined in Chapter 2. Furthermore, this effect seems to become more pronounced with increased RS^- donor strength. However, a delicate balance must be maintained, as strong hydrogen-bonding interactions also affect ligand lability, likely through charge neutralization effects.

Together, these observations strongly favor a scenario by which hydrogen-bonding interactions between the thiolate ligands and solvent dictate the disposition of our Ni-SOD_{red} models under aqueous conditions. These results stand in sharp contrast to a prior S L-edge XAS/DFT study by Darensbourg and Solomon which argues that hydrogen-bonding between coordinated thiolates and water does not actively affect the bonding and physical properties of $Ni(II)N_2S_2$ complexes.[28]

3.5 Relevance to Ni-SOD Active Site Assembly and Conclusions

Complexes **2-5** serve to accurately model structural and electronic aspects of Ni-SOD_{red}. Taking a modular approach to the monodentate thiolate ligand modeling the contribution of Cys6 provided a unique perspective regarding the role solvent interactions play in modulating the electronic properties and stability of these small molecule mimics, and by analogy the Ni-SOD active site. In particular, it seems that the degree to which aqueous solvent engages in hydrogen-bonding with the coordinated thiolate ligands can be correlated to the relative basicity of the exogenously added RS^-, wherein the effects of solvation are most pronounced for complexes possessing the most basic monodentate ligands. Such solvent interactions appear to be stabilizing in terms of RS^- contributions relative to the rest of the Ni(GC-OMe) synthon, as evidenced by electronic absorption and electrochemical measurements and in light of the results discussed in Chapter 2. However, it appears that these solvent hydrogen-bonding interactions also promote RS^- lability and the formation of S,S'-bridging oligomers, an effect that becomes particularly pronounced for the more basic thiolate ligands.

From the above results, it is clear that species of structurally and electronically similar disposition to Ni-SOD_{red} do not possess inherent stability under aqueous, physiologically relevant conditions. Surely, the protein matrix of Ni-SOD provides pre-organized conditions stabilizing mononuclear active sites and eliminates the possibility of Cys6 dissociation and Ni-S oligomerization. Accordingly, the six Ni centers found within the large interior cavity of the hexameric Ni-SOD assembly are located no less than 23 Å from one another.[4-5]

It is generally accepted that ligand dissociation/exchange in square-planar d^8 complexes proceed via associative pathways and it is likely that five-coordinate species are traversed en route to RS^- dissociation.[29] The broad nature of the signals in the ^1H NMR spectra may also be consistent with the formation of Ni species of higher coordination number, perhaps possessing more easily accessible $S = 1$ states. In this regard, recent point mutagenesis studies converting either Cys2, Cy6 or both to a serine residue afford only catalytically inactive, high-spin octahedral Ni-complexes of mixed N/O ligation, highlighting the necessity of *both* cysteinate ligands for active site assembly.[30-31] Hydrogen-bonding induced dissociation of the ligand component modeling Cys6 may trigger an analogous scenario in the model systems at hand. Although Cys6 dissociation is not observed in Ni-SOD, our results support the feasibility of a scenario by which protonation of a cysteine ligand could provide sufficient weakening of the ligand-field environment and allow axial coordination of the His1 side chain, effectively destabilizing the kinetically inert, square-planar active site. This hypothesis is all the more reasonable in light of biochemical and theoretical

studies implicating the cysteinates of Ni-SOD[32-34] and other Ni-S enzymes such as [NiFe]-hydrogenase[35-37] in the storage and shuttling of protons during catalysis.

3.6 Experimental Section

General Information. See Chapter 2, Section 2.7 for information pertaining to common laboratory reagents and solvents. Potassium salts of the monodentate thiolate ligands were prepared according to a modified literature procedure[11] via addition of one mol-equiv of K(0) to the appropriate thiol in dry MeOH.

Physical Methods. See Chapter 2, Section 2.7 for information pertaining to UV-vis, FTIR, ^{1}H and ^{13}C NMR spectroscopy, ESI-MS measurements and elemental analysis. Cyclic voltammetry measurements were performed with a PAR Model 273A potentiostat using a Ag/Ag^{+} (0.01 M $AgNO_3$/0.1 M $^{n}Bu_4NPF_6$ in MeCN) reference electrode, Pt counter electrode, and a Glassy Carbon millielectrode (2 mm in diameter) as the working electrode when measuring in DMF. An Ag/AgCl reference electrode was used when measuring the aqueous samples. Measurements were performed at ambient temperature using 5.0 mM analyte in the appropriate Ar-purged solvent containing 0.1 M $^{n}Bu_4NPF_6$ as the supporting electrolyte in DMF or 0.5 M KNO_3 for aqueous measurements. The "Maximize Stability" mode was utilized in the PAR PowerCV software utilizing a low-pass 5.3 Hz filter. To ensure accuracy in the measured CVs, these experiments were performed in triplicate while polishing the working electrode between each run and we report an average E_{ox}. Additionally, potentials were checked and corrected by recording the CV of a ferrocene standard in DMF or a potassium ferricyanide standard in aqueous conditions (referenced to the

ferro/ferricyanide couple in 50 mM pH 7.0 phosphate buffer)[38] under the same conditions as the complexes before each run.

Synthesis of H_2N-Gly-L-Cys-OMe•TFA (GC-OMe•TFA). The synthesis of the ligand comprised the following steps:

Step 1. H_2N-L-Cys(STrit)-OMe. To a batch of 13.701 g (52.629 mmol) of triphenyl methanol dissolved in 50 mL of trifluoroacetic acid (TFA) was added 9.095 g (52.99 mmol) of L-cysteine methyl ester hydrochloride forming a red-orange solution. The resultant solution was left to stir at RT for 1 h before it was concentrated to an orange oil, which was partitioned between 300 mL of CH_2Cl_2 and 300 mL of H_2O, resulting in bleaching of the orange color. Portions of K_2CO_3 were then slowly added to the aqueous layer until a basic pH sustained for up to 1 h. The organic layer was then separated, washed with satd. $NaHCO_3$(aq) and brine, dried over $MgSO_4$, and concentrated to a pale oil which solidified after overnight stirring in hexanes. The white solids thus obtained were isolated via vacuum filtration (16.104 g, 42.660 mmol, 81%). mp: 57-58 °C. ^{1}H NMR (400 MHz, $CDCl_3$, δ from TMS): 7.48 (d, 6H), 7.32 (t, 6H), 7.25 (t, 3H), 3.68 (s, 3H), 3.24 (m, 1H), 2.64 (dd, 1H), 2.52 (dd, 1H), 1.54 (br s, 2H, N*H*$_2$). ^{13}C NMR (100.6 MHz, $CDCl_3$, δ from TMS): 174.26 (*C*=O), 144.64, 129.67, 128.04, 126.87, 66.94, 53.89, 52.22, 37.01. FTIR (KBr pellet), ν_{max} (cm^{-1}): 3391 (m, N-H), 3318 (w, N-H), 3062 (w), 2997 (w), 2966 (w), 2948 (w), 2920 (w), 1725 (vs, C=O$_{ester}$), 1593 (m), 1487 (s), 1446 (s), 1434 (s), 1371 (m), 1348 (m), 1316 (m), 1260 (m), 1205 (s), 1186 (s), 1172 (s), 1095 (m), 1031 (m), 1020 (m), 1001 (m), 952 (m), 892 (w), 854 (m), 838 (m), 810 (m), 771 (m), 747 (s),

705 (s), 676 (m), 665 (m), 630 (m), 615 (s), 530 (w), 508 (m), 494 (m), 474 (m). LRMS-ESI (*m/z*): $[M + H]^+$ calcd for $C_{23}H_{24}NO_2S$, 378.2; found, 378.2.

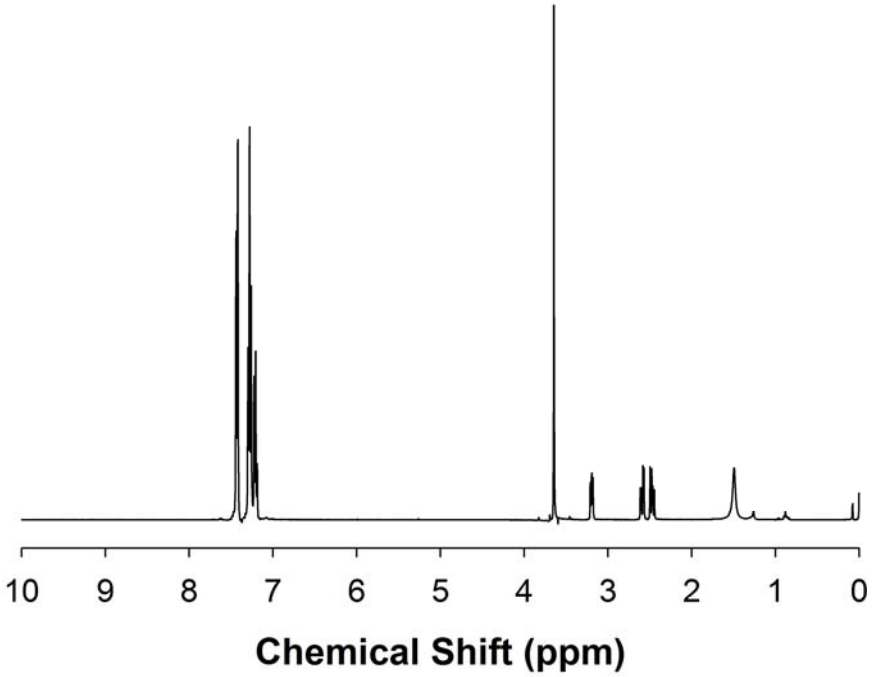

Figure 10. ^1H NMR of NH_2-L-Cys(STrit)-OMe in $CDCl_3$.

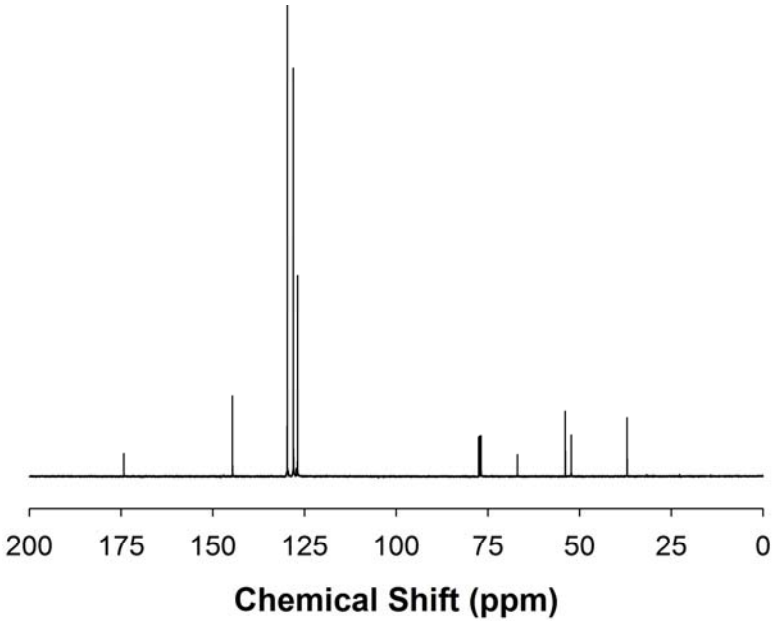

Figure 11. ^{13}C NMR of NH_2-L-Cys(STrit)-OMe in $CDCl_3$ (peak at 77.16 ppm from solvent).

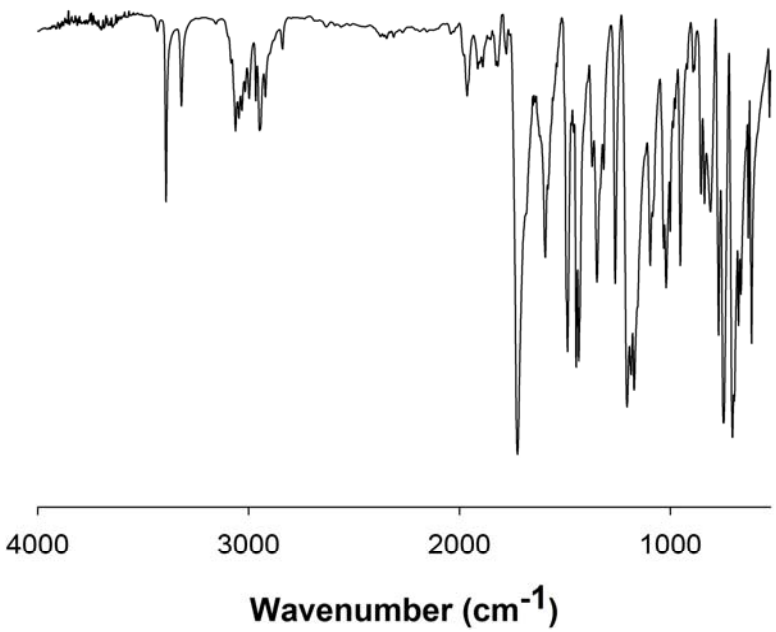

Figure 12. FTIR (KBr matrix) of NH_2-L-Cys(STrit)-OMe.

Step 2. Boc-Gly-L-Cys(STrit)-OMe. A batch of 4.089 g (10.83 mmol) of H_2N-L-Cys(STrit)-OMe and 2.947 g (10.82 mmol) of Boc-Gly-OSu were combined in 200 mL of CH_2Cl_2 and stirred at RT overnight. The solution was then washed with satd. $NaHCO_3$(aq) and brine, and dried over $MgSO_4$ before concentration to a white foam solid (4.934 g, 9.228 mmol, 85%). mp: 59-62 °C. ^{1}H NMR (400 MHz, $CDCl_3$, δ from TMS): 7.44 (d, 6H), 7.33 (t, 6H), 7.26 (t, 3H), 6.80 (br s, 1H, N$H_{peptide}$), 5.38 (br, s, 1H, N$H_{carbamate}$), 4.59 (m, 1H), 3.82 (m, 2H), 3.72 (s, 3H), 2.71 (m, 2H), 1.49 (s, 9H). ^{13}C NMR (100.6 MHz, $CDCl_3$, δ from TMS): 170.70 (C=O$_{ester}$), 169.31 (C=O$_{peptide}$), 155.95 (C=O$_{carbamate}$), 144.27, 129.51, 128.03, 126.92, 80.11, 66.98, 52.64, 51.20, 33.67, 28.32. FTIR (KBr pellet), ν_{max} (cm^{-1}): 3320 (br s, N-H), 3057 (m), 3030 (m), 2977 (s), 2952 (m), 2931 (m), 1746 (vs, C=O$_{ester}$), 1720 (vs, C=O$_{carbamate}$), 1689 (vs, C=O$_{peptide}$), 1595 (w), 1514 (s), 1493 (s), 1434 (m), 1391 (w),

1367 (m), 1248 (m), 1210 (m), 1168 (s), 1083 (w), 1050 (m), 1031 (m), 1001 (w), 985 (w), 941 (w), 862 (w), 766 (m), 744 (s), 701 (s), 675 (m), 621 (m), 544 (w), 505 (w). LRMS-ESI (*m/z*): $[M + K]^+$ calcd for $C_{30}H_{34}KN_2O_5S$, 573.2; found, 573.0.

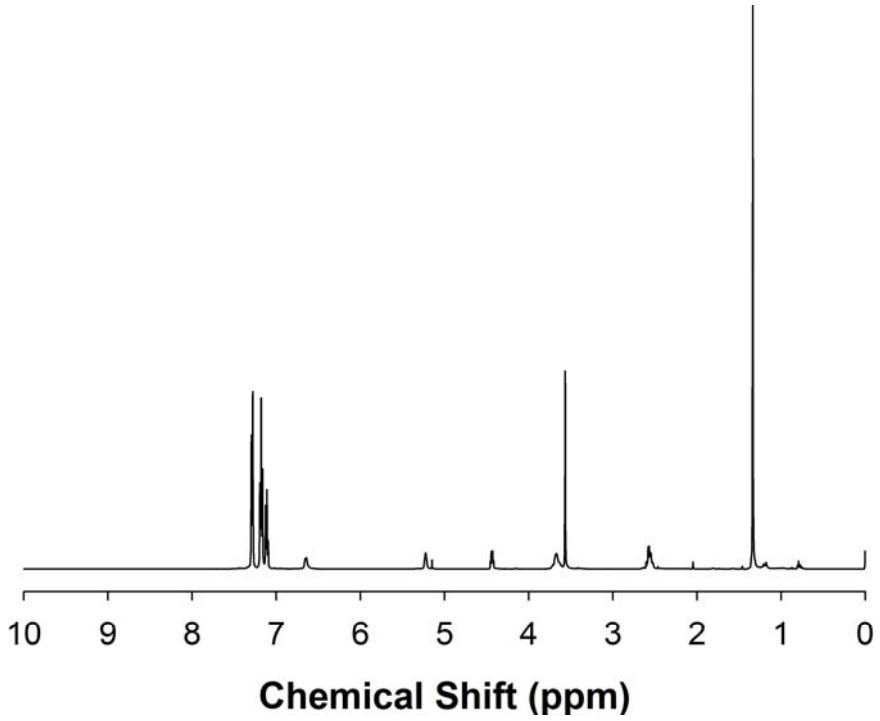

Figure 13. ^1H NMR of Boc-Gly-L-Cys(STrit)-OMe in $CDCl_3$.

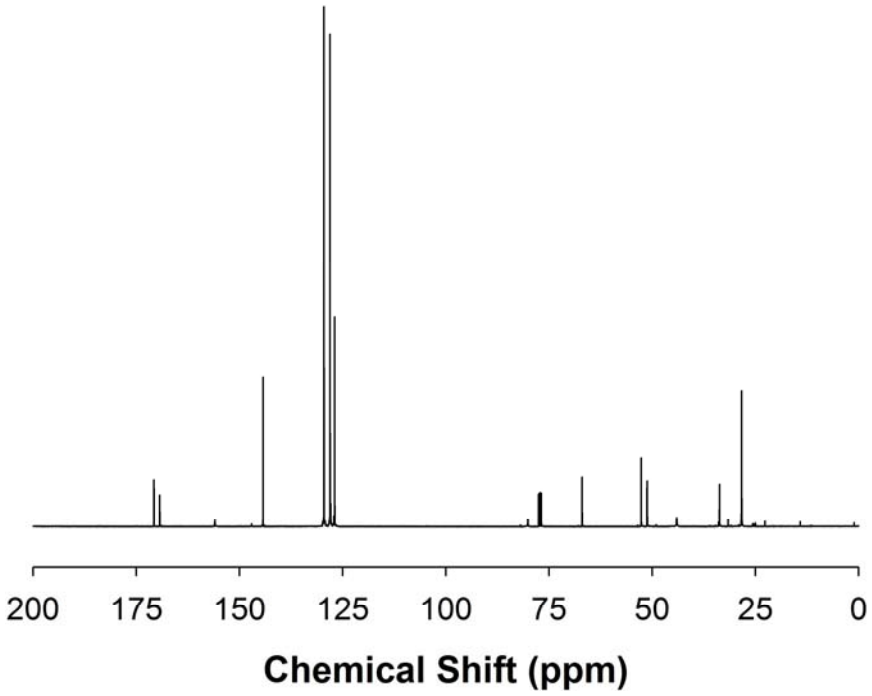

Figure 14. ^{13}C NMR of Boc-Gly-L-Cys(STrit)-OMe in $CDCl_3$ (peak at 77.16 ppm from solvent).

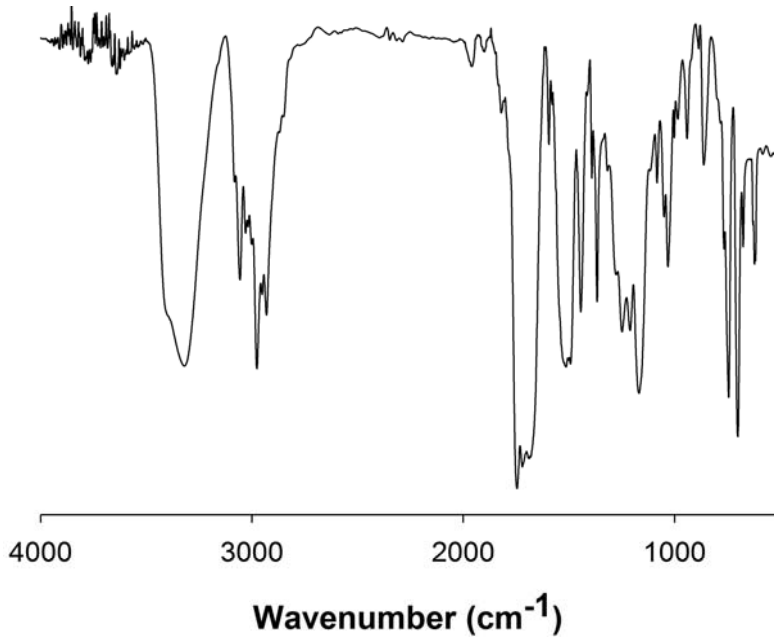

Figure 15. FTIR (KBr matrix) of Boc-Gly-L-Cys(STrit)-OMe.

Step 3. H_2N-Gly-L-Cys-OMe•TFA (GC-OMeH_2•TFA). A batch of 3.748 g (7.010 mmol) of Boc-Gly-L-Cys(STrit)-OMe was dissolved in 40 mL of a 1:1 CH_2Cl_2/TFA solution resulting in a bright-yellow color. After 30 min, 1.092 g (9.391 mmol) of Et_3SiH was added dropwise to the solution, which bleached the bright-yellow solution to a clear and pale-yellow color. After 90 min stirring, the solution was concentrated to ~50% of its original volume and the resulting insoluble triphenyl methane byproduct was filtered off and washed with TFA. The solution was then concentrated to a pale oil, which solidified upon stirring in Et_2O (1.601 g, 5.228 mmol, 75%). mp: 74-77 °C. ^{1}H NMR (500 MHz, CD_3CN, δ from protio solvent): 7.86 (br s, 3H, N*H*$_3$), 7.62 (s, N*H*$_{peptide}$), 4.73 (m, 1H), 3.80 (m, 2H), 3.72 (s, 3H), 2.93 (m, 2H), 1.92 (br s, coincides with solvent protio signal thus difficult to integrate, S*H*). ^{13}C NMR (100.6 MHz, CD_3CN, δ from solvent): 222.35 (*C*=O$_{TFA}$), 171.02 (*C*=O$_{ester}$), 167.09 (*C*=O$_{peptide}$), 55.68, 53.21, 41.52, 31.47, 26.74. ^{1}H NMR (500 MHz, D_2O, δ from protio solvent): 4.82 (m, 1H), 3.94 (s, 2H), 3.82 (s, 3H), 3.03 (m, 2H). FTIR (KBr pellet), ν_{max} (cm^{-1}): 3325 (m, N-H), 3138 (br w, N-H), 1753 (s, C=O$_{ester}$), 1677 (vs, C=O$_{peptide}$), 1631 (w) 1563 (w), 1552 (m), 1536 (w), 1513 (w), 1493 (w), 1434 (m), 1350 (m), 1323 (w), 1208 (s, C-F), 1186 (s, C-F), 1129 (s), 1043 (w), 965 (w), 906 (m), 841 (m), 802 (m), 726 (m), 572 (w). LRMS-ESI (*m/z*): $[M + H]^+$ calcd for $C_6H_{13}N_2O_3S$, 193.2; found, 193.0.

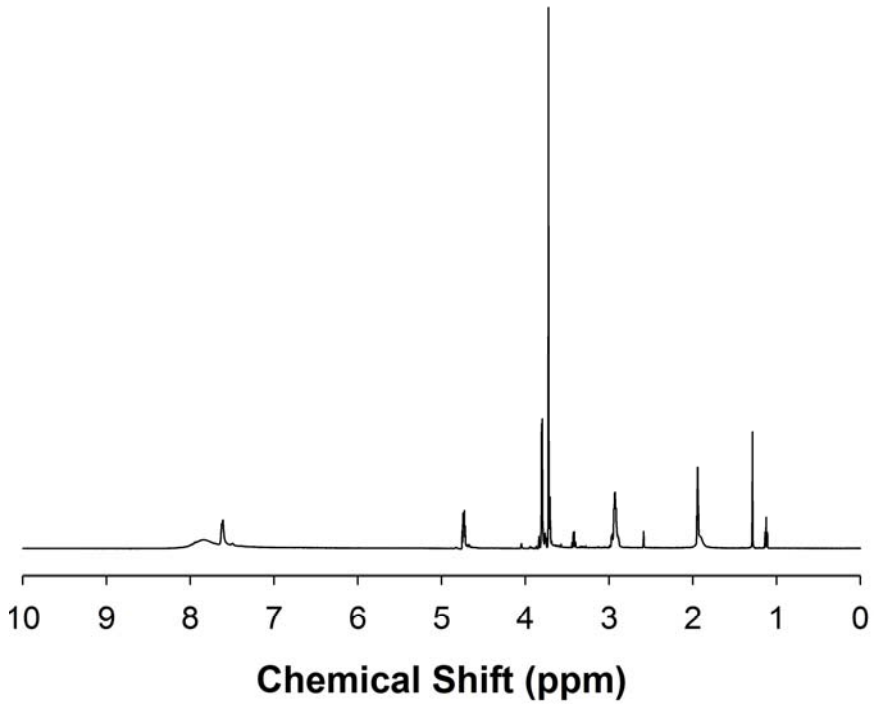

Figure 16. ^{1}H NMR of NH_2-Gly-L-Cys-OMe•TFA in CD_3CN (peak at 1.94 ppm from protio solvent).

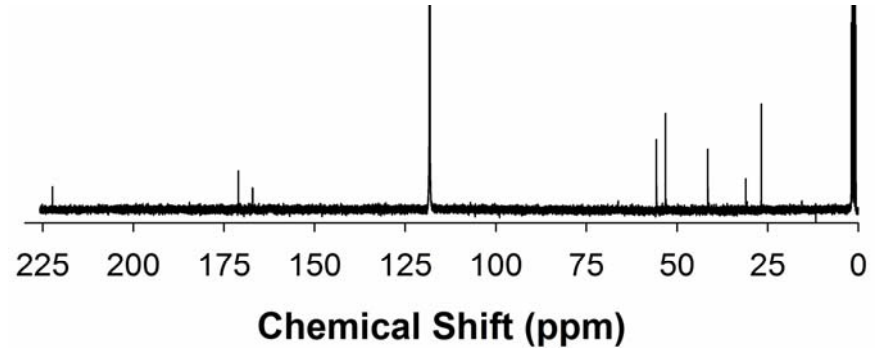

Figure 17. ^{13}C NMR of NH_2-Gly-L-Cys-OMe•TFA in CD_3CN (peaks at 118.26 and 1.32 ppm from solvent).

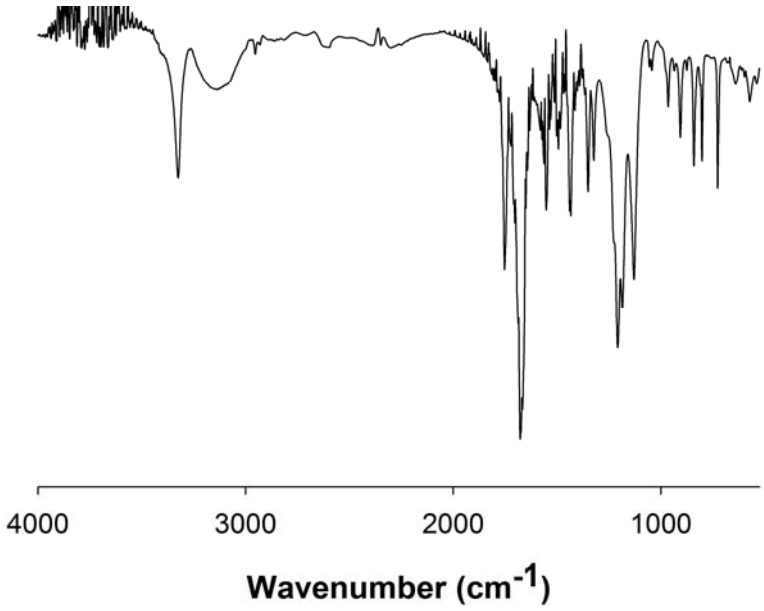

Figure 18. FTIR (KBR matrix) of NH_2-Gly-L-Cys-OMe•TFA.

[Ni_2(GC-OMe)$_2$] (1):

Procedure 1 (TFA adduct): To a batch of 0.174 g (0.699 mmol) of $Ni(OAc)_2$•$4H_2O$ stirring in 12 mL of MeOH was added a 4 mL MeOH solution of GC-$OMeH_2$•TFA (0.217 g, 0.709 mmol) followed by a 3 mL MeOH soltion of NaOAc (0.060 g, 0.731 mmol). The resultant deep orange solution was stirred at RT for 16 h after which the reaction was concentrated to dryness to afford an orange residue. This residue was then stirried in 20 mL of MeCN, which resulted in 0.153 g (0.250 mmol, 72%) of product as peach colored solids. ^{1}H NMR (400 MHz, D_2O, δ from solvent): 4.28 (m, 1H), 3.96 (s, 3H), 3.49 (dd, 1H), 3.32 (dd, 1H), 2.51 (br, s, 1H), 2.31 (d, 1H), 2.08 (s, 1H), 1.94 (s, 1H). FTIR (KBr pellet), ν_{max} (cm^{-1}): 3420 (w, br, OH), 3246 (m, br, N-H), 3119 (m, br, N-H), 2950 (w), 1729 (s, $C=O_{ester}$), 1694 (m, $C=O_{TFA}$), 1601 (vs, $C=O_{peptide}$), 1437 (m), 1409 (s), 1338 (w), 1273 (w), 1205 (s, C-F), 1169 (s, C-F), 1138 (m), 1019 (w), 973 (w), 944 (w), 843 (w), 801 (w), 722 (w),

669 (w), 650 (w), 625 (w), 584 (w), 459 (w). HRMS-ESI (*m/z*): $[M + H]^+$ calcd for $C_{12}H_{21}N_4Ni_2O_6S_2$ (relative abundance), 496.9604 (100), 497.9637 (13), 498.9559 (88), 499.9591 (11), 500.9515 (22); Found, 496.9614 (100), 497.9646 (11), 498.9570 (88), 499.9604 (10), 500.9522 (18). UV-vis (pH 7.5, 50 mM PIPES, 298 K) λ_{max}, nm (ε, M^{-1} cm^{-1}): 338 (4,470), 458 (570). Anal. Calcd for $C_{12}H_{20}N_4Ni_2O_6S_2$•TFA•$2H_2O$: C, 25.95; H, 3.89; N, 8.65. Found: C, 26.13; H, 3.94; N, 8.62.

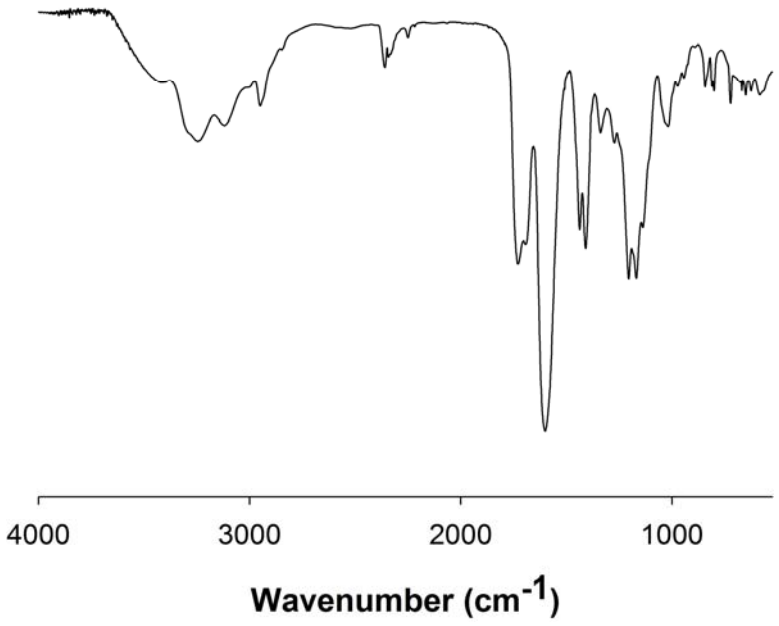

Figure 19. FTIR (KBr matrix) of **1**•TFA•$2H_2O$.

Procedure 2: To a batch of 1.292 g (5.192 mmol) of $Ni(OAc)_2$•$4H_2O$ and 0.428 g (5.22 mmol) of NaOAc dissolved in 80 mL of MeOH was added 1.584 g (5.172 mmol) of GC-OMeH_2•TFA in 10 mL of MeOH. The reaction mixture instantly became a deep red-orange color upon addition of ligand and was subsequently heated to 50 °C for 16 h, which resulted in the precipitation of product as pink solids. The solids were isolated via vacuum filtration to afford 1.100 g (2.210 mmol, 85%) of product. The isolated product is not readily soluble as is the TFA-adduct (see above), but prolonged stirring in D_2O or buffer provided orange solutions

with identical spectral properties (^{1}H NMR, UV-vis, ESI-MS). FTIR reveled no TFA peaks. FTIR (KBr pellet), ν_{max} (cm^{-1}): 3326 (w, N-H), 3228 (w, N-H), 3084 (br w, N-H), 2978 (w), 2962 (w), 2929 (w), 1755 (s, C=O_{ester}), 1578 (vs, C=$O_{peptide}$), 1433 (m), 1404 (m), 1360 (m), 1312 (w), 1265 (w), 1200 (m), 1177 (m), 1150 (m), 1114 (m), 1055 (w), 1030 (w), 993 (w), 969 (w), 946 (w), 853 (w), 801 (w), 717 (w), 660 (w), 603 (w), 573 (w), 483 (w), 424 (m). Anal. Calcd for $C_{12}H_{20}N_4Ni_2O_6S_2$•$0.5H_2O$: C, 28.44; H, 4.18; N, 11.05. Found: C, 28.47; H, 3.94; N, 10.78.

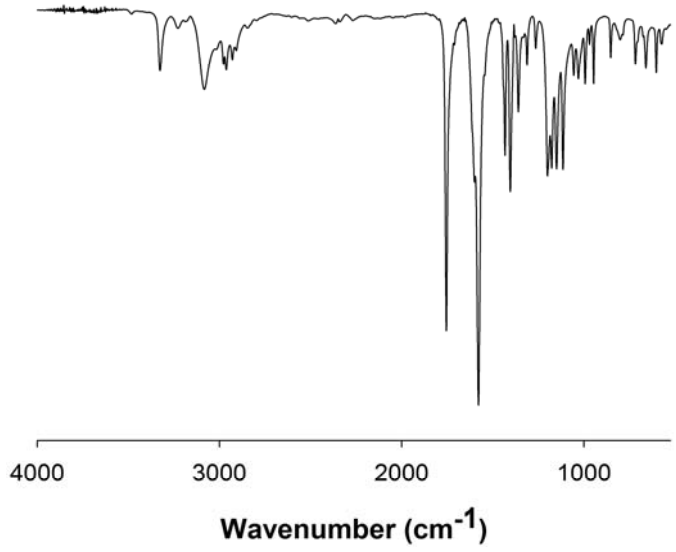

Figure 20. FTIR (KBr matrix) of **1**.

[Ni_2(GC-OMe)$_2$] (1) prepared *in situ*. To a freshly dissolved batch of 18 mg (0.06 mmol) of GC-OMeH_2•TFA in pH 7.5 buffer (50 mM PIPES), was added 15 mg (0.06 mmol) of $Ni(OAc)_2$•$4H_2O$ to form a richly colored orange solution. All spectral properties are in accordance with those of solid batches of isolated **1** upon dissolution.

K[Ni(GC-OMe)(SC_6H_4-*p*-Cl)] (2). To an 8 mL DMF solution containing 0.142 g (0.777 mmol) of KSC_6H_4-*p*-Cl was added a 5 mL DMF slurry of **1** (0.202 g, 0.406 mmol). The resulting purple heterogeneous mixture was heated to 45 °C and stirred at this temperature for 16 h to form a rich mostly homogeneous violet colored solution. The reaction was subsequently cooled to RT, filtered to remove any unreacted **1**, and the violet mother liquor was concentrated to dryness. The resultant purple residue was then taken up in 2 mL of THF, which was then precipiated out by addition of 12 mL of Et_2O. The product was collected as dull violet solids via vacuum filtration (0.316 g, 0.732 mmol, 94%). ^{1}H NMR (500 MHz, D_2O, as isolated product in the presence of one extra mol-equiv of KSC_6H_4-*p*-Cl, δ from protio solvent): 7.53 (d, 1.4H), 7.30 (d, 1.7H, free KSC_6H_4-*p*-Cl), 7.14 (d, 1.4H), 7.08 (d, 1.7H, free KSC_6H_4-*p*-Cl), 4.15 (m, 1H), 3.79 (s, 3H), 3.31 (dd, 1H), 3.15 (dd, 1H), 2.60 (m, 1H), 2.24 (d, 1H). ^{1}H NMR (400 MHz, CD_3CN, as isolated solid, δ from protio solvent): 7.68 (d, 1.3H), 6.93 (d, 1.1H), 3.84 (m, 1H), 3.61 (s, 2.4H), 3.01 (m, 1H), 2.91 (m, 1H), 2.36 (m, 1H), 2.15 (s, 1H, N*H*), 2.13 (m, 1H), 1.87 (br s, 1H, N*H*). FTIR (KBr pellet), ν_{max} (cm^{-1}): 3325 (w, NH), 3195 (br w, N-H), 3108 (br w, N-H), 2948 (m), 2924 (m), 1722 (s, $C{=}O_{ester}$), 1586 (vs, $C{=}O_{peptide}$), 1468 (s), 1437 (m), 1410 (m), 1336 (w), 1265 (w), 1207 (m), 1168 (m), 1090 (s), 1033 (m), 1010 (m), 934 (w), 818 (m), 740 (w), 701 (w), 662 (w), 543 (m), 499 (w), 425 (w). HRMS-ESI (*m/z*): $[M - K]^-$ calcd for $C_{12}H_{14}ClN_2NiO_3S_2$ (relative abundance), 390.9482 (100), 391.9515 (13), 392.9439 (48), 393.9470 (6), 394.9408 (21); Found, 390.9487 (100), 391.9520 (11), 392.9442 (41), 393.9472 (4), 394.9416 (16). UV-vis (DMF, 298 K) λ_{max}, nm (ε, M^{-1} cm^{-1}): 481 (390), 560 (230). UV-vis (pH 7.5, 50 mM PIPES, 298 K) λ_{max}, nm (ε, M^{-1}

cm^{-1}): 471 (430), 560 (240). E_{ox} (DMF): 220 mV. E_{ox} (pH 7.4): 285 mV. Anal. Calcd for $C_{12}H_{14}ClKN_2NiO_3S_2 \bullet 0.5H_2O$: C, 32.71; H, 3.43; N, 6.36. Found: C, 32.63; H, 3.56; N, 6.50.

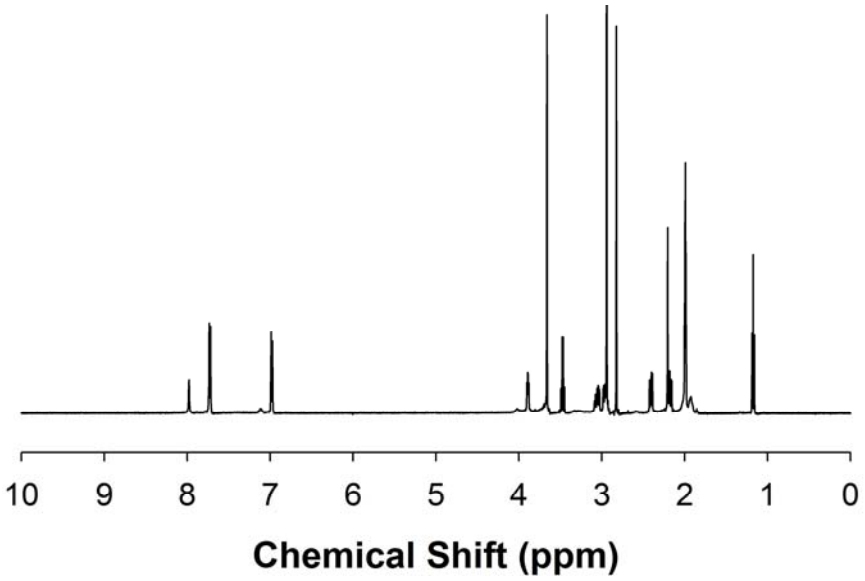

Figure 21. ^1H NMR of **2** in CD_3CN (peaks at 7.92, 2.89 and 2.77 ppm correspond to DMF from the reaction solvent; 3.42 and 1.12 ppm correspond to Et_2O, 1.94 ppm is from protio solvent).

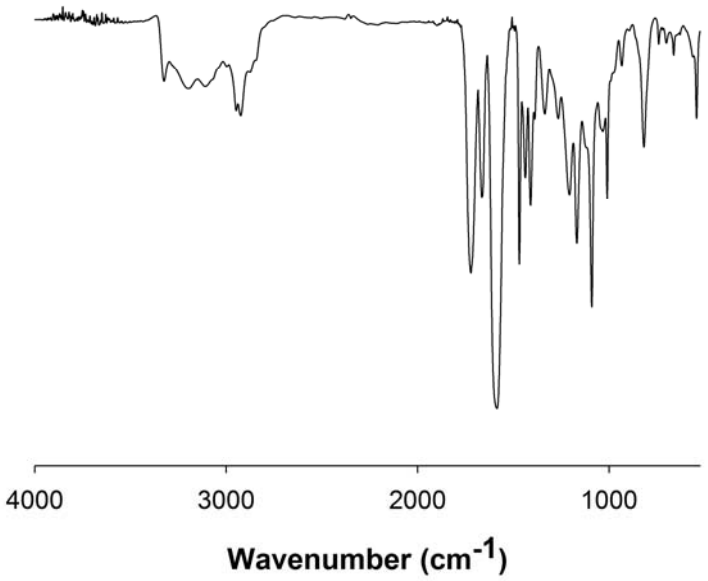

Figure 22. FTIR (KBr matrix) of **2**.

K[Ni(GC-OMe)(S^{t}Bu)] (3). To 115 μL (0.092 g, 1.02 mmol) of *tert*-butyl thiol dissolved in 3 mL of DMF was added 0.040 g (0.997 mmol) of KH as a 4 mL DMF slurry to generate KS^{t}Bu. Immediate effervescence was observed and a pale yellow homogenous solution formed over the course of 20 min. To this solution was added a 5 mL DMF slurry of **1** (0.278 g, 0.558 mmol) resulting in a purple heterogeneous mixture. This solution was then heated to 45 °C and stirred for 16 h to form a rich violet colored solution. The reaction was subsequently cooled to RT, filtered to remove any unreacted **1**, and the violet mother liquor was concentrated to dryness. The resultant purple residue was taken up in 6 mL of THF, which was treated with 25 mL of Et_2O to form free flowing solids. The product was collected as pink solids via vacuum filtration (0.328 g, 0.870 mmol, 87%). ^{1}H NMR (400 MHz, D_2O, as isolated product in the presence of one extra mol-equiv of KS^{t}Bu, δ from protio solvent): 4.01 (d, 1H), 3.71 (s, 3H), 3.30 (dd, 1H), 3.14 (dd, 1H), 2.53 (m, 1H), 2.21 (d 1H), 1.26 (s, 9H). ^{1}H NMR (500 MHz, CD_3CN, as isolated solid, δ from protio solvent): 3.70 (m, 1H), 3.59 (s, 3H), 3.04 (m, 1H), 2.95 (m, 1H), 2.30 (m, 1H), 2.13 (m, 1H), 1.84 (s, 2H, N*H*), 1.31 (s, 9H). FTIR (KBr pellet), ν_{max} (cm^{-1}): 3343 (br w, N-H), 3222 (br w, N-H), 3107 (br w, N-H), 2948 (w), 2887 (w), 2848 (w), 1721 (m, C=O$_{ester}$), 1584 (vs, C=O$_{peptide}$), 1439 (w), 1410 (m), 1355 (w), 1273 (w), 1207 (m), 1166 (m), 932 (w), 742 (w), 646 (w), 586 (w), 465 (w). UV-vis (DMF, 298 K) λ_{max}, nm (ε, M^{-1} cm^{-1}): 358 (1400), 484 (440), 570 (230). E_{ox} (DMF): 80 mV. Anal. Calcd for $C_{10}H_{19}KN_2NiO_3S_2 \bullet H_2O$: C, 30.39; H, 5.36; N, 7.09. Found: C, 30.08; H, 5.02; N, 7.16.

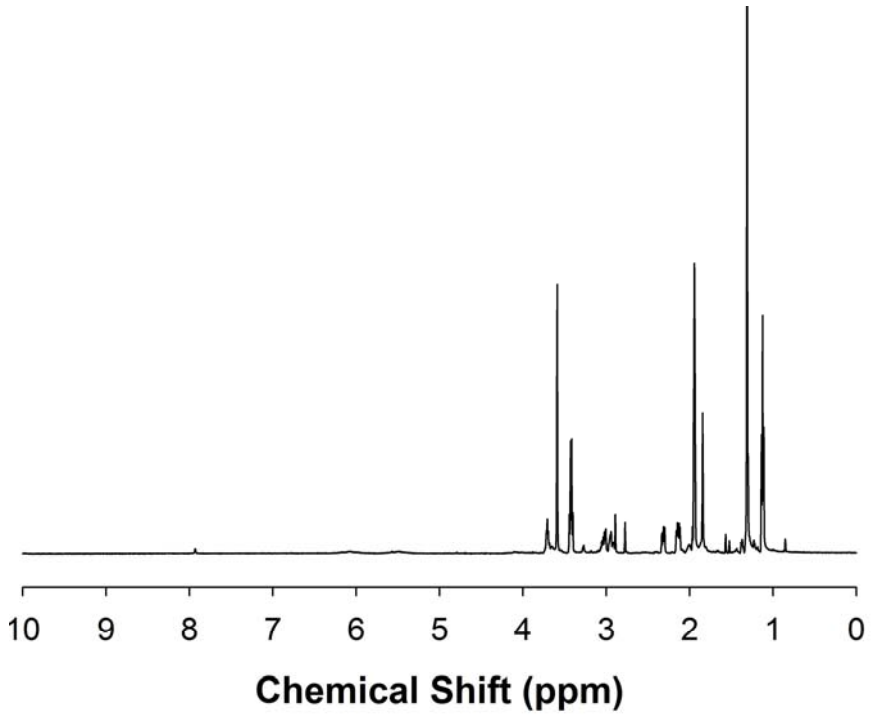

Figure 23. ^{1}H NMR of **3** in CD_3CN (peaks at 7.92, 2.89 and 2.77 ppm correspond to DMF from the reaction solvent; 3.42 and 1.12 ppm correspond to Et_2O, 1.94 ppm is from protio solvent).

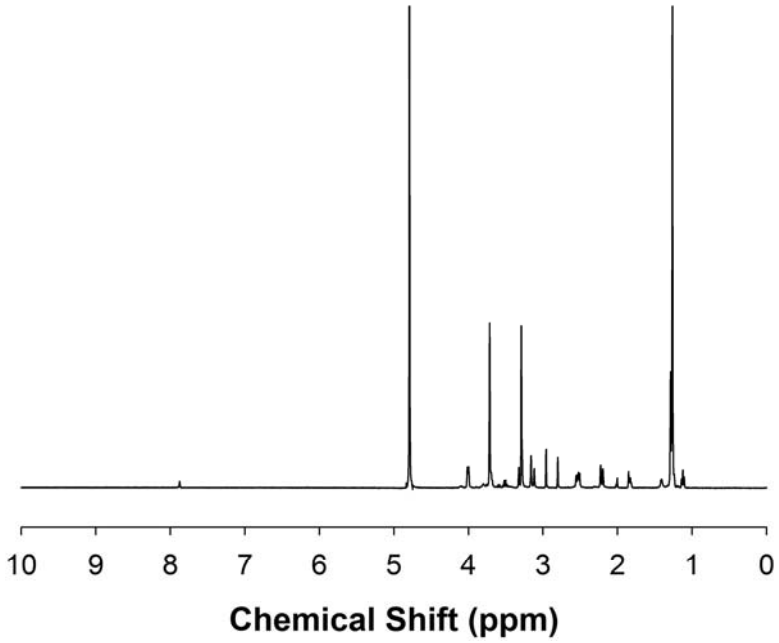

Figure 24. ^{1}H NMR of **3** in D_2O in the presence of 1 mol-equiv. KS^{t}Bu (peaks at 7.92, 3.01 and 2.85 ppm correspond to DMF from the reaction solvent; 4.79 ppm is from protio solvent; free ^{t}BuS$^-$ is coincidental with complex).

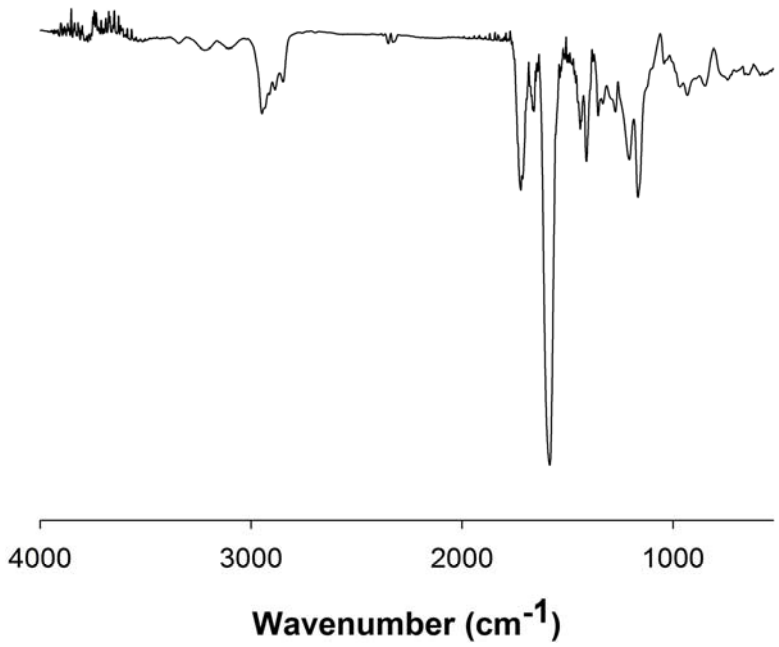

Figure 25. FTIR (KBr matrix) of **3**.

K[Ni(GC-OMe)(SC$_6$H$_4$-*p*-OMe)] (4). To a 3 mL DMF solution containing 0.046 g (0.258 mmol) of KSC$_6$H$_4$-*p*-OMe was added a 3 mL DMF slurry of **1** (0.073 g, 0.147 mmol). The purple heterogeneous reaction mixture that formed was then heated to 45 °C and stirred for 16 h to form a violet-brown mostly homogeneous solution. The reaction was subsequently cooled to RT, filtered to remove any unreacted **1**, and the violet-brown mother liquor was concentrated to dryness. To the resultant red-brown residue was added 5 mL each of THF and Et_2O and the residue was scraped to form free flowing solids. The product was collected as red-brown solids via vacuum filtration (0.096 g, 0.225 mmol, 87% yield). ^{1}H NMR (400 MHz, D_2O, as isolated product in the presence of one extra mol-equiv of KSC$_6$H$_4$-*p*-OMe, δ

from protio solvent): 7.37 (d, 2H), 7.21 (d, 2H, free KSC_6H_4-*p*-OMe), 6.72 (m, 4H, overlap of bound and free KSC_6H_4-*p*-OMe), 4.08 (d, 1H), 3.71 (s, 9H, coincidental peaks from: 3H from OMe of coordinated KSC_6H_4-*p*-OMe, 3H from OMe of free KSC_6H_4-*p*-OMe), 3.23 (dd, 1H), 3.07 (dd, 1H), 2.53 (m, 2H). ^{1}H NMR (500 MHz, CD_3CN, as isolated solid, δ from protio solvent): 7.40 (d, 2H), 6.50 (d, 0.3H), 6.41 (d, 1.7H), 3.75 (t, 1H), 3.55 (s, 3H), 3.44 (s, 3H), 2.93 (m, 2H), 2.17 (m, 1H), 2.08 (m, 1H and br s, 1H, N*H*), 1.85 (br s, 1H, N*H*). FTIR (KBr pellet), ν_{max} (cm^{-1}): 3319 (w, N-H), 3190 (br w, N-H), 3090 (br w, N-H), 2946 (w), 2834 (w), 1720 (s, $C{=}O_{ester}$), 1663 (m, $C{=}O_{DMF}$), 1587 (vs, $C{=}O_{peptide}$), 1486 (s), 1463 (w), 1439 (m), 1409 (m), 1336 (w), 1273 (m), 1235 (s), 1169 (s), 1099 (m), 1028 (m), 933 (w), 826 (w), 796 (w), 638 (w), 625 (w), 561 (w), 525 (w), 470 (w), 425 (w). HRMS-ESI (*m/z*): $[M - K]^-$ calcd for $C_{13}H_{17}N_2NiO_4S_2$ (relative abundance), 386.9978 (100), 388.0011 (14), 388.9933 (48), 389.9965 (7); Found, 386.9980 (100), 388.0011 (14), 388.9936 (46), 389.9983 (11). UV-vis (DMF, 298 K) λ_{max}, nm (ε, M^{-1} cm^{-1}): 480 (500), 565 (200). UV-vis (pH 7.5, 50 mM PIPES, 298 K) λ_{max}, nm (ε, M^{-1} cm^{-1}): 467 (400), 550 (230). E_{ox} (DMF): 170 mV. E_{ox} (pH 7.4): 315 mV. Anal. Calcd for $C_{13}H_{17}KN_2NiO_4S_2 \bullet 0.5H_2O$: C, 35.79; H, 4.16; N, 6.42. Found: C, 35.84; H, 4.46; N, 6.48.

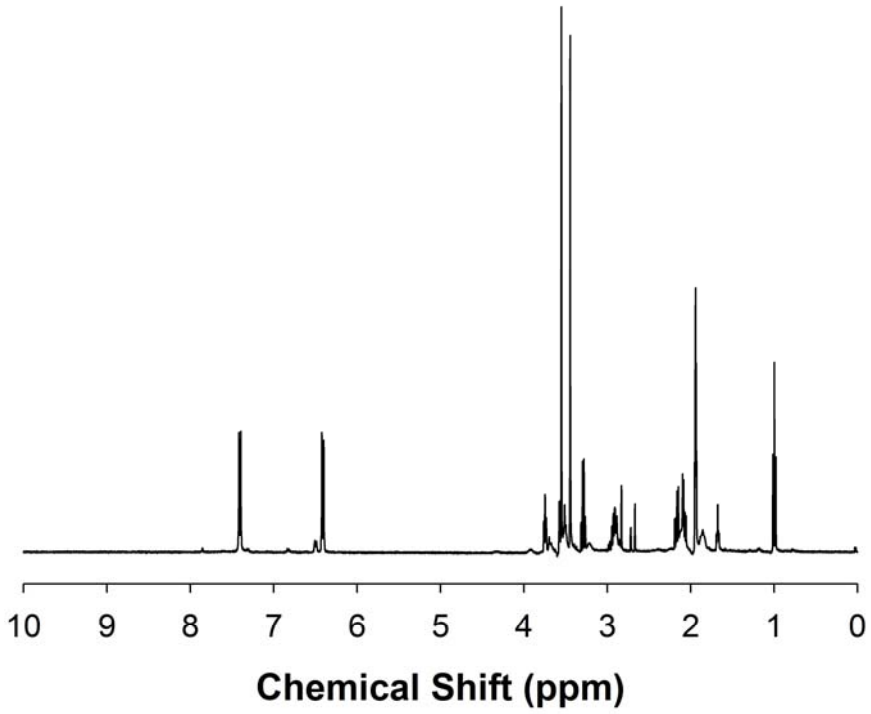

Figure 26. ^{1}H NMR of **4** in CD_3CN (peaks at 7.92, 2.89 and 2.77 ppm correspond to DMF from the reaction solvent; 3.42 and 1.12 ppm correspond to Et_2O, 1.94 ppm is from protio solvent).

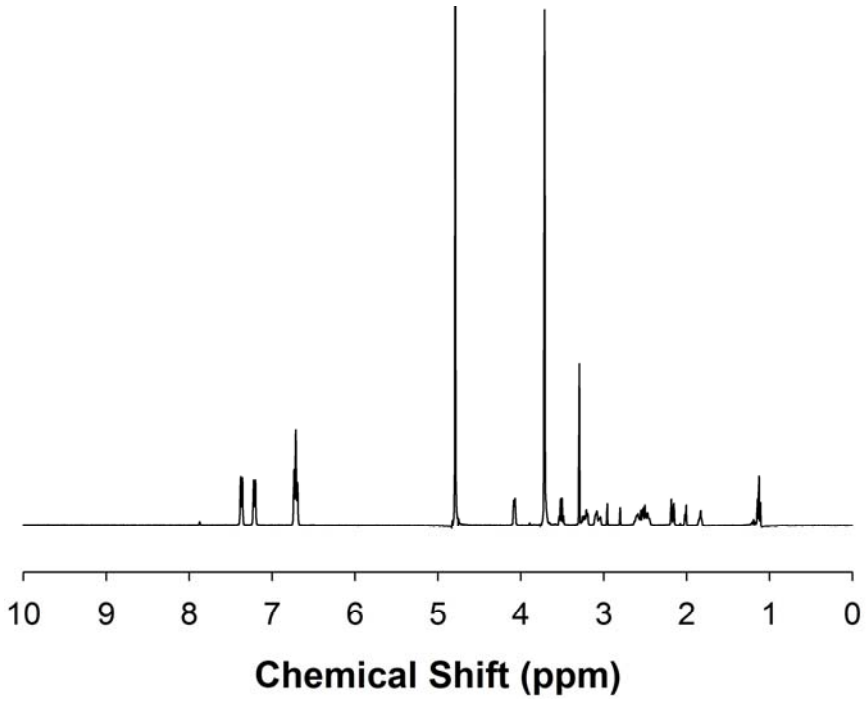

Figure 27. ^{1}H NMR of **4** in D_2O in the presence of 1 mol-equiv. KSC_6H_4-*p*-OMe (peaks at 7.92, 3.01 and 2.85 ppm correspond to DMF from the reaction solvent; 4.79 ppm is from protio solvent; 7.21, 6.71 (coincidental with complex), and 3.71 ppm (coincidental) from free KSC_6H_4-*p*-OMe).

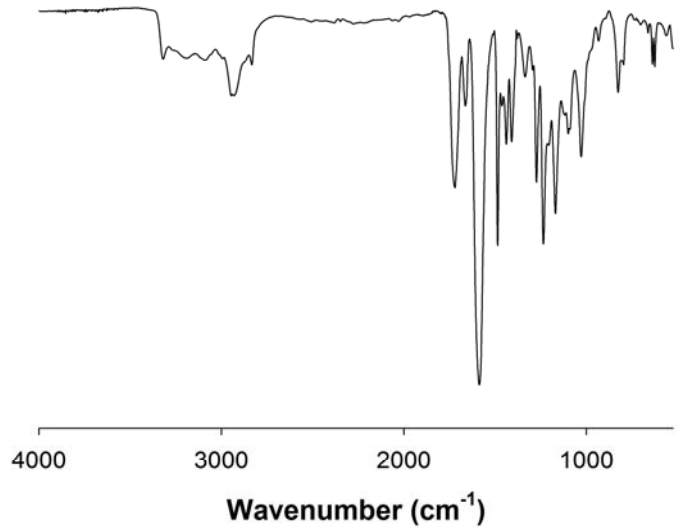

Figure 28. FTIR (KBr matrix) of **4**.

K[Ni(GC-OMe)(S-NAc)] (5). To a 5 mL DMF solution containing 0.094 g (0.249 mmol) of **3** was added a 2 mL DMF solution of *N*-acetyl-L-cysteine methyl ester (0.045 g, 0.254 mmol). The solution rapidly changed from violet to orange-brown and was left to stir at RT for 16 h. The solution was then concentrated to a brick-red colored residue and stirred in 15 mL of a 2:1 Et_2O/THF mixture to afford free flowing solids. The solids were collected via vacuum filtration to yield 0.105 g (0.226 mmol, 91% yield) of product. ^{1}H NMR (400 MHz, D_2O, as isolated product in the presence of one extra mol-equiv of KS-NAc, δ from protio solvent): 4.45 (t, 1H, free KSNAc), 4.32 (t, 1H), 4.11 (d, 1H), 3.73 (s, 6H, coincidental peaks: 3H each from OMe of coordinated $[GC\text{-}OMe]^{2-}$ and $[S\text{-}NAc]^-$, 3H from OMe of free KS-NAc), 3.31 (dd, 1H), 3.17 (dd, 1H), 2.86 (m, 2.5H, free KSNAc), 2.63 (m, 1H), 2.26 (d, 1H), 2.14 (m, 2H), 2.08 (s, 3H), 2.02 (s, 4H, free KSNAc). ^{1}H NMR (500 MHz, CD_3CN, as isolated solid, δ from protio solvent): 8.62 (br s, 1H, N*H*), 4.05 (br s, 1H), 3.90 (br s, 1H), 3.60 (s, 8H, coincidental peaks from: OMe of both coordinated $[GC\text{-}OMe]^{2-}$ and $[SN\text{-}Ac]^-$, residual THF from reaction workup), 3.32 (br s, 1H), 3.05 (m, 1H), 2.97 (m, 1H), 2.51 (m, 1H), 2.14 (m, 10H, integrates slightly high due to overlap with residual H_2O peak). FTIR (KBr pellet), ν_{max} (cm^{-1}): 3246 (br w, N-H), 2950 (w), 2919 (w), 2848 (w), 1731 (s, $C{=}O_{ester}$), 1662 (s, $C{=}O_{SNAC\ peptide}$), 1589 (vs, $C{=}O_{GCOMe\ peptide}$), 1436 (m), 1412 (m), 1372 (w), 1337 (w), 1302 (w), 1268 (w), 1212 (m), 1167 (m), 1122 (w), 1032 (w), 938 (w), 901 (w), 843 (w), 800 (w), 661 (w), 567 (w), 488 (w), 423 (w). HRMS-ESI (*m/z*): $[M - K]^-$ calcd for $C_{12}H_{20}N_3NiO_6S_2$ (relative abundance), 424.0142 (100), 425.0174 (13), 426.0097 (48), 427.0129 (6), 428.0072 (5); Found, 424.0144 (100), 425.0180 (12), 426.0101 (48), 427.0135 (6), 428.0081

(4). LRMS-ESI (*m/z*): $[M - K]^-$ calcd for $C_{12}H_{20}N_3NiO_6S_2$, 424.0; found, 424.0. UV-vis (DMF, 298 K) λ_{max}, nm (ε, M^{-1} cm^{-1}): 358 sh (1,200), 463 (350), 545 (160). UV-vis (pH 7.5, 50 mM PIPES, 298 K) λ_{max}, nm (ε, M^{-1} cm^{-1}): 334 (1,200), 464 (300), 545 (140). E_{ox} (DMF): 310 mV. E_{ox} (pH 7.4): 550 mV. Anal. calcd for $C_{12}H_{20}KN_3NiO_6S_2$•0.33THF•0.33H_2O: C, 32.40; H, 4.76; N, 8.50. Found: C, 32.46; H, 4.80; N, 8.67.

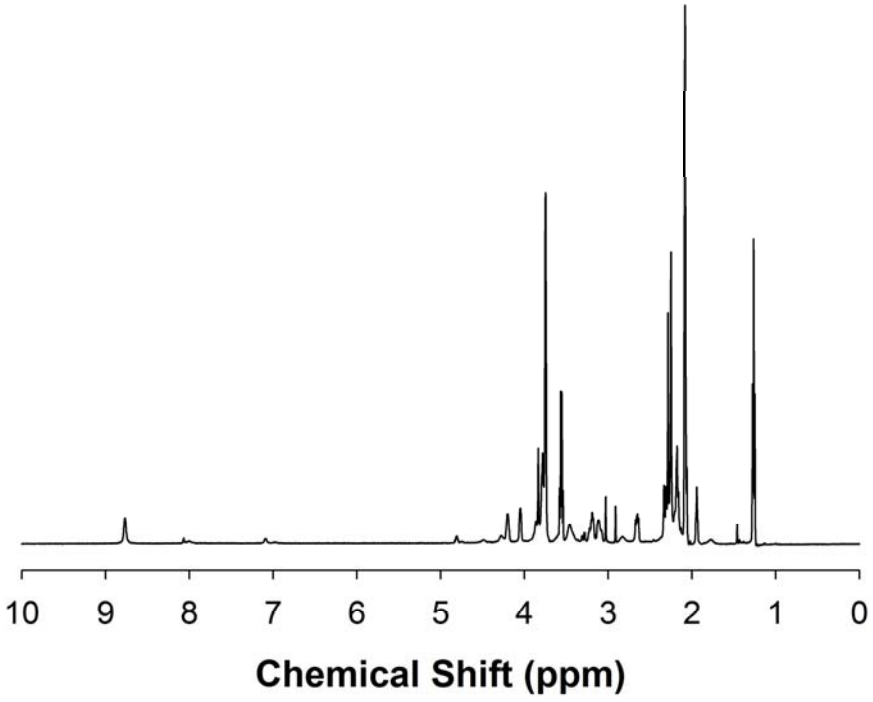

Figure 29. ^1H NMR of **5** in CD_3CN (peaks at 7.92, 2.89 and 2.77 ppm correspond to DMF from the reaction solvent; 3.42 and 1.12 ppm correspond to Et_2O, 1.94 ppm is from protio solvent).

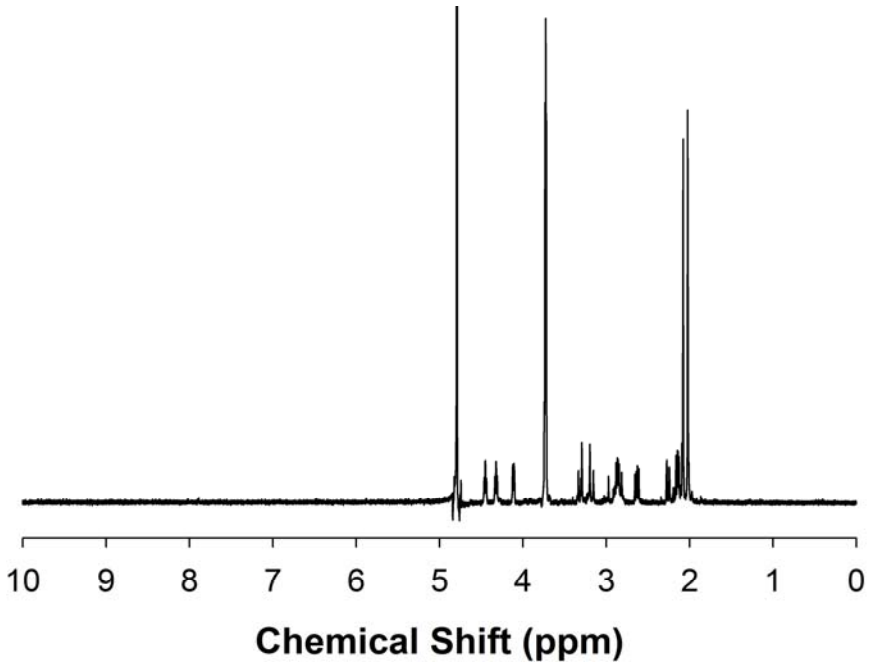

Figure 30. ^{1}H NMR of **5** in D_2O in the presence of 1 mol-equiv. KS-NAc (peak at 4.79 ppm is from protio solvent; 4.50, 3.73 (coincidental with complex), 2.86 and 2.08 ppm from free KS-NAc).

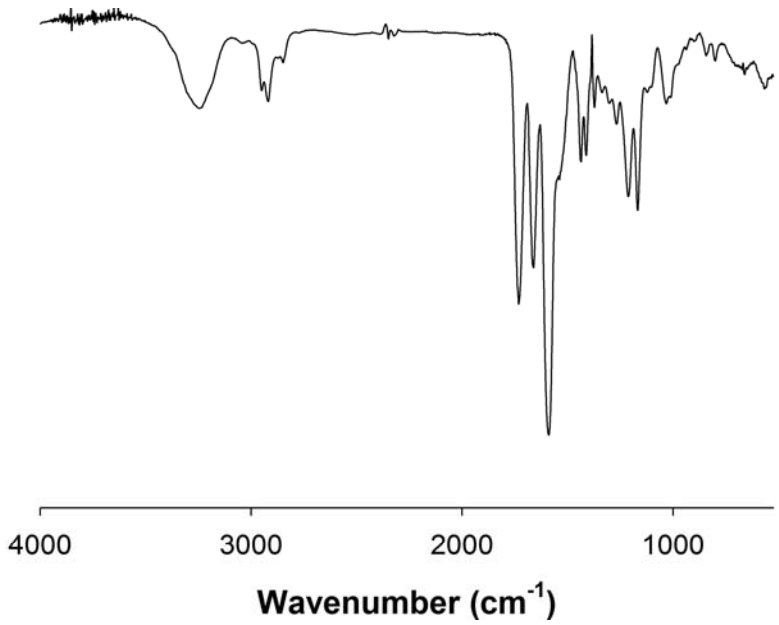

Figure 31. FTIR (KBr matrix) of **5**.

Bulk oxidation of 2. To a batch of 52 mg (0.12 mmol) of **2** in 3 mL of DMF was added 40 mg (0.12 mmol) of ferrocenium hexafluorophosphate in 3 mL of DMF. Instantantaneously, the violet solution developed an orange-brown color and was left to stir at RT for 2 h. The reaction mixture was then concentrated to an orange-brown residue, which solidified upon stirring in Et_2O. Brown solids (45 mg) were separated via vacuum filtration and the yellow mother liquor was concentrated to a pale yellow residue (40 mg). FTIR (KBr), ^{1}H NMR (D_2O), and ESI-MS (positive ion mode) revealed the brown insoluble solids to be comprised of **1** and KPF_6 (87% recovery) while ^{1}H NMR in $CDCl_3$ of the yellow Et_2O-soluble residue to be comprised solely of ferrocene and the disulfide of the thiol HSC_6H_4-*p*-Cl (100% recovery).

X-ray Absorption Studies. Samples were loaded under anaerobic conditions into 0.5 mm thick XAS aluminum sample holders with Mylar-tape windows and quickly frozen in liquid nitrogen prior to XAS data collection. Nickel K-edge XAS data were collected at Stanford Synchrotron Radiation Lightsource (SSRL) on beamline 7-3 with the SPEAR storage ring operating at 3.0 GeV, 345-350 mA. X-ray absorption spectra for the solid samples were recorded with the sample at 10 K using a 1 mm × 4 mm vertical aperture beam incident on a fully tuned Si[220] double-crystal monochromator, and collected using transmission mode. Three ionization chambers with N_2 gas were used, with the first defining I_0. A nickel foil was placed between the second and third ionization chambers I_1 and I_2 to serve as an internal calibration standard, with the first inflection point for the nickel foil assigned at 8331.6 eV. k values were calculated using a threshold (k = 0) energy of 8340 eV. The averaged XAS data for a solid sample represent 5-6 scans, each of 27 minutes

duration; the averaged spectra were calculated as $\log(I_0/I_1)$. Data reduction and analysis were performed with EXAFSPAK software (www-ssrl.slac.stanford.edu/exafspak.html) according to standard procedures as described before.[39] Fourier transforms of the EXAFS spectra were generated using sulfur-based phase correction. Phase and amplitude functions used in the curve fitting were calculated using FEFF version 8.0.[40]

Table 3. Summary of Crystal Data and Intensity Collection and Structure Refinement Parameters for **$(Et_4N)_2[Ni(SC_6H_4$-*p*-$Cl)_4]$**.

[a] $R_1 = \Sigma| \, |F_o| - |F_c| \, | / \Sigma |F_o|$; [b] $wR_2 = \{\Sigma[w(F_o^2 - F_c^2)^2]/ \Sigma[w(F_o^2)^2]\}^{1/2}$.

	$(Et_4N)_2[Ni(SC_6H_4$-*p*-$Cl)_4]$
Formula	$C_{40}H_{56}Cl_4N_2NiS_4$
Formula weight	893.62
Crystal system	Orthorhombic
Space group	Pca2(1)
Crystal color, habit	red
A, Å	24.826(9)
B, Å	11.942(5)
C, Å	14.764(6)
A, deg	90
B, deg	90
Γ, deg	90
V, Å^3	4377(3)
Z	4
ρ_{calcd}, g/cm^3	1.356
T, K	293(2)
abs coeff, μ (Mo Kα), mm^{-1}	0.909
θ limits, deg	2.37 - 26.99
total no. of data	51896
no. of unique data	9538
no. of parameters	460
GOF on F^2	1.064
R_1,[a] %	0.0726
wR_2,[b] %	0.1407
max, min peaks, e/ Å^3	0.8988, 0.7126

3.7 References

(1) Gale, E. M.; Patra, A. K.; Harrop, T. C. *Inorg. Chem.* **2009**, *48*, 5620.

(2) Gale, E. M.; Narendrapurapu, B. S.; Simmonett, A. C.; Schaefer, H. F., III; Harrop, T. C. *Inorg. Chem.* **2010**, *49*, 7080.

(3) Gale, E. M.; Cowart, D. M.; Scott, R. A.; Harrop, T. C. *Inorg. Chem.* **2011**, *50*, 10460.

(4) Barondeau, D. P.; Kassmann, C. J.; Bruns, C. K.; Tainer, J. A.; Getzoff, E. D. *Biochemistry* **2004**, *43*, 8038.

(5) Wuerges, J.; Lee, J.-W.; Yim, Y.-I.; Yim, H.-S.; Kang, S.-O.; Carugo, K. D. *Proc. Natl. Acad. Sci. U.S.A.* **2004**, *101*, 8569.

(6) Youn, H.-D.; Kim, E.-J.; Roe, J.-H.; Hah, Y. C.; Kang, S.-O. *Biochem. J.* **1996**, *318*, 889.

(7) Choudhury, S. B.; Lee, J. W.; Davidson, G.; Yim, Y. I.; Bose, K.; Sharma, M. L.; Kang, S. O.; Cabelli, D. E.; Maroney, M. J. *Biochemistry* **1999**, *38*, 3744.

(8) Bryngelson, P. A.; Arobo, S. E.; Pinkham, J. L.; Cabelli, D. E.; Maroney, M. J. *J. Am. Chem. Soc.* **2004**, *126*, 460.

(9) Silverstein, R. M.; Webster, F. X.; Kiemle, D. J. *Spectrometric Identification of Organic Compounds*; Wiley: Hoboken, NJ, 2005.

(10) Baidya, N.; Olmstead, M. M.; Mascharak, P. K. *Inorg. Chem.* **1991**, *30*, 3967.

(11) Rosenfield, S. G.; Armstrong, W. H.; Mascharak, P. K. *Inorg. Chem.* **1986**, *25*, 3014.

(12) Tennyson, A. G.; Dhar, S.; Lippard, S. J. *J. Am. Chem. Soc.* **2008**, *130*, 15087.

(13) Tietze, D.; Breitzke, H.; Imhof, D.; Kothe, E.; Weston, J.; Buntkowsky, G. *Chem. - Eur. J.* **2009**, *15*, 517.

(14) Mills, D. K.; Reibenspies, J. H.; Darensbourg, M. Y. *Inorg. Chem.* **1990**, *29*, 4364.

(15) Smee, J. J.; Miller, M. L.; Grapperhaus, C. A.; Reibenspies, J. H.; Darensbourg, M. Y. *Inorg. Chem.* **2001**, *40*, 3601.

(16) Farmer, P. J.; Reibenspies, J. H.; Lindahl, P. A.; Darensbourg, M. Y. *J. Am. Chem. Soc.* **1993**, *115*, 4665.

(17) Grapperhaus, C. A.; Maguire, M. J.; Tuntulani, T.; Darensbourg, M. Y. *Inorg. Chem.* **1997**, *36*, 1860.

(18) Colpas, G. J.; Kumar, M.; Day, R. O.; Maroney, M. J. *Inorg. Chem.* **1990**, *29*, 4779.

(19) Hanss, J.; Krüger, H.-J. *Angew. Chem., Int. Ed.* **1998**, *37*, 360.

(20) Krüger, H.-J.; Peng, G.; Holm, R. H. *Inorg. Chem.* **1991**, *30*, 734.

(21) Shearer, J.; Zhao, N. *Inorg. Chem.* **2006**, *45*, 9637.

(22) Mathrubootham, V.; Thomas, J.; Staples, R.; McCraken, J.; Shearer, J.; Hegg, E. L. *Inorg. Chem.* **2010**, *49*, 5393.

(23) Fiedler, A. T.; Bryngelson, P. A.; Maroney, M. J.; Brunold, T. C. *J. Am. Chem. Soc.* **2005**, *127*, 5449.

(24) Neupane, K. P.; Gearty, K.; Francis, A.; Shearer, J. *J. Am. Chem. Soc.* **2007**, *129*, 14605.

(25) Herbst, R. W.; Guce, A.; Bryngelson, P. A.; Higgins, K. A.; Ryan, K. C.; Cabelli, D. E.; Garman, S. C.; Maroney, M. J. *Biochemistry* **2009**, *48*, 3354.

(26) Sawyer, D. T.; Valentine, J. S. *Acc. Chem. Res.* **1981**, *14*, 393.

(27) Perry, J. J. P.; Shin, D. S.; Getzoff, E. D.; Tainer, J. A. *Biochim. Biophys. Acta* **2010**, *1804*, 245.

(28) Dey, A.; Green, K. N.; Jenkins, R. M.; Jeffrey, S. P.; Darensbourg, M. Y.; Hodgson, K. O.; Hedman, B.; Solomon, E. I. *Inorg. Chem.* **2007**, *46*, 9655.

(29) Langford, C. H.; Gray, H. B. *Ligand Substitution Processes*; W. A. Benjamin: New York, 1966.

(30) Ryan, K. C.; Johnson, O. E.; Cabelli, D. E.; Brunold, T. C.; Maroney, M. J. *J. Biol. Inorg. Chem.* **2010**, *15*, 795.

(31) Johnson, O. E.; Ryan, K. C.; Maroney, M. J.; Brunold, T. C. *J. Biol. Inorg. Chem.* **2010**, *15*, 777.

(32) Szilagyi, R. K.; Bryngelson, P. A.; Maroney, M. J.; Hedman, B.; Hodgson, K. O.; Solomon, E. I. *J. Am. Chem. Soc.* **2004**, *126*, 3018.

(33) Pelmenschikov, V.; Siegbahn, P. E. M. *J. Am. Chem. Soc.* **2006**, *128*, 7466.

(34) Prabhakar, R.; Morokuma, K.; Musaev, D. G. *J. Comput. Chem.* **2006**, *27*, 1438.

(35) Pavlov, M.; Siegbahn, P. E. M.; Blomberg, M. R. A.; Crabtree, R. H. *J. Am. Chem. Soc.* **1998**, *120*, 548.

(36) Niu, S. Q.; Thomson, L. M.; Hall, M. B. *J. Am. Chem. Soc.* **1999**, *121*, 4000.

(37) Amara, P.; Volbeda, A.; Fontecilla-Camps, J. C.; Field, M. J. *J. Am. Chem. Soc.* **1999**, *121*, 4468.

(38) O'Reilly, J. E. *Biochim. Biophys. Acta* **1973**, *292*, 509.

(39) Scott, R. A. In *Physical Methods in Bioinorganic Chemistry: Spectroscopy and Magnetism*; Que, L., Jr. , Ed.; University Science Books: Sausalito, CA, 2000, p 465.

(40) Ankudinov, A. L.; Ravel, B.; Rehr, J. J.; Conradson, S. D. *Phys. Rev. B* **1998**, *58*, 7565.

CHAPTER 4

MODELS OF Ni-SOD UTILIZING LIGANDS OF HIGHER DENTICITY FEATURING AN AXIAL NITROGEN DONOR[1]

[1] Gale, E. M., Simmonett, A. C., Telser, J., Schaefer, H. F., III, Harrop, T. C. *Inorg. Chem*. **2011**, *50*, 9216. Reprinted here with permission of publisher.

4.1 Abstract

We present in this chapter a model of Ni-SOD featuring all relevant donor functionalities within a single, penta-dentate chelate and in the proper spatial disposition around the Ni center. X-ray structural analysis, ^{1}H NMR and UV-vis spectroscopy show that Ni(II)N_2S_2 square-planar (S = 0) geometry is maintained in both the solid- and solution-states. Structural analysis indicates that the unbound pyridyl-N ligand, modeling the His1 imidazole side chain, is of a similar disposition to the imidazole ligand of Ni-SOD_{red} and poised to bind by mere rotation of the N-donor. This model is stable under aqueous conditions, as the multi-dentate chelate litigates RS^- dissociation due to favorable solvation interactions. Oxidation of this $[Ni(N_3S_2)]^-$ complex results in quantitative formation of 0.5 mol-equiv. of a disulfide linked, dinuclear $[Ni_2(N_3S)_2]$ species. This dinuclear species can in turn by quantitatively reduced back to $[Ni(N_3S_2)]^-$ form by treatment with a stoichiometric reductant. Trapping oxidized intermediates en route to this disulfide linked product for EPR analysis revealed the presence of a Ni(III) species featuring a g-spread similar to that observed for Ni-SOD_{ox} as well as an isotropic signal, likely due to an unbound thiyl radical present prior to disulfide coupling. Using an analogous model lacking any potential axial N-donor, no paramagnetic intermediates were observed and the reactivity pathway upon oxidation was less controlled and accompanied by demetalation/polymerization. The appended N-donor modeling the His1 imidazole plays a crucial role in stabilizing Ni(III), albeit transiently, and facilitates clean conversion to more thermodynamically favorable species from which starting material can be generated. Thus, we have been able to successfully mimic aspects of

the Ni-SOD redox cycle using a synthetic model. A new species featuring steric bulk around the thiolate modeling Cys6 has been prepared in an effort to hinder or preclude disulfide formation upon oxidation to Ni(III). Although structurally similar, preliminary results reveal unexpected properties for this new system

4.2 Introduction

The ability to readily tune the electronic properties of the ligand component modeling Cys6 in the models discussed in Chapters 2 and 3 facilitated an in-depth analysis as to the nature and role of Ni-S bonding in Ni-SOD_{red}.[1-3] From these studies, along with work completed by others,[4-7] a thorough electronic depiction of Ni-SOD_{red} and how this unique bonding scenario may be used to rationalize aspects of catalytic activity has accumulated.

In the study presented herein,[8] we turn our attention towards the role played by the imidazole side chain of His1. As discussed in Chapter 1, mutants lacking this axial donor ligand display drastically decreased catalytic activity. This ligand has been implicated in stabilization of Ni-SOD_{ox} by way of reshuffling the frontier molecular orbitals so that the cysteinate ligands are no longer significant contributors to the singly occupied HOMO. DFT studies suggest that the resultant HOMO is 77% Ni-based and comprised of the d_z^2 orbital and non-bonding with S-based π-orbitals capable of participating in auto-redox processes.

The system discussed in this chapter represents the first synthetic model of Ni-SOD containing all relevant donor functionalities within a spatially and electronically accurate ligand frame. Analysis of the structural, electronic and reactivity properties

of this model complex provide insights into the role played by this labile axial donor with regards to the oxidized and reduced states of Ni-SOD (Figure 1).

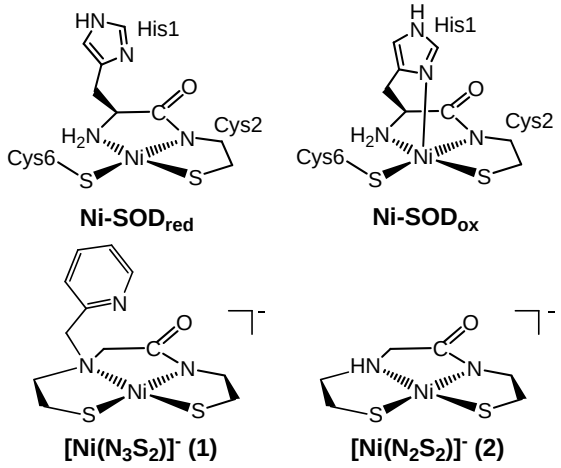

Figure 1. (Top): Active site of Ni-SOD in the reduced and oxidized states. (Bottom): Model complexes used in this study.

4.3 Ligand Design and Preparation of K[Ni(N_3S_2)]

Despite the advantages of modeling Cys6 with an exogenously added ligand amenable to diverse substitution, the mono-dentate and labile nature of this donor made for difficult handling under certain conditions. For example, favorable solvation interactions were sufficient to promote thiolate departure under aqueous conditions, making study difficult under more biologically relevant conditions. Also, observation of Ni(III) species was exceedingly difficult due to departure of this ligand following auto-redox processes. We postulated that tethering all donor groups within a single multi-dentate ligand framework would provide additional stability to the NiN_2S_2 motif via precluding complications arising from ligand lability. By incorporating the axial-N donor into a well behaved square-planar scaffold, we could turn our undivided attention towards this component alone.

The ligand $H_3N_3S_2$ (Scheme 1) (where Hs represent dissociable protons) was designed to coordinate Ni(II) in a square-planar fashion mimicking that observed in Ni-SOD_{red}[9-10] with the amine-N, carboxamido-N and thiolato-S donors positioned accordingly. The pyridyl-N donor, approximating the imidazole side chain of His1, was appended through the amine-N, and poised to bind Ni as part of a stable, five-membered chelate ring. This was achieved through N-alkylation of S-trit-N_2S_2, the preparation of which is described elsewhere,[11] affording the pre-ligand in 62% yield. The S-trityl protecting groups were removed via treatment with triethylsilane in TFA, affording $H_3N_3S_2$ in 81% yield. Overall, this ligand was obtained through five straightforward synthetic steps. Treatment of $H_3N_3S_2$ with KOMe in MeOH followed by treatment with slightly substoichiometric [$Ni(OAc)_2$•$4H_2O$] afforded K[$Ni(N_3S_2)$] (**1**) (Figure 1) as orange solids in 91% yield.

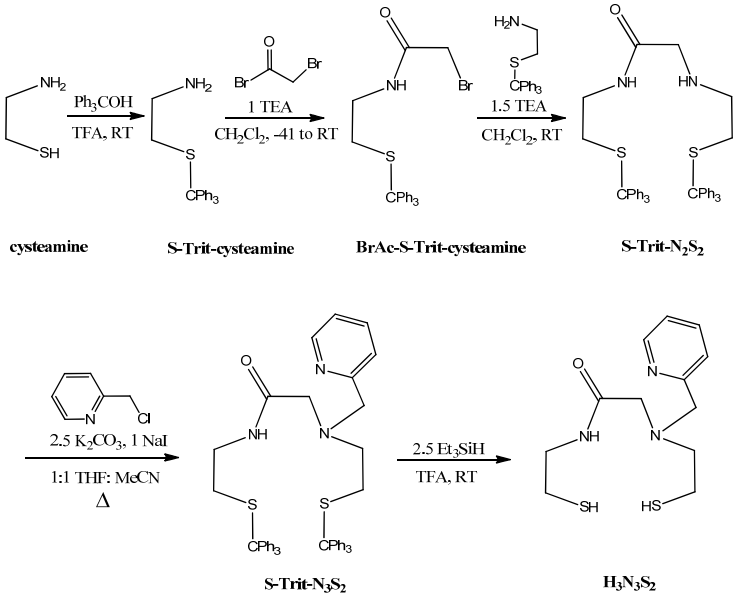

Scheme 1. Synthesis of $H_3N_3S_2$.

4.4 Structure and Properties

Complex **1** could be obtained as small, red, single crystals (formulated as {K[Ni(N_3S_2)]$_2$•2MeOH}) suitable for X-ray diffraction by recrystallization from 1:1 MeOH/Et_2O at RT (one anionic [Ni(N_3S_2)]$^-$ portion is displayed in Figure 2; see Table 1 for metric parameters). The Ni(II) ion in **1** is housed within a N_2S_2 mixed amine/carboxamide/di-thiolate, square-planar coordination environment; similar to that observed in Ni-SOD_{red} (see Table 2 for comparison against Ni-SOD) the appended pyridyl-N donor remains unbound but in close proximity to the Ni(II) center.[9-10] Deviations from a perfect square-plane are slight, with the most acute digression arising from the $N_{carboxamide}$-Ni-N_{amine} bond angle (84.94°; metric parameters given as the average of two unique ions per asymmetric unit), and the most obtuse arising from the S-Ni-S bond angle (94.96°). The electronic asymmetry of the two equatorial N-donors is reflected in the respectively observed bond lengths. The Ni-$N_{carboxamide}$ bond length is 1.8575(2) Å whereas the Ni-N_{amine} bond length is 1.954(2) Å, reflecting the more strongly σ-donating nature of the carboxamide-N ligand. This inequivalency in donor strength is manifested in a slight elongation of the Ni-S bond (2.1805(8) Å) trans to the carboxamide-N donor relative to that trans to the amine-N (2.1739(8) Å). Interactions of both coordinated thiolate ligands with the K^+ cation are observed in the solid-state structure (the pyridine-N, one MeOH and carbonyl of neighboring anion also coordinate K^+), however, and this may somewhat obscure the bonding description as described by ligand contributions alone. The unbound pyridine-N is located 3.210 Å away from the Ni(II) ion. The lone pair of this N-donor is pointed 47° away from the least squares plane defined by Ni and the four

equatorially coordinated atoms. The disposition of the appended pyridine is analogous to the imidazole side chain of His1 observed in Ni-SOD$_{red}$, twisted ~55° from the Ni center and poised to bind upon mere rotation of the Cβ-Cγ bond.[10]

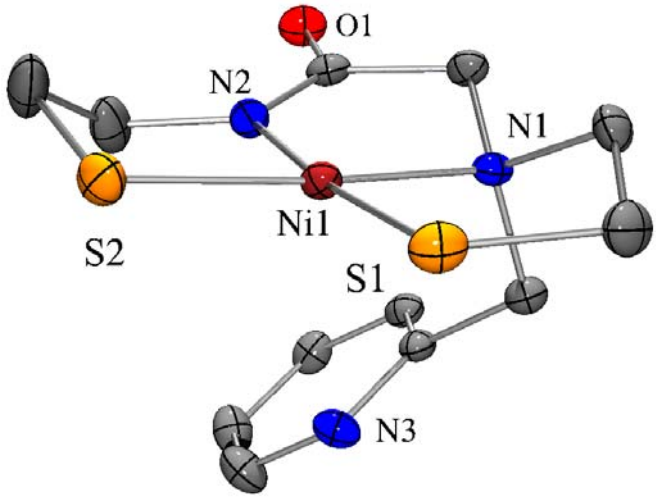

Figure 2. ORTEP diagram of one of the unique anions of K[Ni(N_3S_2)] (**1**) showing 50% thermal ellipsoids for all non hydrogen atoms.

Table 1. Selected bond distances [Å] and angles [deg] for **1**, **2**[7] and **4** (*vide infra*). N(1), N(2), N(3), S(1) and S(2) model the His1 amine-N, Cys2 carboxamide-N, His1 imidazole-N, Cys2 thiolate-S and Cys6 thiolate-S, respectively, of Ni-SOD.[9-10]

	1	**2**[7]	**4**
Ni(1)-N(1)	1.954(2)	1.937(3)	1.943(7)
Ni(1)-N(2)	1.861(2)	1.862(2)	1.859(7)
Ni(1)-N(3)	3.179 (unbound)		3.196 (unbound)
Ni(1)-S(1)	2.1812(8)	2.1671(8)	2.170(3)
Ni(1)-S(2)	2.1797(8)	2.1711(7)	2.165(3)
N(1)-Ni(1)-N(2)	84.88(10)	84.46(12)	86.5(3)
N(1)-Ni(1)-S(1)	91.08(7)	90.62(9)	90.4(2)
N(1)-Ni(1)-S(2)	173.32(7)	172.37(10)	174.6(2)
N(2)-Ni(1)-S(2)	88.66(8)	89.57(7)	88.2(2)
S(1)-Ni(1)-S(2)	95.22(3)	95.47(3)	94.82(10)
N(2)-Ni(1)-S(1)	173.89(8)	174.78(8)	175.5(2)
Ni(1)-S(1)-C(1)	97.97(10)	97.49(12)	100.1(3)
Ni(1)-S(2)-C(6)	97.44(11	97.09(10)	97.9(3)
NiN_2S_2-N(3)[a]	41.15		37.75

Table 2. Comparison of Ni–N/S bond distances (Å) of **1**, **2** and **4** with those reported from the crystal structures of Ni-SOD_{red} from *Streptomyces coelicolor,*[10] *Streptomyces seoulensis,*[18] and EXAFS (*Streptomyces seoulensis*).[12] N(1), N(2), N(3), S(1) and S(2) represent the His1 amine-N, Cys2 carboxamide-N, His1 imidazole-N, Cys2 thiolate-S and Cys6 thiolate S, respectively, of Ni-SOD.

	1	**2**	**4**	**Ni-SOD_{red}**[18]	**Ni-SOD_{red} (EXAFS)**[19]
Ni–N1	1.954(2)	1.937(3)	1.943(7)	2.07	1.87(2)
Ni–N2	1.8575(2)	1.862(2)	1.859(7)	1.94	
Ni–S1	2.1805(8)	2.1671(8)	2.170(3)	2.18	2.154(4)
Ni–S2	2.1739(8)	2.1711(7)	2.165(3)	2.24	
Ni-N3	3.210		3.196	3.96	

The solution spectroscopic properties of **1** are similar to those observed in the models presented in Chapters 2 and 3 as well as other similarly disposed NiN_2S_2 complexes.[5,7] The resonances observed in the ^{1}H NMR spectra of **1** at 298 K in several solvents (CD_3OD, D_2O, d_6-DMSO) are consistent with diamagnetic behavior, indicative that the square-planar (S = 0) coordination observed in the solid-state is maintained in both polar protic and aprotic solvents. Similar to Ni-SOD_{red},[13] the UV-vis spectrum of **1** in pH 7.5 buffer (PIPES) at 298 K displays ligand-field transitions at 449 nm (ε = 230 M^{-1} cm^{-1}) and 570 nm (ε = 50 M^{-1} cm^{-1}) (Figure 3). The UV-vis profile of **1** in MeOH and DMF are highly similar, indicating that the electronic disposition is not perturbed by solvent dielectric to any significant degree.

Interestingly, upon gradually cooling solutions of **1** in CD_3OD from 298 K to 236 K, a loss of well-resolved, diamagnetic character was observed in resonances

arising from the portion of the ligand frame (Figure 4) comprising the square-planar N_2S_2 platform, and the resonances broadened and coalesced. Also, the most downfield shifted resonance at RT (doublet, presumably arising from the proton located α to the pyridyl-N) became broad and shifted further upfield relative to the other resonances at decreased temperature. Interestingly, this behavior is not observed for the similarly disposed model K[Ni(N_2S_2)] (**2**), which affords a nearly structurally and electronically identical square-planar NiN_2S_2 species, but lacking a potential axial N-ligand.[7] Considering the similarities in size and electronic disposition, it is possible that this peak broadening and scrambling observed upon cooling **1** is a result of interactions of the previously unbound N-donor with the Ni(II) center. This interaction appears to be subtle, as the low-temperature (< 236 K) UV-vis spectra of **1** remains unchanged from that seen at 298 K.

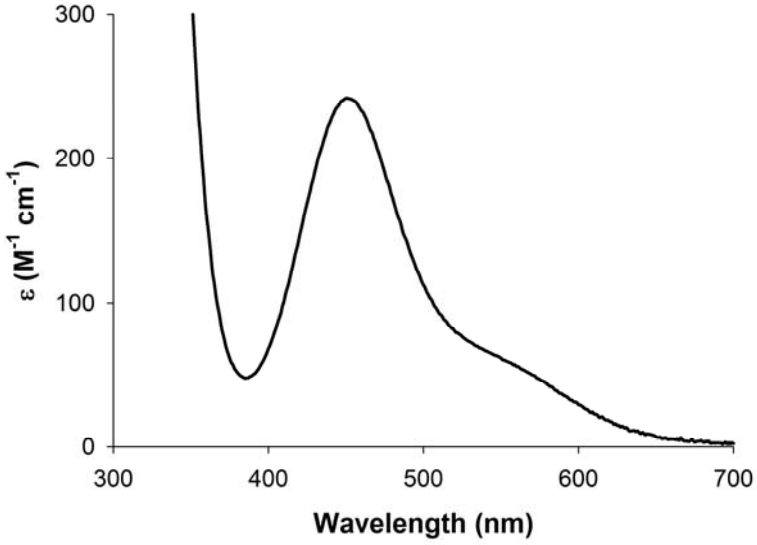

Figure 3. UV-vis profile of **1** in pH 7.5 buffer (50 mM PIPES).

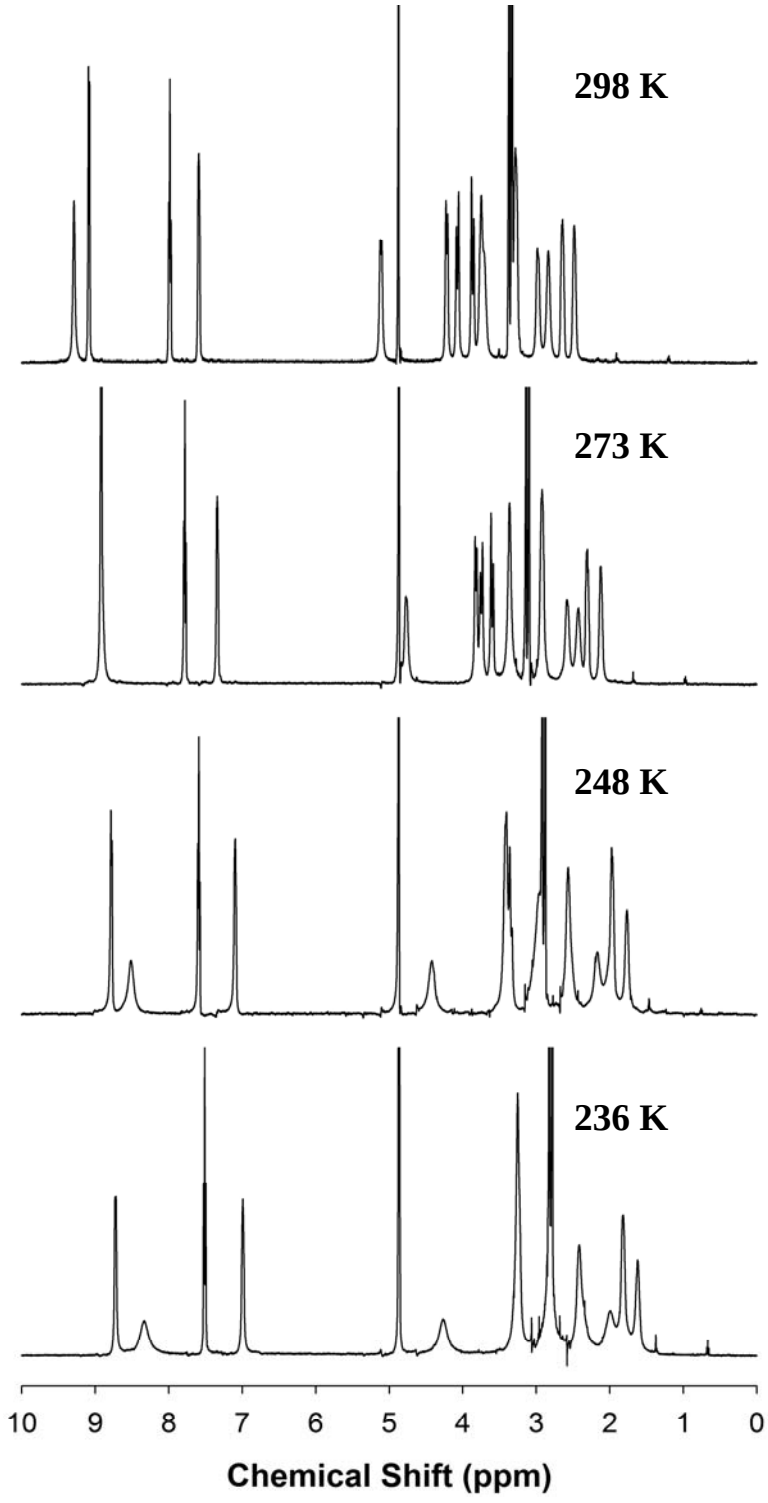

Figure 4. ^{1}H NMR of **1** in CD_3OD at variant temperatures, descending from top: 298 K, 273 K, 248 K, 236 K. (Singlets at 4.87 ppm (all spectra) and 3.31 (RT, shifts slightly as temperature varies) are from residual protio solvent).

4.5 Redox Chemistry/Reactivity

Complex **1** does not display any reversible Ni(II)/Ni(III) chemistry as evidenced by CV measurements, rather, an oxidative event is observed at -0.105 V vs. Ag/AgCl in DMF (Figure 5, top). This oxidation event is 0.16 V more negative than that measured for **2** (0.60 V vs Ag/AgCl)[7] and it appears that the presence of the axial-N ligand, although unbound, may serve to depress the oxidation potential. A reduction event is observed at -1.33 V (Figure 5, middle). Interestingly, the presence of this wave is contingent upon initial oxidation of **1**; if scans begin in the reductive direction poised below the oxidation potential of **1**, this event is not observed.

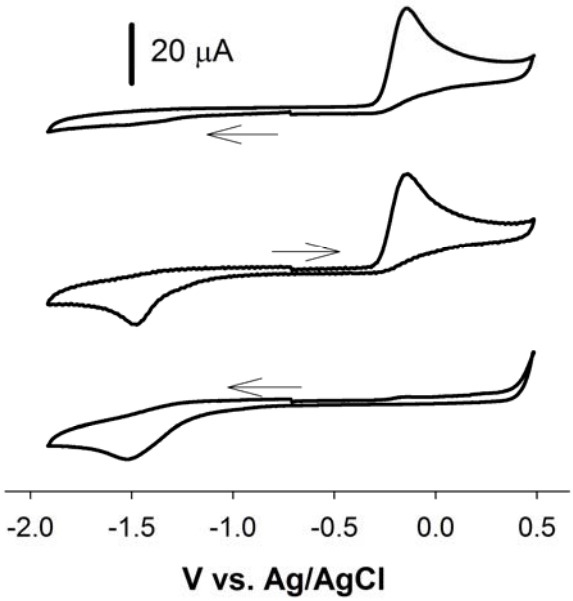

Figure 5. (Top): CV of 5mM **1** in DMF showing oxidation event at -0.105 V. (Middle): CV of 5 mM **1** in DMF showing oxidation event along with reduction of subsequently formed **3**. (Bottom): CV of 5 mM **3** in DMF showing reduction event at -1.325 V (vs. Ag/Ag^+ in MeCN (0.01 M $AgNO_3$, 0.1 M $^nBu_4NPF_6$), 0.1 M $^nBu_4NPF_6$ supporting electrolyte, glassy carbon working electrode, scan rate: 100 mV/s, RT).

In order to discern the nature of the oxidized product of **1** and identify the newly formed species observed in the CV, bulk oxidation was performed. Ferrocenium hexafluorophosphate, used here as a stoichiometric one-electron oxidant, added to **1** in DMF at -41 °C resulted in instantaneous formation of a brown-orange solution from which orange solids of a product identified as [{$Ni_2(N_3S_2)_2$}] (**3**) were isolated. Oxidation to **3** appears to be a clean process, as no other products could be identified by ^{1}H NMR or ESI-MS. It should be noted that oxidation of **2** forms only intractable brown solids upon oxidation, and no paramagnetic intermediates can be trapped. Although characterization is limited by the poor solubility of the resultant product(s), ESI-MS reveals the presence of species corresponding to $[Ni_3(N_3S_2)_2 + H]^+$, consistent with some demetalation processes.

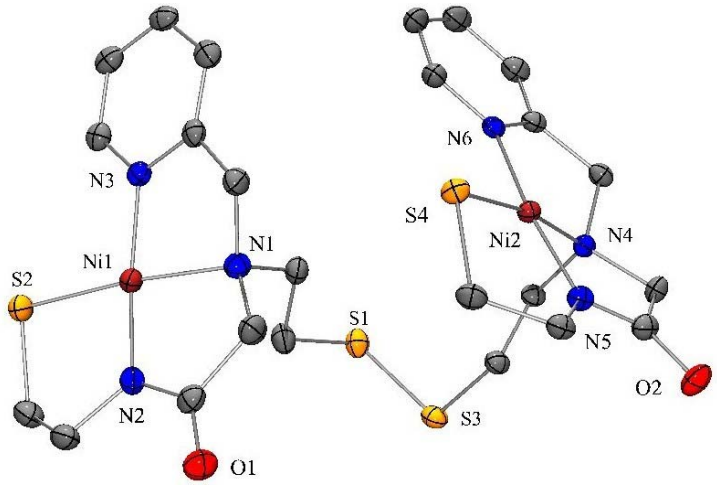

Figure 6. ORTEP diagram of {$Ni_2(N_3S_2)_2$•MeOH} (**3**) showing 50% thermal ellipsoids for all non hydrogen atoms (MeOH solvent of crystallization omitted for clarity).

Table 3. Selected bond distances [Å] and bond angles [deg] for **3** and **5** (*vide infra*). There are two monomers of **5** per asymmetric unit.

	3	**5**
Ni(1)-N(1)	1.9447(19)	1.929(7)
Ni(1)-N(2)	1.830(2)	1.832(9)
Ni(1)-N(3)	1.8947(19)	1.875(8)
Ni(1)-S(2)	2.1573(6)	2.148(3)
N(1)-Ni(1)-N(2)	86.73(8)	85.4(3)
N(1)-Ni(1)-N(3)	84.84(8)	85.2(3)
N(2)-Ni(1)-N(3)	169.02(9)	170.5(3)
N(1)-Ni(1)-S(2)	174.17(6)	172.4(2)
N(2)-Ni(1)-S(2)	89.31(6)	89.8(3)
N(3)-Ni(1)-S(2)	99.60(6)	99.7(2)
Ni(1)-S(2)-C(6)	96.03(8)	99.6(3)
Ni(2)-N(4)	1.9476(18)	1.943(7)
Ni(2)-N(5)	1.8442(18)	1.836(9)
Ni(2)-N(6)	1.8942(18)	1.901(8)
Ni(2)-S(4)	2.1632(6)	2.148(3)
N(4)-Ni(2)-N(5)	85.74(8)	85.4(3)
N(4)-Ni(2)-N(6)	85.35(8)	84.6(3)
N(5)-Ni(2)-Ni(6)	170.12(8)	169.3(3)
N(4)-Ni(2)-S(4)	170.77(6)	172.6(2)
N(5)-Ni(2)-S(4)	88.86(8)	89.7(2)
N(6)-Ni(2)-S(4)	100.47(6)	84.6(3)
Ni(2)-S(4)-C(18)	96.87(7)	
Ni(2)-S(4)-C(20)		98.8(3)

Recrystallization of **3** by slow diffusion of Et_2O into a saturated MeOH solution afforded small orange crystals suitable for X-ray diffraction. Structural analysis of **3** (formulated as [{$Ni_2(N_3S_2)_2$}•MeOH]) revealed two identical square-planar Ni(II)N_3S units connected via a symmetric disulfide linkage. (Figure 6) The disulfide linkage was comprised of the thiolate ligands trans to the carboxamido-N donor in **1** and the appended pyridyl-N donor had taken up this coordinative site. The

Ni-N and Ni-S bond lengths were contracted slightly vs. those observed in **1** as a result of the weakened coordination sphere arising through replacement of the anionic thiolate ligand. The most significant change is observed for the Ni-$N_{carboxamide}$ bond, which contracted ~0.02 Å to 1.8371(19) Å (average of two Ni centers). The Ni-S and Ni-N_{amine} bonds correspondingly contract by ~0.01 Å to 2.1603(6) and 1.9462(19) Å, respectively (Table 3). The newly formed Ni-$N_{pyridine}$ bond measured at 1.8945(19) Å, comparable to that observed in the Ni(nmp) synthon discussed in Chapter 2.

CV measurements of **3** in DMF reveal a reductive wave at -1.325 V (Figure 5, bottom), corresponding to the species generated upon electrochemical oxidation of **1**. Analogously, if initiating scans in the oxidative direction poised above the reduction potential of **3**, no oxidation chemistry was observed. However, upon electrochemical reduction of **3**, a subsequent oxidation event arises corresponding to that observed in the CV of **1**. Additionally, treatment of **3** with 2 mol-equiv. of the one-electron reductant decamethylcobaltocene afforded quantitative regeneration of **1**.

The conversion of **1** to **3** is rapid and difficult to monitor via optical spectroscopy, even at reduced temperatures. Although the ultimate product is indicative of S-oxidation, it is conceivable that a Ni(III) species could be generated transiently before auto-redox and rearrangement to the disulfide linked product. In an attempt to glean insight into the details of this rapid conversion, we trapped intermediates formed immediately upon oxidation *in situ* for EPR analysis. The EPR spectrum of the trapped, oxidized product is dominated by an intense isotropic signal at g = 2.03 (Figure 7), likely arising from a thiyl radical. Also observed is an anisotropic signal with a large g-spread (**g** = [2.26, 2.17]). This lineshape is hallmark

of Ni(III) in tetragonal symmetry and accompanied by g_z signal at ~2.00;[14-15] however, the presence of this feature is difficult to discern in the presence of the large radical signal. Indeed, analogous Ni(III)-based features are observed in Ni-SOD_{ox}[9,12] and the small handful of known Ni(III)N_3S_2 species.[16-20] At first glance, the observed anisotropic signal appears very weak; however, double integration reveals a ratio of roughly 5:1 Ni(III)/proposed S-radical. The intensity of this signal remained constant regardless of reaction concentration used for this *in situ* study.

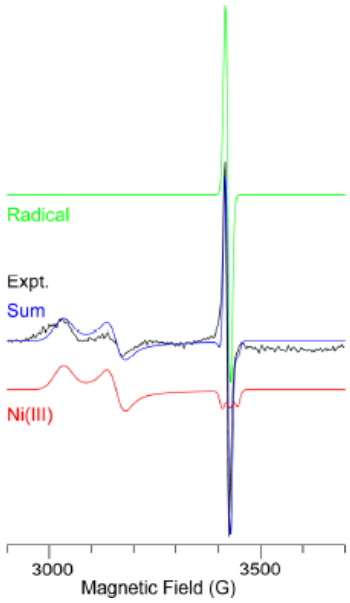

Figure 5. X-band EPR spectrum of the *in situ* oxidized products from the reaction of **1** with ferrocenium hexafluorosphosphate (black) in DMF with QPOWA simulations for $\mathbf{1^{ox}}$ (red trace), $\mathbf{1^{ox}S_{off}}$ (green trace) and summation (blue trace). Experimental EPR parameters: temperature, 7 K; microwave frequency, 9.59 G; microwave power. 1.00 mW; modulation amplitude, 6.48 G; time constant, 41 ns; scan time, 168 s. Simulation parameters: $\mathbf{1^{ox}S_{off}}$ (green trace), g = 2.03, W(Guassian, hwhm) = 20 MHz, scaled to experimental intensity; $\mathbf{1^{ox}}$ (red trace), g = [2.26, 2.17, 2.00], $A(^{14}N)$ =

50 MHz at g = 2.00, W = 80, 60, 20 MHz, scaled to match approximate signal intensities at 3000-3200 G.

Simulations of the EPR parameters of likely paramagnetic candidates were performed in order to further guide our spectral assignments. Simulations of [Ni(III)(N_3S_2)] in five-coordinate square-pyramidal form (**1**^{ox}; it should be noted that the coincidence of the large radical signal with the g_z feature (and expected ^{14}N hyperfine) of **1**^{ox} obscures rigorous assignment as a five-coordinate species) and in four coordinate Ni(II)(N_3S) form with the unpaired electron residing on the S-previously coordinated trans to the carboxamide-N (**1**^{ox}**S**$_{off}$; one-half of **2**) were generated independently and summed in a 5:1 ratio, respectively. The resultant simulated spectrum was in excellent accord with that observed experimentally (Figure 7).

Complex **1** does not show any reactivity in the presence of 12 mol-equiv $O_2^{\bullet-}$ (KO_2 solvated in THF with 18-crown-6) in DMF. Redox in this scenario is unlikely, since $O_2^{\bullet-}$ reduction is generally a proton coupled event. The lack of anion binding (10 mol-equiv. N_3^- also does not bind in DMF) is consistent with the stable square-planar configuration at Ni(II). Addition of a 90 mol-equivs. KO_2 to **1** at pH 7.5 (PIPES buffer) resulted in S-oxygenation, as [**1** + nO]$^-$ (n = 2-4) were observed by ESI-MS analysis. This oxygenation is likely due to H_2O_2; whether this arises from spontaneous dismutation or a Ni(II)-catalyzed process is yet to be determined. Regardless, it appears that **1** undergoes oxidative modifications under pseudo-physiological SOD relevant conditions. Complex **1** is also somewhat sensitive to atmospheric O_2, as observed by UV-vis.

4.6 Computational Evaluation

DFT computations of **1,** square-pyramidal $\mathbf{1}^{ox}$ and $\mathbf{1}^{ox}\mathbf{S}_{off}$ were generated. The input coordinates for **1** and $\mathbf{1}^{ox}$ were obtained from the crystallographic data of **1**, whereas that of $\mathbf{1}^{ox}\mathbf{S}_{off}$ was obtained from one-half of **3** (Figures 8, 9 and 10, respectively). The geometry optimized models were generated using the pure exchange OLYP functional (def2-TZVPP basis set). The metric parameters of geometry optimized **1** and $\mathbf{1}^{ox}\mathbf{S}_{off}$ compare well to the crystallographically determined structures from which the input files were obtained.

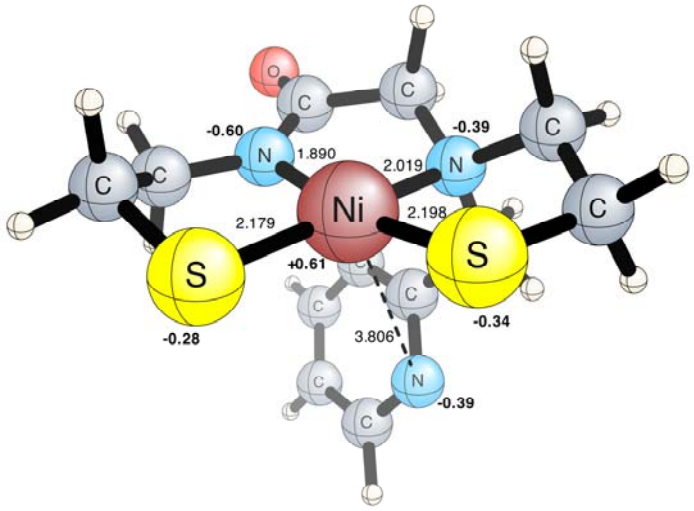

Figure 8. DFT geometry optimized model of the anion of **1** featuring optimized bond lengths (Å) and natural population analysis atomic charges (bold) from OLYP/def2-TZVPP.

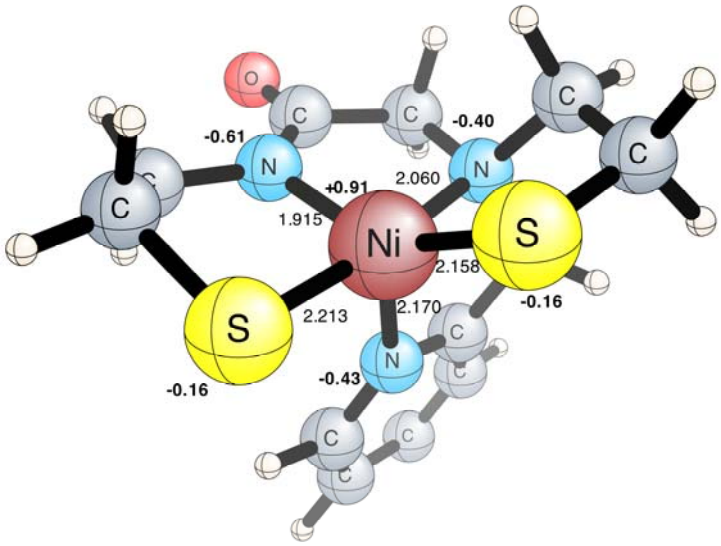

Figure 9. DFT geometry optimized model of $\mathbf{1^{ox}}$ featuring optimized bond lengths (Å) and natural population analysis atomic charges (bold) from OLYP/def2-TZVPP.

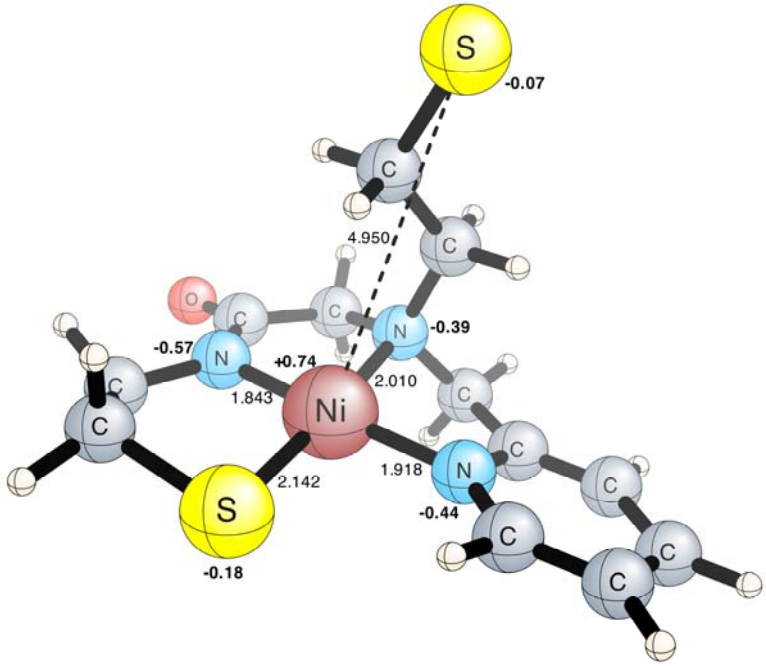

Figure 10. DFT geometry optimized model of $\mathbf{1^{ox}S_{off}}$ featuring optimized bond lengths (Å) and natural population analysis atomic charges (bold) from OLYP/def2-TZVPP.

The DFT optimized structure of **1** accurately models the electronically asymmetric nature of the ligand framework, as the carboxamide-N donor carries significantly more charge density (-0.60) than the amine-N (-0.39) (Figure 8). The more strongly donating nature of the carboxmide-N is also evidenced by the decreased Ni-$N_{carboxamide}$ bond length relative to the Ni-N_{amine} bond (1.890 Å and 2.019 Å, respectively); accordingly, the Ni-S bond trans to the carboxamide-N is elongated (2.198 Å) relative to that trans to the amine-N (2.179 Å). The thiolato-S trans to the carboxamide-N also carries more charge density than that trans to the amine-N (-0.34 and -0.28), making it the more probable candidate for S-based oxidation.

Analysis of the frontier orbitals of **1** (Figure **11**) reveals a largely Ni and S based HOMO, with the Ni(d_{yz}) orbital (along the N-Ni-S vector possessing the carboxamide-N) contributing to 59% of the overall orbital contribution, and the S(p_z) orbitals of the thiolate ligands trans to the carboxamide-N and amine-N contributing 23% and 8%, respectively. Given the highly covalent Ni-S bonding of **1**, it is not surprising that S-based oxidation is manifest in the product isolated.

Geometry optimized $\mathbf{1^{ox}}$ is five-coordinate and intermediate between square-pyramidal and trigonal-bipyramidal geometry (τ = 0.51) (Figure 9). The Ni-$N_{pyridine}$ bond length was 2.17 Å. Only slight changes from that observed in DFT optimized **1** were observed in the remaining Ni-N and Ni-S bond lengths. The charge density at the S-atoms signicantly decreased upon oxidation (-0.16 for both), consistent with covalent bonding to the more electropositive Ni(III) center. Spin density plots (Figure 12) revealed 64% of the total spin resides on the Ni atom, consistent with that

observed by EPR; 23% of the spin density was found on the thiolate-S trans to the carboxamide-N, consistent with a highly covalent Ni-S bond. Unsuprisingly, the vast majority of the spin-density of DFT optimized $\mathbf{1^{ox}S_{off}}$ (Figure 13) was found to reside in the unbound S.

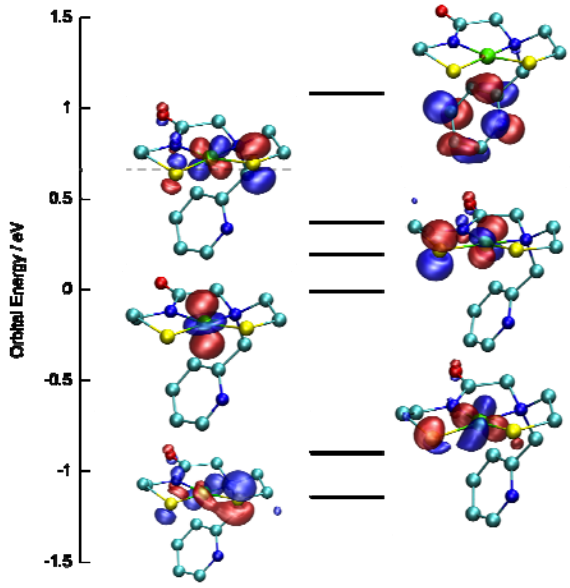

Figure 11. DFT generated isosurface plots from OLYP/deg2-TZV-PP of the frontier MOs of the geometry optimized structure of the anion of **1**. In each column, the MOs descend from LUMO to HOMO-4. The dashed line indicates the level below which orbitals are occupied. H atoms omitted for clarity.

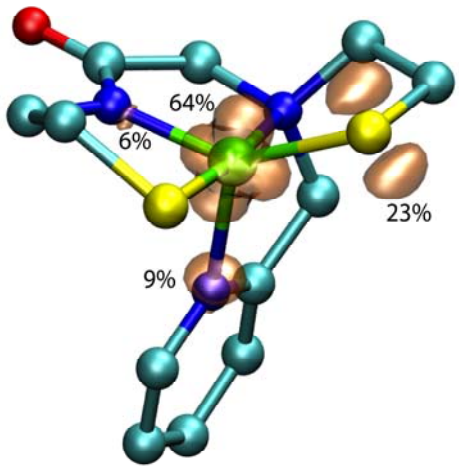

Figure 12. Spin-density plot for $\mathbf{1^{ox}}$. H atoms have been omitted for clarity. Approximate atomic contributions to the overall spin-density are depicted; these were derived by multiplying the difference in the α and β natural atomic populations by 100. Only contributions greater than 5% are labeled.

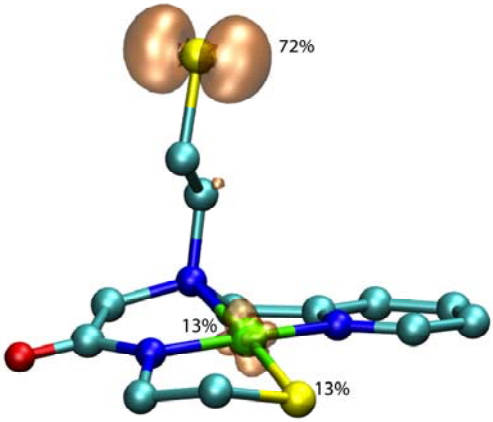

Figure 13. Spin-density plot for $\mathbf{1^{ox}S_{off}}$. H atoms have been omitted for clarity. Approximate atomic contributions to the overall spin-density are depicted; these were derived by multiplying the difference in the α and β natural atomic populations by 100. Only contributions greater than 5% are labeled.

4.7 Mechanistic Considerations

Given the disulfide linked product **3**, spectroscopic evidence of $\mathbf{1^{ox}}$ and $\mathbf{1^{ox}S_{off}}$ en route to product formation and the computational assessment of these species, a mechanistic pathway was formulated (Scheme 2). It appears likely that a five-coordinate species similarly disposed to that observed in Ni-SOD_{ox} is transiently formed upon oxidation of **1**. An auto-redox process likely ensues, generating Ni(II) and a thiyl radical, followed by a subsequent ligand rearrangement resulting in displacement of the thiyl radical by the previously unbound axial pyridine donor. It is possible that these paramagnetic species are in dynamic equilibrium with one another. In fact, the gas phase calculations indicate that $\mathbf{1^{ox}}$ is more stable than $\mathbf{1^{ox}S_{off}}$ by 14.2 kcal/mol; simulation of the solvent dielectric using the conduction-like screening model (COSMO) suggests $\mathbf{1^{ox}}$ is more stable by 13.4 kcal/mol in DMF. Regardless, **3** represents a thermodynamic sink and $\mathbf{1^{ox}}$ and $\mathbf{1^{ox}S_{off}}$ remain short-lived, even at reduced temperatures. It is most likely that reduction by decamethylcobaltocene occurs at the disulfide bond, and the reformed tri-anionic ligand quickly rearranges around Ni(II) to form **1**.

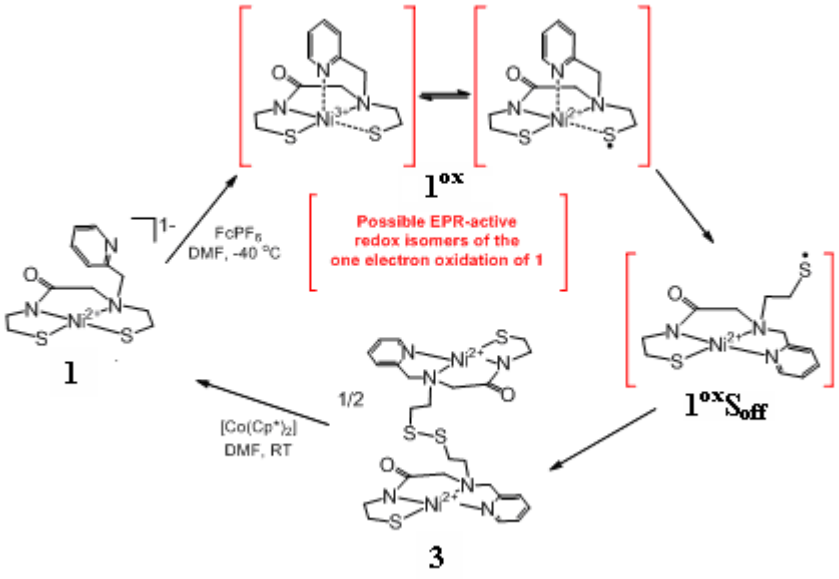

Scheme 2. Proposed mechanism of **1**-to-**3** interconversion; hypothesized intermediates in red brackets.

As discussed above, **2** appears to undergo an uncontrolled decomposition process upon oxidation, although possessing a nearly identically disposed Ni(II) and N_2S_2 framework. Clearly, the presence of an additional N-donor capable of binding Ni(III) is critical for the stabilization, even if transient, and controlled reactivity of Ni-complexes analogous to the Ni-SOD active site.

4.8 Future Directions

Considering the conversion of **1** to **3** upon chemical oxidation, we postulated that we may hinder the kinetics of, or perhaps even preclude, disulfide formation through incorporation of sufficient steric bulk around the thiolate ligands. Indeed, the few spectroscopically observable,[16,19,21] and one isolable,[17] Ni(III)-N/S complexes featuring alkyl-thiolate ligands benefit from the steric encumberence of the S-donors.

Methodology efforts towards incorporating a variety of *R* substituents *α* to the thiolate-S have been ongoing in our laboratory and are discussed in Appendix C.

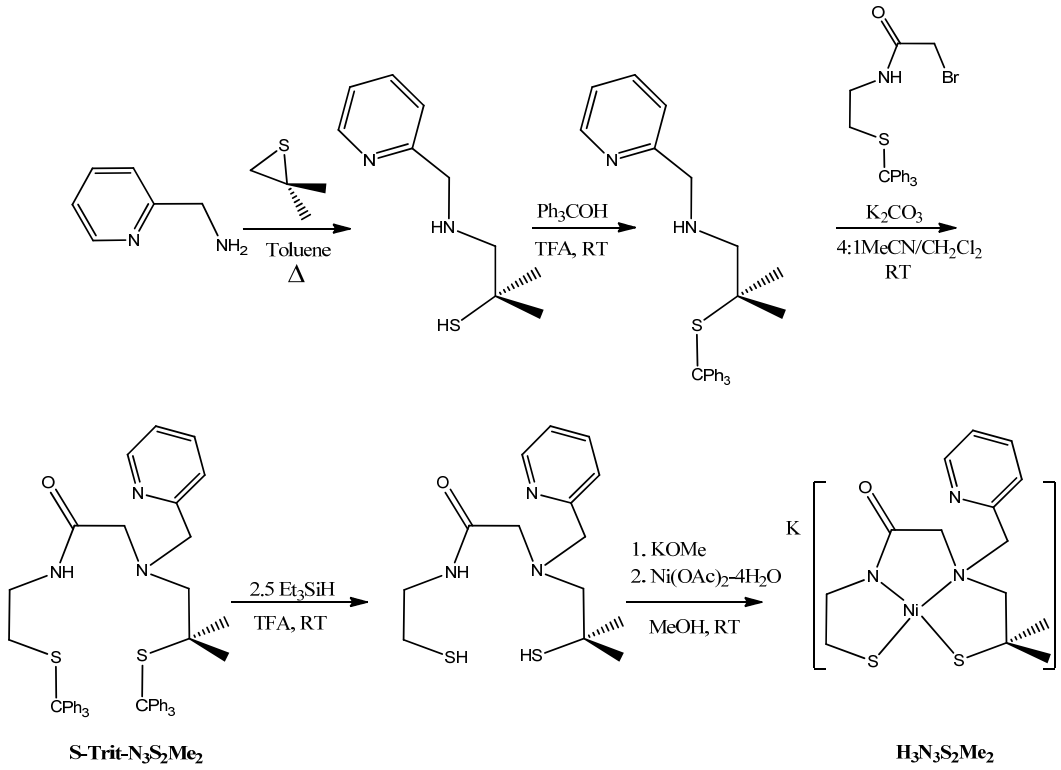

Scheme 3. Synthesis of $H_3N_3S_3Me_2$ and subsequent metalation reaction.

As an initial entry into models within sterically protected ligand frames, we prepared the ligand $H_3N_3S_2Me_2$, with geminal (*gem*-) dimethyl substituents *α* to the S poised to bind trans to the carboxamide-N. Synthesis of this ligand is achieved in six total steps (Scheme 3). Coupling of (2-Methyl-2-triphenylsulfanylpropyl)pyridin-2-ylmethylamine[22] and *N-(* 2-bromoacetyl)-S-(triphenylmethyl)-2-aminoethanethiol[11] (synthesis described elsewhere) by stirring with excess K_2CO_2 in 4:1 $MeCN/CH_2Cl_2$ yielded the pre-ligand S-trityl-$N_3S_2Me_2$ in 35% yield. Removal of the S-trityl protecting group with Et_3SiH in TFA yielded $H_3N_3S_2Me_3$ in 83% yield. Treatment of $H_3N_3S_2Me_3$ with KOMe followed by addition of substoichiometric

$[Ni(OAc)_2 \cdot 4H_2O]$ afforded $K[Ni(N_3S_2Me_2)]$ (**4**) as tan solids in near quantitative yield.

Recrystallization of **4** by slow diffusion of Et_2O into a 1:1 MeOH/MeCN solution of product afforded small, orange-red crystals suitable for X-ray diffraction (Figure 14). From a structural standpoint, **1** and **4** are almost identically disposed. The metric parameters of the square-planar Ni-N_2S_2 match well against those observed for **1**, with no notable divergences evident (Table 1). Even the unbound pyridyl-N is similarly disposed, located 3.196 Å above the Ni(II) ion, and rotated 37.75° from the NiN_2S_2 least-squares plane. However, looking beyond the anionic portion modeling Ni-SOD, it is seen that **4** interacts with the K^+ cation in a similar fashion to **1**, and this interaction likely serves to anchor the unbound N-donor into similar positioning.

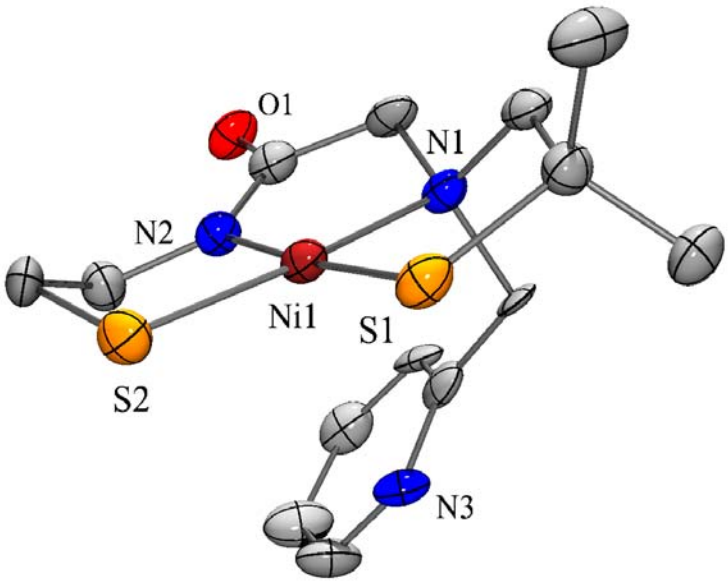

Figure 14. ORTEP diagram of the anion of **4** showing 50% ellipsoids for all non-hydrogen atoms.

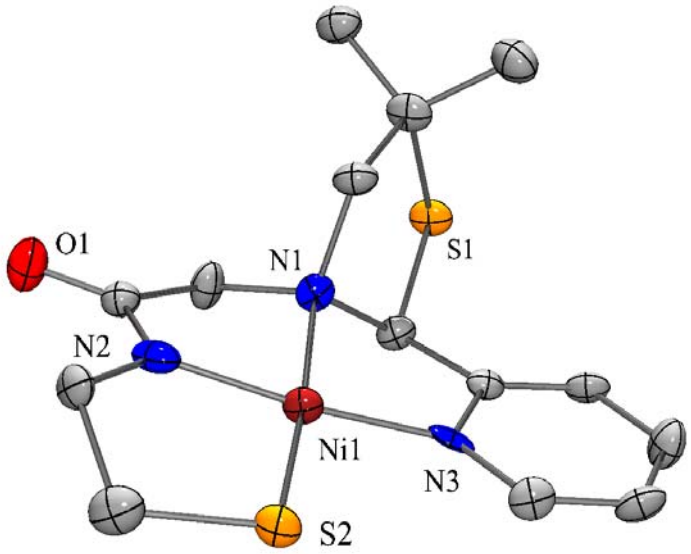

Figure 15. ORTEP diagram of **5** showing 50% ellipsoids for all non-hydrogen atoms.

The UV-vis spectra of **4** in MeOH is also similar to that observed for **1**, with the λ_{max} shifted to slightly lower energy (459 nm (ε = 200 M^{-1} cm^{-1}), shoulder at 570 nm (ε = 70 M^{-1} cm^{-1}), consistent with the more strongly donating nature of the tertiary thiolate ligand (see experimental section). Complex **4** appears to be highly O_2 sensitive, as a species spectroscopically similar to disulfide **3** forms rapidly upon exposure to aerobic atmosphere in MeOH as monitored by UV-vis. In an interesting turn of events, small red crystals harvested from a pseudo-anaerobic (vial prepared under N_2, sealed with electric tape and stored under atmospheric conditions) re-crystallization attempt of **4** were found to consist of the oxidized, ligand-rearranged product **5** (Figure 15, Table 3). It appears that upon aerobic oxidation formation of a heterocylic thioazoline with the C-S bond arising from picolylic carbon and the sterically protected S-donor previously trans to the carboxamido-N. Whether **5**

represents a major product component or a minor byproduct of aerobic oxidation remains to be determined.

CV measurements of **4** reveal an oxidation event at -0.610 V vs. Ag/AgCl, roughly 0.500 V less than that observed for **1**. A reduction event, contingent upon prior oxidation of **4**, is found at -1.860 V. This anodic shift in potential is much larger than expected to arise from incorporation of gem-dimethyl substituents α to one thiolate-S. In fact, incorporation of a total of four methyl groups α to both thiolate-S of a prior studied bis-amide NiN_2S_2 complex resulted only in a –0.080 V shift in redox potential.[16]

Interestingly, the ^{1}H NMR spectra of **4** at 298 K provide resonances which are much broader and ill-resolved as compared to that observed for **1**. This is quite intriguing, although unforeseen chemical interactions due to the presence of impurities can still not be ruled out at this stage in the study. However, it appears that despite the structural similarities between **1** and **4**, the two seemingly analogous complexes may possess markedly different electronic properties and behavior in solution. Studies regarding **4** are ongoing in our laboratory.

4.9 Conclusions

Complex **1** represents the first small molecule Ni-SOD model featuring all relevant donor ligands in the proper spatial disposition. Although different from that observed in the enzyme, **1** models aspects of the Ni-SOD_{red}/Ni-SOD_{ox} redox cycle. Specifically, Ni(III) species consistent with a tetragonal coordination environment is observed upon chemical oxidation. DFT studies suggest that this species is five-

coordinate, and analogous to that observed for Ni-SOD_{ox}. This Ni(III) species is unstable and rapidly undergoes auto-redox and disulfide formation (likely through an unbound thiyl-S radical, also observed by EPR). This conversion to disulfide product is clean, however, and only one product is observed; structurally characterized **3**, featuring two symmetrically linked Ni(II)N_3S units, with the initially unbound N-donor coordinated and tethered via the S previously occupying the position trans to the N-carboxamide. Chemical reduction of this disulfide linked product results in quantititative regeneration of **1**.

Although the axial N-donor is incapable of supporting Ni(III) for prolonged periods, the presence of this labile ligand keeps the coordination sphere intact upon oxidation. Irreversible polymerization and demetalation occurs in the absence of this key interaction. It is likely that coordination of the His1 imidazole side chain in combination with the stabilizing protein structure enforce Ni-SOD_{ox} and enable efficient SOD activity. In light of this, efforts in our laboratory are ongoing to incorporate more sterically robust thiolate ligands with the goal of precluding disulfide decomposition pathways and probing the hitherto unknown reactivity of Ni(III) species analogous to that observed in Ni-SOD.

4.10 Experimental Section

General Information. See Chapter 2, Section 2.7 for information pertaining to common laboratory reagents and solvents. The compounds *N*-(2-(tritylthio)ethyl)-2-((2-(tritylthio)ethyl)amino)acetamide (S-trityl-N_2S_2),[11] S-trityl-cysteamine,[3] 2-methyl-2-triphenylsulfanylpropyl)pyridin-2-ylmethylamine,[22] and *N-(*2-bromoacetyl)-

S-(triphenylmethyl)-2-aminoethanethiol[11] were prepared and checked according to the published procedures. All reactions were performed under an inert atmosphere of N_2 using standard Schlenk line techniques or in an MBraun Unilab glovebox under an atmosphere of purified N_2.

Physical Methods. See Chapter 2, Section 2.7 for information pertaining to UV-vis, FTIR, ^{1}H and ^{13}C NMR spectroscopy, ESI-MS measurements and elemental analysis. Cyclic voltammetry (CV) measurements were performed with a PAR Model 273A potentiostat using a Ag/Ag^+ (0.01 M $AgNO_3$/ 0.1 M $^n Bu_4NPF_6$ in MeCN) reference electrode, Pt-wire counter electrode and a Glassy Carbon working milli-electrode (2 mm diameter). Measurements were performed at ambient temperature using 5.0 mM analyte in the appropriate solvent under Ar containing 0.1 M $^n Bu_4NPF_6$ as the supporting electrolyte. The "Maximize Stability" mode was utilized in the PAR PowerCV software utilizing a low-pass 5.3 Hz filter. To ensure accuracy in the measured CVs, these experiments were performed in triplicate while polishing the working electrode between each run and we report an average E_{ox}. Additionally, potentials were checked and corrected by recording the CV of a ferrocene standard under the same experimental conditions as the complexes before each run. NMR spectra were recorded in the listed deuterated solvent on a 400 MHz Bruker BZH 400/52 NMR Spectrometer or a 500 MHz Varian Unity INOVA NMR spectrometer at 298 K with chemical shifts referenced to TMS or residual protio signal of the deuterated solvent.[23] X-band (9.60 GHz) EPR spectra were obtained on a Bruker ESP 300E EPR spectrometer controlled with a Bruker microwave bridge at 7 K. The EPR was equipped with a continuous-flow liquid He cryostat and a temperature controller

(ESR 9) made by Oxford Instruments, Inc. Low resolution ESI-MS data were collected using a Perkin Elmer Sciex API I Plus quadrupole mass spectrometer and high resolution ESI-MS data were collected using a Bruker Daltonics 9.4 T APEX Qh FT-ICR-MS. Elemental microanalysis for C, H, and N was performed by QTI-Intertek (Whitehouse, NJ).

N-(2-mercaptoethyl)-2-((2-mercaptoethyl)(pyridin-2-ylmethyl)amino)acetamide ($H_3N_3S_2$). This synthesis comprised the following steps:

Step 1: 2-((pyridin-2-ylmethyl)(2-(tritylthio)ethyl)amino)-N-(2-(tritylthio)ethyl)acetamide (S-trityl-N_3S_2). To a 100 mL THF/MeCN (1:1) solution containing 2.790 g (4.109 mmol) of S-trityl-N_2S_2 and 0.689 g (4.20 mmol) of picolyl chloride hydrochloride were added 1.550 g (11.22 mmol) K_2CO_3 and 0.652 g (4.35 mmol) of NaI and the reaction mixture was brought to reflux. After 16 h, reflux was ceased and the reaction mixture was concentrated to a dark red residue which was taken up in 100 mL CH_2Cl_2 and washed with $NaHCO_3$(aq) and brine, dried over $MgSO_4$ and concentrated to a red foam. Flash chromatography on silica gel (95:5 CH_2Cl_2/TEA) followed by several co-evaporations using 5:1 Et_2O/CH_2Cl_2 (to remove residual TEA) yielded 1.961 g (2.547 mmol, 62%) of product as a pale yellow foam solid. mp: 45°C. ^{1}H NMR (400 MHz, $CDCl_3$, δ from TMS): 8.40 (d, 1H), 7.97 (t, 1H), 7.39 (m, 14 H), 7.23 (m, 23 H, integrates higher due to overlap with residual $CHCl_3$), 7.07 (t, 1H), 3.58 (s, 2H), 3.06 (q, 2H), 2.97 (s, 2H), 2.47 (t, 2H), 2.32 (m, 4H). ^{13}C NMR (100.6 MHz, $CDCl_3$, δ from TMS): 170.78 (*C*=O), 158.09, 149.38, 149.34, 144.82, 144.78, 136.70, 136.66, 129.63, 128.02, 126.80, 123.12, 123.08, 122.44, 122.40, 66.92, 66.67, 60.08, 58.01, 37.92, 32.04, 29.81. FTIR (KBr

pellet), ν_{max} (cm^{-1}): 3349 (w, br, N-H), 3081 (w), 3054 (m), 3029 (w), 2958 (w), 2923 (w), 2827 (w), 1674 (vs, C=O), 1592 (s), 1570 (w), 1516 (s), 1488 (s), 1443 (s), 1374 (w), 1318 (w), 1295 (w), 1262 (w), 1246 (w), 1183 (w), 1156 (w), 1129 (w), 1083 (w), 1034 (m), 1001 (w), 975 (w), 924 (w), 886 (w), 848 (w), 800 (w), 743 (vs), 700 (vs), 676 (s), 621 (s), 579 (w), 526 (w), 506 (w). LRMS-ESI (*m/z*): $[M + H]^+$ calcd for $C_{50}H_{48}N_3OS_2$, 770.3; found, 770.0.

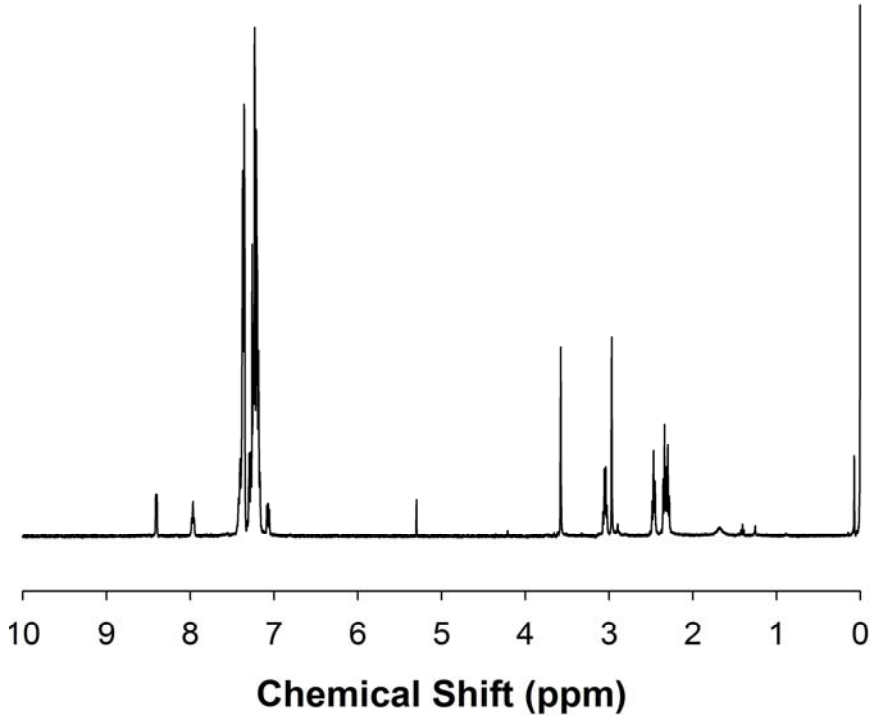

Figure 16. ^1H NMR of S-trityl-N_3S_2 in $CDCl_3$.

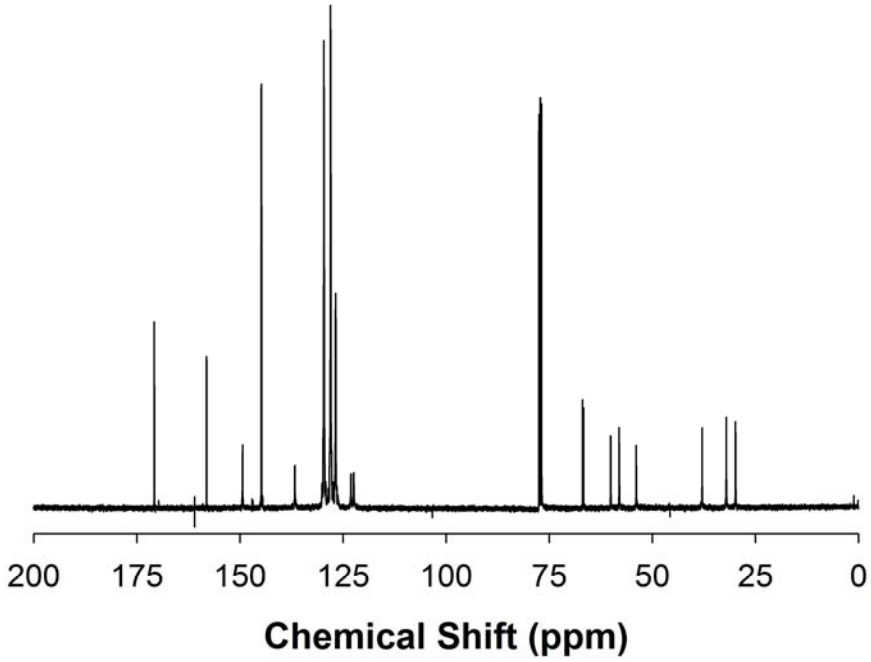

Figure 17. ^{13}C NMR of S-trityl-N_3S_2 in $CDCl_3$. Signal at 77.16 is from solvent.

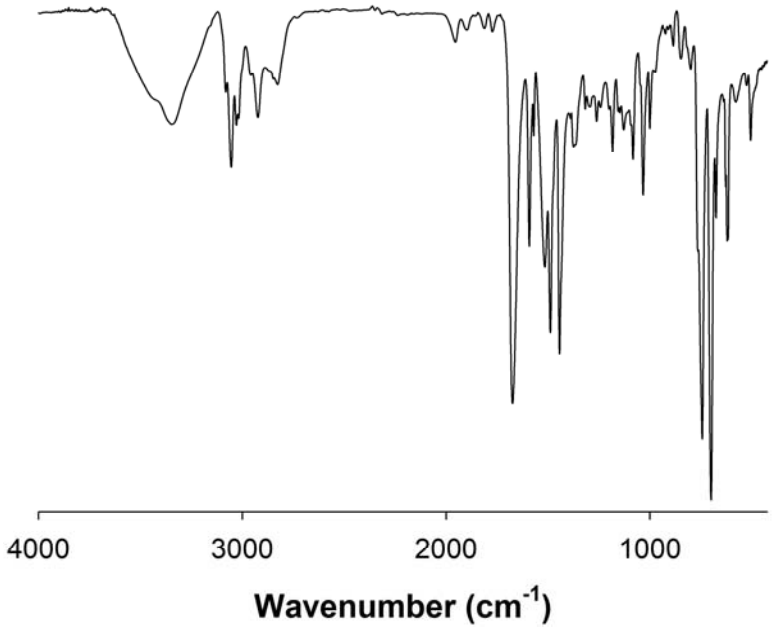

Figure 18. FTIR (KBr matrix) of S-trityl-N_3S_2.

Step 2. N-(2-mercaptoethyl)-2-((2-mercaptoethyl)(pyridin-2-ylmethyl)amino)acetamide ($H_3N_3S_2$). A batch of 1.961 g (2.547 mmol) of S-Trit-N_3S_2 was dissolved in 25 mL of a CH_2Cl_2/TFA (1:1) solution and stirred for 30 min

before 0.728 g (6.26 mmol) of Et_3SiH was added dropwise. After 1 h stirring, the reaction mixture was concentrated to half the original volume and insoluble Ph_3CH was removed via vacuum filtration. The filtrate was then concentrated to a dark orange oil and was washed with several portions of pentane before it was subsequently dissolved in 20 mL of CH_2Cl_2 and stirred over $NaHCO_3$(s). After 16 h, the $NaHCO_3$ was removed via filtration and the resultant yellow filtrate was concentrated to afford 0.590 g (2.07 mmol, 81%) of product as a light yellow oil. ^{1}H NMR (400 MHz, $CDCl_3$, δ from TMS): 8.60 (br s, 1H, N*H*, and d, 1H), 7.69 (t, 1H), 7.30 (d, 1H), 7.23 (t, 1H), 3.80 (s, 2H), 3.49 (q, 2H), 3.27 (s, 2H), 2.82 (t, 2H), 2.67 (m, 4H), 1.67 (br t, S*H*), 1.55 (t, S*H*). ^{13}C NMR (100.6 MHz, $CDCl_3$, δ from TMS): 171.25 (*C*=O), 157.97, 149.67, 136.88, 123.26, 122.76, 60.37, 58.43, 57.86, 42.22, 24.70, 22.84. FTIR (KBr pellet), ν_{max} (cm^{-1}): 3321 (w, br, N-H), 3054 (w), 3009 (w), 2932 (w), 2828 (w), 2539 (w, br, S-H), 1662 (vs, C=O), 1591 (s), 1570 (m), 1525 (s), 1474 (m), 1435 (s), 1360 (w), 1296 (m), 1260 (m), 1200 (m), 1149 (m), 1130 (m), 1095 (m), 1048 (m), 997 (m), 976 (w), 840 (w), 798 (w), 759 (s), 705 (w), 663 (w), 639 (w), 620 (w), 580 (w), 531 (w), 500 (w). LRMS-ESI (*m/z*): $[M + H]^+$ calcd for $C_{12}H_{20}N_3OS_2$, 286.1; found, 286.0.

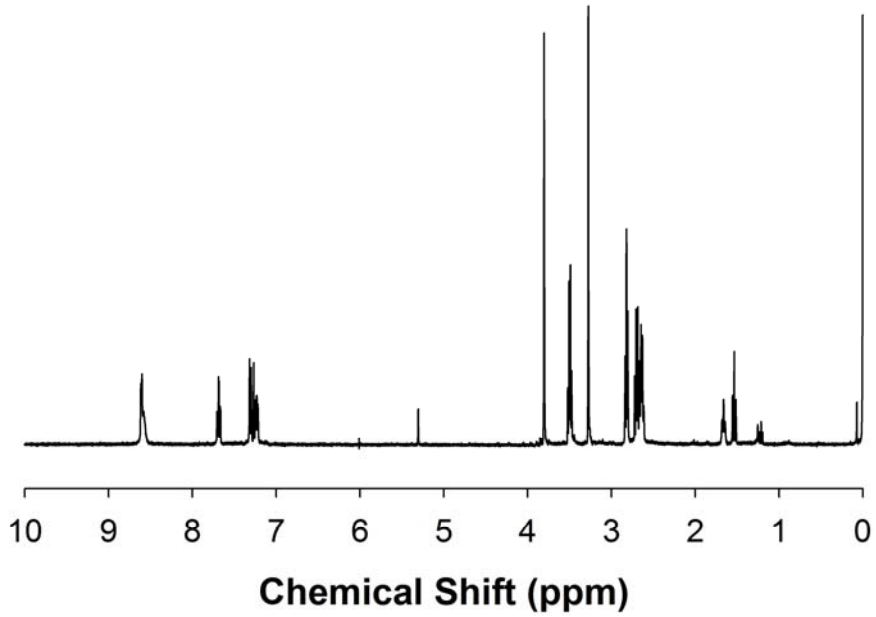

Figure 19. ^{1}H NMR of $H_3N_3S_2$ in $CDCl_3$.

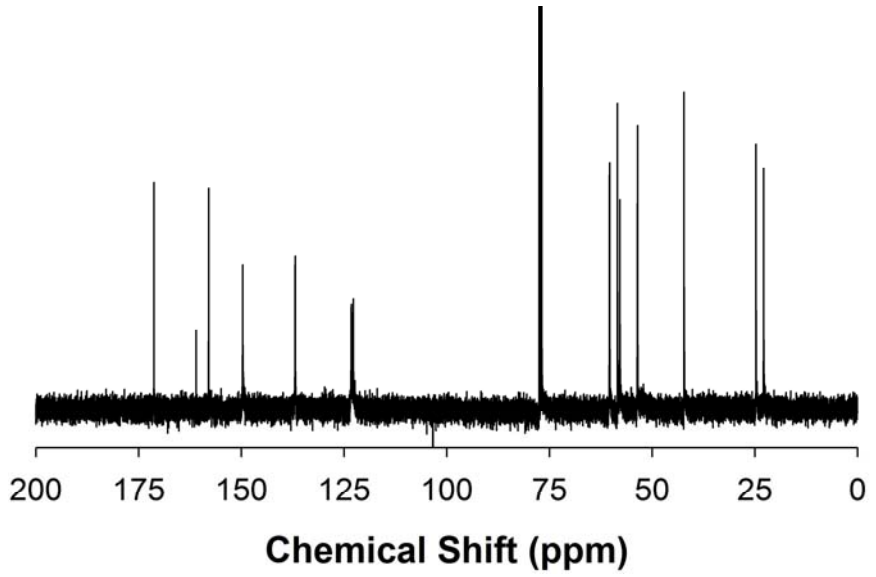

Figure 20. ^{13}C NMR of $H_3N_3S_2$ in $CDCl_3$. Signal at 77.16 is from solvent.

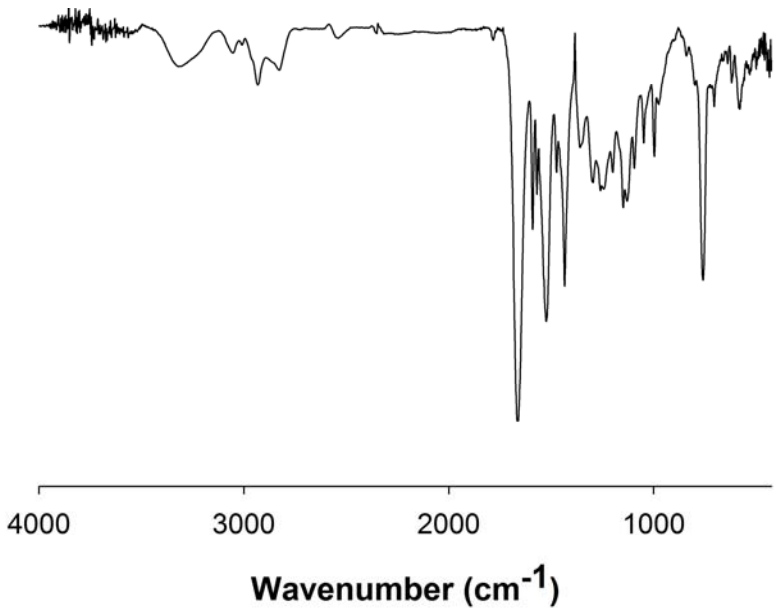

Figure 21. FTIR (KBr matrix) of $H_3N_3S_2$.

2-((2-mercapto-2-methylpropyl)(pyridin-2-ylmethyl)amino)-N-(2-mercaptoethyl)acetamide ($H_3N_3S_2Me_2$). The synthesis comprised the following steps.

Step 1. 2-((2-methyl-2-(tritylthio)propyl)(pyridin-2-ylmethyl)amino)-N-(2-(tritylthio)ethyl)acetamide (S-trityl-$N_3S_2Me_2$). A batch of 0.681 g (1.55 mmol) 2-methyl-2-triphenylsulfanylpropyl)pyridin-2-ylmethylamine, 0.703 g (1.60 mmol) *N-(*2-bromoacetyl)-S-(triphenylmethyl)-2-aminoethanethiol and 2.140 g (15.48 mmol) K_2CO_3 were stirred in 12 mL of 3:1 MeCN/CH_2Cl_2 for 5 d at RT. The K_2CO_3 was then removed by filtration and the residue concentrated to a pale yellow residue. ^{1}H NMR analysis of the crude reaction mixture revealed that the reaction was 50% complete. Product was separated by flash chromatography on basic alumina (3:1 hexane/EtOAc to remove starting materials, followed by CH_2Cl_2 to elute product) yielded 0.430 g (0.54 mmol, 35%) pure product as a white foam. ^{1}H NMR (400 MHz,

$CDCl_3$, δ from TMS): 8.53 (t, 1H, N*H*), 8.27 (d, 1H), 7.25, (d, 1H). 7.43 (m, 7H), 7.31 (m, 8H), 7.10 (m, 22H, integrates higher than expected), 6.99 (m, 2H), 3.48 (s, 2H), 3.05 (q, 2H), 2.39 (t, 2H), 2.24 (s, 2H), 0.65 (s, 6H). ^{13}H NMR (100.6 MHz, $CDCl_3$, δ from TMS): 171.39 (*C*=O). 158.37, 149.59, 144.93, 136.39, 130.17, 129.68, 127.99, 127.67, 126.78, 126.54, 123.50, 122.40, 67.77, 67.68, 66.72, 63.44, 62.15, 53.40, 38.15, 32.06, 27.57. FTIR (KBr pellet), ν_{max} (cm^{-1}): 3288 (w, br, N-H), 3054 (w), 3029 (w), 2963 (m), 2907 (w), 2866 (w), 2841 (w), 1667 (m, C=O), 1592 (m), 1571 (m), 1520 (m), 1488 (s), 1444 (s), 1357 (m), 1318 (m), 1262 (vs), 1183 (m), 1094 (s), 1031 (s), 908 (m), 864 (m), 799 (s), 767 (m), 742 (s), 700 (s), 675 (m), 643 (m), 629 (m), 616 (m), 578 (m), 500 (m). LRMS-ESI (*m/z*): $[M + H]^+$ calcd for $C_{52}H_{52}N_3OS_2$, 799.1; found, 798.5. $[M + Na]^+$ calcd for $C_{52}H_{51}N_3NaOS_2$, 820.5; found, 821.1.

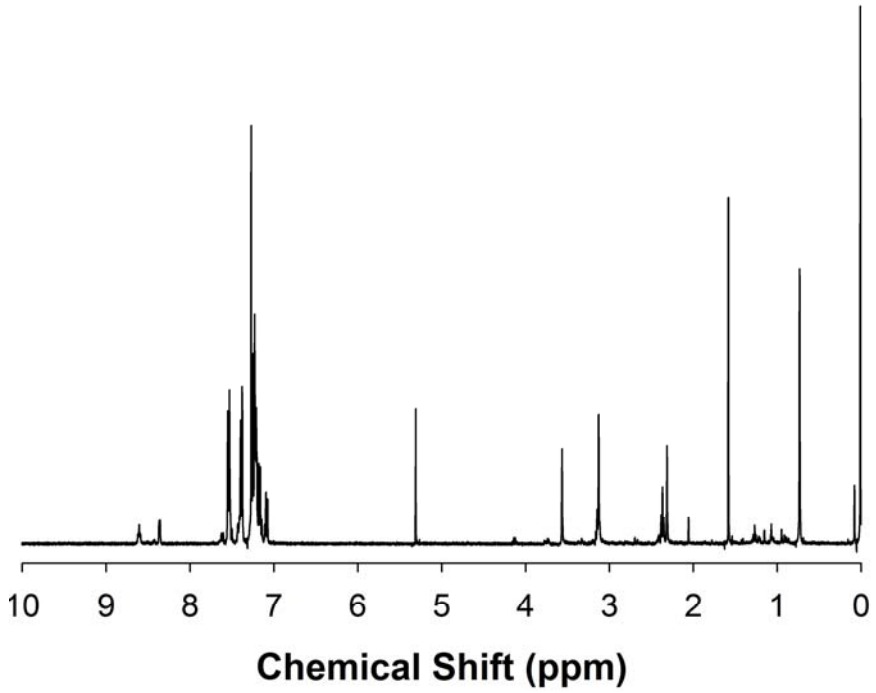

Figure 22. ^{1}H NMR of S-trityl-$N_3S_2Me_2$ in $CDCl_3$. Signal at 5.30 is from residual CH_2Cl_2.

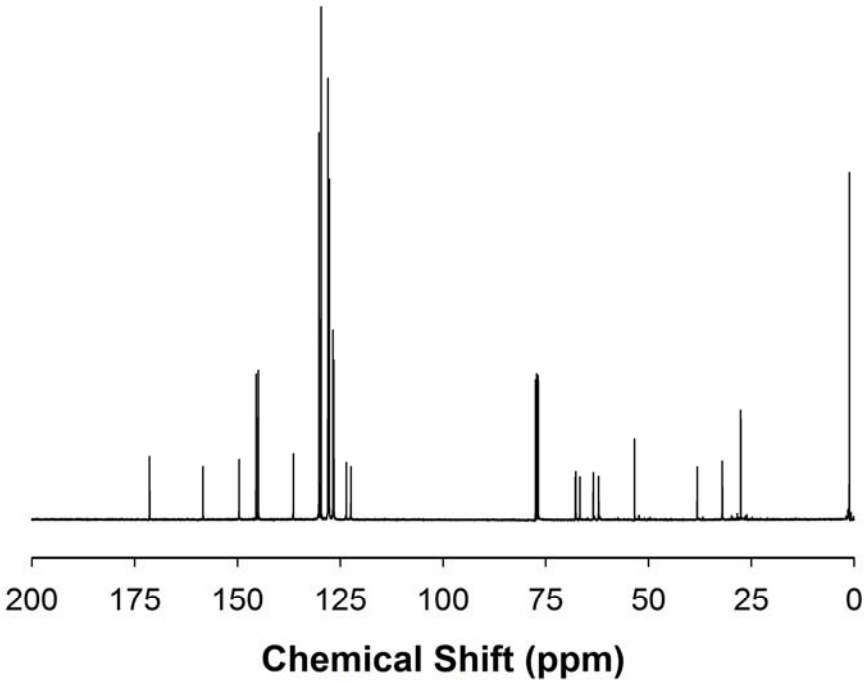

Figure 23. ^{13}C NMR of S-trityl-$N_3S_2Me_2$ in $CDCl_3$. Signal at 77.16 is from solvent.

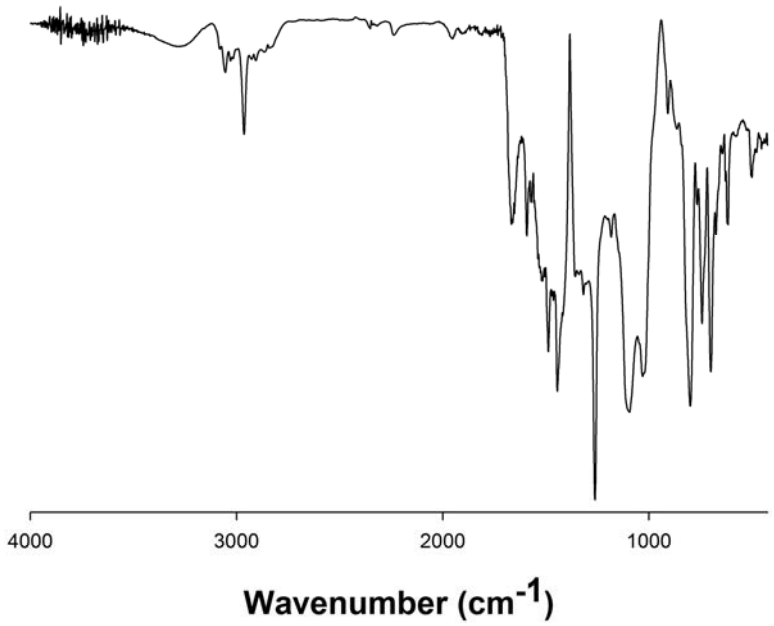

Figure 24. FTIR (KBr matrix) of S-trityl-$N_3S_2Me_2$.

Step 2. 2-((2-mercapto-2-methylpropyl)(pyridin-2-ylmethyl)amino)-N-(2-mercaptoethyl)acetamide ($H_3N_3S_2Me_2$). A batch of 750 mg (0.930 mmol) S-trityl-$N_3S_2Me_2$ was dissolved in 8 mL of 1:1 CH_2Cl_2/TFA at RT and stirred for 1 h before

270 mg (2.30 mmol) Et_3SiH was added dropwise. The bright orange solution loses luster and the resultant reaction mixture is a dull orange color. After 2 h stirring, the reaction mixture was concentrated to ½ its original volume and insoluble Ph_3CH was removed by filtration. The mother liquor was triturated three times with pentane, dissolved in 15 mL CH_2Cl_2 and stirred over $NaHCO_3$(s). After 16 h, the $NaHCO_3$ was removed by filtration and the resultant yellow mother liquor was concentrated to 240 mg (0.770 mmol) of product as a sticky yellow oil. ^{1}H NMR (400 MHz, $CDCl_3$, δ from TMS): 8.99 (s, br, N*H*), 8.63 (d, 1H). 7.67 (t, 1H), 7.28 (m, 2H), 3.84 (s, 2H), 3.57 (q, 2H), 3.52 (s, 2H), 2.80 (s, 2H), 2.76 (q, 2H), 1.78 (s, S*H*), 1.69 (t, S*H*), 1.15 (s, 6H). ^{13}H NMR (100.6 MHz, $CDCl_3$, δ from TMS):171.75 (*C*=O), 158.42, 149.84, 136.88, 123.72, 122.87, 69.80, 63.59, 62.40, 46.13, 42.51, 30.88, 24.88. FTIR (KBr pellet), ν_{max} (cm^{-1}): 3304 (m, br, N-H), 3058 (w), 3009 (w), 2961 (m), 2971 (m), 2864 (m), 2538 (br, w, S-H), 1659 (s, C=O), 1593 (m), 1571 (m), 1527 (m), 1437 (s), 1362 (s), 1305 (s), 1260 (s), 1200 (s), 1149 (s), 1122 (s), 1109 (s), 1094 (s), 1049 (m), 1019 (m), 1001 (m), 906 (w), 843 (w), 802 (m), 763 (s), 731 (m), 702 (m), 639 (m), 623 (m), 605 (m), 593 (w), 577 (w), 543 (w), 523 (w), 515 (w), 471 (w), 463 (w), 447 (w). LRMS-ESI (*m/z*): $[M + H]^+$ calcd for $C_{14}H_{24}N_3OS_2$, 314.5; found, 314.3.

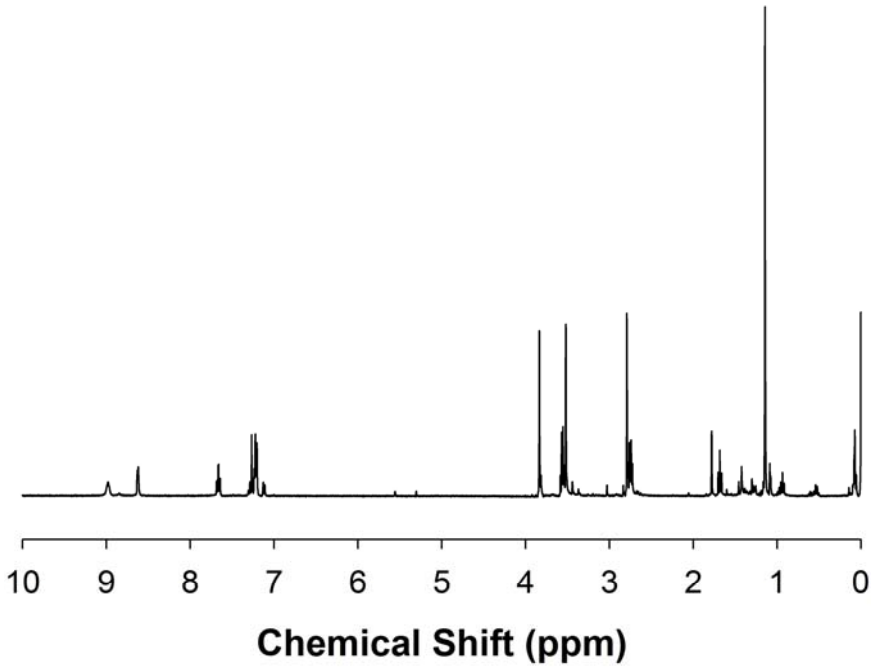

Figure 25. ^{1}H NMR of $H_3N_3S_2Me_2$ in $CDCl_3$.

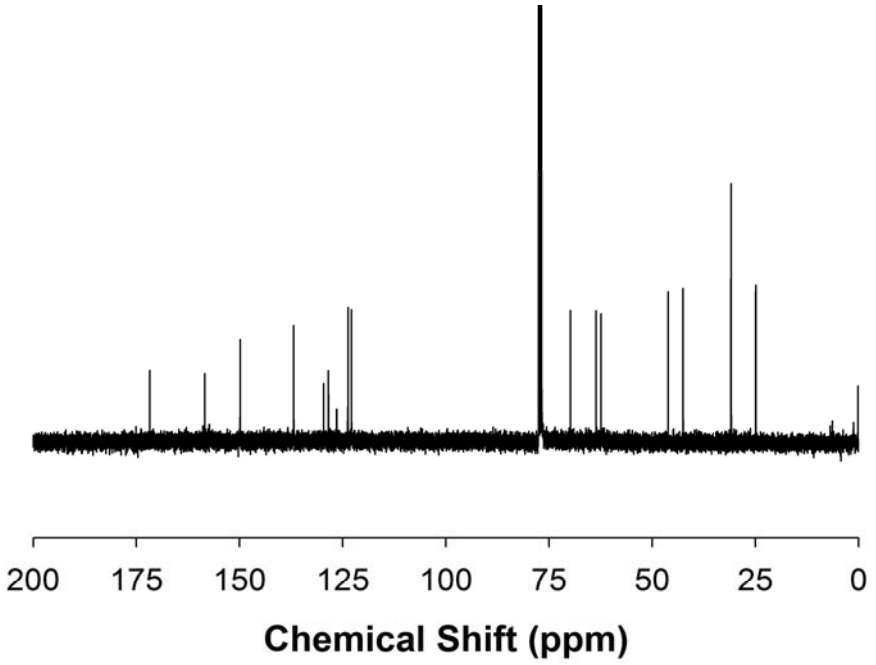

Figure 26. ^{13}C NMR of $H_3N_3S_2Me_2$ in $CDCl_3$. Signal at 77.16 is from solvent.

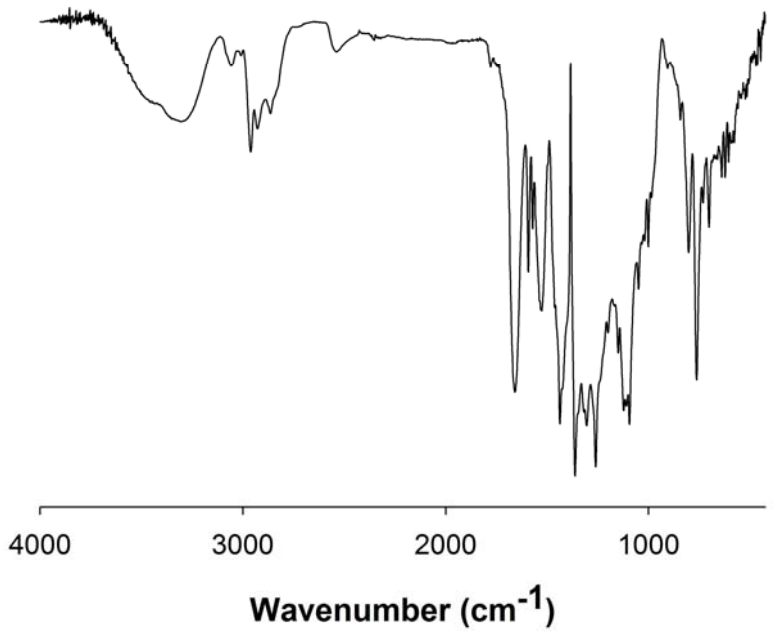

Figure 27. FTIR (KBr matrix) of $H_3N_3S_2Me_2$.

K[Ni(N_3S_2)] (1). Potassium metal (0.140 g, 3.58 mmol) was slowly reacted with 3 mL of dry MeOH to generate KOMe *in situ*. To this solution was added a 5 mL MeOH solution containing 0.341 g (1.20 mmol) of $H_3N_3S_2$ to afford a pale yellow solution. After stirring at RT for 30 min, a solid batch of $Ni(OAc)_2$•$4H_2O$ (0.217 g, 0.872 mmol) was added that generated a deep orange-red solution within seconds. After 90 min stirring at RT, the reaction mixture was filtered to remove insolubles and concentrated to half the original volume. Dropwise addition of an equal volume of Et_2O resulted in the precipitation of tan-orange solids. Collection via vacuum filtration afforded 0.302 g (0.794 mmol, 91%) of product. Tiny red crystals suitable for X-ray diffraction deposited from the mother liquor upon standing for 48 h at RT formulated as the MeOH solvate, $\{K[Ni(N_3S_2)]\}_2$•2MeOH, containing two unique enantiomers in the unit cell. ^{1}H NMR (500 MHz, CD_3OD, δ from protio

solvent): 9.29 (br s, 1H), 9.08, (d, 1H), 7.98 (t, 1H), 7.59 (br s, 1H), 5.11 (d, 1H), 4.22 (d, 1H), 4.07 (d, 1H), 3.86 (d, 1H), 3.75 (br s, 2H), 3.28 (br s, 2H), 2.98 (br s, 1H), 2.84 (br s, 1H), 2.64 (br s, 1H), 2.49 (br s, 1H). ^{1}H NMR (400 MHz, D_2O, δ from protio solvent): 9.33 (d, 1H), 8.97 (s, 1H), 8.13 (t, 1H), 7.63 (t, 1H), 4.92 (d, 1H), 3.98 (d, 1H), 3.79 (d, 1H), 3.60 (d, 2H), 3.52 (m, 1H), 3.00 (br t, 1H), 2.90 (m, 1H), 2.69 (d, 1H), 2.35 (br s, 1H), 2.30 (m, 1H), 2.21 (m, 1H). ^{1}H NMR (500 MHz, d_6-DMSO, δ from protio solvent): 8.53 (d, 1H), 7.91 (d, 1H), 7.80 (t, 1H), 7.33 (t, 1H), 4.38 (d, 1H), 4.22 (d, 1H), 3.42 (d, 1H), 3.13 (d, 1H, coincidental with residual MeOH in the lattice), 2.83 (m, 1H), 2.71 (m, 1H), 2.61 (m, 1H), 2.39 (m, 2H), 1.81 (m, 3H). FTIR (KBr pellet), ν_{max} (cm^{-1}): 3272 (m, br, O-H of lattice MeOH), 2917 (m), 2826 (w), 2837 (m), 1614 (vs, C=O), 1477 (w), 1436 (m), 1414 (m), 1375 (w), 1323 (w), 1307 (w), 1291 (w), 1259 (w), 1203 (w), 1151 (w), 1100 (w), 1086 (w), 1030 (m), 1000 (w), 976 (w), 951 (w), 935 (w), 910 (w), 898 (w), 861 (w), 822 (w), 804 (w), 773 (m), 688 (w), 670 (w), 660 (w), 645 (w), 622 (w), 567 (w), 535 (w), 518 (w), 462 (m). HRMS-ESI (*m/z*): [M - K]$^-$ calcd for $C_{12}H_{16}N_3NiOS_2$ (relative abundance), 340.0088 (100), 341.0122 (13), 342.0045 (48), 343.0076 (5), 344.0018 (5); Found, 340.0087 (100), 341.0121 (13), 342.0042 (49), 343.0077 (5), 344.0019 (5). UV-vis (MeOH, 298 K) λ_{max}, nm (ε, M^{-1} cm^{-1}): 449 (320), 570 (90). UV-vis (50 mM PIPES, pH 7.5, 298 K) λ_{max}, nm (ε, M^{-1} cm^{-1}): 449 (230), 570 (50). UV-vis (DMF, 298 K) λ_{max}, nm (ε, M^{-1} cm^{-1}): 461 (390), 586 (70). E_{ox} (DMF): -0.11 V vs Ag/AgCl; -0.62 V vs. Fc/Fc$^+$. E_{ox} (MeOH): -0.45 mV vs. Fc/Fc$^+$. Anal. Calcd for $C_{12}H_{16}KN_3NiOS_2$•MeOH•H_2O: C, 36.29; H, 5.15; N, 9.77. Found: C, 36.54; H, 4.76; N, 9.73.

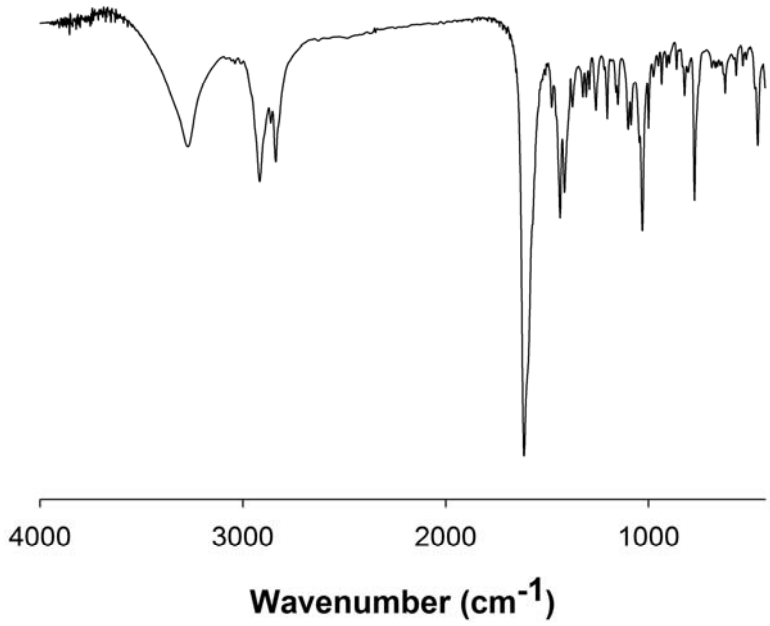

Figure 28. FTIR (KBr matrix) of **1**.

(Et_4N)[Ni(N_3S_2)] (^{Et4N}1). Sodium metal (0.0550 g, 2.39 mmol) was slowly reacted with 3 mL of dry MeOH to generate NaOMe *in situ*. To this solution was added a 4 mL MeOH solution containing 0.193 g (0.676 mmol) of $H_3N_3S_2$ to afford a pale yellow solution. After stirring at RT for 30 min, a solid batch of $Ni(OAc)_2 \cdot 4H_2O$ (0.163 g, 0.655 mmol) was added that generated a deep orange-red solution within seconds. After 1 h stirring at RT, 0.104 g (0.628 mmol) of Et_4NCl was added in 2 mL of MeOH and the solution was stirred for 2 h at RT. The reaction mixture was subsequently concentrated to a red oily residue and taken up in 20 mL of THF/MeCN (1:1) and the insoluble NaOAc and NaCl were removed via vacuum filtration. The mother liquor was then concentrated *en vacuo* to remove all traces of residual MeOH resulting in a red-brown foam. Overnight stirring in THF at RT afforded 0.187 g (0.397 mmol, 63%) of ^{Et4N}**1**. The spectral properties match with **1**, except for the Et_4N^+ signals. ^{1}H NMR (400 MHz, CD_3OD, δ from protio solvent): 9.20 (br s, 1H),

9.00 (d, 1H), 7.92 (t, 1H), 7.53 (br s, 1H), 5.03 (d, 1H), 4.16 (d, 1H), 4.00 (d, 1H), 3.78 (d, 1H), 3.67 (br s, 2H), 3.27 (m 14H, q of $(CH_3CH_2)_4N^+$ coincidental with br s, 2H and solvent residual), 2.89 (br s, 1H), 2.75 (br s, 1H), 2.58 (br s, 1H), 2.40 (br s, 1H), 1.24 (t, 13 H, $(CH_3CH_2)_4N^+$). Anal. Calcd for $C_{20}H_{36}N_4NiOS_2$•$2H_2O$•0.25THF: C, 48.01; H, 8.06; N, 10.66. Found: C, 47.91; H, 8.10; N, 10.37.

$[Ni_2(N_3S_2)_2]$ (3) (Route 1). To a batch of 0.035 g (0.074 mmol) of ^{Et4N}**1** dissolved in 3 mL of DMF at -41°C (CO_2(s)/MeCN slush bath) was added, via cannula, a 5 mL DMF solution containing 0.025 g (0.076 mmol) of $FcPF_6$ also at -41°C. The resultant brown-orange solution was stirred for 10 min at -41°C before slowly warming to RT. After stirring for 1 h at RT, the reaction mixture was concentrated to a brown residue on a high-vacuum line and taken up in 12 mL of MeCN. After stirring for 2 h at RT, 0.0123 g (0.0180 mmol, 49%) of **3** was isolated as orange solids via vacuum filtration. Small red crystals suitable for X-ray diffraction were grown via slow diffusion of Et_2O into a saturated MeOH solution of **3** at RT. FTIR (KBr pellet), ν_{max} (cm^{-1}): 3386 (w, br), 3246 (w, br), 3060 (w), 2920 (m), 2848 (m), 1606 (vs, C=O), 1477 (w), 1444 (m), 1406 (w), 1363 (w), 1292 (w), 1261 (w), 1158 (m), 1100 (m), 1054 (w), 1023 (w), 915 (w), 762 (m), 738 (m), 669 (w), 659 (w), 514 (w), 498 (w), 481 (w), 436 (w). ^{1}H NMR (400 MHz, CD_3OD, δ from protio solvent): 8.15 (d, 1.4H), 7.92 (t, 2H), 7.86 (d, 0.6 H), 7.47 (d, 2H), 7.28 (t, 2H), 5.08 (m, 2H), 4.21 (t, 4H), 3.38 (m, 2H), 3.11 (m, 10H), 2.81 (m, 2H), 2.29 (m, 2H), 2.20 (m, 2H). LRMS-ESI (*m/z*): $[M + H]^+$ calcd for $C_{24}H_{33}N_6Ni_2O_2S_4$, 681.0; found 680.8. Although analytically pure bulk material was not obtained, this

route was employed in order to obtain **3** in the absence of stoichiometric and inseparable KPF_6 which results from oxidation of **1** (as K^+). Another route was employed (vide infra) to obtain analytically pure material.

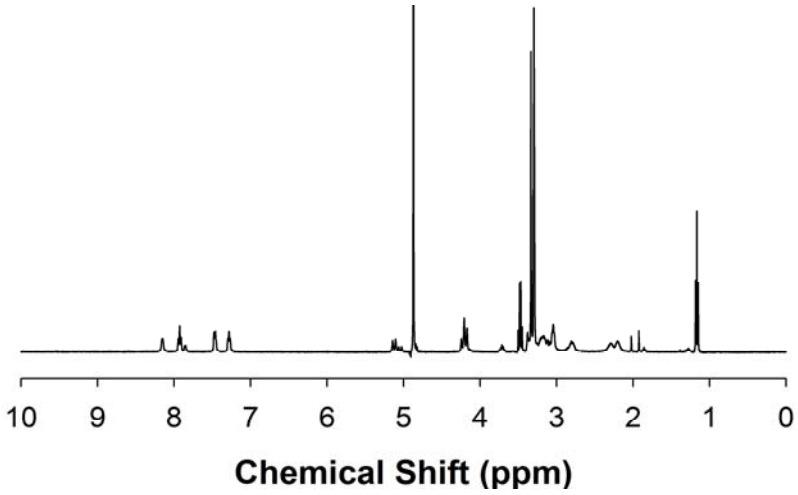

Figure 29. ^{1}H NMR of **3** in MeOH. Signals as 4.87 and 3.31 are from residual protio solvent.

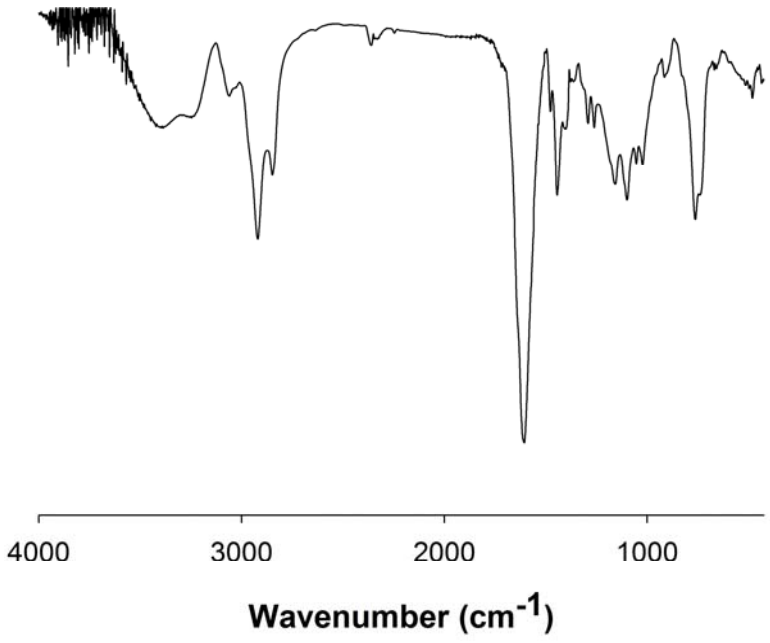

Figure 30. FTIR (KBr matrix) of **3**.

$[Ni_2(N_3S_2)_2]$ (3) (Route 2). To a batch of 0.130 g (0.342 mmol) of **1** in 8 mL of DMF at □41°C (CO_2(s)/MeCN slush bath) was added, via cannula, a 8 mL DMF solution containing 0.111 g (0.335 mmol) of ferrocenium hexafluorophosphate ($FcPF_6$) also at -41°C. The resultant brown-orange solution was stirred for 10 min at -41°C before slowly warming to RT. After stirring for 1 h at RT, the reaction mixture was concentrated to a brown residue on a high-vacuum line and washed with several portions of Et_2O to remove resultant ferrocene, then stirred in Et_2O to afford 0.145 g of solid material that we formulate as **3•2KPF$_6$** (81%). The Et_2O was concentrated to afford 0.046 g (0.247 mmol, 74%) of ferrocene (it should be noted that the DMF distillate affords a yellow color, suggesting that some ferrocene was lost in the collection flask during DMF solvent removal). FTIR (matches product obtained via route 1 except for stretches arising from KPF_6 and lattice DMF, KBr pellet), ν_{max} (cm^{-1}): 3399 (w, br), 3233 (w, br), 3061 (w), 2919 (m), 2845 (m), 1667 (m, C=O, lattice DMF), 1613 (vs, C=O), 1475 (w), 1446 (m), 1406 (m), 1327 (w), 1292 (m), 1262 (m), 1206 (w), 1161 (w), 1100 (m), 1055 (w), 1021 (w), 953 (w), 842 (s, P-F), 765 (m), 740 (w), 660 (w), 559 (s, KPF_6), 534 (w), 482 (w), 433 (w). NMR data matches with the route 1 procedure. HRMS-ESI (*m/z*): $[M + H]^+$ calcd for $C_{24}H_{33}N_6Ni_2O_2S_4$ (relative abundance), 681.0255 (100), 682.0288 (26), 683.0211 (95), 684.0245 (25), 685.0167 (30), 686.0199 (8), 687.0141 (6); Found, 681.0353 (91), 682.0362 (31), 683.0324 (100), 684.0353 (39), 685.0286 (51), 686.0290 (16), 687.0275 (16). UV-vis (DMF, 298 K) λ_{max}, nm (ε, M^{-1} cm^{-1}): 364 (5,720; 2,860/Ni), 440 (930; 465/Ni). E_{red} (DMF): -1.33 V; -1.80 V vs. Fc/Fc^+. E_{red} (MeOH): -1.49 mV

vs. Fc/Fc^+. Anal Calcd for $C_{24}H_{32}N_6Ni_2O_2S_4$•2$KPF_6$•$Et_2O$•0.25DMF: C, 30.22; N, 3.86; N, 7.66. Found: C, 30.25; H, 3.57; N, 7.37.

K[Ni($N_3S_2Me_2$)] (4). A batch of 102 mg (2.54 mmol) KH was added to 3 mL MeOH to generate KOMe *in situ*. To this solution was added 228 mg (0.720 mmol) $H_3N_3S_2Me_2$ in 4 mL MeOH. After stirring at RT for 30 min, a solid batch of $Ni(OAc)_2$•$4H_2O$ (160 mg (0.560 mmol) was added that generated a deep red-brown solution within seconds. After 2 h stirring at RT, the reaction mixture was filtered to remove any insolubles and concentrated to dryness. The resultant brown solid residue was taken up in 4 mL of 1:1 MeOH/MeCN and 10 mL Et_2O was slowly added resulting in the precipitation of 271 mg (0.664 mmol, 119 %, byproducts are present in the isolated product) of **4**. Lustrous red, microcrystalline solids deposited from the mother liquor over 48 h; the FTIR of the bulk and microcrystalline products indicate the same product. Recrystallization of these solids by slow diffusion into a 1:1 MeOH/MeCN solution saturated with **4** afforded tiny red-orange crystals suitable for X-ray diffraction; the crystalline product is formulated as {K[Ni($N_3S_2Me_2$)]•H_2O}. **This procedure is not yet optimized for maximal yield/ purity*. FTIR (KBr pellet), ν_{max} (cm^{-1}): 3397 (m, br), 2984 (w), 2949 (w), 2914 (w), 2838 (w), 1609 (s, C=O), 1573 (s, C=O), 1414 (s), 1575 (w), 1336 (w), 1308 (w), 1258 (w), 1205 (w), 1150 (w), 1098 (w), 1074 (w), 999 (w), 945 (w), 915 (w), 881 (w), 825 (w). 768 (w), 696 (w), 645 (w), 624 (w), 571 (w), 533 (w), 492 (w), 473 (w), 441 (w). UV-vis (MeOH, 298 K) λ_{max}, nm (ε, M^{-1} cm^{-1}): 459 (200), 570 (70). LRMS-ESI (*m/z*): $[M]^-$ calcd for $C_{14}H_{20}N_3NiOS_2$, 368.0; found, 368.0. E_{red} (DMF): -0.61 V

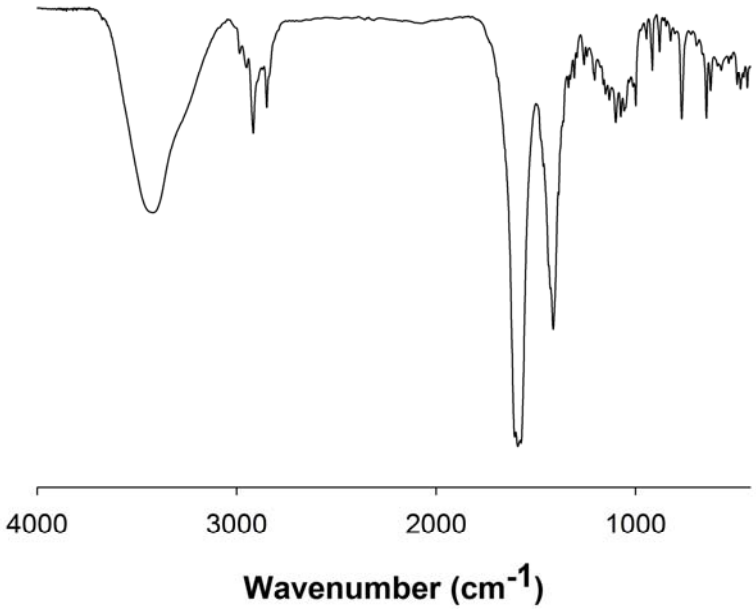

Figure 31. FTIR (KBr matrix) of **4**.

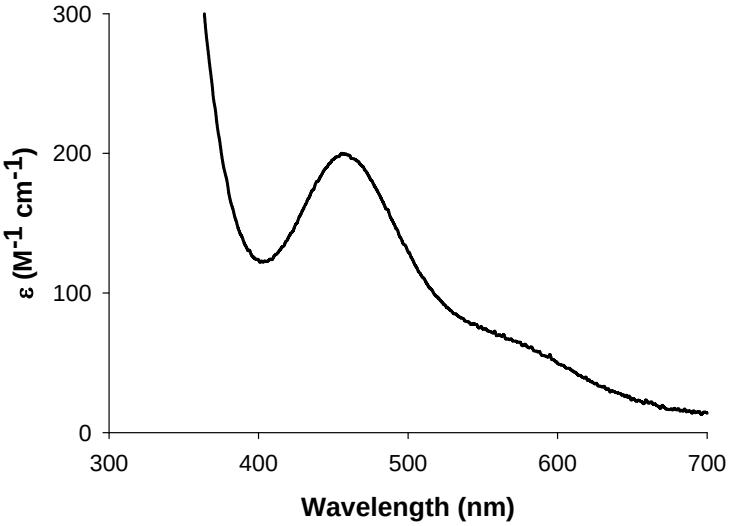

Figure 32. UV-vis spectrum of **4** in MeOH at 298 K.

***In situ* oxidation of 1 to monitor intermediates by EPR**. To 14.4 mg (0.0380 mmol) of **1** in 1 mL of DMF was added 11.8 mg (0.0360 mmol) of $FcPF_6$ in 1 mL DMF as described above. Immediately after mixing with $FcPF_6$, the reaction vessel

was opened under strong positive N_2 pressure and a direct aliquot of the reaction mixture was removed and immediately frozen in an EPR tube and its X-band spectrum was recorded.

***In situ* oxidation of 1 to 3 and re-reduction to 1**. A batch of 30 mg (0.079 mmol) of **1** was dissolved in 3 mL of DMF and a 100 μL aliquot was removed and added to a UV-vis cuvette containing 3 mL of DMF and the UV-vis spectrum was acquired. The reaction vessel was then cooled to -41°C and 25 mg (0.076 mmol) of $FcPF_6$ in 3 mL of DMF (also cooled to -41°C) was added via cannula. The reaction mixture was left to stir for 10 min before slowly warming to RT. After 1 h stirring, a 100 μL aliquot was removed and added to a UV-vis cuvette containing 3 mL of DMF and a UV-vis spectrum was acquired confirming conversion to **3**. Next, 24 mg (0.073 mmol) of bis(pentamethylcyclopentadienyl)cobalt ($[Co(Cp^*)_2]$) was added as a slurry in 3 mL of a 2:1 DMF/THF solvent mixture and the reaction was stirred for 1 h before a 100 μL aliquot was removed and added to a UV-vis cuvette containing 3 mL of DMF and a UV-vis spectrum was acquired confirming consumption of **3** and a spectral profile corresponding to the regeneration of **1** along with contributions from ferrocene and $[Co(Cp^*)_2]^+$. The reaction mixture was concentrated to a brown residue and washed with several portions of Et_2O in order to remove resultant ferrocene and dried in vacuo. The resultant 58 mg (89% mass recovery after ferrocene removal) of light orange solids were analyzed by ^1H NMR and $ESI^{+/-}$ revealing the anion of **1** and $[Co(Cp^*)_2]^+$ as the only identifiable products. Attempts to separate discreet salt products from the product ions ($[Ni(N_3S_2)]^-$ = anion of **1**, $[Co(Cp^*)_2]^+$, K^+ and PF_6^-

(confirmed via FTIR) were unsuccessful and suggest that the ions combine in various permutations.

Bulk reduction of 3. To a solution containing 45 mg of **3•2KPF$_6$** (0.043 mmol) stirring in 4 mL of DMF was added 27 mg (0.082 mmol) of [Co(Cp*)$_2$] as a slurry in 2 mL of DMF. The reaction mixture was stirred for 2 h at RT and checked by UV-vis confirming the **3**-to-**1** conversion. The reaction mixture was then concentrated to dryness and stirred in 12 mL of Et_2O for 16 h at RT after which 52 mg (72% mass recovery) of light orange solids were isolated via filtration. The resultant ^{1}H NMR (CD_3OD) displayed broadened peaks likely due to small amounts of unreacted [Co(Cp*)$_2$] as a paramagnetic impurity. The solids were then stirred in THF at RT for 1 h and 36 mg (50% total mass recovery) of light orange solids were isolated via filtration. The only products identifiable by ^{1}H NMR and ESI$^{+/-}$ analysis (ESI performed pre-THF wash) were [Co(Cp*)$_2$]$^+$ and the anion of **1**.

Reactivity of 1 with N_3^- and $O_2^{\bullet-}$. All reactions with **1** were monitored by electronic absorption spectroscopy and/or ESI-MS under anaerobic conditions in 50 mM PIPES buffer (pH 7.5) or DMF at 298 K.

1 + N_3^-. A 55 μL PIPES aliquot of NaN_3 (0.248 mmol, 10 mol-equiv) was added to a quartz UV-vis cell containing **1** (0.32 mM, 3.1 mL total volume) in PIPES and the UV-vis spectrum was acquired immediately. No change resulted after addition and over a time period of 30 min indicating no formation of a Ni-N_3^- adduct.

1 + $O_2^{\bullet-}$ in DMF. A 5.52 mM DMF stock solution of **1** was prepared, diluted (0.20 mL aliquot, 3.2 mL total volume, 0.35 mM final concentration), and its UV-vis spectrum was recorded. To the DMF stock solution of **1** was added a solid batch of 5

mg (0.07 mmol, 13 mol-equiv) of KO_2 containing 29 mg (0.11 mmol) of 18-crown-6 as a solubilizing agent. No noticeable visible changes occurred by eye. After stirring at RT for 2 h, the solution was filtered through a 0.45 μm nylon filter and 0.20 mL of this solution was added to a UV-vis cell containing 3 mL of DMF (3.2 mL total volume, 0.35 mM final concentration of total Ni-species) and the UV-vis spectrum of the reaction mixture was recorded, which revealed minor changes.

1 + $O_2^{\bullet-}$ in PIPES. To a 0.60 mM solution of **1** (1.3 mL total volume) was added 5 mg (0.07 mmol, 90 mol-equiv) of KO_2 and the solution was left to stir for 1 h at RT. ESI-MS was recorded and revealed S-oxygenation.

EPR analysis. Figure 7 shows the experimental X-band EPR spectrum of the *in situ* formed oxidation products during the **1**-to-**2** conversion (termed Ni-ox) recorded at 7 K in a DMF glass. The spectrum is dominated by a sharp, single first derivative peak at 3420 G (g = 2.00). There are also weaker, broader features at 3030 G (absorption shape, g = 2.26) and 3160 G (first derivative shape, g = 2.17). This spectrum has been analyzed as follows: the sharp peak is assigned to an organic thiyl radical, while the other two features are assigned to the g_{max} and g_{mid}, respectively, components of a Ni(III)-centered paramagnet with slightly rhombic symmetry ($g_{\perp}$ = (g_{max} + g_{mid})/2 ≈ 2.22, which is typical for low-spin Ni(III) in tetragonal symmetry.[14,24-26] The g_{min} ($g_{\|}$) component of this Ni(III) center is not observable, however, we believe that this feature is masked by the radical signal. Low-spin d^7 species typically exhibit $g_{\|}$ = 2.00(1),[14,24-26] so this **g** matrix component would be directly obscured by the radical. We have demonstrated this by simulation with the program QPOWA[27-28] for both the radical signal (using g_{iso} = 2.0025) and the Ni(III)

signal (using **g** = [2.26, 2.17, 2.00]). The simulation intensity of the former is scaled to match that of experiment and the latter scaled to match roughly the $g_{\perp}$ features as shown in the figure and the two are summed to give the net simulation trace. The only effect of the $g_{\parallel}$ component, due to its low intensity, is a slight distortion in the baseline of the radical. This distortion could also be shifted either to slightly higher or lower field if $g_{\parallel}$ is respectively changed to 1.99 or 2.01. The signal-to-noise ratio in the experimental baseline is such that any of these options is viable. It is also possible that the $g_{\parallel}$ feature exhibits hyperfine coupling from an axially coordinated ^{14}N. This is shown in red, which now includes hyperfine coupling to a single ^{14}N with $A(g_{\parallel})$ = 50 MHz. This coupling constant was chosen based on the observed coupling from axially coordinated pyridine in $[Ni(TPP)]^{+}$,[29] which is sufficiently close to our system for illustrative purposes. The weak intensity of the Ni(III) signal and the overlying radical signal preclude us from being definitive about axial coordination by the pendant pyridyl arm. We speculate further that the breadth and possible heterogeneity of the Ni(III) signal in the $g_{\perp}$ region might be the result of species both with and without the axial ligand. Double integration of the Ni(III) and radical species over the field intervals shown in Figure S1 center) gives these two species in the approximate ratio of 5:1, noting that the field interval for the Ni(III) species likely does not include the full parallel region and the field interval for the radical includes some underlying Ni(III) signal intensity, so this ratio is likely a lower limit.

Computational Details. The DFT computations were performed as described in Chapter 2. For selected computations, salvation effects were included via the conductor-like screening model (COSMO) as implements in ORCA.

X-ray Data Collection and Structure Solution Refinement. Tiny red single crystals of **1**, **3** and **4** were grown under anaerobic conditions from standing of a saturated 1:1 MeOH:Et_2O solution of **1**, slow diffusion of Et_2O into saturated solution of **3** in MeOH at RT and slow diffusion of Et_2O into a saturated 1:1 MeOH/MeCN solution of **4**, respectively. Single crystals of **5** were obtained by setting up a saturated 1:1 MeOH/THF for Et_2O slow diffusion in an anaerobically capped vial, sealed with electric tape and stored under atmospheric conditions at RT. Three weeks passed (the setup can no longer be considered anaerobic by this time) before crystals began to deposit. A suitable crystal was mounted inside of a glass capillary or on the top of a glass fiber. All geometric and intensity data were measured at 100 K on a Bruker SMART APEX II CCD X-ray diffractometer system equipped with graphite-monochromatic Mo Kα radiation (λ = 0.71073 Å) with increasing ω (width 0.5° per frame) at a scan speed of 10 s/frame or 15 s/frame controlled by the SMART software package.[30] The intensity data were corrected for Lorentz-polarization effects and for absorption[31] and integrated with the SAINT software. Empirical absorption corrections were applied to structures using the SADABS program.[32] The structures were solved by direct methods with refinement by full-matrix least-squares based on F^2 using the SHELXTL-97 software[33] incorporated in the SHELXTL 6.1 software package.[34] The hydrogen atoms were fixed in their calculated positions and refined using a riding model. All non-hydrogen atoms were refined anisotropically. Perspective views of the complexes were obtained using ORTEP.[35] Crystallographic properties are reported in Table 4.

Table 4. Summary of Crystal Data and Intensity Collection and Structure Refinement Parameters for **1**, **3**, **4** and **5.**

[a] $R_1 = \Sigma| \, |F_o| - |F_c| \, | / \Sigma |F_o|$; [b] $wR_2 = \{\Sigma[w(F_o^2 - F_c^2)^2] / \Sigma[w(F_o^2)^2]\}^{1/2}$.

Parameters	**1**	**3**	**4**	**5**
Formula	$C_{26}H_{40}N_6Ni_2O_2S_4$	$C_{25}H_{36}N_6Ni_2O_3S_4$	$C_{14}H_{22}KN_3NiO_2S_2$	$C_{14}H_{19}N_3NiOS_2$
Formula weight	824.50	714.26	426.28	368.15
Crystal system	Monoclinic	Triclinic	Monoclinic	Triclinic
Space group	$P2_1/c$	P-1	C_2/C	P-1
Crystal color, habit	red rectangle	red plate	red plate	red rectangle
a, Å	16.4659(12)	10.9850(6)	18.565(7)	10.950(7)
b, Å	11.9297(9)	11.9682(6)	11.991(4)	12.603(8)
c, Å	17.6594(13)	12.4322(7)	16.388	13.560(8)
α, deg	90.00	73.8700(10)	90.00	65.451(7)
β, deg	95.5710(10)	73.0770(10)	98.339(5)	67.752(8)
γ, deg	90.00	75.2250(10)	90.00	89.678(9)
V, Å^3	3452.5(4)	1474.92(14)	3610(2)	1549.7(16)
Z	4	2	8	4
ρ_{calcd}, g/cm^3	1.586	1.608	1.569	1.578
T, K	100(2)	100(2)	100(2)	100(2)
abs coeff, μ (Mo Kα), mm^{-1}	1.615	1.599	1.548	1.522
θ limits, deg	2.06-29.68	2.409-33.028	2.03-25.00	1.90-25.00
total no. of data	51631	17421	13717	5425
no. of unique data	9776	5794	3173	5425
no. of parameters	395	388	208	380
GOF on F^2	1.066	1.055	1.180	1.048
R_1,[a] %	4.34	2.91	8.53	8.62
wR_2,[b] %	10.26	7.24	22.49	25.03
max, min peaks, e/ Å^3	1.355, -0.637	1.098, -0.378	1.088, -0.982	3.339, -1.533

4.11 References

(1) Gale, E. M.; Cowart, D. M.; Scott, R. A.; Harrop, T. C. *Inorg. Chem.* **2011**, *50*, 10460.

(2) Gale, E. M.; Narendrapurapu, B. S.; Simmonett, A. C.; Schaefer, H. F., III; Harrop, T. C. *Inorg. Chem.* **2010**, *49*, 7080.

(3) Gale, E. M.; Patra, A. K.; Harrop, T. C. *Inorg. Chem.* **2009**, *48*, 5620.

(4) Neupane, K. P.; Shearer, J. *Inorg. Chem.* **2006**, *45*, 10552.

(5) Shearer, J.; Zhao, N. *Inorg. Chem.* **2006**, *45*, 9637.

(6) Shearer, J.; Dehestani, A.; Abanda, F. *Inorg. Chem.* **2008**, *47*, 2649.

(7) Mathrubootham, V.; Thomas, J.; Staples, R.; McCraken, J.; Shearer, J.; Hegg, E. L. *Inorg. Chem.* **2010**, *49*, 5393.

(8) Gale, E. M.; Simmonett, A. C.; Telser, J.; Schaefer, H. F., III; Harrop, T. C. *Inorg. Chem.* **2011**, *50*, 9216.

(9) Barondeau, D. P.; Kassmann, C. J.; Bruns, C. K.; Tainer, J. A.; Getzoff, E. D. *Biochemistry* **2004**, *43*, 8038.

(10) Wuerges, J.; Lee, J.-W.; Yim, Y.-I.; Yim, H.-S.; Kang, S.-O.; Carugo, K. D. *Proc. Natl. Acad. Sci. U.S.A.* **2004**, *101*, 8569.

(11) O'Neil, J. P.; Wilson, S. R.; Katzenellenbogen, J. A. *Inorg. Chem.* **1993**, *33*, 319.

(12) Choudhury, S. B.; Lee, J. W.; Davidson, G.; Yim, Y. I.; Bose, K.; Sharma, M. L.; Kang, S. O.; Cabelli, D. E.; Maroney, M. J. *Biochemistry* **1999**, *38*, 3744.

(13) Fiedler, A. T.; Bryngelson, P. A.; Maroney, M. J.; Brunold, T. C. *J. Am. Chem. Soc.* **2005**, *127*, 5449.

(14) Lappin, A. G.; Murray, C. K.; Margerum, D. W. *Inorg. Chem.* **1978**, *17*, 1630.

(15) Sugiura, Y.; Mino, Y. *Inorg. Chem.* **1979**, *18*, 1336.

(16) Krüger, H.-J.; Peng, G.; Holm, R. H. *Inorg. Chem.* **1991**, *30*, 734.

(17) Hanss, J.; Krüger, H.-J. *Angew. Chem., Int. Ed.* **1998**, *37*, 360.

(18) Fiedler, A. T.; Brunold, T. C. *Inorg. Chem.* **2007**, *46*, 8511.

(19) Gennari, M.; Orio, M.; Pécaut, J.; Neese, F.; Collomb, M.-N.; Duboc, C. *Inorg. Chem.* **2010**, *49*, 6399.

(20) Stenson, P. A.; Board, A.; Marin-Becerra, A.; Blake, A. J.; Davies, E. S.; Wilson, C.; McMaster, J.; Schröder, M. *Chem. - Eur. J.* **2008**, *14*, 2564.

(21) Gennari, M.; Orio, M.; Pécaut, J.; Bothe, E.; Neese, F.; Collomb, M. N.; Duboc, C. *Inorg. Chem.* **2011**, *50*, 3707.

(22) Nolan, E. M.; Racine, M. E.; Lippard, S. J. *Inorg. Chem.* **2006**, *45*, 2742.

(23) Fulmer, G. R.; Miller, A. J. M.; Sherden, N. H.; Gottlieb, H. E.; Nudelman, A.; Stoltz, B. M.; Bercaw, J. E.; Goldberg, K. I. *Organometallics* **2010**, *29*, 2176.

(24) Gore, E. S.; Busch, D. H. *Inorg. Chem.* **1973**, *21*, 1139.

(25) Lovecchio, F. V.; Gore, E. S.; Busch, D. H. *J. Am. Chem. Soc.* **1974**, *96*.

(26) Telser, J. *J. Braz. Chem. Soc.* **2010**, *21*, 1139.

(27) Belford, R. L.; Nilges, M. J. In *EPR Symposium, 21st Rocky Mountain Conference* Denver, Co, 1979.

(28) Belford, R. L.; Belford, G. G. *J. Chem. Phys.* **1973**, *59*, 853.

(29) Seth, J.; Palaniappan, V.; Bocian, D. F. *Inorg. Chem.* **1995**, *34*, 2201.

(30) *SMART: Software for the CCD Detector System, v5.626*; Bruker AXS: Madison, WI, 2000.

(31) Walker, N.; Stuart, D. *Acta Crystallogr.* **1983**, *A39*, 158.

(32) Sheldrick, G. M. *SADABS: Area Detector Absorption Correction*; University of Göttingen: Göttingen, Germany, 2001.

(33) Sheldrick, G. M. *Program for Refinement of Crystal Structures*; University of Göttingen: Göttingen, Germany, 1997.

(34) Sheldrick, G. M. *SHELXTL 6.1, Crystallographic Computing System*; Siemans Analytical X-Ray Instruments: Madison, WI, 2000.

(35) Johnson, C. K. *ORTEP-III, Report ORNL - 5138*; Oak Ridge National Laboratory: Oak Ridge, TN, 1976.

CHAPTER 5

CONCLUSIONS

We have successfully developed and studied a small library of synthetic Ni-complexes designed after, and accurately modeling, the Ni-SOD active site. In this regard, we pursued a modular strategy by which we could prepare models amenable to manipulation of a singular ligand component, leaving other aspects unperturbed. Through the development of various versatile synthetic protocols, systems were successfully designed that allowed for facile substitution of the ligand component modeling the Cys6 donor with thiolate ligands of variant nature.

By way of this approach, electronic modifications and secondary sphere functional groups such as peptides capable of hydrogen-bonding to coordinated thiolates could be readily introduced. Rigorous analysis of the resultant structural, spectroscopic and reactivity properties revealed how seemingly subtle modulation of this key component could be of drastic consequence. For example, introduction of a single thiolate-S directed hydrogen-bonding interaction could afford six-fold kinetic protection against S-oxidation in the presence of large excess of reactive oxygen species, signifying a possible mode of protection during enzyme catalysis. Indeed, close inspection of the protein structure reveals multiple hydrogen-bonding interactions directed at the coordinated cysteinates.

Our models featuring exchangeable thiolates are stable in aprotic solvents, however, dissolution in H_2O results in thiolate dissocation and oligomeric S,S'-bridging interactions. In fact, general correlations can be made between the magnitude of this process and the relative basicity of exogenously added thiolate ligand, with stronger donors displaying more labile behavior. This behavior highlights a key stabilizing role for the protein framework in Ni-SOD. Also, considering the fact that ligand dissociation in square-planar d^8 complexes is proceeded by formation of higher coordinate species, this finding implies that relatively weak interactions with the cysteinate ligands may be sufficient to trigger imidazole binding. Square-planar Ni(II) is notoriously inert and one can envision cysteinate protonation or solvent exposure as a means triggering formation of a more reactive, five-coordinate Ni(II) species.

We also demonstrated the stabilizing role of the axial N-imidazole component with regards to high-valent enzymatic intermediates via synthetic removal/ introduction of ligand contributions modeling this key interaction. Specifically, we demonstrated that upon oxidation, the presence of an appended N-donor afforded transient stabilization of species spectroscopically similar to that observed for Ni-SOD_{ox}. This intermediate follows a controlled rearrangement pathway to a dimeric species from which our initial model can be readily regenerated. In the absence of this interaction, oxidation results only in irreversible polymerization/ demetalation processes with no relevance to the Ni-SOD catalytic cycle.

In summary, the synthesis and study of carefully designed models accurately mimicking the Ni-SOD active site have provided a means of probing several hypothesis regarding the unusual assembly and mechanism of this catalytic species via an approach grounded in experimental rigor. Ultimately, an in depth chemical knowledge pertaining to a hitherto ill-understood mechanism of anti-oxidant defense has amounted as a consequence of this research.

APPENDIX A

DIVERGENT REACTIVITY OF TWO ISOMERIC Ni(II)-N_2S_2 COMPLEXES TUNED BY THE POSITIONING OF A SECONDARY SPHERE AMINE

A.1. Synthesis, Characterization and Reactivity

The isomeric complexes (Et_4N)[Ni(nmp)(SC_6H_4-*p*-NH_2)] (**1**) and (Et_4N)[Ni(nmp)(SC_6H_4-*o*-NH_2)] (**2**) (Figure 1) were initially conceived and prepared to probe the effects of S-directed hydrogen-bonding in two otherwise electronically equivalent models of Ni-SOD_{red}. Both complexes were crystallographically characterized (Figures 2 and 3 for **1** and **2**, respectively) and display similarly disposed square-planar NiN_2S_2 coordination motifs to one another and to other complexes featuring the nmp^{2-} ligand framework (Chapter 2 contains a detailed structural description). Intramolecular hydrogen-bonding is observed in the solid-state structure of **2**, and unlike analogous systems featuring NH•••S bonding, the Ni-S_{exo} bond is slightly elongated (2.2169(7) Å) as compared to its congener lacking hydrogen bonding (2.2049(14) Å for **1**). Otherwise, no noteworthy divergences in the structural data are observed (see Table 1).

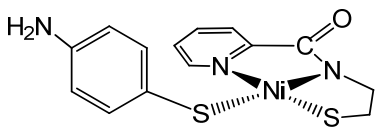

[Ni(nmp)(SC_6H_4-*p*-NH_2)]$^-$
(1)

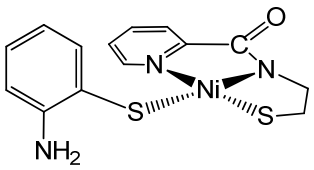

[Ni(nmp)(SC_6H_4-*o*-NH_2)]$^-$
(2)

Figure 1. Anionic portions of (Et_4N)[Ni(nmp)(SC_6H_4-*p*-NH_2)] (**1**) and (Et_4N)[Ni(nmp)(SC_6H_4-*o*-NH_2)] (**2**).

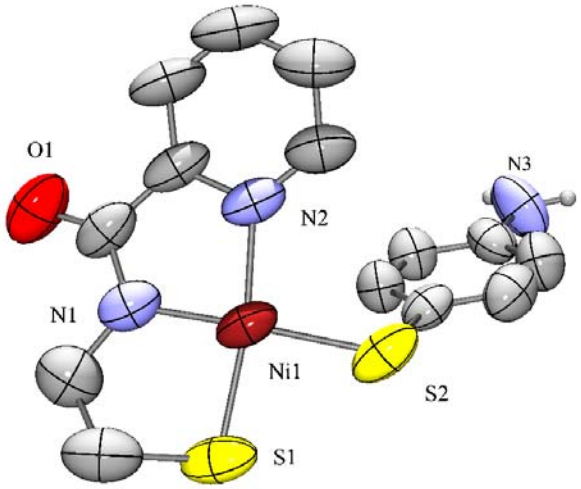

Figure 2. ORTEP diagram of the anion of **1** showing 50% thermal ellipsoids for all non-hydrogen atoms. Hydrogen atoms omitted for clarity with the exception of that attached to N3.

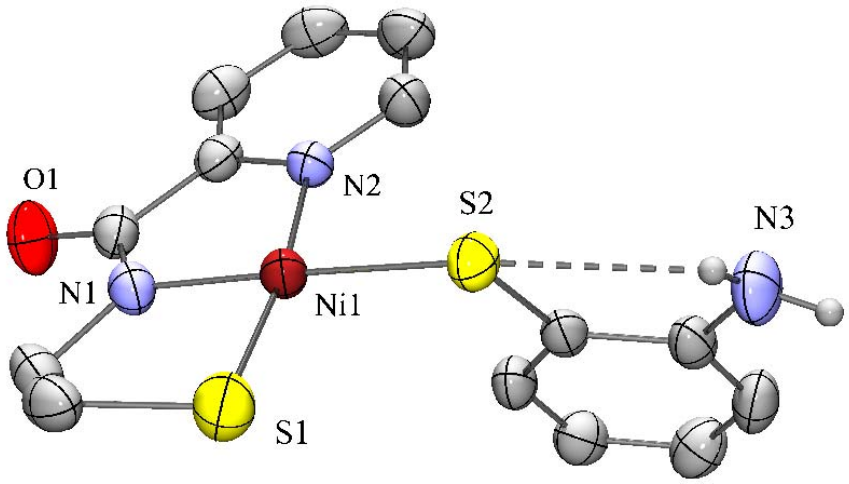

Figure 3. ORTEP diagram of the anion of **2** showing 50% thermal ellipsoids for all non-hydrogen atoms. Hydrogen atoms omitted for clarity with the exception of that attached to N3.

Table 1. Selected bond distances [Å] and bond angles [deg] for **1** and **2**.

	1	**2**
Ni(1)-N(1)	1.869(4)	1.8649(16)
Ni(1)-N(2)	1.937(4)	1.9397(18)
Ni(1)-S(1)	2.1435(15)	2.1379(12)
Ni(1)-S(2)	2.2049(14)	2.2169(7)
N(1)-Ni(1)-N(2)	83.79(18)	83.23(7)
N(1)-Ni(1)-S(1)	87.82(12)	88.49(5)
N(1)-Ni(1)-S(2)	177.65(13)	178.26(5)
N(2)-Ni(1)-S(1)	171.43(14)	171.69(5)
N(2)-Ni(1)-S(2)	98.47(14)	97.77(5)
S(1)-Ni(1)-S(2)	89.94(6)	90.52(2)
Ni(1)-S(1)-C(1)	98.73(16)	98.91(8)
Ni(1)-S(2)-C(9)	106.54(14)	104.67(6)

Both **1** and **2** afford ^{1}H NMR spectra displaying resonances consistent with square-planar d^8 (S = 0) coordination in CD_3CN. Hydrogen-bonding appears to be present in the solution structure of **2** as evidenced by the downfield shift by 1.35 ppm

of the NH_2 resonance (from 3.44 ppm for **1** to 4.79 ppm for **2**). Complexes **1** and **2** provide analogous UV-vis spectra (Figure 4, left). Both complexes display irreversible oxidation peaks at -44 mV and –79 mV vs. Ag/AgCl in MeCN, respectively (Figure 4, right), and both quantitatively decompose to the dimeric product $Ni_2(nmp)_2$ and the respective disulfide of RS_{exo}^- upon oxidation with ferrocenium hexafluorophosphate at RT. Electronic structure calculations reveal analogous dispositions in terms of molecular geometry and frontier molecular orbital analysis.

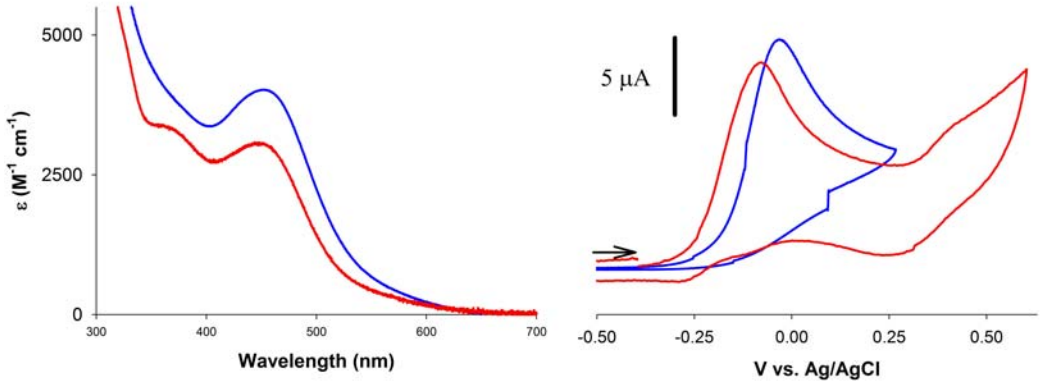

Figure 4. (Left): UV-vis spectra of **1** (blue) and **2** (red) in MeCN at 298 K. (Right): Cyclic voltammograms of 5 mM solutions of **1** and **2** (vs. Ag/AgCl in MeCN, 0.1 M $^nBu_4NPF_6$ supporting electrolyte, glassy carbon working electrode, scan rate 100 mV/s, RT).

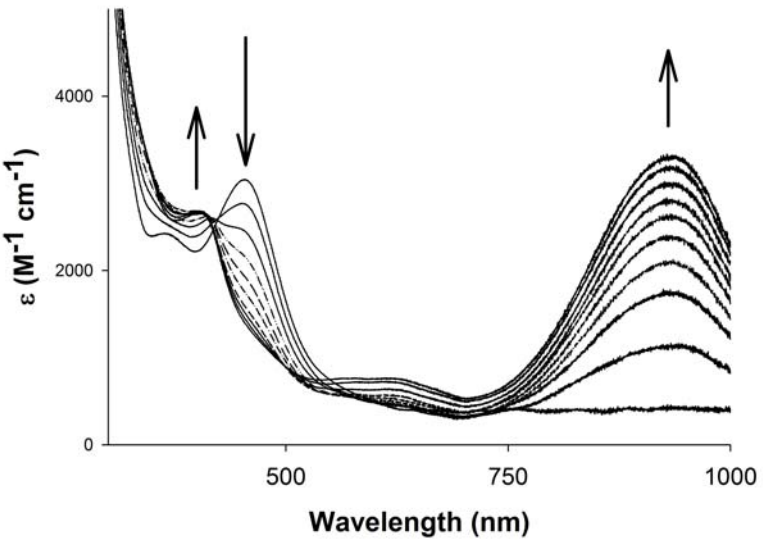

Figure 5. Complex **2** (0.09 mM) in MeCN exposed to atmospheric O_2 over 90 min (arrows show direction of change).

Despite the similarities between these two species, divergent reactivity with O_2 and ROS are observed. Complex **1** reacted with O_2 and H_2O_2 in a manner analogous to the $[Ni(nmp)(SR)]^-$ species discussed in Chapter 2, following a S-based oxygenation and disulfide forming decomposition pathway. However, upon exposure of MeCN solutions of **2** to aerobic atmosphere, a large optical transition appeared at 930 nm as monitored by UV-vis (Figure 5). This transition gains intensity for roughly 90 min before slow decomposition to intractable byproducts which we believe to be largely comprised of $Ni_2(nmp)_2$ based on FTIR analysis. That this chemistry is affected by O_2 exposure is confirmed by treatment of **2** in MeCN with dry O_2(g); however, reactivity is much more rapid and difficult to study under these conditions, even under brief O_2 purge (< 5 s). Similar reactivity is observed upon treatment of **2** with 2 equiv. H_2O_2, or 2 equiv. $O_2^{\bullet-}$ (KO_2 solubilized by 18-crown-6 in THF), which

generates small amounts of this newly formed, oxidized species as monitored by UV-vis. Benzoic acid also acts as an accelerant in the observed O_2 and $O_2^{\bullet-}$ reactivity. Interestingly, FTIR analysis of material isolated from the oxidant treated reaction mixtures revealed no stretches characteristic of S-oxygenates (strong bands between 1000-1200 cm^{-1}).

The product(s) formed upon treatment of **2** with O_2 and ROS are inherently unstable, and structural analysis remains elusive. However, EPR analysis at 10 K in DMF of solutions of **2** after prolonged exposed to aerobic atmosphere or treatment with 2.3 mol-equiv. H_2O_2 reveals a rhombic EPR spectrum (**g** = [2.14, 2.12, 2.03, 2.00]); perhaps due to more than one species (Figure 5). This signal is similar in appearance to that observed by Wieghardt for an anionic Ni-N/S complex featuring *o*-iminothionebenzoquinonate ligands in which a ligand based radical is proposed to be a major resonance contributor.[1] This chemistry has also been observed in similar Ni-N/E (E = S, Se, Te) species by Liaw.[2] In fact, both complexes display low-energy transitions analogous to the large 930 nm transition observed upon exposure of oxidation of **2** by O_2 and ROS; this transition is believed to arise from an *o*-iminothionebenzoquinonate based π-radical.

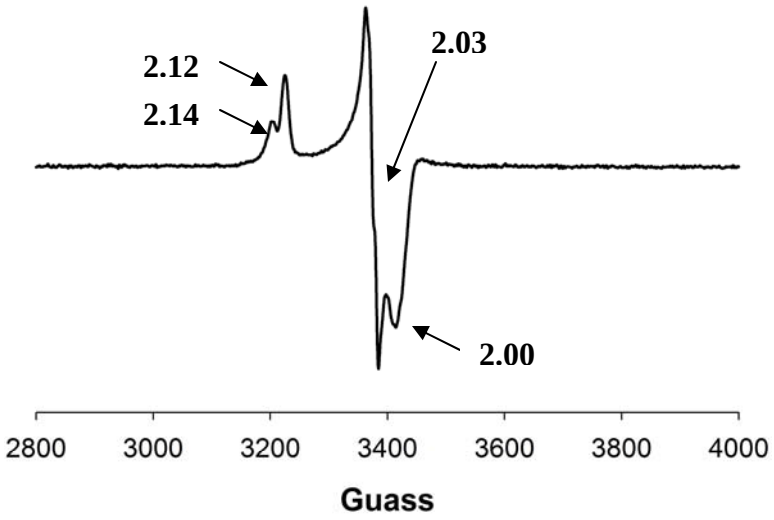

Figure 5. X-band EPR spectrum of **2** after 12 h atmospheric O_2 exposure in DMF at 10 K.

Although we have not rigorously established the nature of the species arising from oxidation of **2**, it appears likely that we are observing a species in which *o*-iminothionebenzoquinonate is a large contributor to the overall electronic structure. This mode of reactivity represents a surprising divergence from the SOD-type chemistry we had aimed to model. The mechanistic details of this oxidation process remain unresolved at present; however, the observation that the otherwise electronically identical **1** displays no such reactivity highlights that the positioning of the amino functional group near the NiN_2S_2 coordinative motif as a key parameter towards observing this chemistry. It is also interesting to note that similarly positioned amide functional groups do not promote this reactivity. The mechanisms of O_2 oxidation by Ni-S containing complexes is also a poorly defined process and few insights can be gleaned into this process from literature precedence.

It is worth noting that while NH•••S bonding afforded significant protection against S-modification from H_2O_2, no such protection was observed against O_2, perhaps indicative of oxidation at the Ni ion. It is also worth noting is that the kinetic profile of O_2 affected decomposition of (Et_4N)[Ni(nmp)(S-*o*-babt)] is more rapid than that observed for (Et_4N)[Ni(nmp)(SC_6H_4-*p*-Cl)] by a full order of magnitude (see Chapter 2, Table 4). Taken together, the chemistry observed upon O_2 treatment of **2**, the observation that benzoic acid accelerates this process, and the aforementioned increase in O_2 reactivity upon introduction of a peptide near the NiN_2S_2 bonding motif in complexes featuring aromatic-S_{exo} donors, the possibility that proton coupled reduction of O_2 to ROS is traversed along the reaction coordinate seems reasonable. It appears that complex **2**, featuring a presciently positioned amine functional group amenable to H-atom abstraction, may serve as an indirect marker of such O_2 activating processes through product analysis.

Efforts are currently underway in or laboratory to determine the validity of this hypothesis and to elucidate the mechanistic details of O_2 oxidation of NiN_2S_2 species inspired by Ni-SOD.

A.2. Experimental Section

General Information. See Chapter 2, Section 2.7 for information pertaining to common laboratory reagents and solvents.

Physical Methods. See Chapter 2, Section 2.7 for information pertaining to FTIR, ^{1}H NMR, UV-vis, CV and ESI measurements. See Chapter 4, Section 4.10 for information pertaining to EPR.

(Et_4N)[Ni(nmp)(SC_6H_4-*p*-NH_2)] (1). A batch of 49.4 mg (0.108 mmol) of K[Ni(nmp)(S^{t}Bu)] (see Chapter 2) and 14.5 mg (0.116 mmol) of 4-aminothiophenol were combined in 6 mL of MeCN at RT. After 16 h stirring, the reaction mixture was concentrated to a red residue and stirred in 10 mL of THF for 1 h to obtain free flowing solids. The majority of the THF was decanted off and the mixture was saturated with Et_2O and stirred for 1 h. After stirring, 39.4 mg (0.080 mmol, 73.9%) of product was isolated via vacuum filtration. Dark red plates suitable for X-ray analysis were obtained via slow diffusion of Et_2O into a saturated 4:1 THF/DMF solution of **1**. ^{1}H NMR (500 MHz, $CDCl_3$, δ from TMS): 8.59 (d, 1H), 7.69 (m, 4H), 7.14 (t, 1H), 6.42 (d, 2H), 3.44 (m, 4H, OC-NH-CH_2-CH_2-S and NH_2), 3.30 (q, 8H, $(CH_3CH_2)_4N$)), 2.31 (t, 2H, OC-NH-CH_2-CH_2-S), 1.28 (t, 12H, $(CH_3CH_2)_4N$). FTIR (KBr pellet) ν_{max} (cm^{-1}): 3300 (w, NH), 3192 (w, NH), 2978 (w), 2910 (w), 2839 (w), 1616 (s, C=O), 1591 (s, C=O), 1484 (m), 1392 (m), 1279 (w), 1170 (w), 1087 (w), 999 (w), 814 (w), 767 (w), 689 (w), 632 (w), 557 (w), 512 (w), 484 (w), 439 (w). UV-vis (MeCN) λ_{max}, nm (ε): 451 (4290). Anal. Calcd for $C_{22}H_{36}N_4NiO_2S_2$: C, 51.67; H, 7.10; N, 10.96. Found: C, 51.31; H, 6.48; N, 10.33. E_{ox} (MeCN): -44 mV.

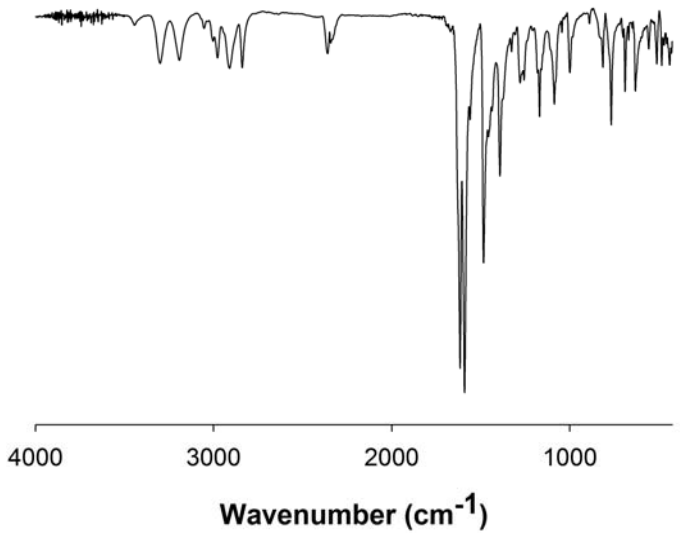

Figure 6. FTIR (KBr matrix) of **1** (stretches at 2360 cm^{-1} and 2341 cm^{-1} from atmospheric CO_2).

(Et_4N)[Ni(nmp)(SC_6H_4-*o*-NH_2)] (2). To a batch of 36.9 mg (0.080 mmol) (Et_4N)[Ni(nmp)(S^tBu)] stirring in 5 mL MeCN at RT was added 9.5 μL (0.09 mmol) of 2-aminothiophenol. After overnight stirring any turbidity was filtered off and the mother liquor was concentrated to a red-orange residue. Standing in Et_2O yielded 25 mg (0.05 mmol, 63% yield) of (Et_4N)[Ni(nmp)(SC_6H_4-*o*-NH_2)] as red-orange solids. Red blocks suitable for X-ray analysis were obtained via slow diffusion of Et_2O in a saturated 5:1 chlorobenzene/DMF solution of **2**. ^1H NMR (500 MHz, $CDCl_3$, δ from TMS): 8.49 (d, 2H), 8.12 (d, 2H), 7.67 (m, 2H), 7.10 (t, 2H), 6.75 (t, 2H), 6.48 (m, 2H), 4.79 (d, 2H, N*H*$_2$), 3.44 (t, 2H, SCH_2*C*H_2NH), 3.28 (q, 8H, (CH_3*C*H_2)$_4$N), 2.32 (t, 2H, S*C*H_2CH_2NH), 1.27 (t, 12H, (*C*H_3CH_2)$_4$N). FTIR (KBr pellet) ν_{max} (cm^{-1}): 3406 (m, N-H), 3308 (m, N-H), 3069 (m), 3035 (m), 2974 (m), 2944 (w), 2915 (m), 2896 (m), 2847 (m), 1617 (vs, C=O), 1594 (vs, C=O), 1568 (s), 1560 (s), 1476 (s), 1447 (m), 1437 (m), 1392 (s), 1370 (w), 1329 (w), 1293 (m), 1258 (m), 1172 (m), 1156 (w), 1080 (m), 1046 (m), 1025 (m), 999 (m), 981 (w), 972 (w), 927 (w), 887

(w), 853 (w), 815 (w), 786 (m), 762 (m), 755 (w), 700 (w), 687 (m), 675 (m), 651 (w), 624 (w), 558 (w), 485 (m), 472 (w), 450 (w), 436 (m). UV-vis (MeCN) λ_{max}, nm (ε): 451 (3040). E_{ox} (MeCN): -79 mV

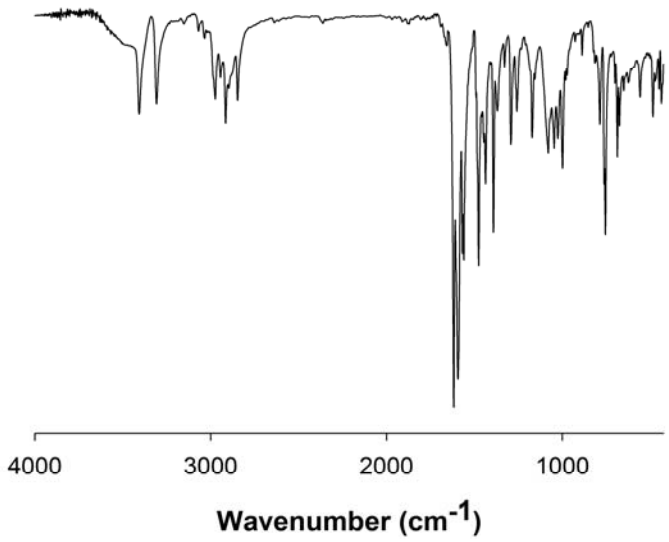

Figure 7. FTIR (KBr matrix) of **2**.

Reaction of 1 with O_2 and H_2O_2. Complex **1** was tested against O_2(g) and H_2O_2 as described in Chapter 2, Section 2.7.

Reaction of 2 with O_2. Solutions of **2** were reacted with atmospheric O_2 simply by exposure. FTIR (KBr pellet) ν_{max} (cm^{-1}): FTIR (KBr pellet) ν_{max} (cm^{-1}): 3350 (m br), 3197 (m, br), 2985 (w), 2949 (w), 1663 (s), 1616 (s, C=O), 1588 (s, C=O), 1560 (s), 1481 (s), 1458 (s), 1443 (s), 1392 (s), 1345 (m), 1305 (m), 1276 (w), 1261 (m), 1234 (w), 1212 (m), 1183 (m), 1172 (m), 1085 (m), 1053 (w), 1020 (m), 1001 (m), 968 (w), 944 (w), 883 (w), 868 (w), 839 (w), 784 (w), 751 (w),

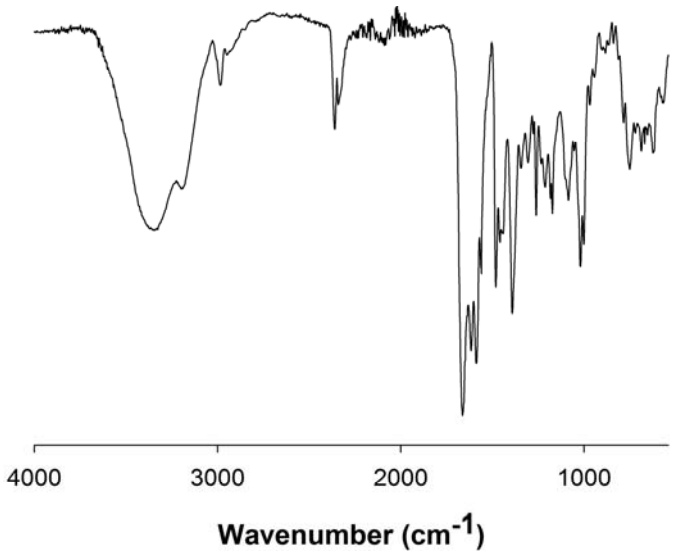

Figure 8. FTIR (KBr matrix) of **2** after overnight exposure to atmospheric O_2 (stretches at 2360 cm^{-1} and 2341 cm^{-1} from atmospheric CO_2).

Reaction of 2 with H_2O_2: To a batch of 29.6 mg (0.060 mmol) of **2** stirring in 5 mL DMF at -40°C was added 9.5 μL (0.14 mmol) of 50% H_2O_2 by wt. in H_2O - no change was observed. The slush bath was then removed and the reaction mixture was allowed to slowly warm to RT. Upon warming, the solution changed from red-orange to dark brown and was left to equilibrate at RT. After 1 h stirring, the reaction mixture was concentrated to 1 mL and saturated with Et_2O to precipitate out dark brown solids. 18.2 mg (0.037 mmol, 62% yield) were collected via vacuum filtration. FTIR (KBr pellet) ν_{max} (cm^{-1}): 3427 (vs, br, N-H), 2988 (w), 2944 (w), 2888 (w), 1625 (m, C=O), 1587 (s, C=O), 1563 (m, C=O), 1484 (m) 1461 (m), 1396 (m), 1385 (m), 1347 (w), 1296 (w), 1266 (w), 1218 (w), 1184 (w) 1174 (w), 1154 (w), 1122 (m), 1109 (w), 1069 (w), 1025 (w), 1003 (w), 966 (w), 784 (w), 759 (m), 687 (m), 636 (m), 620 (w), 524 (w).

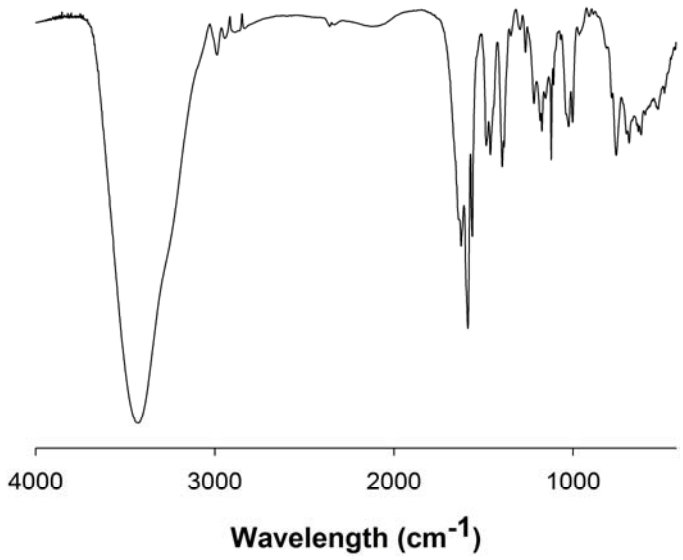

Figure 9. FTIR (KBr matrix) of product isolated upon treatment of **2** with 2 mol-equiv. H_2O_2 in DMF.

X-ray Data Collection and Structure Solution Refinement. A suitable crystal was mounted inside of a glass capillary or on the top of a glass fiber. All geometric and intensity data were measured at 293 K on a Bruker SMART APEX II CCD X-ray diffractometer system equipped with graphite-monochromatic Mo Kα radiation (λ = 0.71073 Å) with increasing ω (width 0.5° per frame) at a scan speed of 10 s/frame or 15 s/frame controlled by the SMART software package.[3] The intensity data were corrected for Lorentz-polarization effects and for absorption[4] and integrated with the SAINT software. Empirical absorption corrections were applied to structures using the SADABS program.[5] The structures were solved by direct methods with refinement by full-matrix least-squares based on F^2 using the SHELXTL-97 software[6] incorporated in the SHELXTL 6.1 software package.[7] The hydrogen atoms were fixed in their calculated positions and refined using a riding model. All non-hydrogen

atoms were refined anisotropically. Perspective views of the complexes were obtained using ORTEP.[8] Crystallographic properties are reported in Table 2.

Table 2. Summary of Crystal Data and Intensity Collection and Structure Refinement Parameters for **1** and **2**.

[a] $R_1 = \Sigma| \, |F_o| - |F_c| \, | / \Sigma |F_o|$; [b] $wR_2 = \{\Sigma[w(F_o^2 - F_c^2)^2] / \Sigma[w(F_o^2)^2]\}^{1/2}$.

Parameters	**1**	**2**
Formula	$C_{22}H_{34}N_4NiOS_2$	$C_{22}H_{34}N_4NiOS_2$
Formula weight	493.36	493.36
Crystal system	Monoclinic	Monoclinic
Space group	C_1/c_1	P_{121}/n_1
Crystal color, habit	red block	red plate
a, Å	11.5892(15)	11.686(5
b, Å	13.7505(18)	10.127(5)
c, Å	16.076(2)	20.281(5)
α, deg	90.00	90.000(5)
β, deg	105.588(2)	92.641(5)
γ, deg	90.00	90.000(5)
V, Å^3	2467.7(6)	2397.6(17)
Z	4	4
ρ_{calcd}, g/cm^3	1.328	1.367
T, K	293(2)	293(2)
abs coeff, μ (Mo Kα), mm^{-1}	0.976	1.004
θ limits, deg	2.35-27.88	2.25-28.24
total no. of data	16320	5933
no. of unique data	5843	4347
no. of parameters	271	395
GOF on F^2	0.950	1.021
R_1,[a] %	4.15	3.44
wR_2,[b] %	10.43	7.51
max, min peaks, e/ Å^3	0.267, -0.169	0.331, -0.205

A.3 References

(1) Herebian, D.; Bothe, E.; Bill, E.; Weyhermuller, T.; Wieghardt, K. *J. Am. Chem. Soc.* **2001**, *123*, 10012.

(2) Hsieh, C. H.; Hsu, I. J.; Lee, C. M.; Ke, S. C.; Wang, T. Y.; Lee, G. H.; Wang, Y.; Chen, J. M.; Lee, J. F.; Liaw, W. F. *Inorg. Chem.* **2003**, *42*, 3925.

(3) *SMART: Software for the CCD Detector System, v5.626*; Bruker AXS: Madison, WI, 2000.

(4) Walker, N.; Stuart, D. *Acta Crystallogr.* **1983**, *A39*, 158.

(5) Sheldrick, G. M. *SADABS: Area Detector Absorption Correction*; University of Göttingen: Göttingen, Germany, 2001.

(6) Sheldrick, G. M. *Program for Refinement of Crystal Structures*; University of Göttingen: Göttingen, Germany, 1997.

(7) Sheldrick, G. M. *SHELXTL 6.1, Crystallographic Computing System*; Siemans Analytical X-Ray Instruments: Madison, WI, 2000.

(8) Johnson, C. K. *ORTEP-III, Report ORNL - 5138*; Oak Ridge National Laboratory: Oak Ridge, TN, 1976.

APPENDIX B

FOOTNOTE PERTAINING TO $(Et_4N)_2[Ni(SC_6H_4\text{-}p\text{-}Cl)_4]$ STRUCTURAL DATA

B.1 Synthesis

Single crystals of $(Et_4N)_2[Ni(SC_6H_4\text{-}p\text{-}Cl)_4]$ were isolated from recrystallization attempts of $(Et_4N)[Ni(ama)(SC_6H_4\text{-}p\text{-}Cl)]$ ($amaH_2$ = 2-amino-N-(2-mercaptoethyl)acetamide; H represents dissociable protons) (**1**) in the presence of $(Et_4N)(SC_6H_4\text{-}p\text{-}Cl)$ by slow diffusion of Et_2O into a saturated MeCN solution at RT (Scheme 1). The spectral properties of $(Et_4N)[Ni(ama)(SC_6H_4\text{-}p\text{-}Cl)]$ are nearly identical to those observed for $(Et_4N)[Ni(GC\text{-}OMe)(SC_6H_4\text{-}p\text{-}Cl)]$ (see Chapter 3). Solutions of $(Et_4N)[Ni(GC\text{-}OMe)(SC_6H_4\text{-}p\text{-}Cl)]$ will eventually deposit $(Et_4N)_2[Ni(SC_6H_4\text{-}p\text{-}Cl)_4]$ as single crystals as well, even if no free thiolate is present.

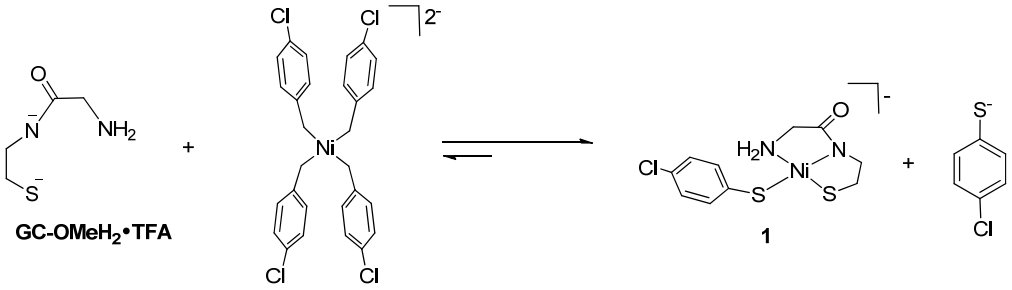

Scheme 1. In the presence of excess $SC_6H_4\text{-}p\text{-}Cl$-, single crystals of $[Ni(SC_6H_4\text{-}p\text{-}Cl)_4]^{2-}$ (as the Et_4N^+ salt) will eventually deposit.

The N_2S-chelate amaH_2•TFA was prepared by coupling S-trityl protected cysteamine and BOC-Gly-OSu in quantitative yield (Scheme 2). Subsequent deprotection of the S- and N- protecting groups by stirring with Et_3SiH in TFA afforded amaH_2•TFA in 89% yield. Deprotonation of amaH_2•TFA with NaH in MeCN followed by treatment with $(Et_4N)_2[Ni(SC_6H_4\text{-}p\text{-}Cl)_4]$ resulted in purple solutions of **1**. Complete removal of resultant $(Et_4N)(SC_6H_4\text{-}p\text{-}Cl)]$ proved exceedingly difficult. Although the equilibrium of the reaction displayed in Scheme 1 ultimately favors formation of **1** and no remaining $(Et_4N)_2[Ni(SC_6H_4\text{-}p\text{-}Cl)_4]$ is detected by ^{1}H NMR, crystals of the tetra-thiolato complex will deposit from standing solutions over time.

Usage of amaH_2•TFA was eventually discontinued in favor of GC-OMeH_2, as it is a more electronically accurate mimic of the His1Cys2 tri-dentate chelate of Ni-SOD_{red}. The usage of tetra-thiolato Ni(II) complexes as synthons was also ceased in favor of more effective methodology (see Chapters 2 and 3).

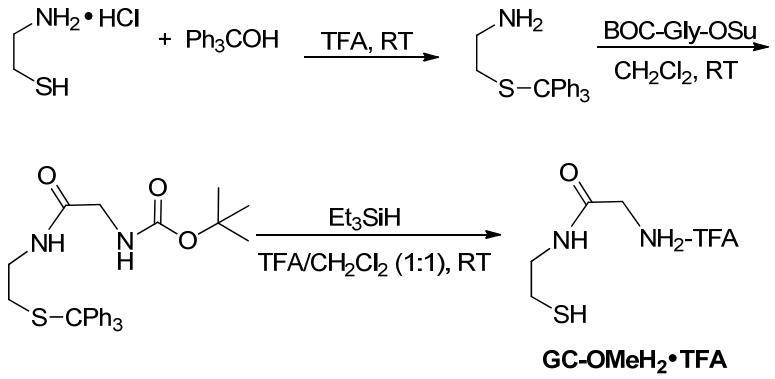

Scheme 2. Synthesis of amaH_2•TFA.

B.2 Experimental Section

General Information. See Chapter 2, Section 2.7 for information pertaining to common laboratory reagents and solvents.

Physical Methods. See Chapter 2, Section 2.7 for information pertaining to FTIR, ^{1}H NMR and ^{13}C NMR spectroscopy, UV-vis and ESI measurements.

2-amino-N-(2-mercaptoethyl)acetamide•TFA ($amaH_2$•TFA). The synthesis followed an analogous protocol to GC-$OMeH_2$•TFA (Chapter 3, Section 5). A batch of 988 mg (3.09 mmol) of S-trityl-protected cystamine and 846 mg (3.11 mmol) were stirred together in 40 mL CH_2Cl_2. After 16 h, the reaction mixture was washed with satd. $NaHCO_3$ and brine, dried over $MgSO_4$ and concentrated to 1.508 g (100%) of the N-BOC protected pre-ligand. ^{1}H NMR (400 MHz, $CDCl_3$, δ from TMS): 7.43-7.17 (m, 15H), 6.02 (br s, 1H, N*H*), 5.01 (br s, 1H, N*H*), 3.64 (d, 2H), 3.04 (t, 2H), 2.40 (t, 2H), 1.42 (s, 9H). ^{13}C NMR (100.6 MHz, $CDCl_3$, δ from TMS): 169.28 (*C*=$O_{peptide}$), 156.09 (*C*=$O_{carbamate}$), 144.71, 129.92, 129.64, 128.10, 126.93, 80.36, 66.96, 44.38, 38.22, 31.89, 28.41.

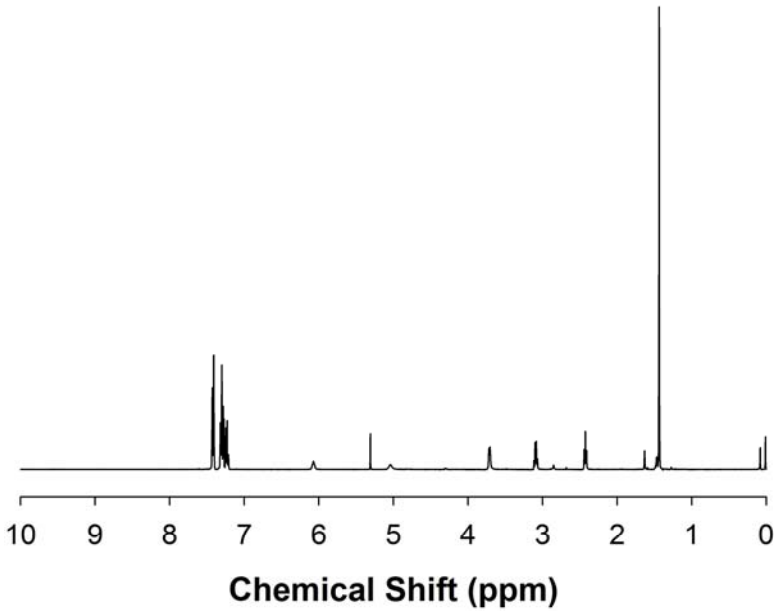

Figure 1. ^{1}H NMR of the N-BOC and S-trityl protected pre-ligand in $CDCl_3$ (peak at 5.30 ppm is from residual CH_2Cl_2).

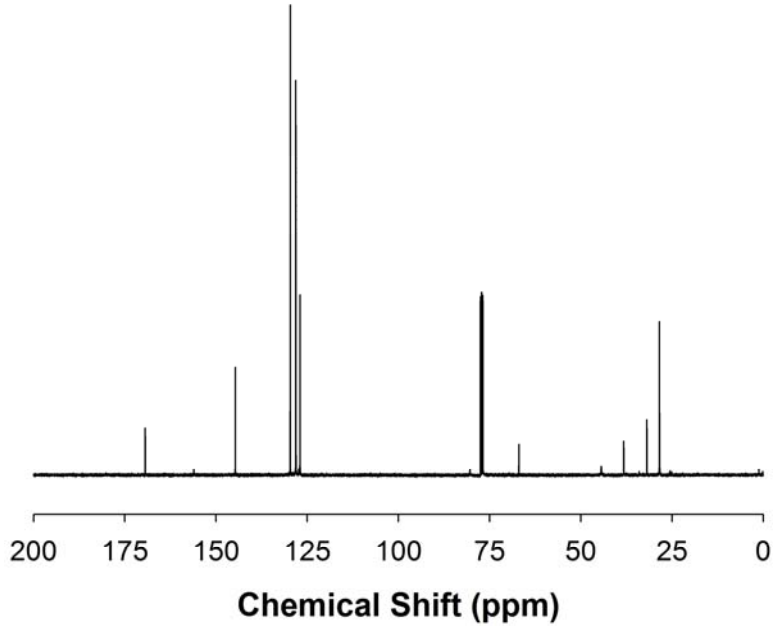

Figure 2. ^{13}C NMR of the N-BOC and S-trityl protected pre-ligand in $CDCl_3$ (peak at 77.16 is from solvent).

To deprotect, 792 mg (1.67 mmol) of the pre-ligand was stirred in 10 mL of 1:1 TFA:CH_2Cl_2. After 1 h, 284 mg (2.44 mmol) of triethylsilane was added to the bright orange solution and the color bleached. The clear solution was concentrated to ½ the original volume and solid Ph_3CH was removed via filtration. The mother liquor ws concentrated to residue and triturated with cold Et_2O to leave 343 mg (1.48 mmol, 89%) of amaH_2•TFA as a beige residue. ^{1}H NMR (400 MHz, $CDCl_3$, δ from TMS): 7.80 (s, br s, 3H, N*H*$_3$), 7.60 (s, br, 1H, N*H*$_{peptide}$), 3.79 (s, 2H), 3.40 (t, 2H), 2.61 (t, 2H), 1.78 (t, 1H). ^{13}C NMR (100.6 MHz, $CDCl_3$, δ from TMS): 166.99 (*C*=O$_{peptide}$), 160.94 (*C*=O$_{TFA}$), 43.52, 41.88, 31.17. FTIR (KBr pellet) ν_{max} (cm^{-1}): 3264 (w, br, N-H), 2094 (w, br, N-H), 1653 (s, C=O). LRMS-ESI (m/z): $[M + H]^+$ calcd for $C_4H_{11}N_2OS$, 135.1; found, 135.0.

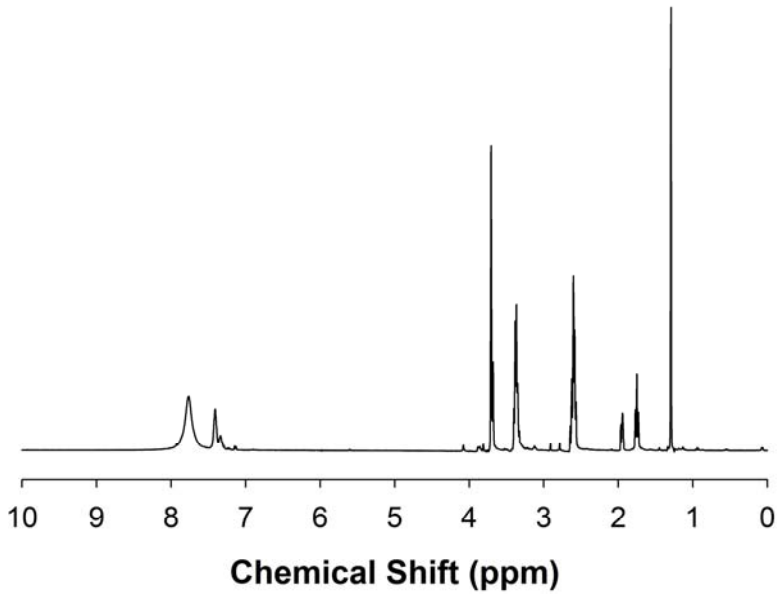

Figure 3. ^{1}H NMR of amaH_2•TFA in CD_3CN (peak at 1.94 ppm is from residual protio solvent).

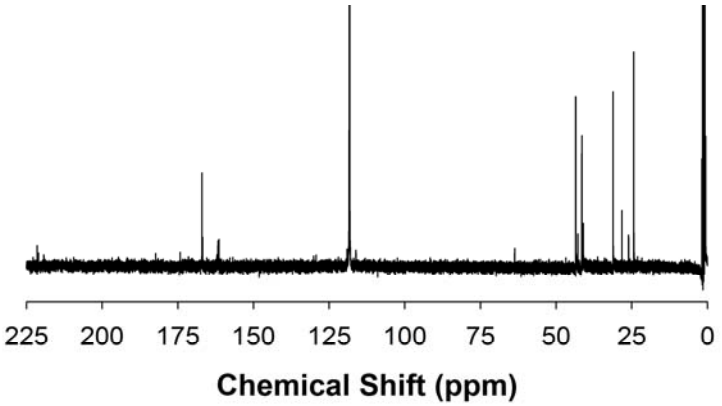

Figure 4. ^{13}C NMR of amaH_2•TFA in CD_3CN (peaks at 118.26 and 1.32 ppm are from solvent).

(Et_4N)[Ni(ama)(SC_6H_4-*p*-Cl)]. To 447 mg (0.940 mmol) of amaH_2•TFA in 25 mL MeCN was added 72 mg (3.00 mmol). Immediate effervescence was observed and the solution slowly became opaque over 20 min. A batch of 705 mg (0.790 mmol) $(Et_4N)_2[Ni(SC_6H_4\text{-}p\text{-}Cl)_4]$[1] was added and the resulting dark violet solution stirred for 4h at 40 °C. The reaction mixture was concentrated to dryness and taken up in 8 mL THF and stirred for 16 h before white solids were removed via filtration. The solution was concentrated to 286 mg (91%) of sticky purple solids. Free $(Et_4N)(SC_6H_4\text{-}p\text{-}Cl)$ remained as evidenced by ^1H NMR, however, no spectral evidence of $(Et_4N)_2[Ni(SC_6H_4\text{-}p\text{-}Cl)_4]$ remained. Dark red blocks of $(Et_4N)_2[Ni(SC_6H_4\text{-}p\text{-}Cl)_4]$ grew from slow diffusion of Et_2O into saturated solutions of $(Et_4N)[Ni(ama)(SC_6H_4\text{-}p\text{-}Cl)]$ in MeCN with free $Et_4NSC_6H_4$-*p*-Cl present at RT. ^1H NMR (400 MHz, $CDCl_3$, δ from TMS): 7.64 (d, 2H), 6.96 (d, 2H), 3.17 (q, 8H, Et_4N^+; 2H, coincidental, integrates higher due to presence of free $(Et_4N)(SC_6H_4\text{-}p\text{-}Cl)$), 3.02 (t, 2H), 2.82 (t, 2H), 2.62 (t, 1H), 2.15 (br t, 2H), 1.22 (t, 12H, integrates

higher due to presence of free $(Et_4N)(SC_6H_4$-*p*-Cl)). FTIR (KBr pellet) ν_{max} (cm^{-1}): 1574 (s, C=O). LRMS-ESI (m/z): M^- calcd for $C_{10}H_{12}ClN_2NiOS_2$, 332.9; found, 333.0.

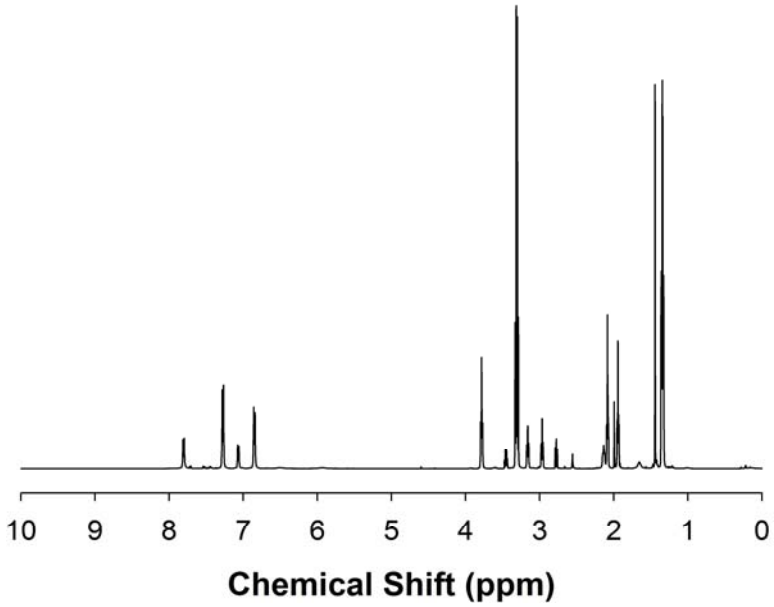

Figure 5. ^1H NMR of **1** in CD_3CN (peaks at 7.18 and 6.86 ppm are from free $(Et_4N)(SC_6H_4$-*p*-Cl), 3.64 and 1.80 ppm are from residual THF and 1.94 ppm from residual protio solvent).

B.3 References

(1) Rosenfield, S. G.; Armstrong, W. H.; Mascharak, P. K. *Inorg. Chem.* **1986**, *25*, 3014.

APPENDIX C

SYNTHETIC STUDIES TOWARDS LIGAND FRAMEWORKS FEATURING STERICALLY ENCUMBERED THIOLATES

C.1 Synthesis

The synthesis of N and S rich ligand frames featuring steric bulk around the S-donor groups was explored with the aim of enforcing Ni(III) by preclusion of decomposition via disulfide forming pathways. Introduction of thiols into densely functionalized molecules is no trivial task; thiols are highly reactive and prone to disulfide formation, oxygenation, H_2S elimination and in the presence of carbonyls, rearrangement to S-containing heterocycles.[1] Introduction of thiols at highly substituted carbons represents further difficulties as such attempts are almost invariantly met with elimination of H_2S; or of RSH if introduced as a thioether or thioester.[2] Additionally, modification of functional groups ancillary to thiols at highly substituted carbons is difficult because tertiary thiols tend to be sensitive to all but the mildest conditions. Regardless, we are tantalized by the rich chemistry to be explored upon stabilization/isolation of Ni(III) species relevant to Ni-SOD_{ox} and have embarked on various synthetic endeavors in order to achieve this end. Described below are our efforts towards the introduction of sterically protected, tertiary thiols into N and S containing compounds representing potentially useful synthons towards ligand frameworks modeling that of Ni-SOD.

Lawesson's Reagent affords high yield conversion into carbonyl groups and benzylic alcohols into corresponding thionyls and thiols, respectively.[3] However, this method is generally only applicable for the simplest carbonyls and alcohols, due to the reactivity of this reagent with most commonly encountered functional groups.[3] Regardless, there is some precedence of selective thionation of benzylic alcohols in molecules containing the carbamate functionality.[4] In this regard, we explored the possibility of conversion of BOC-N protected β-hydroxyamine (**1**)[5] to the corresponding protected β-aminothiol (**2**) (Scheme 1). In an ideal scenario, we envisioned high yield thionation at the benzylic position followed by S-protection and BOC removal to afford the sterically enforced, S-protected β-aminothiol synthon. Treatment of **1** with 0.5 mol-equiv Lawesson's Reagent in wet toluene at 50 °C afforded the desired thiol **2** in 43% yield, along with elimination product **3** in 43% yield, a product believed to be the cyclic thiocarbamate **4** in 14% yield (by ^{1}H NMR). The conditions employed have been reported to litigate thiol elimination pathways,[6] but we found that these conditions did not provide any marked improvement over refluxing in dry toluene, the most commonly utilized conditions for Lawesson's Reagent.[3] Because of inherent sensitivity of this newly introduced thiol group to several commonly utilized techniques for S-protection/BOC-N deprotection,[7] we did not pursue any further chemistry with this synthon. However, this route does serve as a viable method for thiol incorporation positioned β to a protected amine. Future S-protection/N-de-protection is foreseeable, but will require a judicious choice of reagents.

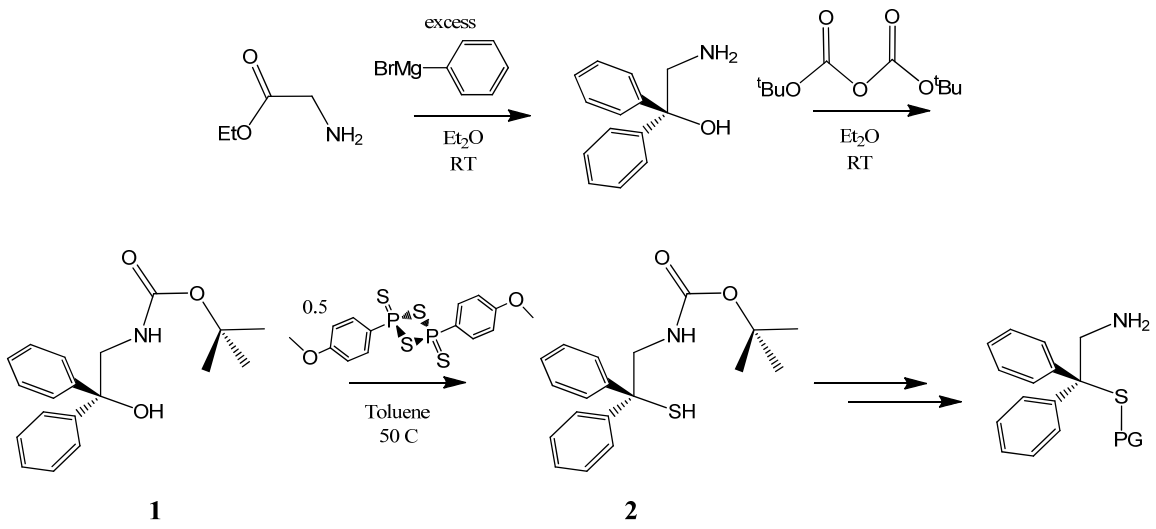

Scheme 1. Envisioned strategy to obtain *β*-aminothiol synthon by conversion of benzylic alcohol to thiol.

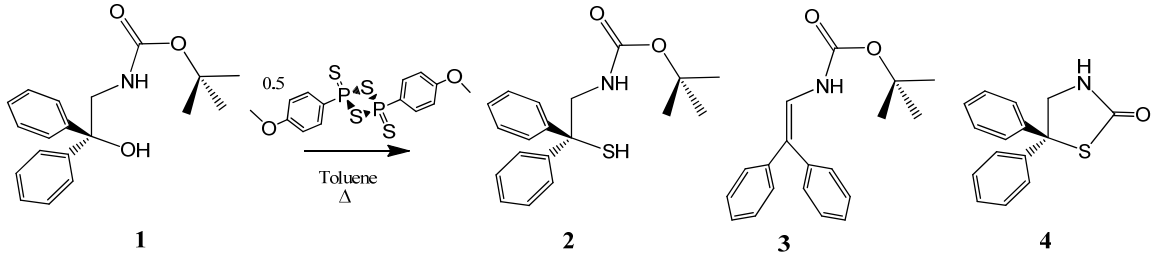

Scheme 2. Synthesis of **1** and products upon treatment with Lawesson's reagent

.

Another strategy considered involved conversion of *β*-hydroxynitriles to *β*-mercaptonitriles using Lawesson reagent. The envisioned strategy involved subsequent reduction of the nitrile to the resultant amine, affording a suitable N/S synthon. Surprisingly, the attempted thionation reactions of **5** and **6**[8] returned only starting material. Attempts at conversions to *β*-bromonitriles using PBr_3, with the aim of subsequent substitution with RS^-, resulted exclusively in elimination products.

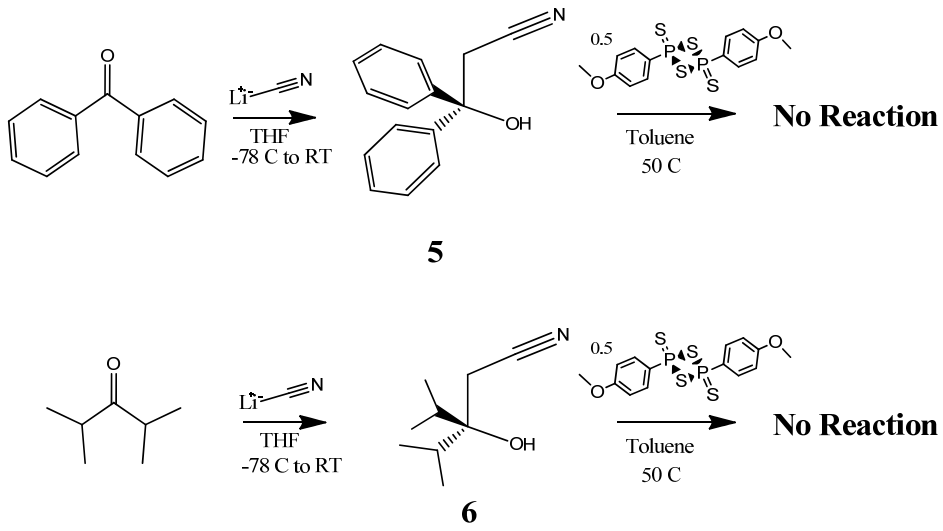

Scheme 3. Attempted thionation of *β*-hydroxynitriles.

Addition of lithiated acetonitrile to thiobenzophenone[9] was also attempted in order to obtain similar products. Elimination to the conjugated product **7** and resultant *β*-hydroxynitrile (**6**) were the only products formed, however. More success was observed upon addition of lithiated acetonitrile to 2-thioadamantanone (**8**), and the resultant thiol (**9**) could be isolated cleanly in 45% yield.

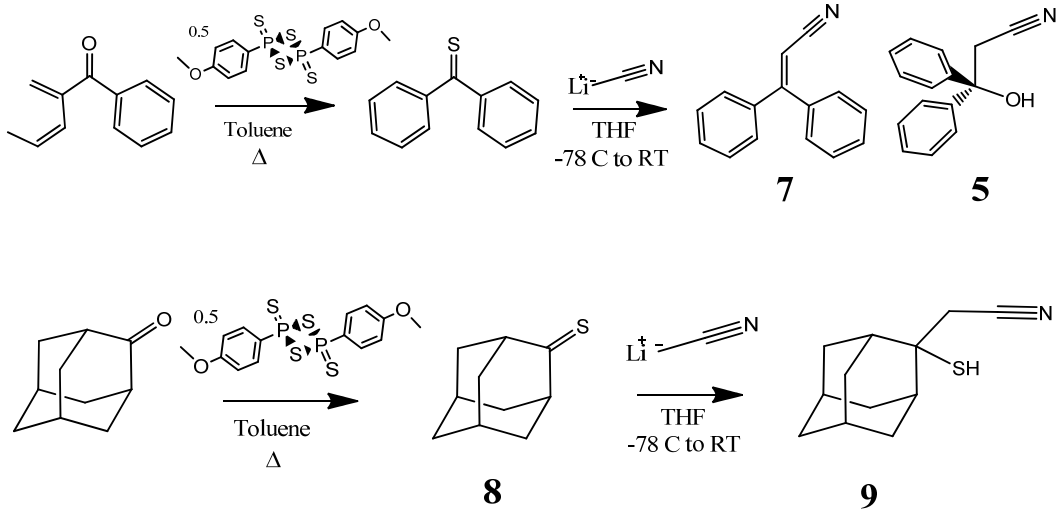

Scheme 4. Addition of lithiated acetonitrile to thioketones.

Another strategy for sterically robust γ-aminothiol formation involved S-THP (THP = 2-tetrahydropyranyl) protection of a benzylic, secondary thiol followed ionization at the benzylic position and addition to bromoacetonitrile. This reaction was inspired by methods employed by Berg and Holm to prepared sterically enforced, symmetrically substituted N/S ligands to avoid S,S'-bridging in Mo complexes modeling O-atom transfer enzymes.[10] This reaction formed the desired product (**10)** in 50% yield and unreacted starting material. Considering the similar pK_a values of bromoacetonitrile and the benzylic proton (~30),[11-12] it is likely that deprotonation of bromoacetonitrile is a competitive pathway in this reaction. Compound **10** could be reduced to the S-THP protected γ-aminothiol (**11**) in 77% yield. Surprisingly, peptide coupling of **11** with acid bromides, however, resulted in several species. None of which could be identified as the desired S-THP γ-mercaptopeptide or starting material.

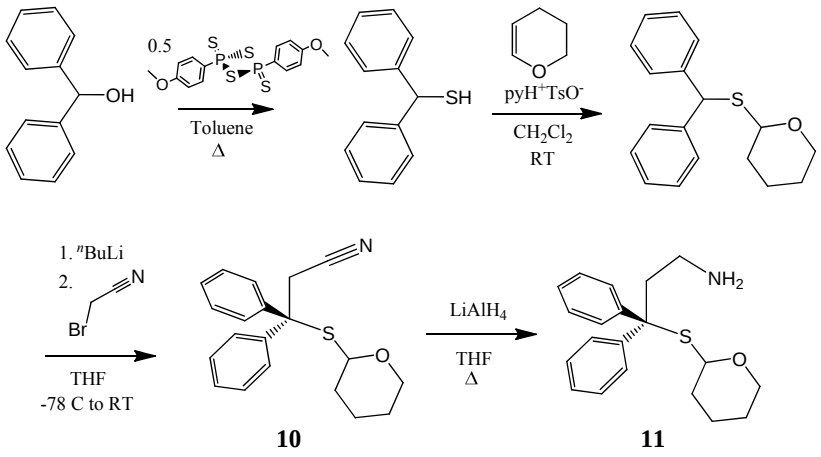

Scheme 5. Strategy towards γ-aminothiol synthons

Reduction of symmetric α-hydroxylimino- and α-iminodisulfides with $LiAlH_4$ was also explored (Scheme 6). The disulfide precursors were derived via treatment of isobutyraldehyde with sulfur dichloride[13] followed by shiff base condensation with the appropriate hydroxylamine[14] or amine. However, this strategy was met with mixed results. Reduction of **12** to **13** has been reported in the literature, but this reaction did not provide us with the desired product. Rather, several species were formed. The major product by ^1H NMR revealed a chemical inequivalence between the two methylene protons α-to the resultant amine, as if the desired β-aminothiol was incorporated into a rigid ring structure. Intriguingly, analysis by ESI revealed evidence of the product chelation to $[Al(OEt)]^{2+}$, with the EtO^- arising from workup conditions.[14] Treatment with strong acid did not effect the nature of this product. Reduction of α-iminodisulfide (**14**) yielded the desired β-aminothiol (**15**). However, the same product could be prepared in better yield and purity by treatment of picolylamine with isobutylene sulfide in refluxing toluene (Scheme 7).[15] This product was involved in the synthesis of $H_3N_3S_2Me_2$, discussed in Chapter 4.

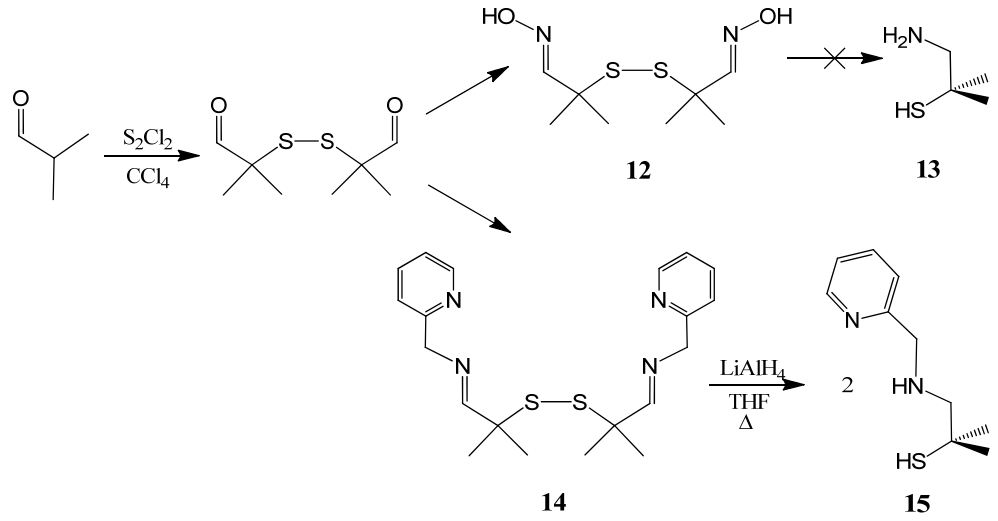

Scheme 6. Preparation of β-aminothiols from reduction of α-hydroxylimino- and iminodisulfides.

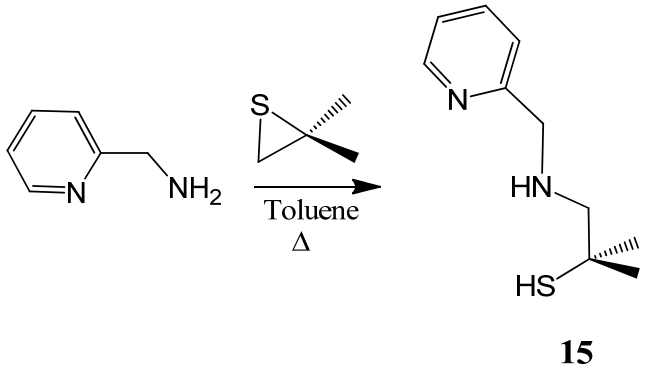

15

Scheme 7. Preparation of β-aminothiol by reaction of primary amine with thioepoxide.

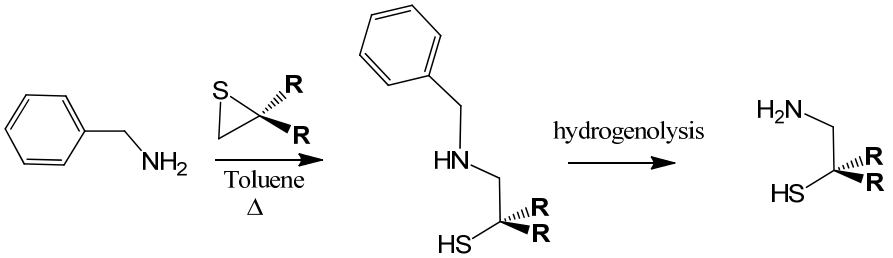

Scheme 8. Proposed general procedure towards preparation of β-aminothiol synthons featuring primary amine.

Several routes of tertiary thiol introduction into potential synthons for the desired N/S ligands were explored. Despite some successes, it appears that the cleanest and simplest method involved addition of a primary amine to a thioepoxide. The synthesis of thioepoxides from epoxides is robust and well established.[16] Given the numerous methods of epoxide formation,[2] several synthons can be envisioned as arising from this strategy. Preparation of *β*-aminothiols featuring primary amines suitable for amide formation may be more challenging. A potential strategy could employ addition of an benzylamine to the desired thioepoxide, followed by removal of the benzyl group by hydrogenolysis[7] (Scheme 8). The efforts described above should serve as a useful starting point towards the synthesis of more sterically robust and densely functionalized N and S rich frameworks for this project.

C.2. Experimental Section

General Information. See Chapter 2, Section 2.7 for information pertaining to common laboratory reagents and solvents.

Physical Methods. See Chapter 2, Section 2.7 for information pertaining to FTIR, ^{1}H and ^{13}C NMR spectroscopy and ESI measurements.

tert-butyl (2-hydroxy-2,2-diphenylethyl)carbamate (1). To a batch of 534 mg (2.50 mmol) 1,1'-diphenylethanolamine[5] and 290 mg (2.90 mmol) triethylamine stirring in 5 mL CH_2Cl_2 was added 544 mg (2.49 mmol) Boc_2O. After 16 h stirring at RT, the reaction mixture was washed with satd. $NaHCO_3$(aq) and brine, dried over $MgSO_4$ and concentrated to **1** as light oil which solidified to 519 mg (1.66 mmol, 67%). ^{1}H NMR (400 MHz, $CDCl_3$, δ from TMS): 7.46 (d, 4H), 7.37 (t, 4H), 7.30 (t,

2H), 4.82 (br s, 1H, N*H*), 3.97 (d, 2H), 3.54 (br s, O*H*), 1.42 (s, 9H). ^{13}C NMR (100.6 MHz, $CDCl_3$, δ from TMS): 157.06 (*C*=O). 144.82, 128.27, 127.20, 126.25, 79.81, 78.37, 50.28, 28.31. FTIR (KBr pellet) ν_{max} (cm^{-1}): 3370 (s, br, N-H, O-H), 3085 (w), 3067 (w), 3035 (w), 3010 (w), 2982 (m), 2967 (w), 2934 (w), 1680 (s, C=O), 1598 (w), 1533 (s), 1493 (m), 1445 (m), 1435 (w), 1387 (m), 1366 (m), 1355 (m), 1303 (m), 1288 (m), 1274 (m), 1254 (m), 1165 (s), 1122 (m). 1103 (m), 1071 (m), 1058 (s), 1030 (w), 985 (w), 948 (w), 876 (m), 852 (w), 787 (w), 771 (w), 760 (w), 747 (s), 721 (m), 700 (s), 648 (w), 597 (m), 568 (w), 548 (m), 527 (m), 486 (w), 438 (m). LRESI-MS *(m/z)*: $[M + H]^+$ calcd for $C_{19}H_{24}NO_3$, 314.4; found, 314.2.

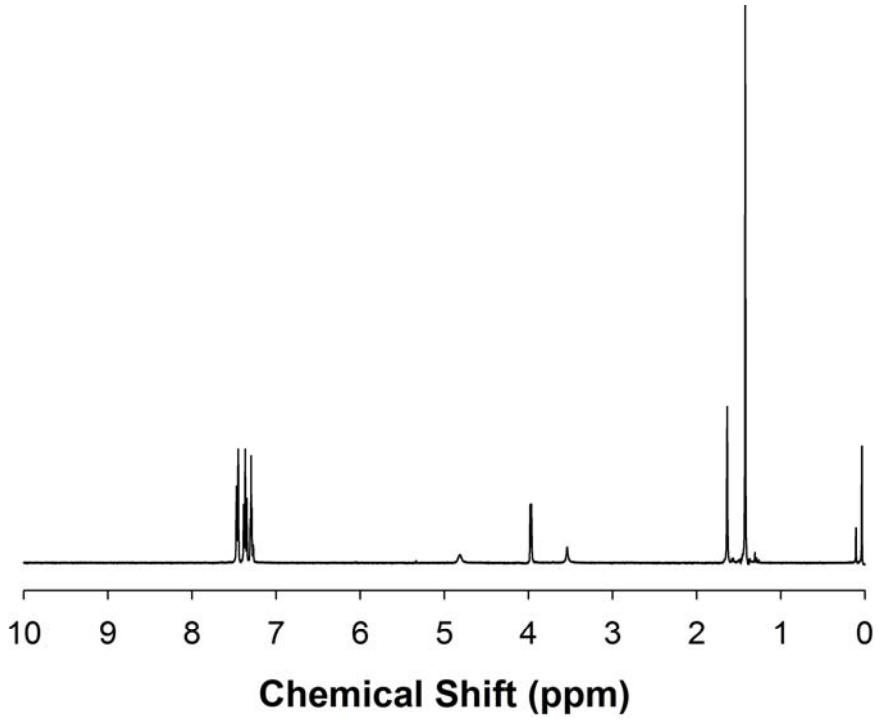

Figure 1. ^{1}H NMR of **1** in $CDCl_3$ (peak at 1.60 ppm is from H_2O present in sample).

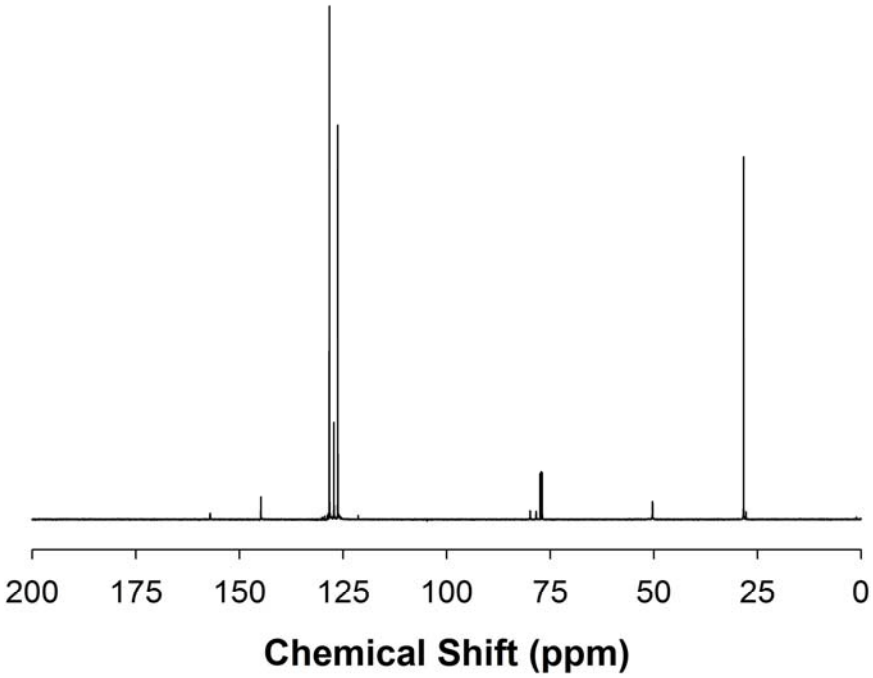

Figure 2. ^{13}C NMR of **1** in $CDCl_3$ (signal at 77.16 ppm is from solvent)

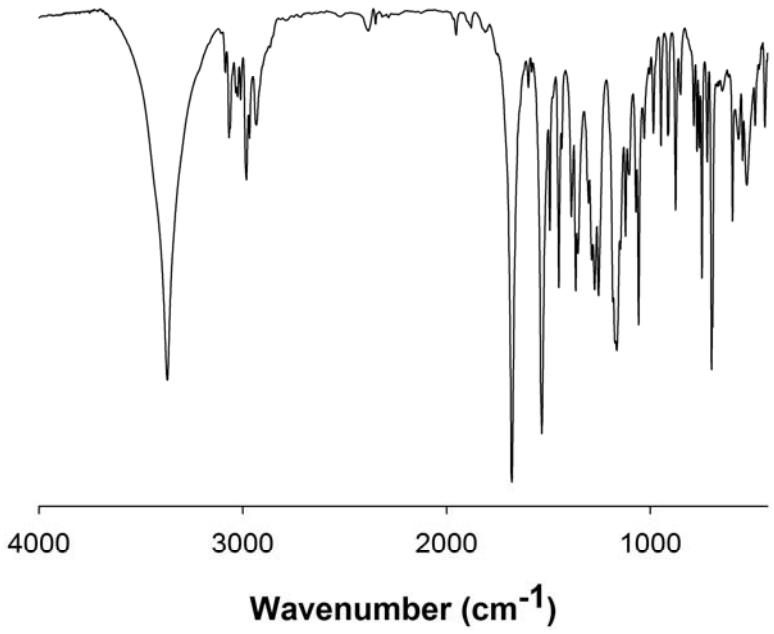

Figure 3. FTIR (KBr matrix) of **1**.

tert-butyl (2-mercapto-2,2-diphenylethyl)carbamate (2). A batch of 204 mg (0.651 mmol) 1 and 15.0 mg (0.833 mmol) H_2O were dissolved in 10 mL

degassed toluene and 164 mg (0.405 mmol) Lawesson's Reagent was added. The solution was warmed to 50 °C. After 2 h, the reaction mixture was cooled to RT, concentrated to dryness, taken up in CH_2Cl_2, washed with satd. $NaHCO_{3(aq)}$ and brine, dried over $MgSO_4$ and concentrated to a yellow residue. ^1H NMR analysis revealed products formulated as **2**, **3** and **4** in roughly 43%, 43% and 14% yield, respectively. Compound **4** was isolated by trituration from hexanes; **2** and **3** were isolated from the mother liquor by preparative TLC (silica gel, 15:1 hexane/EtoAc). Characterization for **2** is as follows: ^1H NMR (400 MHz, $CDCl_3$, δ from TMS): 7.43 (d, 4H), 7.36 (t, 4H), 7.21 (d, 2H, coincidental with protio solvent). FTIR (KBr pellet) ν_{max} (cm^{-1}): 3446 (m, br, NH), 2963 (m), 2925 (m), 2853 (m), 1717 (m, C=O), 1697 (m, C=O), 1685 (m, C=O), 1507 (m), 1497 (m), 1457 (m), 1449 (m), 1385 (m), 1376 (m), 1339 (w), 1261 (s), 1169 (s), 1096 (s), 1027 (s), 877 (w), 803 (s), 758 (w), 700 (w), 599 (w), 473 (w). LRMS-ESI (*m/z*): $[M + H]^+$ calcd for $C_{19}H_{24}NO_2S$, 330.2; found, 330.2. M^- calcd for $C_{19}H_{22}NO_2S$, 328.1; found, 328.2.

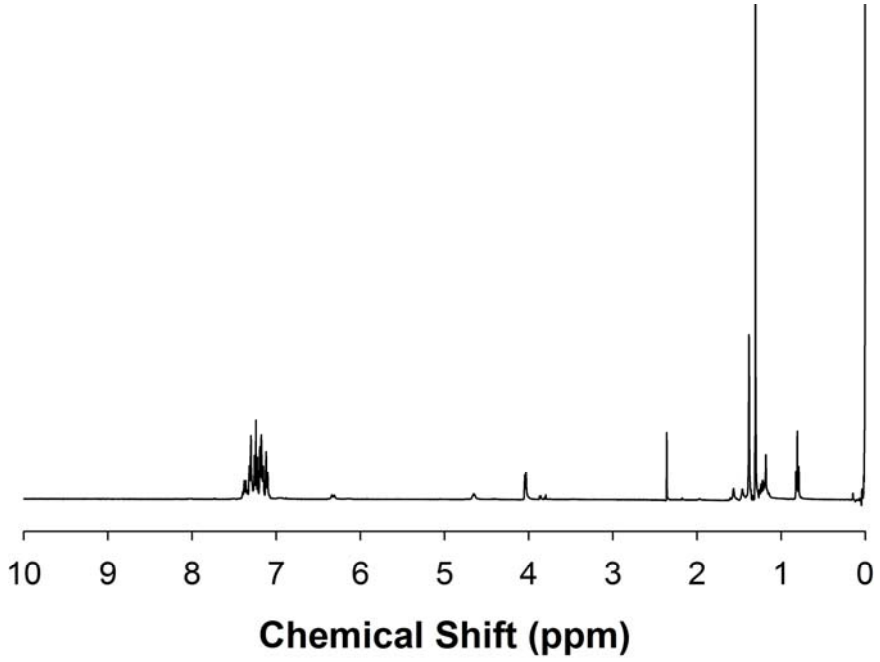

Figure 4. ^{1}H NMR of **2** and **3** (1:0.6, respectively) in $CDCl_3$. Although **2** can be isolated in pure form, minute amounts were obtained and the exchangeable protons (NH and SH) were not observed in the corresponding spectrum.

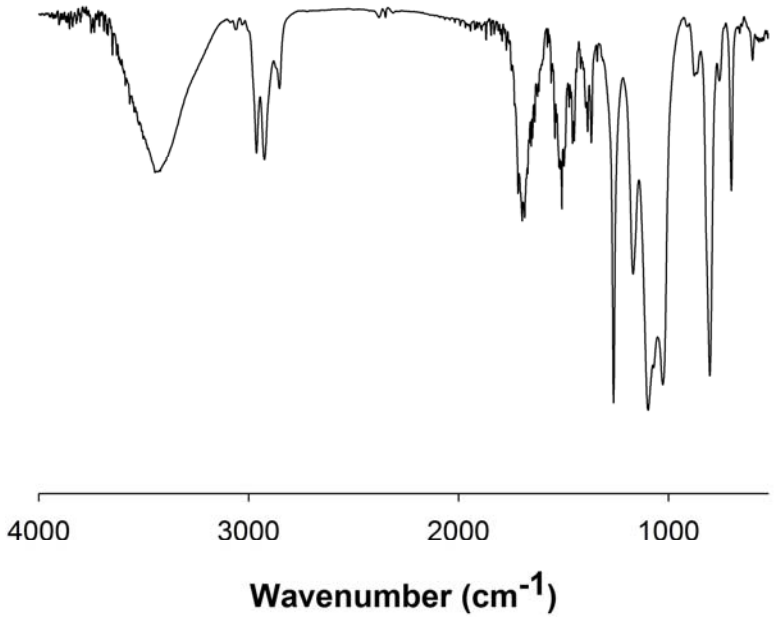

Figure 5. FTIR (KBr matrix) of **2**.

tert-butyl (2,2-diphenylvinyl)carbamate (3). ^{1}H NMR (400 MHz, $CDCl_3$, δ from TMS): 7.48 (t, 2H), 7.37 (t, 1H), 7.23 (m, 7H), 6.40 (d, 1H), 1.46 (s, 9H). FTIR (KBr pellet) ν_{max} (cm^{-1}): 3432 (m, N-H), 3420 (m, N-H), 3081 (w), 3067 (m), 3056 (w), 3023 (w), 2992 (w), 2967 (m), 2917 (w), 2868 (w), 2849 (w), 1723 (s, C=O), 1645 (s, C=O), 1496 (s), 1479 (s), 1471 (s), 1456 (s), 1444 (s), 1392 (m), 1369 (m), 1365 (m), 1354 (m), 1308 (w), 1277 (s), 1268 (s), 1225 (s), 1158 (s), 1149 (s), 1140 (s), 1071 (m), 1059 (s), 1026 (m), 931 (w), 907 (m), 889 (w), 881 (m), 865 (s), 791 (m), 768 (s), 757 (s), 706 (s), 699 (s), 630 (m), 607 (m), 584 (m), 556 (s), 516 (w), 465 (w). LRMS-ESI (*m/z*): $[M + H]^+$ calcd for $C_{19}H_{22}NO_2$, 296.4; found, 296.2.

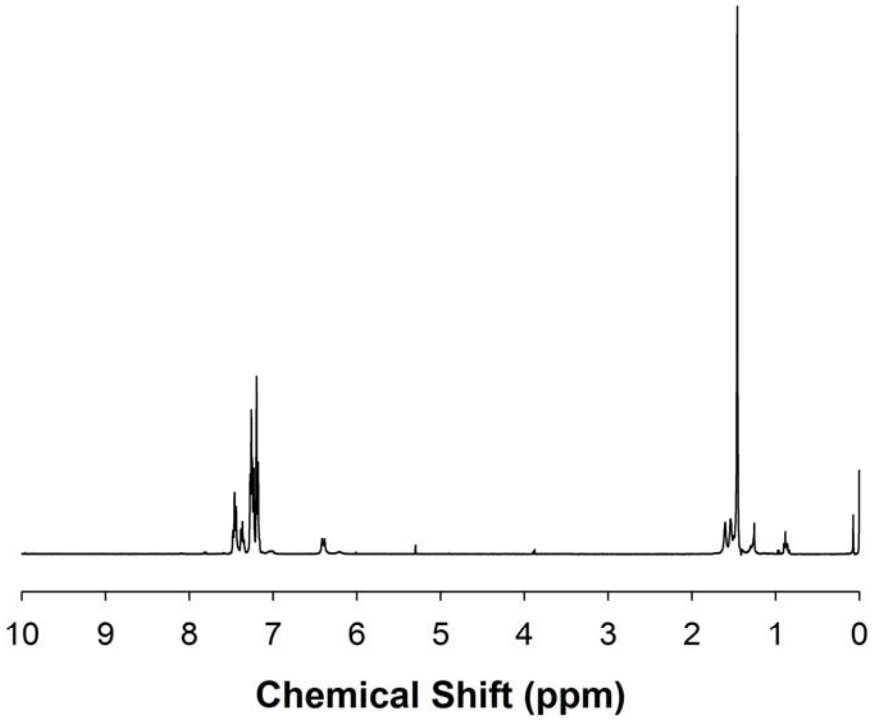

Figure 6. ^{1}H NMR of **3** in $CDCl_3$ (signal at 5.30 ppm is from CH_2Cl_2 present in sample; 1.26 and 0.88 ppm are from hexane).

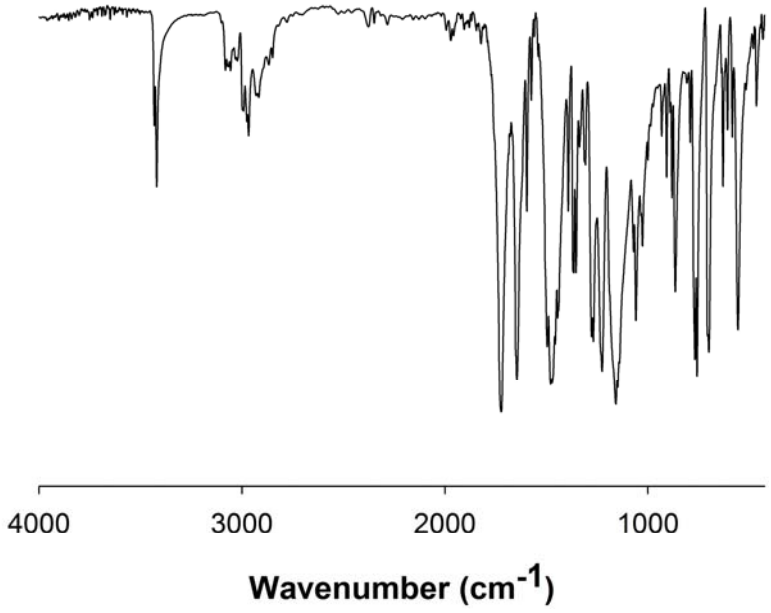

Figure 7. FTIR (KBr matrix) of **3**.

5,5-diphenylthiazolidin-2-one (4). 7.32 (d, 4H), 7.38 (t, 4H), 733 (t, 2H), 5.22 (s, 1H, N*H*), 4.22 (s, 2H). FTIR (KBr pellet) ν_{max} (cm^{-1}): 3434 (w, br, N-H), 2963 (m), 2906 (w), 2853 (w), 1741 (m, C=O), 1635 (w), 1598 (w), 1499 (w), 1449 (w), 1413 (w), 1364 (w), 1262 (s), 1096 (s), 1020 (s), 865 (m), 800 (s), 698 (m), 662 (w), 620 (w), 570 (w), 520 (w), 492 (w), 471 (w).

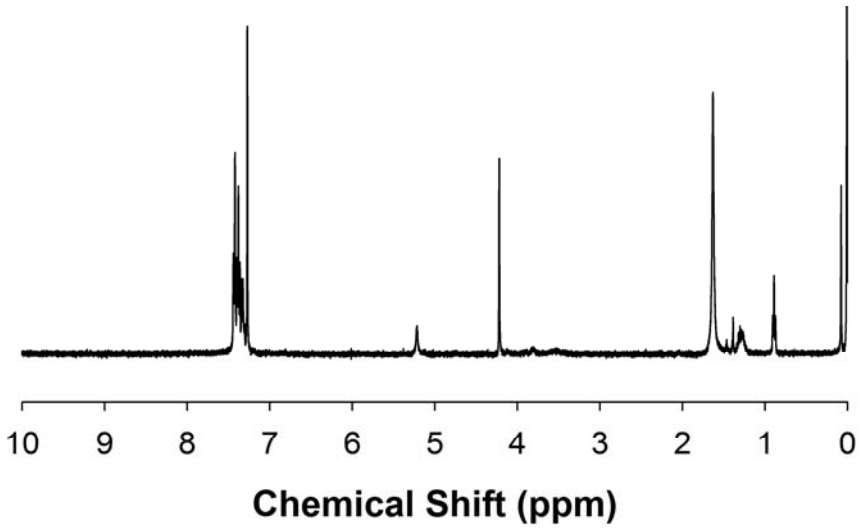

Figure 8. ^{1}H NMR of **4** in $CDCl_3$ (signal at 1.60 ppm is from D_2O present in sample; 1.26 and 0.88 ppm are from hexane).

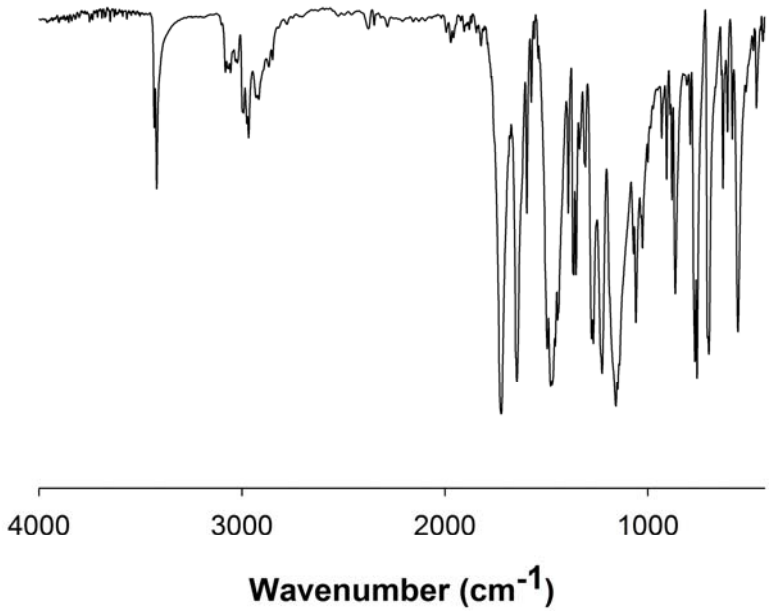

Figure 9. FTIR (KBr matrix) of **4**.

2-thioadamantanone (8). A batch of 1.06 g (7.03 mmol) 2-adamantanone and 1.790 g (4.43 mmol) Lawesson's Reagent were dissolved in 80 mL degassed toluene and the solution heated to reflux for 16 h. The resultant pink solution was removed cooled to RT and concentrated to dryness; caution must be taken in this step not to heat the reaction mixture as the volume decreases. The resultant solid residue was purified by flash chromatography (silica gel, 10:1 hexane/EtOAc), in most instances the product (R_f = 0.59, 2:1 hexane/EtOAc) must be chromatographed more than once. 0.355 g (2.13 mmol, 30%) of **8** was isolated as foul smelling, pink-orange solids. ^{1}H NMR (400 MHz, $CDCl_3$, δ from TMS): 3.46 (s, 2H), 2.10 (m, 8H), 2.01 (m, 4H). ^{13}C NMR (100.6 MHz, $CDCl_3$, δ from TMS): 57.70, 41.35, 36.77, 27.63 *(*C*=S not observed). FTIR (KBr pellet) ν_{max} (cm^{-1}): 2962 (m), 2913 (s), 2850 (m), 1468 (w), 1448 (m), 1403 (w), 1380 (m), 1351 (w), 1303 (s), 1282 (m), 1261 (s),

1220 (m), 1147 (s), 1094 (s), 1050 (s), 1021 (s), 962 (w), 947 (m), 862 (m), 800 (s), 724 (w), 701 (w), 693 (w), 660 (w), 627 (w), 595 (w), 542 (w), 465 (w), 438 (w).

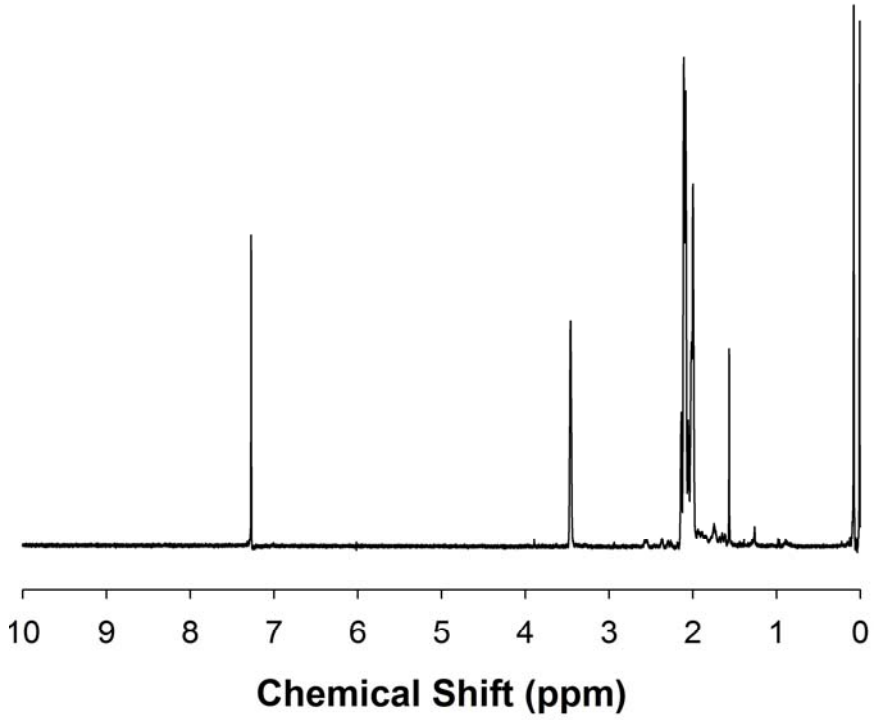

Figure 10. ^{1}H NMR of **8** in $CDCl_3$ (signal at 7.27 ppm is from protio solvent).

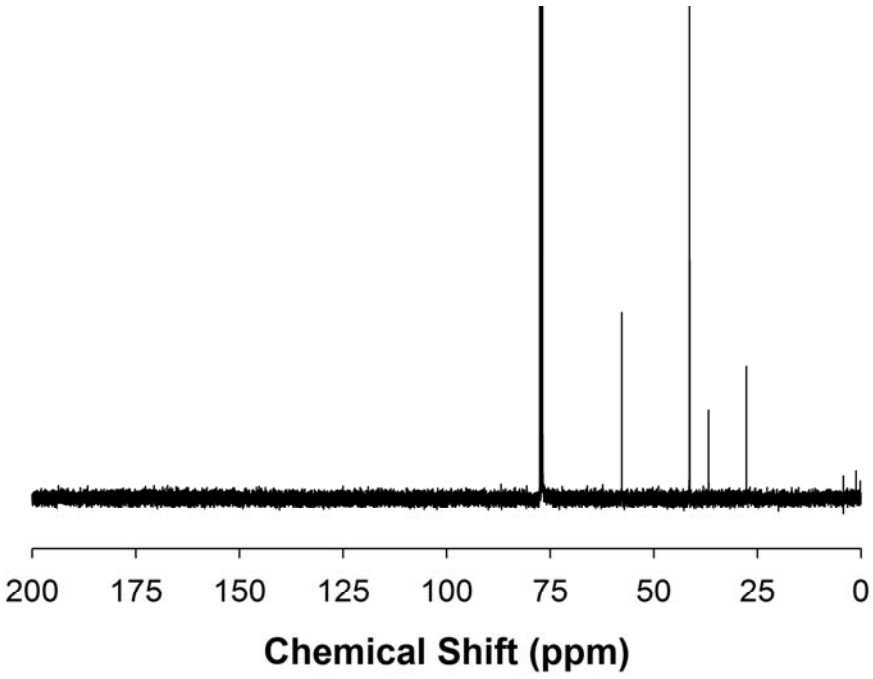

Figure 11. ^{13}C NMR of **8** in $CDCl_3$ (signal at 77.16 ppm is from solvent)

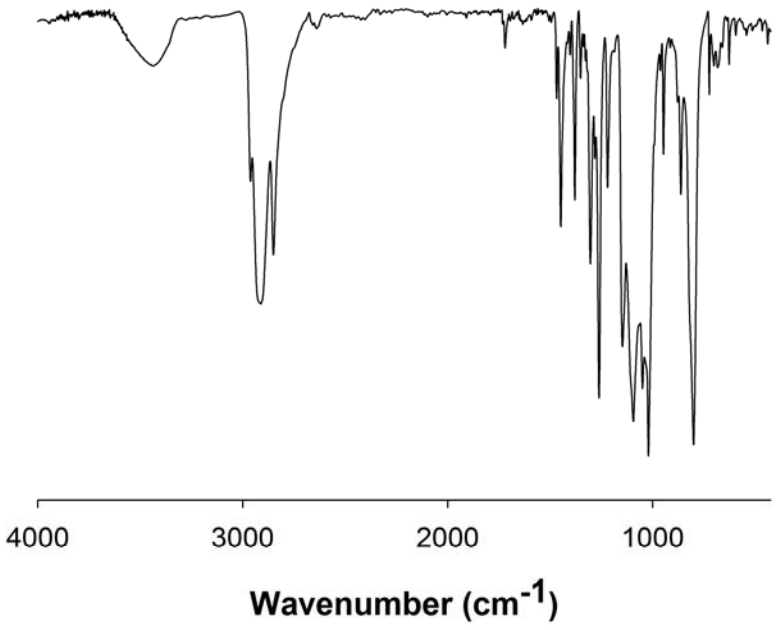

Figure 12. FTIR (KBr matrix) of **8**.

(2-mercaptoadamantan-2-yl)acetonitrile (9). A batch of 118 mg (2.87 mmol) acetonitrile in 5 mL THF was cooled to -78 °C (dry ice/ acetone bath) and 1.50 mL of 1.60 M ^{n}BuLi in hexanes (2.40 mmol) was carefully added. After 1 h stirring, 420 mg (2.53 mmol) **8** was added in 5 mL THF. After 15 min, the reaction mixture was allowed to warm to RT. After 90 min stirring at RT, the reaction mixture was quenched with satd. $NH_4Cl_{(aq)}$ (stronger acid will affect thiol elimination), and diluted with 50 mL Et_2O. The reaction mixture was washed with brine, dried over $MgSO_4$ and concentrated to a colorless oil. Flash chromatography (silica gel, 4:1 hexane/EtOAc) afforded 224 mg (1.08 mmol, 45%) **9** as a white residue. ^{1}H NMR (400 MHz, $CDCl_3$, δ from TMS): 3.08 (s, 2H0, 2.49 (d, 2H), 2.06 (s, 1H, S*H*), 1.92 (m, 6H), 1.75 (m, 6H).). ^{13}C NMR (100.6 MHz, $CDCl_3$, δ from TMS): 117.68 (*C*N), 53.33, 38.80, 37.73, 34.02, 33.26, 33.18, 27.48, 26.78. FTIR (KBr pellet) ν_{max} (cm^{-1}): 2961 (w), 2911 (s), 2859 (m), 2668 (w, S-H), 2556 (w, S-H), 2247 (w, CN), 1473 (w), 1457 (m), 1442 (w), 1418 (m), 1352 (w), 1340 (w), 1304 (w), 1261 (s), 1240 (w), 1192 (w), 1098 (s), 1021 (s), 978 (m), 950 (w), 918 (w), 866 (w), 800 (s), 678 (w), 669 (w), 658 (w), 608 (w), 501 (w). LRMS-ESI (*m/z*): M^- calcd for $C_{12}H_{16}NS$, 206.1; found, 206.0. $[M + H]^+$ calcd for $C_{12}H_{18}NS$, 208.1; found, 208.0.

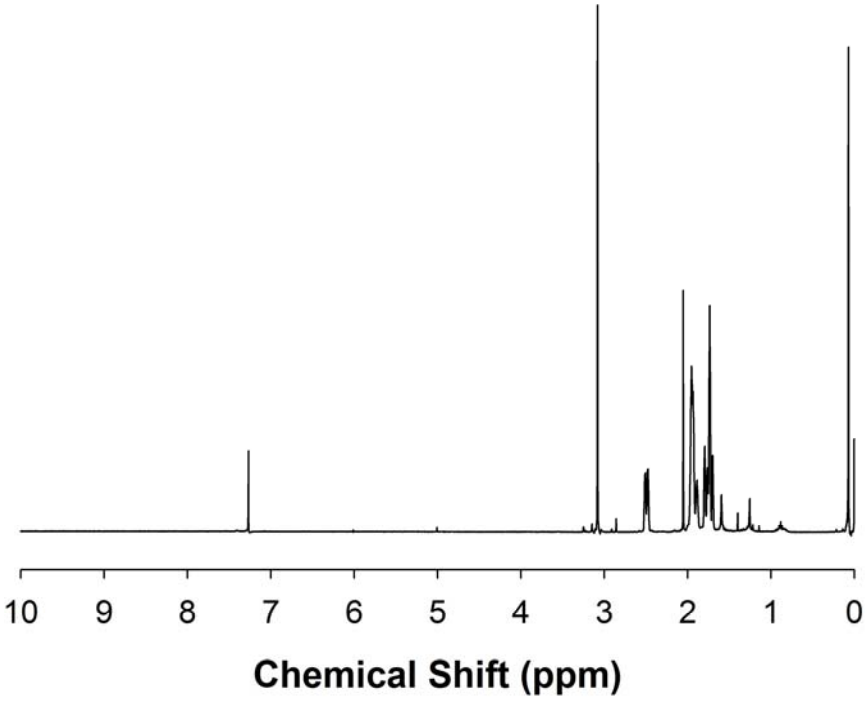

Figure 13. ^{1}H NMR of **9** in $CDCl_3$ (signal at 7.27 ppm is from protio solvent).

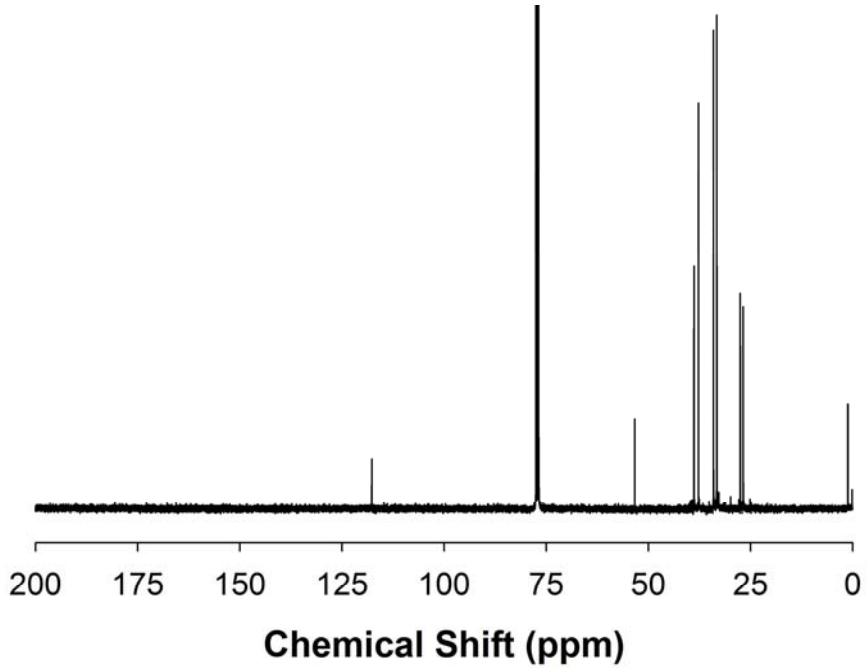

Figure 14. ^{13}C NMR of **9** in $CDCl_3$ (signal at 77.16 ppm is from solvent).

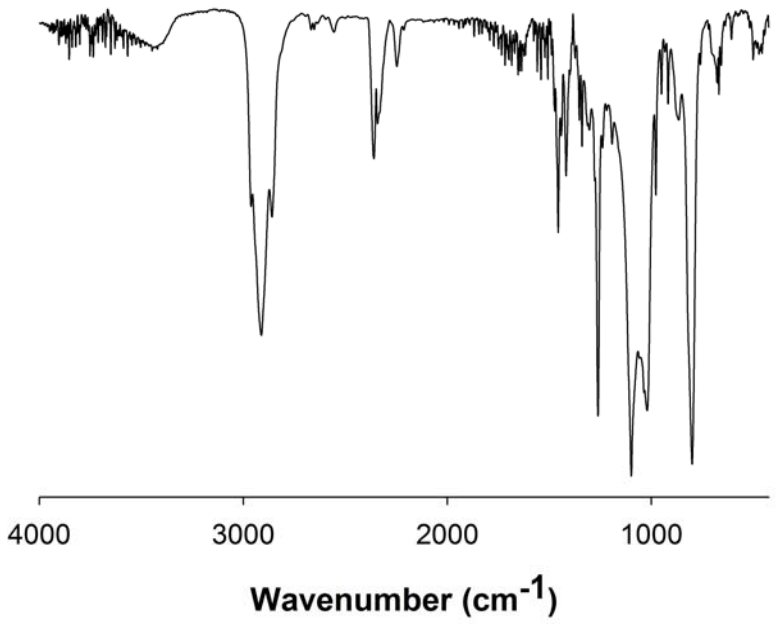

Figure 15. FTIR (KBr matrix) of **9**.

3,3-diphenyl-3-((tetrahydro-2H-pyran-2-yl)thio)propanenitrile (10). A batch of 1.080 g (3.81 mmol) 2-(benzhydrylthio)tetrahydro-2H-pyran[10] was dissolved in 30 mL Et2O and cooled to -78 °C (dry ice/ acetone bath) and 2.60 mL of 1.6 M ^{n}BuLi in hexanes (4.20 mmol) was carefully added and the reaction mixture subsequently warmed to 0 °C and stirred for 1 h. The deep orange reaction mixture was cooled to -78 °C and 413 mg (3.45 mmol) bromoacetonitrile in 15 mL Et_2O was added. The reaction warmed to RT and the resultant brown mixture stirred for 16 h. The reaction mixture was washed with water and brine, and the aqueous pool subsequently extracted with Et_2O. The organic portions were pooled and concentrated to a brown residue. Flash chromatography (silica gel, 19:1 hexanes/EtOAc) afforded 559 mg (1.73 mmol, 50%) of **10** as a pale, yellow oil which solidified upon standing. ^{1}H NMR (400 MHz, $CDCl_3$, δ from TMS): 7.36 (m, 10H),

4.16 (m, 2H), 3.66 (q, 2H), 3.40 (s, 1H), 1.74 (m, 2H), 1.62 (m, 2H), 1.50 (m, 2H). ^{13}C NMR (100.6 MHz, $CDCl_3$, δ from TMS): 143.83, 142.12, 128.58, 128.55, 128.38, 128.00, 127.86, 127.74, 117.86 (*C*N), 81.80, 64.48, 58.03, 38.54, 31.26, 25.52, 21.79. FTIR (KBr pellet) ν_{max} (cm^{-1}): 3086 (w), 3058 (w), 3033 (w), 2941 (m), 2909 (w), 2862 (w), 2842 (w), 2247 (w, CN), 1599 (w), 1580 (w), 1493 (w), 1463 (w), 1444 (m), 1384 (s), 1335 (m), 1323 (w), 1284 (w), 1264 (m), 1200 (w), 1188 (m), 1172 (w), 1101 (s), 1076 (s), 1034 (s), 1007 (s), 984 (m), 912 (w), 896 (w), 881 (w), 866 (w), 828 (w), 809 (m), 761 (m), 744 (s), 720 (m), 698 (s), 661 (m), 637 (m), 618 (w), 593 (w), 582 (w), 547 (w), 510 (w), 481 (w).). LRMS-ESI (*m/z*): $[M + Na]^+$ calcd for $C_{20}H_{21}NNaOS$, 346.1; found, 346.2.

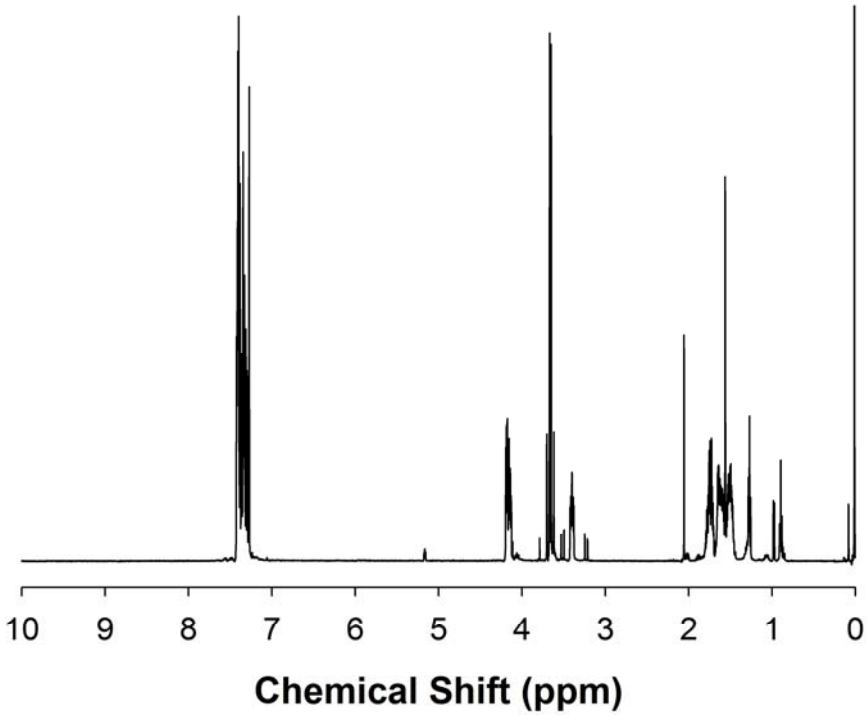

Figure 16. ^1H NMR of **10** in $CDCl_3$ (sharp signal at 1.60 is from H_2O present in the sample; 1.26 and 0.88 ppm are from residual hexane).

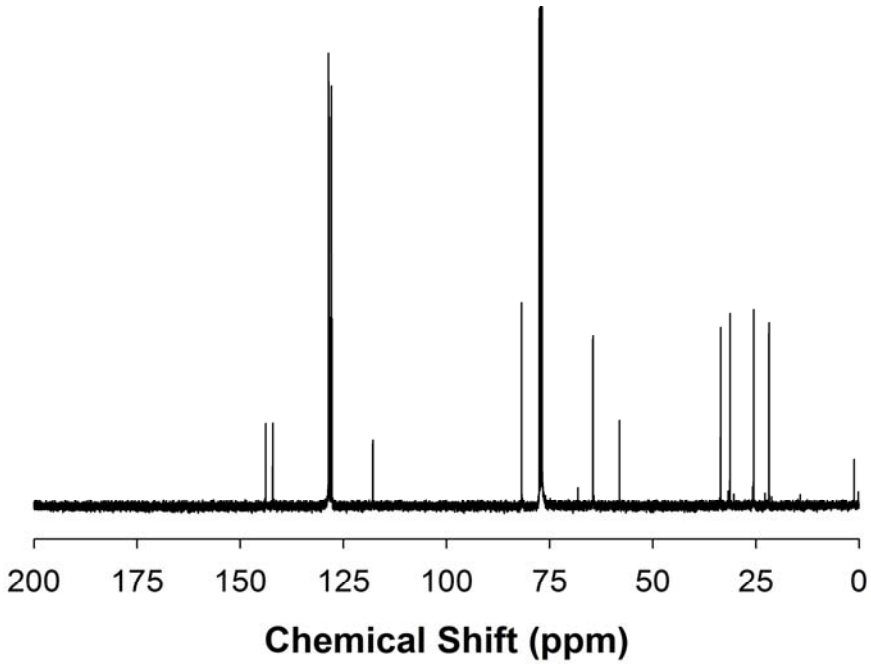

Figure 17. ^{13}C NMR of **10** in $CDCl_3$ (signal at 77.16 ppm is from solvent).

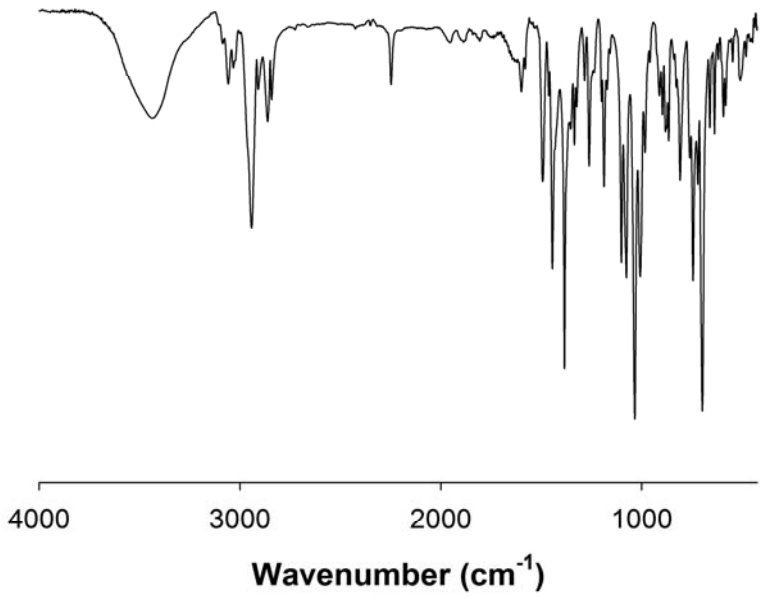

Figure 18. FTIR (KBr matrix) of **10**.

3,3-diphenyl-3-((tetrahydro-2H-pyran-2-yl)thio)propan-1-amine (11). A batch of 560 mg (1.73 mmol) **10** was dissolved in 15 mL THF and 98.0 mg (2.58

mmol) $LiAlH_4$ was added. Immediate effervescence was observed and the reaction mixture changed from yellow to brown. The reaction mixture was heated to reflux for 2h, than cooled to RT. A few drops H_2O were carefully added to quench any remaining $LiAlH_4$. The copious precipitate was removed by filtration and washed with 25 mL 4:1 CH_2Cl_2/MeOH. The filtrate was dried over $MgSO_4$ and concentrated to 434 mg (1.33 mmol, 77%) **11** as an amber oil. ^{1}H NMR (400 MHz, $CDCl_3$, δ from TMS): 7.26 (m, 10H), 4.05 (t, 1H), 3.63 (m, 2H), 2.59 (m, 2H), 2.53 (m, 1H), 2.24 (3H, including N*H*$_2$), 1.57 (m, 6H). ^{13}C NMR (100.6 MHz, $CDCl_3$, δ from TMS): 144.69, 128.63, 127.92, 126.37, 62.70, 48.89, 40.53, 38.94, 33.87, 32.40, 32.28, 24.69. FTIR (KBr pellet) ν_{max} (cm^{-1}): 3418 (m, br, N-H), 3084 (w), 3059 (w), 3026 (w), 2934 (w), 2860 (w), 1599 (m), 1538 (w), 1494 (m), 1451 (m), 1393 (w), 1335 (w), 1261 (w), 1189 (w), 1155 (w), 1074 (m), 1051 (m), 1031 (m), 919 (w), 877 (w), 866 (w), 805 (w), 751 (m), 701 (s), 631 (m), 618 (m), 587 (m), 563 (m), 538 (w), 477 (w). LRMS-ESI (*m/z*): $[M + H]^+$ calcd for $C_{20}H_{26}NOS$, 328.2; found, 328.2.

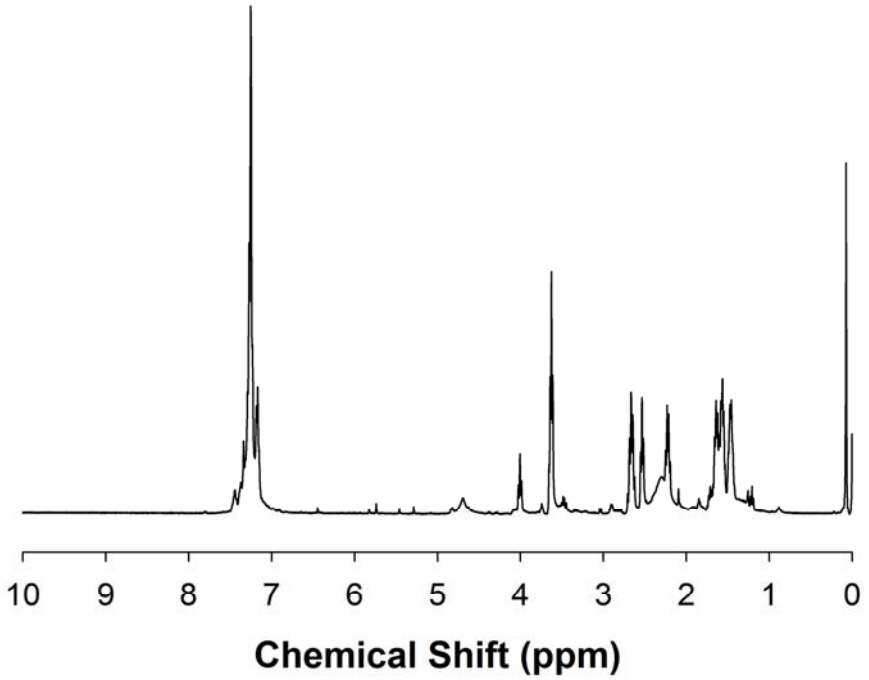

Figure 19. ^{1}H NMR of **11** in $CDCl_3$.

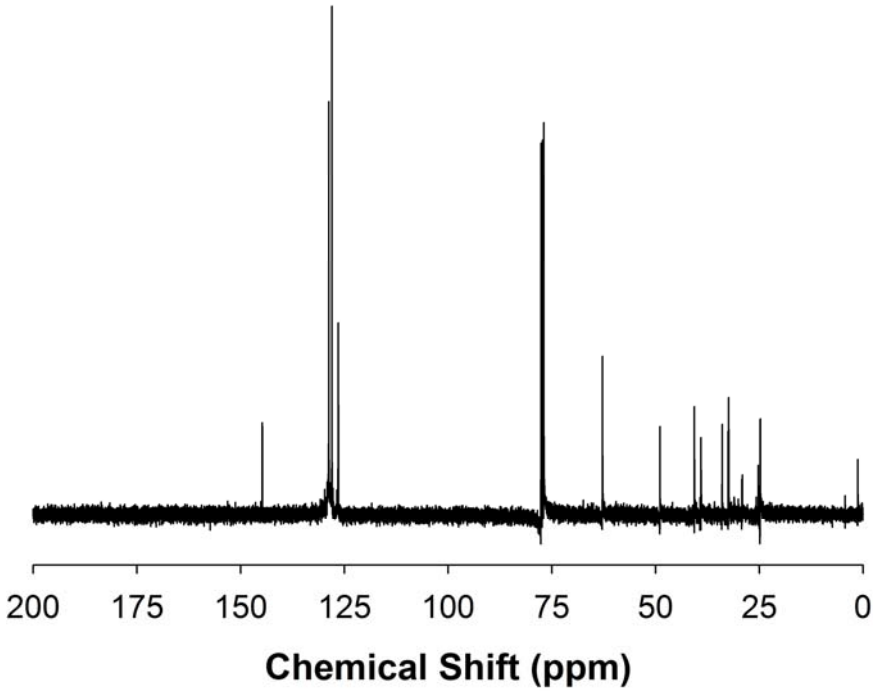

Figure 20. ^{13}C NMR of **11** in $CDCl_3$ (signal at 77.16 ppm is from solvent).

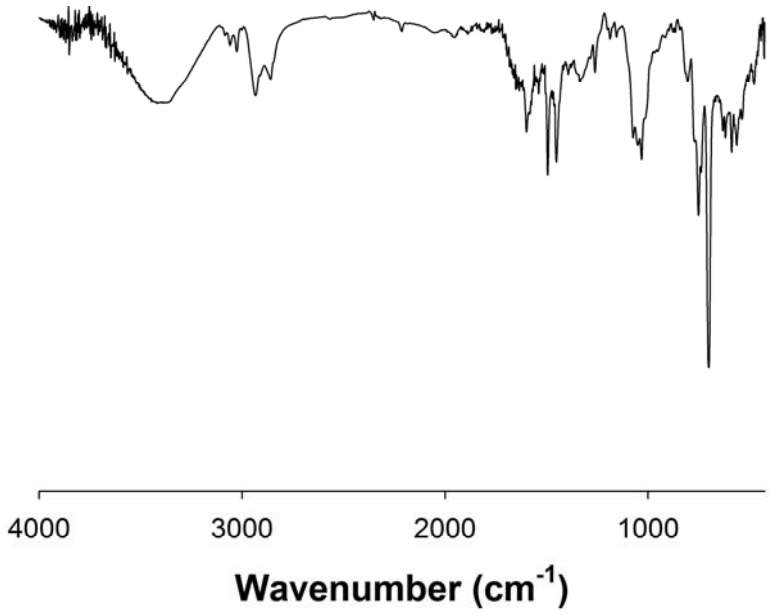

Figure 21. FTIR (KBr matrix) of **11**.

N,N'-(disulfanediylbis(2-methylpropan-2-yl-1-ylidene))bis(1-(pyridin-2-yl)methanamine (14). A batch of 2.355 g (11.41 mmol) 2,2,5,5-tetramethyl-3,4-dithiahexane-1,6-dial[14] and 2.549 g (23.57 mmol) picolylamine were combined in 25 mL dry MeOH heated to reflux. After 3 h, the golden-yellow solution was cooled to RT, dried over Na2SO3 and concentrated to 3.991 g (10.32 mmol, 90%) of **14** as a golden-yellow oil. This product decomposes over the course of days at RT. ^{1}H NMR (400 MHz, $CDCl_3$, δ from TMS): 8.53 (d, 2H), 7.66 (m, 4H), 7.38 (d, 2H), 7.15 (t, 2H), 4.76 (s, 4H), 1.44 (s, 12H). FTIR (KBr pellet) ν_{max} (cm^{-1}): 3369 (w), 3299 (w), 3051 (w), 3008 (w), 2963 (m), 2922 (m), 2859 (m), 1657 (s), 1588 (w), 1569 (m), 1473 (s), 1432 (s), 1383 (m), 1361 (s), 1329 (m), 1251 (w), 1211 (w), 1167 (w), 1147 (m), 1114 (s), 1072 (m), 1048 (m), 992 (s), 966 (m), 922 (m), 836 (w), 816 (w), 749 (s), 729 (s), 702 (m), 675 (m), 632 (m), 608 (s), 508 (w), 468 (w).

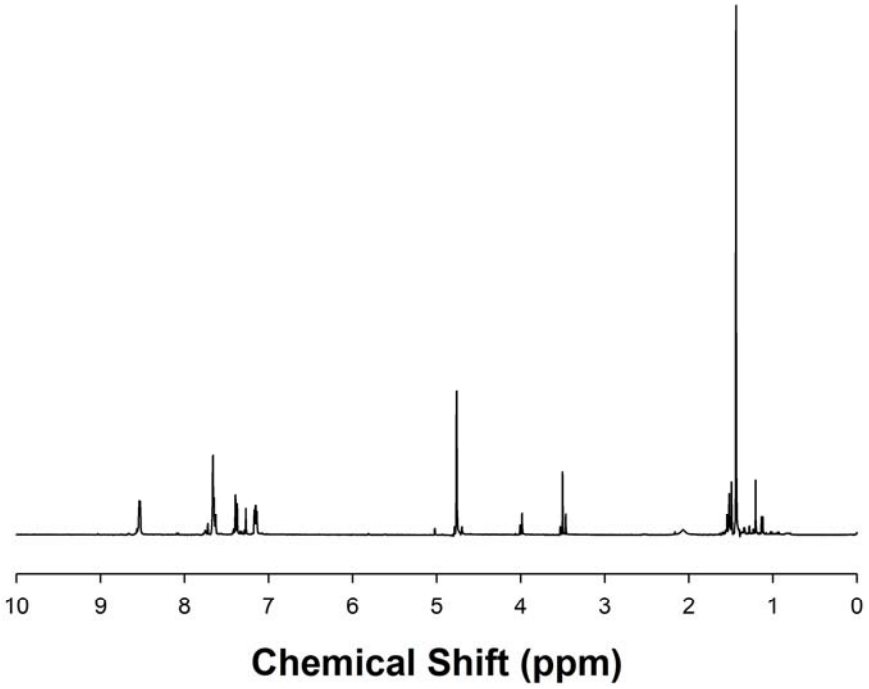

Figure 22. ^{1}H NMR of **14** in $CDCl_3$ (signal at 7.27 ppm is from protio solvent).

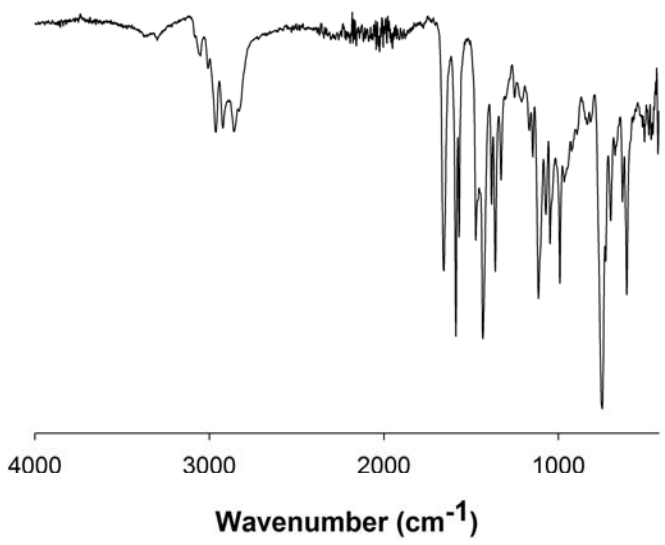

Figure 23. FTIR (KBr matrix) of **14**.

C.3 References

(1) Harrop, T. C.; Rodriguez, K.; Mascharak, P. K. *Synth. Commun.* **2003**, *33*, 1943.

(2) Smith, M. B.; March, J. *March's Advanced Organic Chemistry*; Wiley & Sons, Inc.: Hoboken, 2007.

(3) Ozturk, T.; Ertas, E.; Mert, O. *Chem. Rev.* **2007**, *107*, 5210.

(4) Nishio, T. *J. Org. Chem.* **1997**, *62*, 1106.

(5) Niederl, J. B.; Lay, R. *J. Am. Chem. Soc.* **1941**, *63*, 1498.

(6) Ohno, M.; Miyamoto, M.; Hoshi, K.; Takeda, T.; Yamada, N.; Ohtake, A. *J. Med. Chem.* **2005**, *48*, 5279.

(7) Wuts, P. G. M.; Greene, T. W. *Protective Groups in Organic Synthesis*; Wiley: New York, 1999.

(8) Kaiser, E. M.; Hauser, C. R. *J. Org. Chem.* **1968**, *33*, 3402.

(9) Zhang, X.; Jiang, X.; Zhang, K.; Mao, L.; Luo, J.; Chi, C.; Chan, H. S. O.; Wu, J. *J. Org. Chem.* **2010**, *75*, 8069.

(10) Berg, J. M.; Holm, R. H. *J. Am. Chem. Soc.* **1985**, *107*, 917.

(11) Bordwell, F. G.; Matthews, W. S.; Vanier, N. R. *J. Am. Chem. Soc.* **1975**, *97*, 442.

(12) Matthews, W. S.; Bares, J. E.; Bartmess, J. E.; Bordwell, F. G.; Cornforth, F. J.; Drucker, G. E.; Margolin, Z.; McCallum, R. J.; McCollum, G. J.; Vanier, N. R. *J. Am. Chem. Soc.* **1975**, *107*, 7006.

(13) Fox, S.; Stibrany, R. T.; Potenza, J. A.; Knapp, S. E.; Schugar, H. J. *Inorg. Chem.* **2000**, *39*, 4950.

(14) Roy, B.; du Moulinet d'Hardemare, A.; Fontecave, M. *J. Org. Chem.* **1994**, *59*, 7019.

(15) Brand, U.; Vahrenkamp, H. *Inorg. Chim. Acta* **2000**, *308*, 97.

(16) Snyder, H. R.; Stewart, J. M.; Ziegler, J. B. *J. Am. Chem. Soc.* **1947**, *69*, 2672.